

# Maximum Entropy Method in Superspace Crystallography

Von der Universität Bayreuth zur Erlangung der Würde  
eines Doktors der Naturwissenschaften (Dr. rer. nat.)  
genehmigte Abhandlung

vorgelegt von Lukáš Palatinus  
geboren am 12.06.1977 in Ústí nad Orlicí, Tschechische Republik

1. Gutachter: Prof. Dr. Sander van Smaalen
2. Gutachter: Prof. Dr. Jürgen Küppers

Tag der Einreichung: 2. September 2003  
Tag des Kolloquiums: 17. Dezember 2003



# Contents

<b>Abstract</b>	<b>vii</b>
<b>1 Introduction</b>	<b>1</b>
1.1 Introduction to superspace crystallography . . . . .	3
1.1.1 Aperiodic crystals . . . . .	3
1.1.2 Reciprocal space of modulated crystals . . . . .	5
1.1.3 Superspace embedding of the diffraction pattern . . . . .	6
1.1.4 Superspace electron density . . . . .	7
1.1.5 Atoms in superspace . . . . .	9
1.1.6 Composite crystal structures . . . . .	9
1.2 Maximum Entropy Method in crystallography . . . . .	12
1.2.1 The principle of the Maximum Entropy Method . . . . .	13
1.2.2 Crystallographic MEM equations . . . . .	14
1.2.3 Sakata-Sato algorithm . . . . .	16
1.2.4 Cambridge algorithm . . . . .	17
1.2.5 Maximum Entropy Method in superspace . . . . .	18
<b>2 Development of BAYMEM</b>	<b>19</b>
2.1 Introduction . . . . .	19
2.2 MEMSYS5 package . . . . .	20
2.2.1 Structure of the MEMSYS5 package . . . . .	20
2.2.2 Interface BAYMEM - MEMSYS . . . . .	21
2.2.3 The “True Bayesian” MEM . . . . .	26
2.2.4 Comparison of Cambridge and Sakata-Sato algorithms . . . . .	27
2.3 Static weighting . . . . .	30
2.4 Generalized F-constraints . . . . .	30
2.5 G-constraints . . . . .	30
2.6 Two-channel entropy . . . . .	33
2.7 Prior-derived F-constraints . . . . .	33
2.8 Prior electron density - program PRIOR . . . . .	34
2.9 Analysis of $\rho_{MEM}$ - program EDMA . . . . .	36
2.9.1 Interpolation . . . . .	37

2.9.2	Charge partitioning . . . . .	40
2.9.3	Definition of atomic position . . . . .	41
2.9.4	Positions of atoms in higher-dimensional electron density . . . . .	43
<b>3</b>	<b>The Generalized F-constraint</b>	<b>45</b>
3.1	Introduction . . . . .	45
3.2	The Method . . . . .	46
3.3	Computational details . . . . .	48
3.4	Results and Discussion . . . . .	53
3.4.1	The uniform prior . . . . .	53
3.4.2	The procrystal prior . . . . .	61
3.5	Conclusions . . . . .	62
<b>4</b>	<b>The Prior-derived F-constraints</b>	<b>65</b>
4.1	Introduction . . . . .	65
4.2	Theory . . . . .	65
4.3	A simple one-dimensional example . . . . .	67
4.4	Simulated data of oxalic acid dihydrate . . . . .	76
4.5	Conclusions . . . . .	77
<b>5</b>	<b>(LaS)<sub>1.14</sub>NbS<sub>2</sub></b>	<b>79</b>
5.1	The structure model and experimental data . . . . .	79
5.2	Details of the computations . . . . .	81
5.3	Discussion . . . . .	84
<b>6</b>	<b>Incommensurate Bi-III</b>	<b>89</b>
6.1	Introduction . . . . .	89
6.2	Experimental . . . . .	92
6.3	Structure refinements . . . . .	94
6.3.1	The basic structure . . . . .	94
6.3.2	The modulated structure . . . . .	95
6.3.3	The commensurate approximation . . . . .	98
6.4	Application of the MEM . . . . .	98
6.5	Discussion . . . . .	103
6.6	Conclusions . . . . .	107
<b>7</b>	<b>Incommensurate (NH<sub>4</sub>)<sub>2</sub>BeF<sub>4</sub></b>	<b>109</b>
7.1	Introduction . . . . .	110
7.2	Experimental . . . . .	111
7.3	Structure refinements . . . . .	113
7.4	The ferroelectric structure as commensurately modulated structure . . . . .	116
7.5	The Maximum Entropy Method . . . . .	116
7.6	Discussion . . . . .	121

7.6.1	Description of the modulated structure . . . . .	121
7.6.2	Hydrogen bonding scheme . . . . .	125
7.6.3	The ferroelectric phase transition . . . . .	128
7.7	Conclusions . . . . .	130
<b>8</b>	<b>Conclusions</b>	<b>133</b>
<b>9</b>	<b>Zusammenfassung</b>	<b>137</b>
<b>A</b>	<b>BAYMEM - User manual</b>	<b>141</b>
A.1	Introduction . . . . .	141
A.2	Basic operation of BAYMEM . . . . .	142
A.3	Algorithms . . . . .	143
A.3.1	Sakata-Sato algorithm . . . . .	143
A.3.2	MEMSYS5 package . . . . .	144
A.4	Technical details . . . . .	148
A.4.1	Programming language and system requirements . . . . .	148
A.4.2	Execution . . . . .	148
A.5	Specification of input . . . . .	149
A.5.1	Types of input . . . . .	149
A.5.2	Format of the ASCII input file . . . . .	149
A.5.3	Specification of keywords . . . . .	149
A.5.4	Examples of typical input files . . . . .	161
A.6	Description of the output . . . . .	163
A.6.1	Electron density . . . . .	163
A.6.2	File jobname.BMout . . . . .	164
A.6.3	File jobname.BMlog . . . . .	167
A.6.4	File jobname.BMhst . . . . .	170
A.6.5	File jobname.BMcheck . . . . .	172
A.6.6	File jobname.BMsymb . . . . .	173
A.7	Run-time interaction with the program . . . . .	174
A.7.1	Program-to-user communication . . . . .	174
A.7.2	User-to-program communication . . . . .	174
A.8	Troubleshooting . . . . .	175
<b>B</b>	<b>EDMA - User manual</b>	<b>177</b>
B.1	Introduction . . . . .	177
B.2	Technical details . . . . .	178
B.2.1	Programming language and system requirements . . . . .	178
B.2.2	Execution . . . . .	178
B.2.3	Standard run of the program . . . . .	178
B.3	Specification of the input . . . . .	179
B.3.1	Types of input . . . . .	179

B.3.2	Format of the ASCII input file . . . . .	179
B.3.3	Specification of keywords . . . . .	180
B.3.4	Examples of input files . . . . .	186
B.4	Description of the output . . . . .	188
B.4.1	File outputbase.coo . . . . .	188
B.4.2	t-maps . . . . .	190
B.4.3	Atomic basins . . . . .	190
	<b>Bibliography</b>	<b>199</b>
	<b>List of Figures</b>	<b>201</b>
	<b>List of Tables</b>	<b>205</b>
	<b>Acknowledgements</b>	<b>207</b>
	<b>Erklärung</b>	<b>209</b>

# Abstract

This thesis discusses several aspects of the combination of the Maximum Entropy Method (MEM) for the reconstructions of the electron density with the superspace approach to the description of structures of aperiodic crystals. It is shown that the MEM in superspace provides a parameter-free reconstruction of the modulation functions with sufficient accuracy.

The MEM in superspace has been applied to diffraction data of several compounds. The computer program BAYMEM was developed for this purpose. BAYMEM allows electron densities of the ordinary 3D structures and the superspace electron densities of the aperiodic structures to be reconstructed using the same general principles. The program has been extended by adding features improving its versatility and accuracy of the results. The improvements include attaching of the set of subroutines MEMSYS5 to BayMEM, implementation of the method of the Generalized F-constraints and the static weighting, implementation of the G-constraints, of the Prior-derived F-constraints and of the two-channel entropy.

The second major computer program EDMA is a software tool for analysis of the electron densities in arbitrary dimension. The program analyzes the MEM electron density and extracts quantitative information about the atoms according to Bader's formalism "Atoms in molecules".

Two new variants of the constraints in the MEM have been developed in order to solve the problems with artifacts in the MEM reconstructions. The two methods are the Generalized F-constraints and the Prior-derived F-constraints. The concept of the Generalized F-constraints is based in the observation, that the standard F-constraint is not sufficiently strong to constrain the histogram of the normalized residuals of the structure factors to the expected Gaussian shape. Higher moments of the distribution of the normalized residuals were therefore used as the constraint in the MEM calculations. With these constraints significantly improved histograms were obtained.

The source of some artifacts in the MEM electron densities was identified to be the tendency of the MEM to estimate incorrectly those structure factors, that are not included in the experimental dataset. It is shown in that the missing structure factors can successfully be replaced by the structure factors derived from the procrystal electron density, that is known from the standard structure

refinement. If the structure factors derived from the procrystal prior electron density (the Prior-derived F-constraints) are used as additional constraints in the MEM calculation, the result is free of sharp artifacts and the quality of the reconstruction of the electron density is comparable with the results of multipole refinements.

To test the accuracy of the MEM in superspace, the method was applied to the dataset of the misfit-layer composite structure of  $(\text{LaS})_{1.14}\text{NbS}_2$ . It has been shown, that the MEM on the model structure factors reproduces the model modulation functions with accuracy better than 10% of the pixel size of the grid, on which the electron density was sampled.

The structure of the high-pressure phase III of Bi provided a prominent example illustrating the advantages of the MEM in superspace over the standard structure refinements. The MEM in superspace was applied to the diffraction data of Bi-III to extract more information about the modulation than obtained from the standard structure refinement. The modulation functions extracted from the MEM electron density revealed a block-wave-like shape of the modulation function of the Bi atom of the host structure, that indicates shifts of the atom between two stable environments rather than smooth harmonic variation of the position indicated by the modulation function from the standard refinement. Secondly, the MEM modulation function of the Bi atoms in channels allowed to better understand the nature of the most prominent feature of the modulated structure — the occurrence of the pairs of Bi atoms along the channels.

The incommensurately modulated structure of ammonium tetrafluoroberylate  $(\text{NH}_4)_2\text{BeF}_4$ , stable between 175K and 182K, was solved and refined in superspace. The known two-fold low-temperature superstructure of  $(\text{NH}_4)_2\text{BeF}_4$ , that is stable below 175K has been described in superspace as a commensurately modulated structure. With aid of this description the close relationship between the two structures has been found. The MEM was applied to the incommensurate structure to test the appropriateness of the refined harmonic structure model. The MEM has shown that the harmonic model is very accurate.

The principal result of this work is that the MEM in superspace was established as a reliable tool for the structure solutions of the modulated structure. Individual chapters present various aspects of the MEM applied to reconstructions of the electron densities in general and of the superspace electron densities in particular. Together they form a framework, that allows to use the MEM in superspace to extract novel information from the diffraction data of both the periodic and aperiodic structures, that cannot be obtained from the structure refinements.

# Chapter 1

## Introduction

The objective of this thesis is to present the application of the Maximum Entropy Method (MEM) to description of the structures of aperiodic crystals in superspace. The Maximum Entropy Method (Section 1.2) is a powerful tool, that can be used for model-free image reconstructions in many fields of science. Combination of this method with the superspace structure refinements (Section 1.1) opens new possibilities in the crystallography of aperiodic crystals, because it allows to infer a parameter-free shape of the modulation functions. Determination of the shape of the modulation functions is one of the main outputs of the structure analysis of aperiodic crystals. In the thesis the results are presented of the effort to combine the two methods. Such an effort spans a wide range of topics, including improvements of the methods (Chapters 3, 4), software development (Chapter 2) and application of the new method to real problems (Chapters 5, 6 and 7). Some chapters of this thesis have been published or are submitted as separate articles or as a part of an article. These chapters are included here exactly in the published form, without any changes apart from the layout of figures and tables. This work contains 8 chapters and 2 appendices:

**Chapter 1: Introduction:** Introduction to the superspace crystallography and description of the Maximum Entropy Method in crystallography.

**Chapter 2: Development of program BAYMEM after the year 2000:** Description of the changes in the computer program BAYMEM for the electron-density reconstruction from the diffraction data by the MEM in arbitrary dimensions. Theory underlying the operation of supplementary computer programs EDMA and PRIOR is also described.

**Chapter 3: The Generalized F-constraint in the Maximum Entropy Method – a study on simulated data:** An improvement to the MEM formalism is described that yields superior MEM results compared to the classical formalism. Published in: Palatinus, L. and van Smaalen, S. (2001) Acta Crystallogr. A **58**, pp. 559-567.

**Chapter 4: The Prior-derived F-constraints in the Maximum Entropy**

**Method:** Another method improving performance of the MEM on crystallographic problems is described.

**Chapter 5: The inorganic misfit layer compound  $(\text{LaS})_{1.14}\text{NbS}_2$  studied by the Maximum Entropy Method:**

The application of the MEM in superspace to the modulated structure of the layer composite structure of  $(\text{LaS})_{1.14}\text{NbS}_2$ . Published in: van Smaalen, S., Palatinus, L. and Schneider, M. (2003), *Acta Crystallogr. A* **59**, pp 459-469.

**Chapter 6: Origin of the incommensurability of the crystal structure of**

**the high-pressure phase III of Bi:** The structure of the high-pressure elemental composite structure of Bi-III is presented. The structure was solved by a combination of refinements in superspace and the Maximum Entropy Method in superspace. To be submitted as: Palatinus, L., van Smaalen, S., McMahon, M., Nelmes, R. I. and Degtyareva, O. (2003), *Acta Crystallogr. B*.

**Chapter 7: The structure of the incommensurate ammonium tetrafluoroberyllate studied by structure refinements and the Maximum entropy Method:**

The MEM in superspace is used to confirm the refined structure of  $(\text{NH}_4)_2\text{BeF}_4$  and to assess the observability of weak features in the electron density based on incomplete diffraction data. Submitted as: Palatinus, L., Amami, M. and van Smaalen, S. (2004), *Acta Crystallogr. B*.

**Chapter 8: Conclusions:** Summary of the results. The achievements of the Maximum Entropy Method in superspace are evaluated.**Appendix A: The crystallographic MaxEnt program BayMEM — User**

**manual:** User manual to the program BAYMEM. The program BAYMEM has been used in all applications of the MEM presented in this thesis.

**Appendix B: EDMA — a computer program for analysis of electron**

**densities in arbitrary dimension — User manual:** User manual to the program EDMA (Section 2.9). EDMA is able to extract the structural information from both ordinary and superspace electron densities.

## 1.1 Introduction to superspace crystallography

### 1.1.1 Aperiodic crystals

Crystals are assemblies of atoms, that exhibit a long-range positional order. The vast majority of the crystal structures<sup>1</sup> are three-dimensionally (3D) periodic, that means, that the structure of the whole crystal can be constructed as a periodic repetition of a small part of the crystal (unit cell) along three linearly independent directions (Giacovazzo et al., 1995). Aperiodic crystals lack this 3D periodicity, while they are still long-range ordered. The aperiodic crystals can be divided into three main classes (van Smaalen, 1995):

- Incommensurately modulated structures: These structures have an average 3D periodic structure, but the atoms are periodically shifted from their average position according to a modulation function with a period that is incommensurate with the periodicity of the basic structure. (Fig. 1.1). The real structure is therefore not periodic.

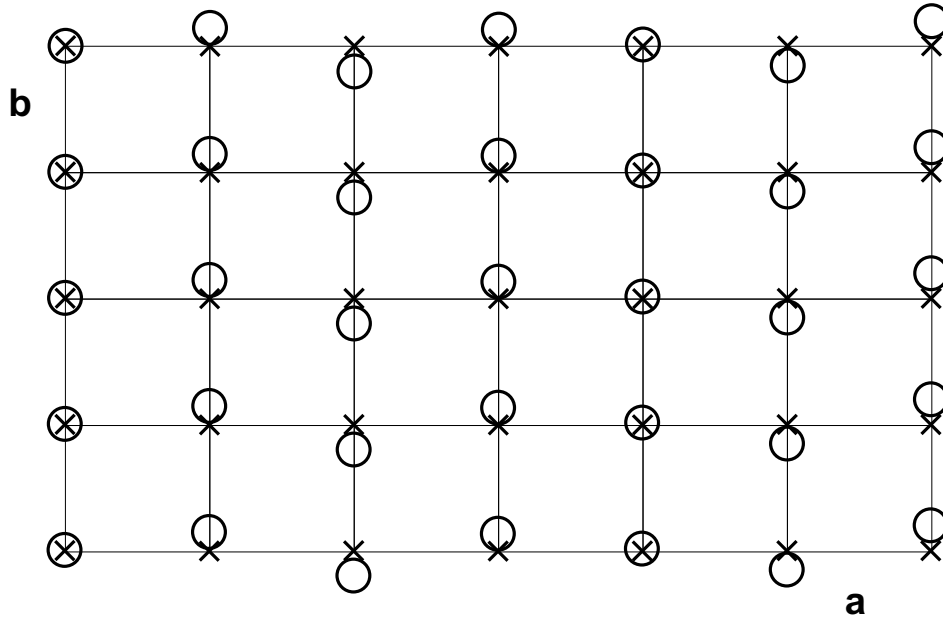


Figure 1.1: Schematic representation of a two-dimensional modulated crystal structure with one atom in the origin of the unit cell of the basic structure. Crosses represent the periodic basic structure, circles represent the positions in the modulated structure. The wavevector is  $\vec{q} = 0.372\vec{a}^*$  and the modulation function is  $\vec{u} = 0.2\vec{b}\sin(2\pi\vec{r}\cdot\vec{q})$ .

<sup>1</sup>The crystal structure is an idealized construction that describes the position of atoms in the crystal without taking into account disturbances like dislocations, inclusions etc.

- Composite crystal structures: These structures can be described as an intergrowth of two or more substructures (subsystems), each of them periodic in first approximation. The subsystems have a mutually incommensurate ratio of the unit cell dimensions in at least one direction. This incommensurateness disturbs the periodicity of the whole composite structure. Moreover, the interactions between the subsystems lead to incommensurate modulations in both subsystems (Fig. 1.2).

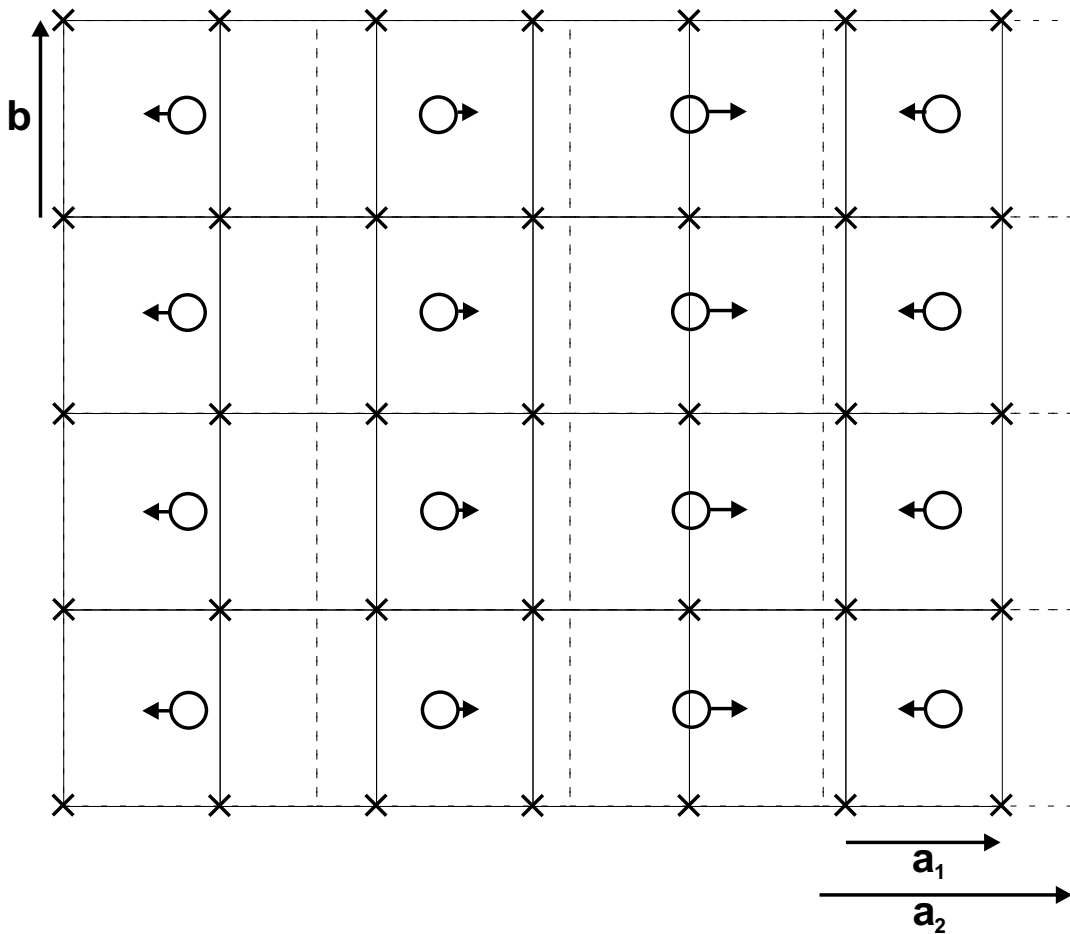


Figure 1.2: Schematic representation of a two-dimensional composite crystal with two subsystems. Crosses represent the first subsystem with one atom in the origin of the unit cell. Circles represent the second subsystem with one atom in the center of the unit cell. The first and second subsystems have the basic lattice vectors  $\vec{a}_1, \vec{b}$  and  $\vec{a}_2, \vec{b}$ , respectively. Full and dashed lines outline the lattice of the first and second subsystem, respectively. The ratio  $a_1/a_2 = 0.611$ . The arrows schematically denote the shifts of the atoms of the second subsystem due to the interactions with the atoms of the first subsystem. Shifts in the first subsystem are omitted for clarity.

- Quasicrystals: Quasicrystals exhibit a non-crystallographic point-symmetry, for example a 5-fold or 8-fold axis. Such symmetry is forbidden in periodic structures. The structures of quasicrystals are described using a different approach than is used for the description of the structures of incommensurately modulated crystals and composite crystals. Quasicrystals are not discussed in this thesis and the considerations in following sections are related only to the modulated structures and composite structures.

### 1.1.2 Reciprocal space of modulated crystals

The diffraction pattern of both periodic and aperiodic crystals is discrete. This is a direct consequence of the long-range order in both structures. However, an important difference between the two classes of crystals exist: The diffraction pattern of aperiodic crystals is not indexable with three integer indices, while the diffraction pattern of the ordinary periodic crystals is. The diffraction pattern of modulated crystals consists of reflections corresponding to the periodicity of the basic structure (main reflections) and reflections corresponding to the modulation wave (satellites, Fig. 1.3). Main reflections can be indexed with three

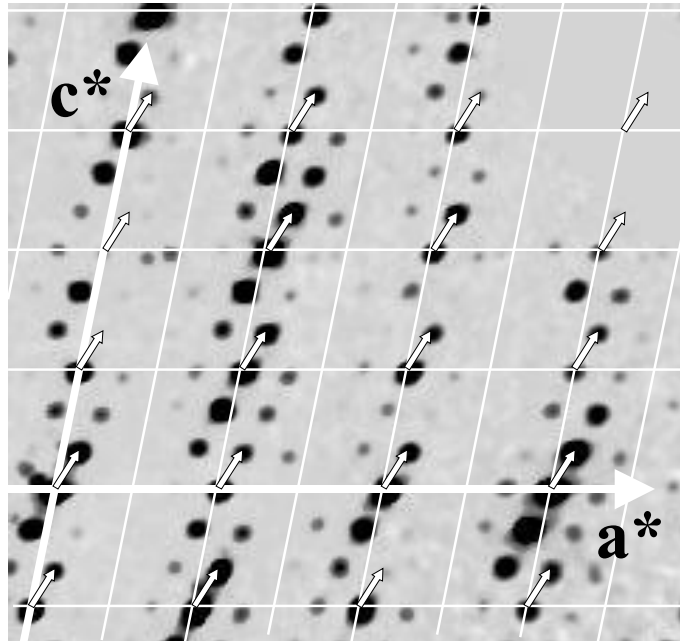


Figure 1.3: Diffraction pattern of the modulated  $\gamma$ -phase of  $\text{Na}_2\text{CO}_3$  in the  $h0l$  plane. Thin white lines connect main reflections. Satellites can be indexed with one wavevector  $\vec{q} = 0.182\vec{a}^* + 0.322\vec{c}^*$  (small white arrows). In this rare case satellites up to fourth order are visible. Reprinted with permission from Dušek et al. (2003).

basic vectors, while  $d$  additional vectors (q-vectors) are necessary to index the satellites. These  $(3 + d)$  vectors are not linearly independent and the q-vectors can be expressed as a linear combination of the first three reciprocal vectors (van Smaalen, 1995):

$$\vec{a}_{3+j}^* = \sum_{i=1}^3 \sigma_{ij} \vec{a}_i^*, \quad j = 1, \dots, d \quad (1.1)$$

At least one component of every row of the  $3 \times d$  matrix  $\sigma$  must be irrational, otherwise an alternative description could be found that indexes the diffraction pattern using less than  $(3 + d)$  integers. The rows of the matrix  $\sigma$  are formed by the components of the modulation wavevectors with respect to the three basic reciprocal vectors.

The diffraction vector  $\vec{H}$  of every Bragg reflection can then be indexed by  $(3 + d)$  integers:

$$\vec{H} = \sum_{k=1}^{3+d} h_k \vec{a}_k^* \quad (1.2)$$

### 1.1.3 Superspace embedding of the diffraction pattern

The diffraction pattern of an aperiodic crystal can be considered to be a projection on 3D space of a  $(3 + d)$ D weighted lattice (Fig. 1.4). Projections in general are not reversible, but due to the discrete nature of the diffraction pattern and limited number of reflections with significant intensity the  $(3 + d)$ D weighted lattice can be unambiguously reconstructed from the 3D projection (Fig. 1.4). In the  $(3 + d)$ D reciprocal space the reciprocal vectors become linearly independent. The usual construction of the basis  $\Sigma^*$  in  $(3 + d)$ D space is (van Smaalen, 1995):

$$\Sigma^* : \begin{cases} \vec{a}_{si}^* & = (\vec{a}_i^*, 0), & i = 1, 2, 3 \\ \vec{a}_{s,3+j}^* & = (\vec{a}_{3+j}^*, \vec{b}_j^*), & j = 1, \dots, d \end{cases} \quad (1.3)$$

The vectors  $\vec{b}_j^*$  are perpendicular to real space. Since they do not have any physical meaning, their length is arbitrary and can be set to one.

The direct superspace basis to the reciprocal basis in Eq. 1.3 is (van Smaalen, 1995):

$$\Sigma : \begin{cases} \vec{a}_{si} & = \left( \vec{a}_i, -\sum_{j=1}^d \sigma_{ji} \vec{b}_j \right), & i = 1, 2, 3 \\ \vec{a}_{s,3+j} & = (0, \vec{b}_j), & j = 1, \dots, d \end{cases} \quad (1.4)$$

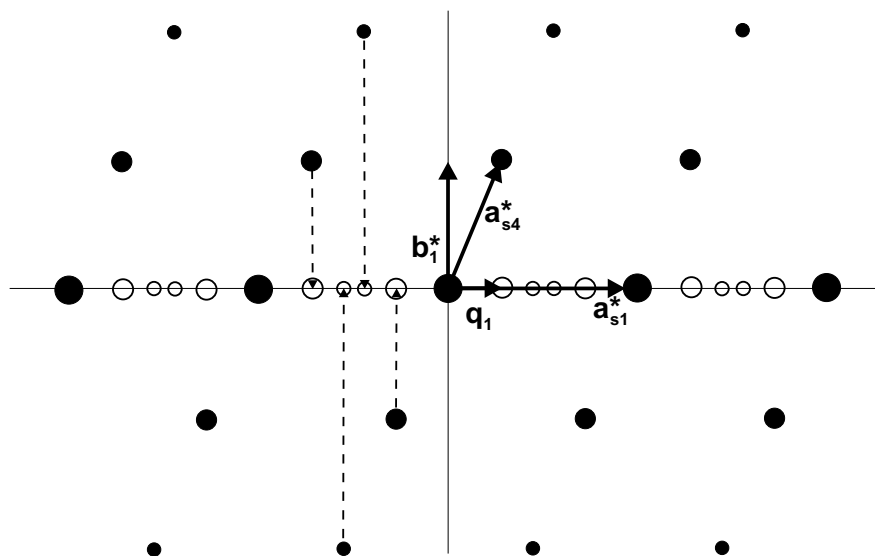


Figure 1.4: Diffraction pattern of a modulated crystal as a projection of the higher-dimensional weighted lattice. Section  $a_{s1} - a_{s4}$  of a four-dimensional superspace is shown. Empty circles denote satellites obtained as projections along  $b^*$  of the superspace lattice points. Satellites up to  $2^{nd}$  order are shown.

### 1.1.4 Superspace electron density

The general relation between the diffracted intensity and the structure is (Wilson & Prince, 1999):

$$I(\vec{H}) \propto |F(\vec{H})|^2 \quad (1.5)$$

$$F(\vec{H}) = \int_V \rho(\vec{r}) \exp(2\pi i \vec{H} \cdot \vec{r}) d\vec{r} \quad (1.6)$$

$\rho(\vec{r})$  stands for the electron density of the crystal. The integration in Eq. 1.6 runs over the whole volume of the crystal. The electron density at point  $\vec{r}$  in the crystal is thus obtained by an the inverse Fourier transform of the structure factors  $F(\vec{H})$ :

$$\rho(\vec{r}) = \sum_{\vec{H}} F(\vec{H}) \exp(-2\pi i \vec{H} \cdot \vec{r}) \quad (1.7)$$

where the summation is over all reciprocal lattice vectors  $\vec{H}$ .

The theory of the Fourier transform shows, that a discrete Fourier spectrum indexable by  $n$  integers can be always related to a periodic function defined in  $n$  dimensions. Thus, we can always *construct* a  $n$ -dimensional ( $nD$ ) periodic density function (superspace density,  $\rho_s(\vec{r}_s)$ ), that is the  $nD$  inverse Fourier transform of the structure factors indexed in  $n$  dimensions by integers:

$$\rho_s(\vec{r}_s) = \sum_{\vec{H}_s} F(\vec{H}_s) \exp(-2\pi i \vec{H}_s \cdot \vec{r}_s) \quad (1.8)$$

The subscript  $s$  denotes quantities defined in superspace. Quantities defined in real space are without subscript. For ordinary structures,  $n = 3$  and the density  $\rho_s(\vec{r}_s)$  represents the real electron density of the crystal. Diffraction patterns of the aperiodic crystals are indexed by  $(3+d)$  integers ( $d > 0$ ) and  $\rho_s(\vec{r}_s)$  is defined on a  $(3+d)$ D space.

The relation between the superspace electron density and the real density follows from the condition, that the real-space electron density at point  $\vec{r}$  and the superspace density at point  $\vec{r}_s$  are equal only if the right sides of Eqs. 1.6 and 1.8 are equal. This is fulfilled if

$$\vec{H}_s \cdot \vec{r}_s = \vec{H} \cdot \vec{r} \quad \text{mod integer} \quad (1.9)$$

for any  $\vec{H}$ . The relation between the components  $h_{si}$  of the vector  $\vec{H}_s$  and components  $h_i$  of the vector  $\vec{H}$  follows from Eqs. 1.1 and 1.3:

$$h_i = h_{si} + \sum_{j=1}^d \sigma_{ij} h_{s,3+j} \quad (1.10)$$

Thus, Eq. 1.9 can be rewritten to

$$\sum_{i=1}^{3+d} h_{si} r_{si} = \sum_{i=1}^3 \left[ \left( h_{si} + \sum_{j=1}^d \sigma_{ij} h_{s,3+j} \right) (r_i + L_i) \right] \quad (1.11)$$

or - in matrix notation - to

$$\vec{H}_s \cdot \vec{r}_s = \vec{H}_s^T \begin{pmatrix} \mathbf{I} \\ \boldsymbol{\sigma} \end{pmatrix} (\vec{r}_r + \vec{L}_r) \quad \text{mod integer} \quad (1.12)$$

The vector  $\vec{L}$  is a vector with arbitrary integer components. The matrix in brackets is a juxtaposition of a  $3 \times 3$  unit matrix  $\mathbf{I}$  and of the matrix  $\boldsymbol{\sigma}$  from Eq. 1.1. Eq. 1.12 is fulfilled for any  $\vec{H}_s$  if and only if  $\vec{r}_s = (\vec{r} + \vec{L}, \boldsymbol{\sigma}(\vec{r} + \vec{L}))$ . If we compare this result with the definition of the direct superspace basis (Eq. 1.4), we see that this relation is equivalent to a linear 3D section through the  $(3+d)$ D superspace density perpendicular to the additional dimensions (Fig. 1.5).

As a consequence of the periodicity of  $\rho_s(\vec{r}_s)$ , any basic unit cell anywhere in the (non-periodic) real-space electron density can be mapped onto a reference unit cell of  $\rho_s$  (Fig. 1.5). The shift of such a mapped section from the origin along the internal dimensions is denoted as a shift by a vector  $\vec{t}$ . Each basic unit cell anywhere in the structure can be mapped onto a section of a single reference superspace unit cell with the shift  $t_j \in \langle 0, 1 \rangle; j = 4, \dots, d$ . Thus, all structural properties like distances, bond valences etc. can be expressed as a function of  $\vec{t}$ . Characterization of any structural property in the interval  $\vec{t} \in \langle 0, 1 \rangle^d$  is equivalent to full characterization of the property in the whole structure.

### 1.1.5 Atoms in superspace

Let us have an atom at an average position  $\bar{r}^0$ . Let the atom be shifted from its average position according to a periodic function  $\vec{u}(\sigma\vec{r})$  with periodicity one in each component of its argument. At least one component of each row of  $\sigma$  is irrational and therefore the superposition of the average position and the modulation is non-periodic. Using the periodicity of  $\rho_s(\vec{r}_s)$ , the atom can be mapped onto a reference superspace unit cell (Fig. 1.5). As a result, the atom in superspace forms a string parallel to the internal dimension, that has exactly the form of the modulation function  $\vec{u}$ . These strings (planes, volumes or hypervolumes depending on the dimension of the superspace) are called atomic domains. Thus, an atom in the superspace density is characterized by its average position in a basic unit cell  $\bar{r}^0$  and by the shape of its atomic domain (modulation function  $\vec{u}(\bar{r}_{s4}, \dots, \bar{r}_{s(3+d)})$ ). The position of the atom is (van Smaalen, 1995):

$$\begin{aligned} \bar{r}_i &= l_i + \bar{r}_i^0 \\ \bar{r}_{si} &= \bar{r}_i \\ \bar{r}_{s(3+j)} &= t_j + \sum_{k=1}^3 \sigma_{jk} \bar{r}_k \\ r_i &= \bar{r}_i + u_i(\bar{r}_{s4}, \dots, \bar{r}_{s(3+d)}) \\ i &= 1, 2, 3 \\ j &= 1, \dots, d \end{aligned} \tag{1.13}$$

The modulation function  $\vec{u}$  is usually expressed as a Fourier series. In case of a one-dimensional modulation,  $\vec{u}$  of an atom  $\mu$  becomes (van Smaalen, 1995):

$$u_i^\mu(\bar{x}_4) = \sum_{n=1}^{\infty} A_{ni}^\mu \cos(2\pi n \bar{x}_4) + B_{ni}^\mu \sin(2\pi n \bar{x}_4) \quad i = 1, 2, 3 \tag{1.14}$$

Modulation of other structural properties like the displacement parameters or the occupancy can be defined analogically.

### 1.1.6 Composite crystal structures

Incommensurate composite crystal structures are intergrowths of two or more substructures (subsystems) that have incommensurate ratio of at least one lattice parameter (Fig. 1.2). The diffraction pattern is slightly different from the diffraction pattern of a simple modulated structure. Let us consider explicitly the most frequent case of the intergrowth of two subsystems. The diffraction pattern of such a structure consists of the main reflections of the first subsystem, of the main reflections of the second subsystem and of the satellite reflections arising due to the intersubsystem interactions (Fig. 1.6). Similarly as in the case of the incommensurately modulated structures, the diffraction pattern cannot be

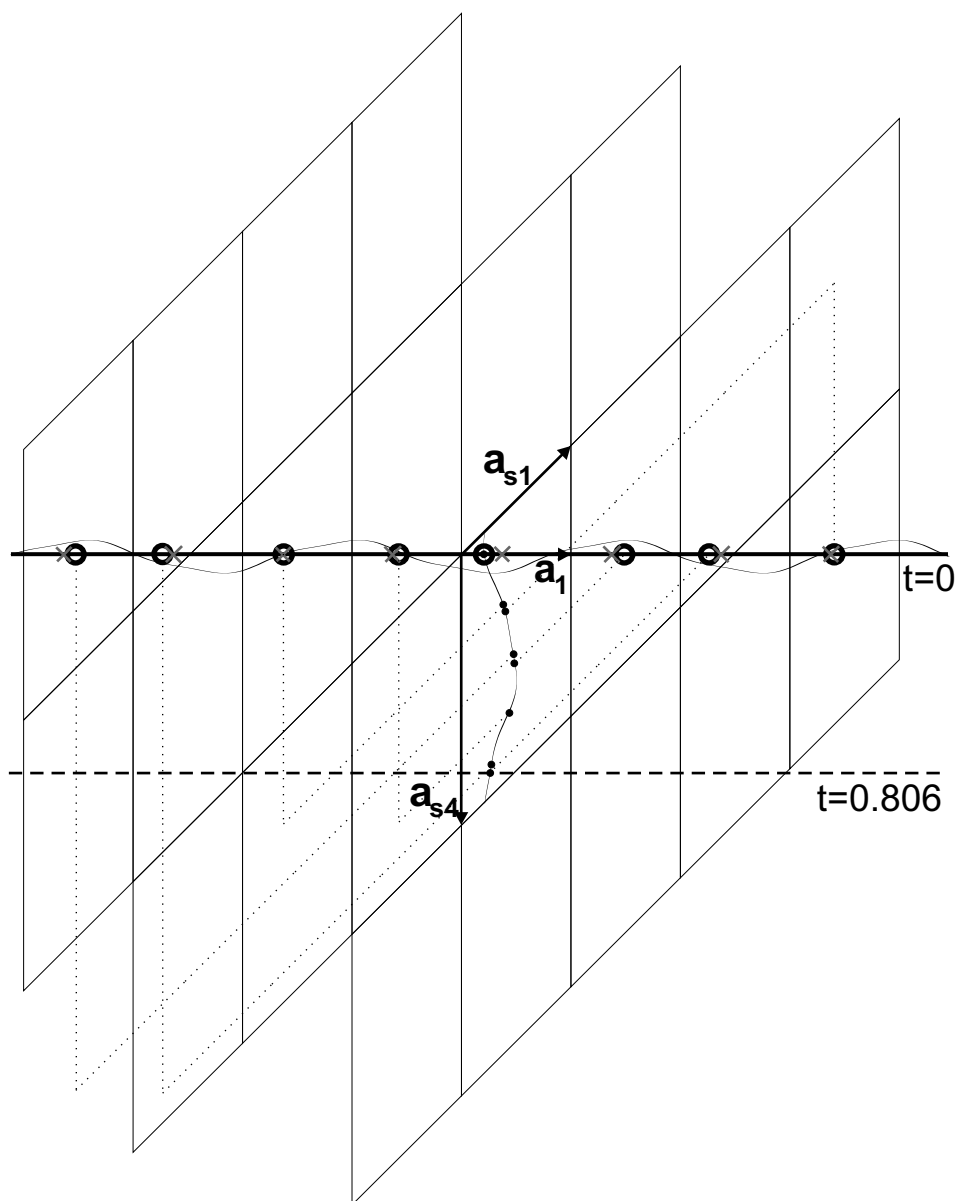


Figure 1.5: Construction of the atomic domain in superspace. The atoms are shifted from their average positions (crosses) to the modulated positions (open circles) along the real space (bold line) according to the modulation function with period  $2.481\vec{a}_1$ . The atoms can be brought to equivalent position in the reference superspace unit cell (filled circles) by superspace lattice translations. Some of the possible translations are shown by dotted lines. If all atoms of the structure are translated into the reference unit cell, they form the atomic domain in superspace (wave parallel to  $\vec{a}_{s4}$ ). The dashed line shows an alternative real space section at  $t = 0.806$ , which represents the same structure shifted by  $-2\vec{a}_1$  with respect to the structure at  $t = 0$ .

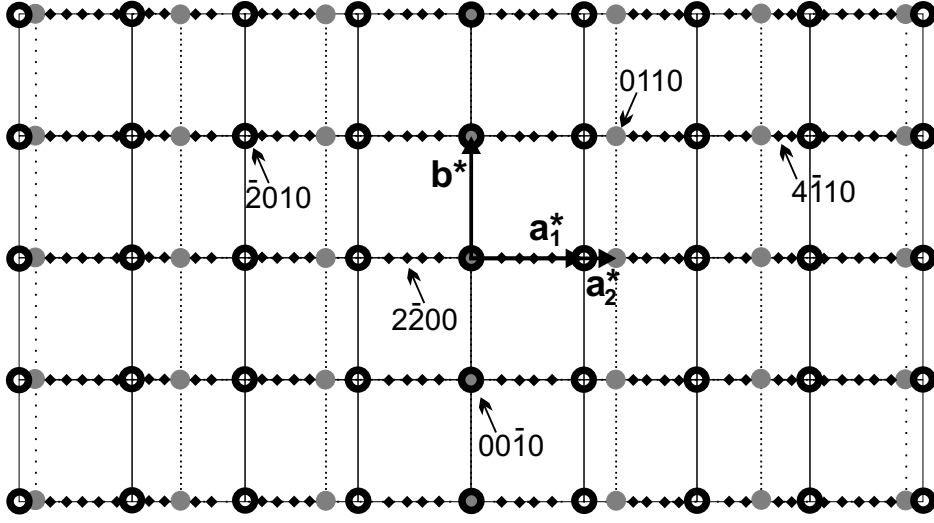


Figure 1.6: Schematic representation of a diffraction pattern of a composite crystal with two subsystems in plane  $\vec{a}^*, \vec{b}^*$ . The incommensurate lattice parameter is  $\vec{a}, \vec{b}$  is common for both subsystems. Black open (grey filled) circles mark main reflections of the first (second) subsystem. Diamonds show positions of the satellite reflections up to  $2^{nd}$  order ( $\max(|h_1|, |h_2|) \leq 2$ ). They can be generated as satellites of the first subsystem with the modulation vector  $\vec{a}_2^*$ , or as satellites of the second subsystem with the modulation vector  $\vec{a}_1^*$ . Indices  $(h_1 h_2 k l)$  of some reflections in the basis  $(\vec{a}_1^*, \vec{a}_2^*, \vec{b}^*, \vec{c}^*)$  are shown.

indexed with three integers, but it can be indexed with  $(3 + d)$  integers. Selecting the  $(3 + d)$  basic vectors in the diffraction pattern, we can map the diffraction pattern onto the superspace similarly as in the case of simple modulated structures (Eqs. 1.1 and 1.3). The superspace reciprocal basis of a subsystem  $\nu$  is related to the selected general basis  $\Sigma^*$  by a  $(3 + d) \times (3 + d)$  matrix  $\mathbf{W}^\nu$  with integer components (van Smaalen, 1991b):

$$\Sigma_\nu^* = \mathbf{W}^\nu \Sigma^* \quad (1.15)$$

$\Sigma_\nu^*$  is a setting of the reciprocal basic vectors, that allows to describe the subsystem  $\nu$  as an ordinary modulated structure. The modulation wavevectors (components of the matrix  $\boldsymbol{\sigma}$ , Eq. 1.1) of one subsystem are determined by the periodicity of the second subsystem (Fig. 1.6). To obtain components of  $\boldsymbol{\sigma}^\nu$  we decompose the matrix  $\mathbf{W}^\nu$  to:

$$\mathbf{W}^\nu = \begin{pmatrix} \mathbf{Z}_3^\nu & \mathbf{Z}_d^\nu \\ \mathbf{V}_3^\nu & \mathbf{V}_d^\nu \end{pmatrix} \quad (1.16)$$

Matrices  $\mathbf{Z}$  have three rows, matrices  $\mathbf{V}$  have  $d$  rows. The subscript denotes the number of columns. The matrix  $\boldsymbol{\sigma}^\nu$  is then obtained from (van Smaalen, 1991b):

$$\boldsymbol{\sigma}^\nu = (\mathbf{V}_3^\nu + \mathbf{V}_d^\nu \boldsymbol{\sigma})(\mathbf{Z}_3^\nu + \mathbf{Z}_d^\nu \boldsymbol{\sigma})^{-1} \quad (1.17)$$

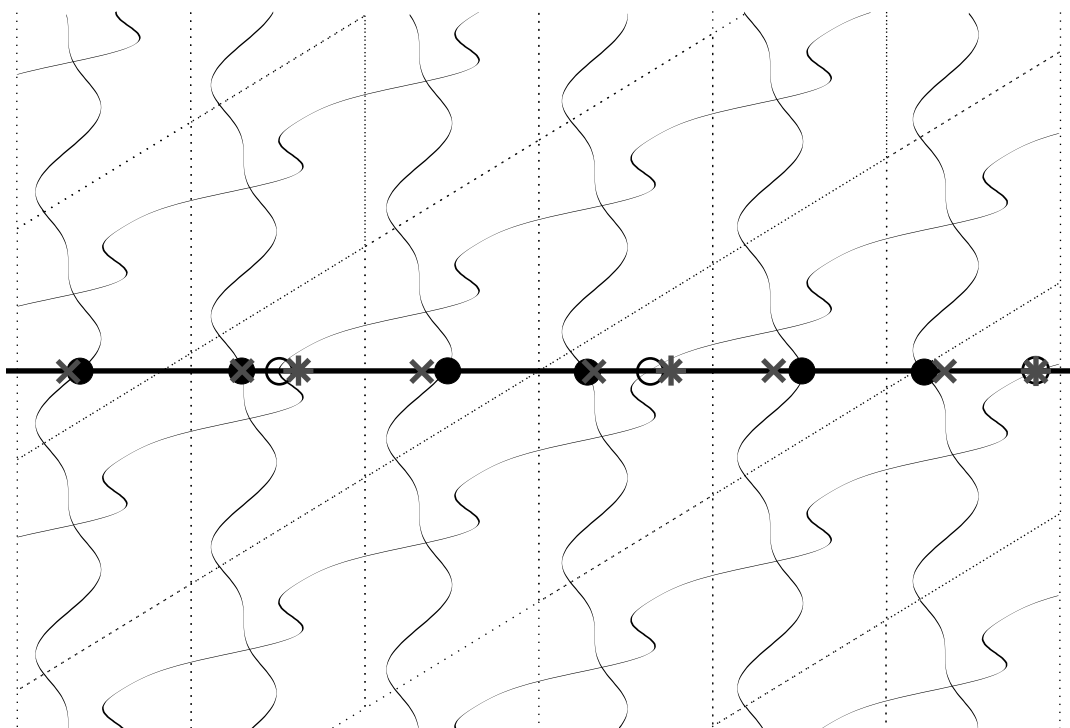


Figure 1.7: Schematic representation of a superspace description of a composite structure with two subsystems. Atomic domains of the subsystems are parallel to different directions in superspace. The strings cut the real space (bold line) with mutually incommensurate average periodicities (grey crosses and stars) and the modulated positions of the atoms are given by the intersections of the atomic domains with the real space (full and empty circles).

In the superspace description of the composite structure, the atoms of different subsystems form strings parallel to different superspace directions. The intersections of the sets of strings with the real space generate the atomic positions in the real space. The atomic domains of individual subsystems intersect the real space under different angles. This results in different periodicities of the subsystems in the real space, while the structure is still periodic in superspace (Fig. 1.7).

## 1.2 Maximum Entropy Method in crystallography

The standard way of solving crystal structures from X-ray diffraction data is to approximate the electron density  $\rho(\vec{r})$  in the unit cell of the crystal by a model electron density, which is parametrized by a relatively small number of

parameters. Values of these parameters are then determined that correspond to the best fit to the measured dataset. This is possible thanks to the small number of parameters compared to the number of data. Usually some hundreds or thousands of reflections are available for the determination a few dozens of parameters. Usually only one optimal solution exists. Another case occurs, if  $\rho(\vec{r})$  should be described by its values in an arbitrarily dense grid in the unit cell. The number of values to be determined can now be much higher than the number of the individual data. In such a case an infinite number of equally good solutions exists, and some additional criterion is needed, that chooses the best solution. Treatment of this problem leads to the Maximum Entropy Method (MEM).

### 1.2.1 The principle of the Maximum Entropy Method

The MEM is a very general principle applicable to nearly every field of science (von der Linden et al., 1998). Here the case of the X-ray scattering experiments will be considered explicitly. The electron density  $\rho(\vec{r})$  in the unit cell is sampled on a dense  $n$ -dimensional grid.  $n = 3$  for electron densities of ordinary structures,  $n > 3$  for superspace electron densities. The number of pixels along each dimension  $i$  is  $N_i$ . The total number of pixels in the grid is:

$$N_{pix} = N_1 \times N_2 \times \dots \times N_n \quad (1.18)$$

The positions of the grid points must obey the symmetry of the unit cell. Each grid point must be transformed onto itself or onto another grid point by all symmetry operators. This puts restrictions on the choice of origin of the grid. Either the grid points lie on the symmetry elements or the symmetry elements lie on the boundaries between the grid points. The first choice is more favorable (van Smaalen et al., 2003). The symmetry puts also restrictions on the divisions  $N_i$  (van Smaalen et al., 2003). For example, if a  $6_1$  axis is among the symmetry operators, then the division along that axis must be a six-fold integer.

It is the aim of the structure analysis to determine the values  $\rho_i$  in every point  $i$  of the grid. It is the assembly of the values  $\rho_i$ ,  $i = 1, \dots, N_{pix}$ , that is denoted  $\rho$  in this section, in contrast to  $\rho(\vec{r})$ , which stands for the continuous electron density.  $\rho$  is related to the structure factors  $F$  via a discrete Fourier transform. The amplitudes of the structure factors can be determined experimentally and thus each trial  $\rho$  can be accepted or rejected based on its agreement with the experimental data. Because the number of grid points can be arbitrarily large, there is an infinitely large number of solutions that account for the finite number of the measured data. A criterion is required, which selects the most probable solution among all solutions that fit the data. Mathematically, a functional of  $\rho$  must be found, that can be used as a measure of probability of  $\rho$ . The electron density that fits the data and maximizes this functional is selected to be the most probable electron density with respect to the experimental data.

The functional used is the information entropy:

$$S = - \sum_{i=1}^{N_{pix}} \rho_i \ln \frac{\rho_i}{\tau_i} \quad (1.19)$$

$\tau_i$  is the value of the so-called prior electron density (prior in short) in a grid point  $i$ .  $\tau$  should incorporate all the information available about the electron density prior to using the experimental data in the MEM. If no prior information is available, a uniform prior ( $\tau_i = \text{constant}$ ) should be used. The entropy functional has a single maximum  $S = 0$  for  $\rho_i = \tau_i$ ,  $i = 1, \dots, N_{pix}$ , and decreases monotonically in all directions. The name (information) entropy has been selected for its formal (and in some sense factual, too) similarity to the thermodynamic entropy (Shannon, 1948).

The MEM has been originally designed for the estimation of the probability distributions, e.g. for the distributions, that are everywhere-positive and that add up to one. However, it can be easily generalized toward distributions that are not normalized to one. The electron density fulfills the positivity condition and therefore it can be optimized using this method.

Many different approaches leading to the Principle of the Maximum Entropy for different classes of problems have been presented in the literature (Shannon, 1948; Shore & Johnson, 1980; Gull & Skilling, 1984; Jaynes, 1996; Sivia, 1997 and references therein). It has been shown, that no other functional fulfills the basic conditions imposed on any functional  $\Phi$ , that can be used as the selection criterion among different probability distributions. These conditions are (Jaynes, 1996; Sivia, 1997):

1.  $\Phi$  is continuous.
2.  $\Phi$  corresponds to "common sense" in simple cases. In particular, if no information is available about different hypothesis, it should assign equal probabilities to them.
3.  $\Phi$  must not introduce correlations between independent hypotheses.
4.  $\Phi$  must be self-consistent.

During the long years of extensive usage of the MEM in various fields of the data analysis and probability evaluations no inconsistency with these conditions has been discovered in the entropy functional (Jaynes, 1996; Sivia, 1997).

### 1.2.2 Crystallographic MEM equations

The maximum-entropy criterion selects only among the solutions that fit the data. The data are supposed to be noisy with a Gaussian distribution of the errors.

Therefore the most probable solution is not the one corresponding exactly to the data, but the one, which satisfies the condition

$$C_F = -1 + \frac{1}{N_F} \sum_{i=1}^{N_F} \left( \frac{|F_{obs}(\vec{H}_i) - F_{MEM}(\vec{H}_i)|}{\sigma(\vec{H}_i)} \right)^2 = 0 \quad (1.20)$$

or some of its variants (Chapters 2, 3, 4).  $F_{obs}(\vec{H})$  denotes the observed structure factors,  $F_{MEM}(\vec{H})$  denotes the structure factors calculated for the current estimate of  $\rho$ , and  $\sigma(\vec{H})$  is the standard error of  $F_{obs}(\vec{H})$ .  $N_F$  is the number of observed structure factors.

Another constraint is usually used in crystallographic applications of MEM. It is the normalization constraint:

$$C_N = N_{el} - \frac{V_{UC}}{N_{pix}} \sum_{i=1}^{N_{pix}} \rho_i = 0 \quad (1.21)$$

$N_{el}$  is the number of electrons in the unit cell and  $V_{UC}$  is the volume of the unit cell.

Having constructed  $N_C$  constraints, we need to perform the constrained entropy maximization with respect to  $\rho$ . Using the method of Lagrange undetermined multipliers, this is equivalent to unconstrained maximization with respect to  $\rho$  and  $\lambda_j$ ,  $j = 1, \dots, N_C$  of the Lagrangian

$$Q(\rho) = S(\rho) - \sum_{j=1}^{N_C} \lambda_j C_j(\rho) \quad (1.22)$$

Differentiating the above equation with respect to  $\rho_i$  gives the condition

$$\frac{\partial Q}{\partial \rho_i} = \frac{\partial S}{\partial \rho_i} - \sum_{j=1}^{N_C} \lambda_j \frac{\partial C_j}{\partial \rho_i} \quad (1.23)$$

Written explicitly for the two constraints  $C_F$  and  $C_N$  (Eqs. 1.20 and 1.21) and using the definition of entropy (Eq. 1.19) we get:

$$\frac{\partial Q}{\partial \rho_i} = -1 - \ln \frac{\rho_i}{\tau_i} - \lambda_F \frac{\partial C_F}{\partial \rho_i} - \lambda_N = 0 \quad (1.24)$$

This gives an implicit solution for the MaxEnt electron density  $\rho_{MEM}$  in the form

$$\rho_i = \tau_i \exp(-1 - \lambda_N) \exp\left(-\lambda_F \frac{\partial C_F}{\partial \rho_i}\right) \quad (1.25)$$

Substituting into the normalization condition (Eq. 1.21) yields:

$$\sum_{i=1}^{N_{pix}} \tau_i \exp(-1 - \lambda_N) \exp\left(-\lambda_F \frac{\partial C_F}{\partial \rho_i}\right) = \frac{N_{el} N_{pix}}{V_{UC}} \quad (1.26)$$

The two Eqs. 1.25 and 1.26 can be combined to eliminate the Lagrange multiplier  $\lambda_N$ . The final result for the normalized electron density is:

$$\rho_i = \frac{N_{el}N_{pix}}{V_{UC}} \tau_i \exp\left(-\lambda_F \frac{\partial C_F}{\partial \rho_i}\right) / \sum_{j=1}^{N_{pix}} \tau_j \exp\left(-\lambda_F \frac{\partial C_F}{\partial \rho_j}\right) \quad (1.27)$$

Eq. 1.27 together with Eq. 1.20 give a set of  $N_{pix}+1$  nonlinear equations, which cannot be solved analytically. Several algorithms have been developed, that solve the maximization problem iteratively (see overview in Skilling & Bryan, 1984). The two commonly used algorithms will be described in following two sections.

### 1.2.3 Sakata-Sato algorithm

The right-hand side of Eq. 1.27 depends on  $\rho_i$ , because the constraint is a function of  $\rho_i$ . The Sakata-Sato algorithm (Sakata & Sato, 1990) solves this problem by using two approximations. The first one is:

$$\left. \frac{\partial C}{\partial \rho_i} \right|_{\rho_i^{(n+1)}} \approx \left. \frac{\partial C}{\partial \rho_i} \right|_{\rho_i^{(n)}} \quad (1.28)$$

where  $\rho_i^{(n)}$  and  $\rho_i^{(n+1)}$  are the values of electron densities at  $n^{th}$  and  $(n+1)^{th}$  cycle of the iteration. This is equivalent to making a zero'th order Taylor expansion of  $\frac{\partial C}{\partial \rho_i}$  around  $\rho_i = \rho_i^{(n)}$ .

The second approximation is:

$$\tau_i^{(n+1)} \approx \rho_i^{(n)} \quad (1.29)$$

This means, that the MEM electron density of the cycle  $n$  is used as a prior electron density of the cycle  $n+1$ .

With these two approximations, Eq. 1.27 gives the basic formula for the iteration in the Sakata-Sato algorithm:

$$\rho_i^{(n+1)} = \frac{N_{el}N_{pix}}{V_{UC}} \rho_i^{(n)} \exp\left(-\lambda_F \left. \frac{\partial C_F}{\partial \rho_i} \right|_{\rho_i^{(n)}}\right) / \sum_j \rho_j^{(n)} \exp\left(-\lambda_F \left. \frac{\partial C_F}{\partial \rho_j} \right|_{\rho_j^{(n)}}\right) \quad (1.30)$$

The described approximations have been named the zero'th-order single-pixel approximation (ZSPA; Kumazawa et al., 1995).

The Sakata-Sato algorithm is iterative. At cycle  $n$  of the iteration, the new density  $\rho_i^{(n+1)}$  is calculated using Eq. 1.30 from the prior density  $\rho_i^{(n)}$ . The iteration is started with  $\rho_i^{(1)} = \tau_i$ . The value of the constraint decreases in each cycle. The iteration is repeated until the condition  $C_F \leq 1$  is fulfilled.

The last problem is to determine the value of  $\lambda_F$ . It has been shown (Sakata & Sato, 1990; Kumazawa et al., 1995) that the result of the ZSPA is not sensitive to

the exact value of  $\lambda_F$ , if it is small enough to assure convergence of the iteration. If too large value of  $\lambda_F$  is chosen, the iteration diverges, i.e. the value of the constraint increases between consecutive cycles.

It is obvious, that the second approximation (Eq. 1.29) is not valid, especially if a uniform prior density is used. This approximation has been used to overcome the convergence problems, that occur in the Gull-Daniels algorithm (Gull & Daniel, 1978). Surprisingly, in despite of the inaccuracy of the approximations used, the MEM electron densities obtained with the Sakata-Sato algorithm are very close to the electron densities that correspond to exact MaxEnt solutions (Section 2.2.4).

### 1.2.4 Cambridge algorithm

The Cambridge MaxEnt algorithm (Skilling & Bryan, 1984) is based on simultaneous optimization of the Lagrange multiplier  $\lambda$  and of the image. This is in contrast with the Sakata-Sato algorithm, where  $\lambda$  is fixed and only the image is optimized. For the purposes of the Cambridge algorithm, the total optimized Lagrangian is written as (compare Eq. 1.22):

$$Q(\rho) = \alpha S(\rho) - C(\rho) \quad (1.31)$$

The Lagrange multiplier  $\lambda$  is now replaced by the factor  $\alpha$ . This is only a change of convention and does not influence the resulting MaxEnt image  $\rho$ .

For given  $\alpha$ , a unique image  $\rho$  exists, that maximizes  $Q$ . The value of  $C(\rho)$  is determined by the choice of  $\alpha$ , supposing that  $C(\rho)$  is convex in all points, which is the case for the F-constraint. The task to find the maximum of  $Q(\rho)$  for given  $C(\rho)$  can thus be reduced to finding the maximum of  $Q(\rho)$  for given  $\alpha$ . Then, the value of  $\alpha$  could be changed, until the constraint reaches its final value  $C = C_{aim}$ .

The Cambridge algorithm searches for the  $\rho_{MEM}$  iteratively. The iteration starts with very large value of  $\alpha$ , which corresponds to almost unconstrained entropy maximization.  $\rho_{MEM}(\alpha \rightarrow \infty) = \rho_{prior}$  and the starting  $\rho_{MEM}$  is thus known. Each iteration cycle starts with changing the value of  $\alpha$ , usually downwards. After that, the image  $\rho^{(n+1)}$  is found, that maximizes  $Q(\rho)$  and the new value of  $C^{(n+1)}$  is calculated. This is repeated, until the condition  $C = C_{aim}$  is satisfied.

The non-trivial task is to find  $\rho^{(n+1)}$ . To facilitate this task, a local quadratic approximation of  $Q(\rho)$  is formed around the image of the previous cycle  $\rho^{(n)}$ :

$$Q(\rho^{(n)} + \delta\rho) = Q(\rho^{(n)}) + \delta\rho^T \nabla Q + \delta\rho^T \nabla \nabla Q \delta\rho \quad (1.32)$$

Within this approximation, the maximization of  $Q(\rho)$  with respect to  $\rho$  becomes feasible and it is one of the strengths of the Cambridge algorithm and MEMSYS package, that this maximization is performed effectively using the method of conjugate gradients (Skilling & Bryan, 1984; Gull & Skilling, 1999b).

The local quadratic approximation is valid only in a limited interval around  $\rho^{(n)}$ . This is the reason, why the algorithm must search for the MaxEnt solution iteratively. The change of  $\alpha$  must not be too large, otherwise  $\rho^{(n+1)}$  would lie too far from  $\rho^{(n)}$ , the quadratic approximation would not be valid there, and  $\rho^{(n+1)}$  could not be reliably determined.

### 1.2.5 Maximum Entropy Method in superspace

The applications of the MEM for the reconstruction of the electron densities were first derived for ordinary 3D-periodic structures (Collins, 1982; Sakata & Sato, 1990). The first attempt to use the MEM in reconstructions of the superspace electron densities has been made by Steurer (1991), but the results were not quantitatively analyzed and the method was not further developed. Recently van Smaalen et al. (2003) give a full account on the application of the MEM to the superspace electron densities. It has been shown, that the MaxEnt formalism can be generalized towards superspace in a straightforward manner. The nD superspace electron density is sampled on a nD grid. The entropy is defined as a function of all pixels of the superspace electron density. Thus, the ordinary 3D and superspace electron densities can be analyzed by MEM within the same formalism and the 3D electron densities can be treated as a special case of the general n-dimensional problem (van Smaalen et al., 2003). A computer program BAYMEM has been developed that has the capability of performing the MEM analysis of electron densities in arbitrary dimensions within a unique framework (Schneider, 2001; Chapter 2).

# Chapter 2

## Development of the program BayMEM after the year 2000

### 2.1 Introduction

BAYMEM is a computer program that has been developed for applications of the MEM in charge-density reconstructions of both ordinary and modulated crystal structures. It allows to reconstruct the MaxEnt electron density from at least partially phased experimental structure factors measured by X-ray diffraction.

The first version of BAYMEM has been written by Martin Schneider and described in his Ph.D. Thesis (Schneider, 2001). This version contained following basic features:

- General n-dimensional Fast Fourier Transform based on Beevers-Lipson algorithm (Schneider & van Smaalen, 2000).
- General handling of symmetry of discretized unit cell in arbitrary dimension (van Smaalen et al., 2003).
- Implementation of the Sakata-Sato MEM algorithm (Sakata & Sato, 1990).
- Constraint based on phased structure factors (F-constraint).
- MaxEnt calculation with both uniform and non-uniform prior electron density.
- Regularization function introducing correlation between the values of the electron density at neighboring pixels of the grid.

This functionality has been extended by adding various features improving BAYMEM's ability to produce reliable and informative MEM results. These improvements are described in following sections.

## 2.2 MEMSYS5 package

MEMSYS5 is a set of subroutines, that implements the Cambridge algorithm (Skilling & Bryan, 1984; Section 1.2.4) for general solution of MaxEnt problems. The system is not a self-standing program. The user must provide subroutines implementing the transformations specific for his MaxEnt problem and the program interface to the MEMSYS5 package. The subroutines are provided as Fortran 77 and C-language source code. The Fortran code of MEMSYS5, Version 1.2 from September 6, 1999 (Gull & Skilling, 1999a; Gull & Skilling, 1999b), has been used in BAYMEM and is described in this section.

### 2.2.1 Structure of the MEMSYS5 package

MEMSYS5 provides three main subroutines. One of them - subroutine MEM5 - serves for reconstructions of the MaxEnt image. The other two - MOVIE5 and MASK5 - enable various properties of the MaxEnt image to be inferred, like different samples of the final MaxEnt probability distribution or integral properties of the distribution and its standard error. BAYMEM uses only the subroutine MEM5.

The subroutine MEM5 performs one iteration cycle per call. MEM5 must be called repeatedly, until the iteration is converged.

Apart from the subroutines included in the MEMSYS5 package, four other important subroutines are necessary. These subroutines must be supplied by the user. They are specific to each MaxEnt problem, and they implement different mathematical operations on the image or on the data. If the experiment is linear (which is the case for many experiments, including diffraction experiments), the data  $F_{obs}$  and the image  $\rho$  are related by a matrix equation:

$$F_{obs} = \mathbf{R}\rho \quad (2.1)$$

The operator  $\mathbf{R}$  must be implemented in a subroutine named OPUS, the transpose operator  $\mathbf{R}^T$  is represented by a subroutine TROPUS. The basic assumption underlying the MaxEnt formalism is that the points of the image are not correlated. However, in practice, this is not always true and there is some kind of correlation usually present in the image. Such a correlation can be introduced in the MaxEnt formalism as a function called Intrinsic Correlation Function (ICF). The “real” image (visible image) is considered to be obtained by “blurring” the actually optimized image (hidden image) by the ICF. The independence of the pixels of the hidden image is given by definition, and all the correlations are moved to the ICF. The relation of the hidden image  $h$  to the visible image  $\rho$  is

$$\rho = \mathbf{C}h \quad (2.2)$$

and the relation of the hidden image to the data becomes:

$$F^{obs} = \mathbf{R}\mathbf{C}h \quad (2.3)$$

The matrix operator  $\mathbf{C}$  represents the ICF and should be supplied as subroutine `ICF`, its transpose  $\mathbf{C}^T$  must be implemented in subroutine `TRICF`. The hidden image does not correspond to a physically meaningful quantity. The final result of the MEM analysis is the visible image  $\rho$ . BAYMEM employs other means to introduce correlations between pixels (the regularization function; Schneider, 2001) and the subroutines `ICF` and `TRICF` are therefore empty.

### 2.2.2 Interface BAYMEM - MEMSYS

Any interface with the MEMSYS5 package must fulfill two main tasks: Supplying the data in a form readable by MEMSYS5 and providing the code for the transformation subroutines.

#### *Format of the data*

The data are passed to MEMSYS5 in one large array called `ST`, that is subdivided into several parts called areas. Each area contains one set of related variables. The list of areas used by BAYMEM and their contents is given in Table 2.1. The data are of type real. That means, that complex numbers like the structure factors must be supplied and handled as two separate real numbers. The coding used in BAYMEM is such, that each complex number is represented in the array `ST` by two consecutive real numbers representing its real in imaginary component.

Table 2.1: Areas of the array `ST` filled explicitly in BAYMEM. Those areas not listed here are either used as a workspace by MEMSYS5 (areas  $\langle 2 \rangle, \langle 23 \rangle - \langle 28 \rangle$ ), or are not occupied.

area nr.	description
$\langle 1 \rangle$	the MEM electron density
$\langle 3 \rangle$	prior
$\langle 4 \rangle$	pixel multiplicities
$\langle 21 \rangle$	experimental structure factors
$\langle 22 \rangle$	weights of the structure factors: $\langle 22 \rangle = \frac{\sqrt{w(F_{obs})}}{\sigma(F_{obs})}$ (see Section 2.3 for explanation of the factor $w(F_{obs})$ )
$\langle 31 \rangle$	static weights $w(F_{obs})$ (see Section 2.3)

The most important part of the array `ST` is the area  $\langle 1 \rangle$  - the image, and the area  $\langle 21 \rangle$  - the experimental data. In crystallography, the image and the experimental data correspond to the electron density and the experimental structure factors. A choice has to be made, whether the two quantities will be supplied as independent data (density in an asymmetric unit and independent structure

factors), or expanded (density of the whole unit cell and all structure factors). The disadvantage of the first choice is, that the transformation subroutines **OPUS** and **TROPUS** become somewhat more complicated, and the expression for entropy and its derivatives must be modified (see below). However, these disadvantages are compensated by the memory savings, that are achieved in comparison with the expanded datasets. Especially the values of the electron density form a large array and the difference between the size of arrays containing the expanded and independent part can be several hundred MB. Because the effective use of the memory is one of the main objectives of BAYMEM, the first choice has been made.

Despite the fact, that only the independent part of the density is passed to MEMSYS5, the entropy must remain defined on the whole unit cell:

$$S = \sum_{j=1}^{N_{pix}} \rho_j - \tau_j - \rho_j \ln \frac{\rho_j}{\tau_j} \quad (2.4)$$

This general expression for entropy is used in MEMSYS5. The first two terms in the sum reflect the contribution to the entropy of the (possible) difference in the sum of the image and the prior (Gull & Skilling, 1999b).

Expressed with the pixels in the asymmetric part of the unit cell, this definition changes to:

$$S = \sum_{j=1}^{N_{pix}^{AU}} m_j \left[ \rho_j - \tau_j - \rho_j \ln \frac{\rho_j}{\tau_j} \right] \quad (2.5)$$

where only the  $N_{pix}^{AU}$  symmetry-independent pixels are included in the summation.

Related quantities used in MEMSYS are:

$$\frac{\partial S}{\partial \rho_j} = -m_j \ln \frac{\rho_j}{\tau_j} \quad (2.6)$$

and

$$\begin{aligned} \frac{\partial^2 S}{\partial \rho_j^2} &= -\frac{m_j}{\rho_j} \\ \frac{\partial^2 S}{\partial \rho_j \partial \rho_k} &= 0, j \neq k \end{aligned} \quad (2.7)$$

This is equivalent to saying that each independent pixel has a weight equal to the multiplicity of the pixel. MEMSYS5 does not have capacity to handle such a weighting. Therefore, the code handling entropy and related quantities had to be modified. All the calculations concerning entropy and related quantities are concentrated into subroutine **MEMENT** and subroutines called therefrom. Appropriate changes must be made in these subroutines. The changes are listed in the User manual to BAYMEM (Appendix A.3.2).

*The transformation routines*

The transformation subroutine **OPUS** contains the implementation of the matrix operator  $\mathbf{R}$ , that transforms the image to the data. Subroutine **TROPUS** applies the transpose operator  $\mathbf{R}^T$ . In contrary to the impression made by the MEMSYS5 manual, the operator  $\mathbf{R}^T$  does not have to be exactly the data-to-image transform, it only must be the transpose matrix operator to  $\mathbf{R}$ . Although  $\mathbf{R}$  is a matrix operator, its implementation as simple matrix multiplication would be very inconvenient and slow. Instead of that, the FFT subroutine as implemented in **BAYMEM** can be used to obtain a result equivalent to the matrix multiplication. The formulas necessary for expressing matrices  $\mathbf{R}$  and  $\mathbf{R}^T$  by means of the FFT will be derived here:

The electron density and the structure factors are related by Fourier transform:

$$F(\vec{H}) = \int_{V_{UC}} \rho(\vec{r}) \exp(2\pi i \vec{H} \cdot \vec{r}) dV \quad (2.8)$$

The integration spans the volume  $V_{UC}$  of one unit cell. In a discrete case, with the unit cell divided into  $N_{pix}$  pixels, Eq. 2.8 becomes:

$$F(\vec{H}) = \frac{V_{UC}}{N_{pix}} \sum_{j=1}^{N_{pix}} \rho(\vec{r}_j) \exp(2\pi i \vec{H} \cdot \vec{r}_j) \quad (2.9)$$

Symmetry requires, that the relation

$$\rho(\mathbf{R}_l \vec{r}_j + \vec{\tau}_l) = \rho(\vec{r}_j) \quad (2.10)$$

Is valid for each symmetry operator  $\{\mathbf{R}_l | \vec{\tau}_l\}$ ,  $l = 1, N_{sym}$  from the  $N_{sym}$  symmetry operators of the space group. This makes it possible to rewrite Eq. 2.9 in form:

$$F(\vec{H}) = \frac{V_{UC}}{N_{pix}} \sum_{j=1}^{N_{pix}} \frac{m_j}{N_{sym}} \rho(\vec{r}_j) \sum_{l=1}^{N_{sym}} \exp(2\pi i \vec{H} \cdot (\mathbf{R}_l \vec{r}_j + \vec{\tau}_l)) \quad (2.11)$$

The summation runs over  $N_{AU}$  symmetry independent pixels.  $m_j$  is the multiplicity of the position  $j$ . The factor  $m_j/N_{sym}$  corrects for the fact, that the pixels lying on a special position are taken into account more than once in the inner sum.

We can construct a “data vector”  $\vec{F}$  with  $N_F$  independent experimental structure factors as components:  $\vec{F} = (F(\vec{H}_1), F(\vec{H}_2), \dots, F(\vec{H}_{N_F}))^T$ . Analogically we define a “density vector”  $\vec{\rho} = (\rho(\vec{r}_1), \rho(\vec{r}_2), \dots, \rho(\vec{r}_{N_{pix}}))^T$ . We can now rewrite Eq. 2.11 in a matrix form:

$$\vec{F} = \frac{V_{UC}}{N_{pix}} \mathbf{T} \begin{bmatrix} \mathbf{m} \\ \mathbf{N}_{sym} \end{bmatrix} \vec{\rho} = \frac{V_{UC}}{\underbrace{N_{sym} N_{pix}}_{\mathbf{U}}} \mathbf{T}[\mathbf{m}] \vec{\rho} \quad (2.12)$$

In this and all following equations, the notation  $[\mathbf{x}]$  denotes a square diagonal matrix with elements of vector  $\vec{x}$  on the diagonal. In this particular case, the matrix  $[\mathbf{m}]$  denotes a diagonal matrix with multiplicity  $m_j$  of the  $j^{\text{th}}$  pixel in row  $j$ . The operational effect of such a matrix on a matrix  $\mathbf{M}$  to the right (left) is, that it multiplies every row (column)  $j$  of the matrix  $\mathbf{M}$  by a number in row  $j$  of the diagonal matrix. The matrix  $\mathbf{T}$  with  $N_F$  rows and  $N_{pix}^{AU}$  columns is a symmetry-adapted Fourier transform matrix with coefficients:

$$T_{kj} = \sum_{l=1}^{N_{sym}} \exp\left(2\pi i \vec{H}_k \cdot (\mathbf{R}_l \vec{r}_j + \vec{\tau}_l)\right) \quad (2.13)$$

To summarize, the Fourier Transform in Eq. 2.9 and the matrix equation Eq. 2.12 are equivalent and the Fast Fourier Transform subroutine of BAYMEM on the expanded set of data and pixels can be used as a computationally equivalent operator to the matrix operator  $\mathbf{U}$  applied to the unique set of pixels. Thus, the subroutine **OPUS** contains merely an expansion of the unique pixels to the unit cell and a call of the FFT subroutine.

To envisage the operation of the subroutine **TROPUS**, which implements a transpose matrix operator to **OPUS**, let us first derive the expression for the data-to-density transform. The electron density is related to the structure factor through a discrete Fourier transform. The summation runs over all possible integer diffraction vectors  $\vec{H}$ :

$$\rho(\vec{r}) = \frac{1}{V_{UC}} \sum_{\vec{H}} F(\vec{H}) \exp\left(-2\pi i \vec{H} \cdot \vec{r}\right) \quad (2.14)$$

The following equation is valid for each symmetry operator  $\{\mathbf{R}_l | \vec{\tau}_l\}$  and each structure factor  $F(\vec{H})$  (see for example Giacovazzo et al., 1995):

$$F(\mathbf{R}_l^T \vec{H}) = F(\vec{H}) \exp(-2\pi i \vec{H} \cdot \vec{\tau}_l) \quad (2.15)$$

Using this equation and summing only over the measured structure factors we can rewrite Eq. 2.14 into a form:

$$\rho(\vec{r}) = \frac{1}{V_{UC}} \sum_{k=1}^{N_F} \frac{n_k}{N_{sym}} F(\vec{H}_k) \sum_{l=1}^{N_{sym}} \exp(-2\pi i \vec{H}_k \cdot \vec{\tau}_l) \exp\left(-2\pi i \vec{H}_k^T \mathbf{R}_l \vec{r}\right) \quad (2.16)$$

which can be in turn written as:

$$\rho(\vec{r}) = \frac{1}{V_{UC}} \sum_{k=1}^{N_F} \frac{n_k}{N_{sym}} F(\vec{H}_k) \sum_{l=1}^{N_{sym}} \exp\left(-2\pi i \vec{H}_k \cdot (\mathbf{R}_l \vec{r} + \vec{\tau}_l)\right) \quad (2.17)$$

$n_k$  is the point-group multiplicity of the reciprocal vector  $\vec{H}_k$ .

Using the same approach as in the step between Eqs. 2.11 and 2.12, we can rewrite the transform between the experimental structure factors and the electron density of the unique pixels in a matrix form:

$$\vec{\rho} = \frac{1}{\underbrace{N_{sym} V_{UC}}_{\mathbf{V}}} \mathbf{S}[\mathbf{n}] \vec{F} \quad (2.18)$$

The matrix  $\mathbf{S}$  has  $N_F$  columns and  $N_{pix}^{AU}$  rows and coefficients:

$$S_{jk} = \sum_{l=1}^{N_{sym}} \exp\left(-2\pi i \vec{H}_k \cdot (\mathbf{R}_l \vec{r}_j + \vec{\tau}_l)\right) \quad (2.19)$$

Comparison of the expressions for the matrices  $\mathbf{S}$  (Eq. 2.19) and  $\mathbf{T}$  (Eq. 2.13) shows that they are each others Hermitian conjugate:

$$\mathbf{S} = \bar{\mathbf{T}}^T \quad (2.20)$$

For this moment we will ignore the fact, that we have Hermitian conjugate matrices and we need simple transpose matrices. This issue will be discussed at the end of the derivation. So, apart from the complex conjugation, the matrices  $\mathbf{S}$  and  $\mathbf{T}$  are transposes of each other, but the complete transformation matrices  $\mathbf{U}$  (Eq. 2.12) and  $\mathbf{V}$  (Eq. 2.18) are not. Thus, a simple inverse Fourier transform represented by matrix  $\mathbf{V}$  cannot be used in the subroutine TROPUS and further modifications are necessary. These modifications must transform matrix  $\mathbf{V}$  into matrix  $\mathbf{V}'$  that fulfills the condition:

$$\mathbf{V}' = \bar{\mathbf{U}}^T = \frac{V_{UC}}{N_{sym} N_{UC}} [\mathbf{m}] \bar{\mathbf{T}}^T \quad (2.21)$$

Here we used the fact, that any real diagonal matrix is invariant to both transposition and complex conjugation.

By comparing Eqs. 2.21, 2.12 and 2.18 we can see, that the matrix  $\mathbf{V}'$  can be expressed as:

$$\mathbf{V}' = \frac{V_{UC}^2}{N_{UC}} [\mathbf{m}] \mathbf{V}[\mathbf{n}]^{-1} \quad (2.22)$$

It is this matrix, that has to be implemented in the transformation subroutine TROPUS. Thus, the transformation in TROPUS proceeds in three steps:

- Multiplication of the input reciprocal-space data by inverses of the multiplicities  $n$ .
- Expansion of the data and calculation of the FFT.
- Multiplication of the result of FFT by corresponding pixel multiplicities and the prefactor  $\frac{V_{UC}^2}{N_{UC}}$ .

This method assures, that the subroutines `OPUS` and `TROPUS` work as transpose matrix operators on the unique data, but use the efficient multidimensional FFT subroutines of `BAYMEM`.

The last issue to be explained is the Hermitian conjugation of the matrices  $\mathbf{U}$  and  $\mathbf{V}'$ . As mentioned above, the data passed to `MEM5` are real numbers. Thus, the complex matrices  $\mathbf{U}$  and  $\mathbf{V}'$  must be transformed to equivalent real matrices. If the vectors with complex components are transformed into real vectors with alternating real and imaginary part of the complex components, then any complex matrix acting on the complex vector must be transformed into real matrix with doubled number of rows and columns, and each complex element will be represented by four real elements according to rule:

$$\left(\exp(i\varphi)\right)_{ij} = \begin{pmatrix} \cos(\varphi)_{(2i-1)(2j-1)} & -\sin(\varphi)_{(2i-1)(2j)} \\ \sin(\varphi)_{(2i)(2j-1)} & \cos(\varphi)_{(2i)(2j)} \end{pmatrix} \quad (2.23)$$

Obviously, transposition of such a real matrix requires not only transposition of the complex matrix, but also exchange of the signs at the sine terms. This is equivalent to taking a complex conjugate number to  $\exp(i\varphi)$ .

### 2.2.3 The “True Bayesian” MEM

The maximum entropy algorithms (both Sakata-Sato and Cambridge algorithms) converge from large values of the constraint down to small values. Theoretically, the constraint can attain arbitrarily small values and therefore some value of the constraint must be defined as a stopping criterion. At that value the calculation is considered to be converged. Traditionally, the stopping criterion has been chosen to be  $\chi^2 = N_F$ . This is based on a statistical analysis showing that the number of observations is the most probable value of  $\chi^2$ , if the noise is random and Gaussian. The authors of `MEMSYS5` (Gull & Skilling, 1999b) have derived another stopping criterion, based on the Bayesian probability theory. According to this stopping criterion, the value of the constraint at the point of convergence is always lower than  $N_F$ . The exact value is inferred from the particular data in a computationally complicated procedure.

Several tests have been performed with this “true Bayesian” stopping criterion. The results of all tests were similar and will be illustrated for the structure of  $\alpha'$ - $\text{NaV}_2\text{O}_5$ .<sup>1</sup> Fig. 2.1 shows comparison of the electron density obtained with the classical  $\chi^2 = N_F$  stopping criterion and with the “true Bayesian” stopping criterion. The final value of  $\chi^2/N_F$  in the latter case was 0.051 instead of expected 1.0. Obviously, such a low value of the final  $\chi^2$  leads to a dramatic overfitting of the data and much more pronounced spurious features in the electron density.

---

<sup>1</sup>for details about the experimental data the structure refinements see van Smaalen et al. (2003)

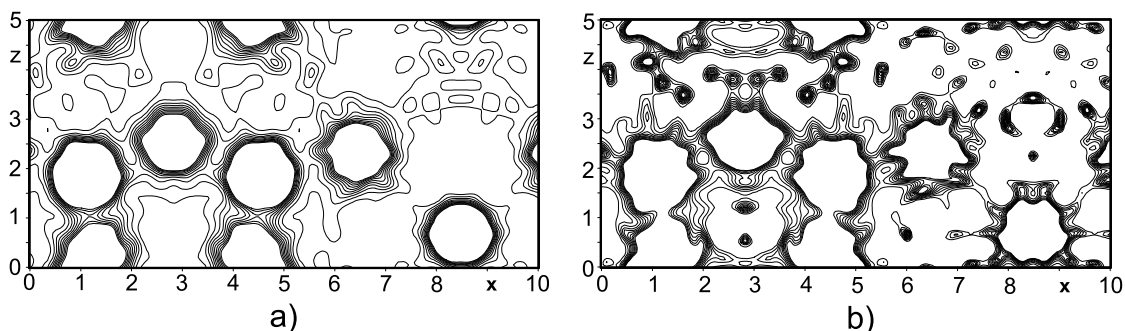


Figure 2.1: Section through  $\rho_{MEM}$  of  $\alpha' - NaV_2O_5$  obtained with a) the classical  $\chi^2 = N_F$  stopping criterion and b) with the “true Bayesian” stopping criterion. Contours  $0.2 \text{ e}/\text{\AA}^3$ , cut-off  $2 \text{ e}/\text{\AA}^3$ .

Although the “true Bayesian” stopping criterion is claimed to be theoretically more correct than the classical stopping criterion, the practice shows that - at least in case of the reconstruction of nD images from its Fourier coefficients - it leads to less preferable results than the classical stopping criterion. All MEM calculations described in this thesis have been made using the classical stopping criterion.

### 2.2.4 Comparison of the Cambridge and Sakata-Sato algorithms<sup>2</sup>

BAYMEM works with both the Cambridge and the Sakata-Sato algorithms. Thus the performance of the two algorithms can be compared under otherwise identical conditions. To be able to assess the quality of the MaxEnt reconstructions we have used simulated, noisy data of oxalic acid dihydrate, that were obtained from calculated structure factors of a model electron density (for details see Chapter 3).

For the optimum electron density  $\rho_{MEM}$ , the entropy and constraint should fulfill the following set of equations:

$$\frac{\partial S}{\partial \rho_i} = \lambda \frac{\partial C}{\partial \rho_i} \quad (2.24)$$

for  $i = 1, \dots, N_{pix}^{au}$ . Alternatively they should fulfill the equivalent set of equations in reciprocal space:

$$\frac{\partial S}{\partial F_j} = \lambda \frac{\partial C}{\partial F_j} \quad (2.25)$$

<sup>2</sup>This section was published as Section 3.2 of van Smaalen, S., Palatinus, L. & Schneider, M. (2003), *Acta Crystallogr.* **A59**, pp. 459-469.

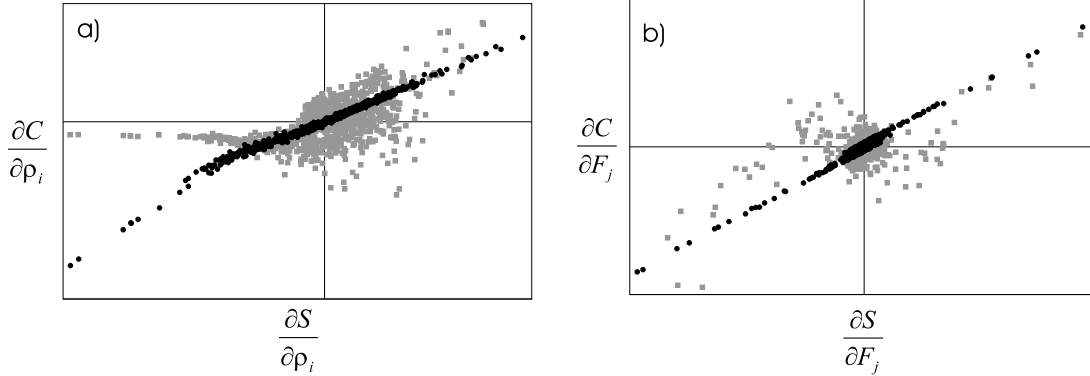


Figure 2.2: Graphical representation of a) Eq. 2.24, and b) Eq. 2.25. Grey squares: Sakata-Sato algorithm. Black circles: Cambridge algorithm. Only about 1% of all points shown in a. For an ideal MaxEnt solution all points lie on a straight line.

for  $j = 1, \dots, N_F$ .

The Cambridge algorithm is supposed to produce an electron density that is close to the real MaxEnt solution, because  $\rho$  and  $\lambda$  are optimized simultaneously. On the other hand, there is no a priori reason to expect that the Sakata-Sato algorithm will produce an electron density that fulfills Eqs. 2.24 and 2.25, because the Sakata-Sato algorithm uses an estimated value for  $\lambda$  and it determines  $\rho^{MEM}$  by an approximate iterative procedure. The numerical evaluation for the case of oxalic acid dihydrate confirms these expectations. The electron density produced by the Cambridge algorithm is relatively close to the perfect solution, while the Sakata-Sato algorithm produces distribution far away from the optimum (Fig. 2.2).

Of practical importance is to know how close the optimized electron density  $\rho_{MEM}$  is to the true electron density  $\rho_{true}$ . The latter is known for the simulated data that were used here. For the Sakata-Sato algorithm it will be shown in Chapter 3 that  $\Delta\rho_{S-S} = \rho_{MEM}(\text{Sakata-Sato}) - \rho_{true}$  is small in the case of a procrystal prior while it has variations up a few electrons per  $\text{\AA}^3$  in the case of a flat prior. Here we will directly compare the optimized electron densities of the Sakata-Sato and Cambridge algorithms, employing the quantity

$$\frac{|\Delta\rho_{Cambridge}|}{|\Delta\rho_{Cambridge}| + |\Delta\rho_{S-S}|} \quad (2.26)$$

where  $\Delta\rho_{Cambridge}$  is defined analogously to  $\Delta\rho_{S-S}$ . A value less than 0.5 indicates a point where the Cambridge algorithm produced more accurate density value, while values larger than 0.5 indicate points where the Sakata-Sato algorithm was more accurate. Depending on the resolution of the map and the noise level of the data, average values of Eq. 2.26 were found to lie between 0.46 and 0.47 in

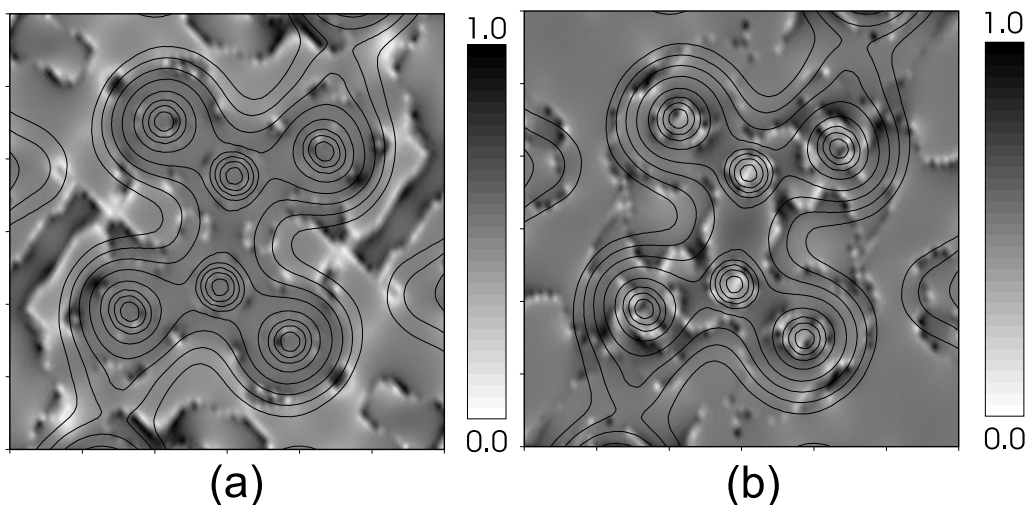


Figure 2.3: Comparison of the electron densities obtained with the Sakata-Sato and Cambridge algorithms. a) for a flat prior, and b) for a procrystal prior. A section through the plane of the oxalic acid molecule is shown. Contour lines at intervals  $2^n$ ,  $n = -2, \dots, 5$  indicate  $\rho_{true}$ . The values of Eq. 2.26 are represented on a grayscale. Light tones mark areas where Cambridge algorithm produces better density values, and dark tones mark areas where the Sakata-Sato algorithm produces better values. Computations were performed with BAYMEM employing the dataset n1r1.00 (for details see Chapter 3).

the case of a flat prior, and between 0.495 and 0.499 in the case of a procrystal prior. These values show that on average the Cambridge algorithm produces a slightly better density than the Sakata-Sato algorithm. However, none of the algorithms is clearly superior, and the variations of the values of Eq. 2.26 over the individual points show that there are regions where one and regions where the other algorithm performs better (Fig. 2.3).

The third criterion for comparison is the speed of convergence of the algorithms. In our tests, the Cambridge algorithm was usually faster than the Sakata-Sato algorithm, if the classical  $F_2$ -constraint was used. A serious problem with the Sakata-Sato algorithm is that the convergence sometimes effectively stops before the constraint is fulfilled. This happens especially for large problems and cases where the standard uncertainties have been underestimated.

Because the Cambridge algorithm produces an electron density that is closer to the true electron density than the Sakata-Sato algorithm, and because it converges faster and more reliably, its use is recommended, if the  $F_2$ -constraint is used. However, the Cambridge algorithm does not allow to use any other constraint than the  $F_2$ -constraint. The  $F_n$ -constraint with  $n$  equal to 4 or 6 was shown to converge significantly faster and to lead to better results than the  $F_2$ -constraint, especially in the medium and low density regions (Palatinus & van

Smaalen, 2002). This improvement turns out to be larger than the difference between the electron densities obtained with the Cambridge and Sakata-Sato algorithms. Thus, if the fine features of the electron density are investigated, the use of Sakata-Sato algorithm with  $F_4$ - or  $F_6$ -constraint is preferred.

## 2.3 Static weighting

The objective of the static weighting (De Vries et al., 1994) is to solve the problem with a non-Gaussian shape of the distribution of normalized residuals  $\nu = (|F_{obs}| - |F_{MEM}|) / \sigma(F_{obs})$ . It has been observed that the low-angle strong reflections have often been fitted extremely bad, while the high-angle weak reflections have been fitted very well. Therefore, the expression for constraint has been extended by a weighting factor  $w(F_{obs})$ :

$$C_w = -1 + \frac{1}{N_F} \sum_{i=1}^{N_F} w(F_{obs}(\vec{H}_i)) \left( \frac{|F_{obs}(\vec{H}_i) - F_{calc}(\vec{H}_i)|}{\sigma(F_{obs}(\vec{H}_i))} \right)^2 \quad (2.27)$$

The weighting factor should be selected so, that the low-angle reflections become more weight in the fitting process and consequently become better fitted. In BAYMEM the weighting factor can be defined either as  $w(F_{obs}(\vec{H})) = 1/|\vec{H}|^n$  or as  $w(F_{obs}(\vec{H})) = |F_{obs}(\vec{H})|^n$ , where  $|\vec{H}|$  is the length of the diffraction vector and  $|F_{obs}(\vec{H})|$  is the amplitude of the corresponding structure factor.  $n$  is a user-definable parameter.

## 2.4 Generalized F-constraints

The generalized F-constraints - similarly to the static weighting described in previous section - improve the distribution of the normalized residuals and consequently improve the quality of  $\rho_{MEM}$ . The generalized F-constraint is defined as:

$$C_{F_n} = -1 + \frac{1}{m_n(Gauss)} \frac{1}{N_F} \sum_{i=1}^{N_F} \left( \frac{|F_{obs}(\vec{H}_i) - F_{calc}(\vec{H}_i)|}{\sigma(F_{obs}(\vec{H}_i))} \right)^n \quad (2.28)$$

$m_n(Gauss)$  is the value of the  $n^{th}$  central moment of the Gaussian distribution. The generalized F-constraints are extensively described in Chapter 3.

## 2.5 G-constraints

Sometimes phases or even amplitudes of individual structure factors cannot be determined reliably. This is often the case for the powder diffraction data, where

the occurrence of groups of overlapping reflections is a frequent phenomenon. In these groups of reflections, only the sum of the intensities of several reflections can be measured. This limited information can be used in the MEM calculations by introducing so-called G-constraints (Sakata & Takata, 1996). G-constraints are defined as:

$$C_G = -1 + \frac{1}{N_G} \sum_{i=1}^{N_G} \left( \frac{G_{obs}^i - G_{MEM}^i}{\sigma(G_{obs}^i)} \right)^2 \quad (2.29)$$

$N_G$  is the total number of different groups of reflections.  $G^i$  is a so-called ‘‘group amplitude’’:

$$G^i = \sqrt{\sum_{j=1}^{N_g^i} \left( \frac{m_j}{\sum m_j} |F(\vec{H}_j)|^2 \right)} \quad (2.30)$$

$N_g^i$  is the number of reflections in group  $i$ ,  $m_j$  is the point-group multiplicity of reflection  $j$ . The summation runs over the symmetry-independent structure factors. The total maximized Lagrangian with the G-constraint is (compare Section 1.2.1):

$$L = S - \lambda_F C_F - \lambda_G C_G - \lambda_N C_N \quad (2.31)$$

To facilitate the MaxEnt analysis, the F- and G-constraints are usually combined in one constraint with a common lagrange multiplier  $\lambda_{FG}$  (Sakata & Takata, 1996):

$$L = S - \lambda_{FG}(C_F + C_G) - \lambda_N C_N \quad (2.32)$$

The formal solution of the maximum entropy equation then becomes (compare Eq. 1.27):

$$\rho_i = \frac{N_{el} N_{pix}}{V_{UC}} \tau_i \exp \left( -\lambda_{FG} \left( \frac{\partial C_F}{\partial \rho_i} + \frac{\partial C_G}{\partial \rho_i} \right) \right) / \sum_j \tau_j \exp \left( -\lambda_{FG} \left( \frac{\partial C_F}{\partial \rho_j} + \frac{\partial C_G}{\partial \rho_j} \right) \right) \quad (2.33)$$

Thus, the implementation of G-constraints in the Sakata-Sato algorithm is straightforward, it is only necessary to find a proper expression for the derivative of  $C_G$ :

$$\frac{\partial C_G}{\partial \rho_k} = \frac{1}{N_G} \frac{\partial}{\partial \rho_k} \sum_{i=1}^{N_G} \left( \frac{G_{obs}^i - G_{MEM}^i}{\sigma(G_{obs}^i)} \right)^2 = \frac{1}{N_G} \sum_{i=1}^{N_G} 2 \left( \frac{G_{MEM}^i - G_{obs}^i}{\sigma(G_{obs}^i)^2} \right) \frac{\partial G_{MEM}^i}{\partial \rho_k} \quad (2.34)$$

And the derivative of  $G_{MEM}$  is:

$$\begin{aligned} \frac{\partial G_{MEM}}{\partial \rho_k} &= \frac{1}{2G_{MEM}} \sum_{j=1}^{N_g} \frac{m_j}{\sum m_j} \frac{\partial |F(\vec{H}_j)|^2}{\partial \rho_k} = \\ &= \frac{1}{2G_{MEM}} \sum_{j=1}^{N_g} \frac{m_j}{\sum m_j} \left[ F^*(\vec{H}_j) \frac{\partial F(\vec{H}_j)}{\partial \rho_k} + c.c. \right] = \\ &= \frac{1}{G_{MEM}} \sum_{j=1}^{N_g} \frac{m_j}{\sum m_j} \Re \left[ F(\vec{H}_j) \frac{\partial F^*(\vec{H}_j)}{\partial \rho_k} \right] \end{aligned} \quad (2.35)$$

$F(\vec{H}_j)$  is a Fourier coefficient of a Fourier Transform of the electron density, and therefore the expression in the square brackets becomes:

$$F(\vec{H}_j) \frac{\partial F^*(\vec{H}_j)}{\partial \rho_k} = F(\vec{H}_j) \frac{m_k}{N_s} \sum_{s=1}^{N_s} \exp \left[ -2\pi i \vec{H}_j \cdot (\mathbf{R}_s \vec{r}_k + \vec{\tau}_s) \right] \quad (2.36)$$

where  $\{\mathbf{R}_s | \tau_s\}$  are the symmetry operators of the space group of the crystal and  $m_k$  is the multiplicity of the pixel  $k$ . Two structure factors related by a point-group symmetry operator  $\mathbf{R}_s$  fulfill equation:

$$F(\mathbf{R}_s^T \vec{H}_j) = F(\vec{H}_j) \exp(-2\pi i \vec{H}_j \cdot \vec{\tau}_s) \quad (2.37)$$

and Eq. 2.36 can be therefore rewritten as:

$$F(\vec{H}_j) \frac{\partial F^*(\vec{H}_j)}{\partial \rho_k} = \frac{m_k}{N_s} \sum_{s=1}^{N_s} F(\mathbf{R}_s^T \vec{H}_j) \exp(-2\pi i \vec{H}_j^T \mathbf{R}_s \vec{r}_s) \quad (2.38)$$

We can see, that the right-hand side is a summation over all symmetry-related structure factors. We can extend the sum in 2.35 from  $N_g$  symmetry-independent structure factors to all symmetry-equivalent structure factors of one group ( $N_{gs}$ ). If we substitute Eq. 2.38 in Eq. 2.35 and merge the inner summation over  $N_s$  and the outer summation over  $N_g$ , we must take into account the multiplicity  $m_j$  of vector  $\vec{H}_j$ . We get:

$$\frac{\partial G_{MEM}}{\partial \rho_k} = \Re \left\{ \frac{1}{G_{MEM}} \sum_{j=1}^{N_{gs}} \frac{m_j}{\sum m_j} \frac{m_k}{m_j} \left[ F(\vec{H}_j) \exp(-2\pi i \vec{H}_j \cdot \vec{r}_k) \right] \right\} \quad (2.39)$$

Substitution of 2.39 to 2.34 yields the final expression of the derivative of the G-constraint:

$$\frac{\partial C_G}{\partial \rho_k} = \frac{2m_k}{N_G} \Re \left\{ \sum_{i=1}^{N_G} \sum_{j=1}^{N_{gs}} \left[ \frac{(G_{MEM}^i - G_{obs}^i)}{G_{MEM}^i \sigma(G_{obs}^i)^2} \frac{1}{\sum m_j} F(\vec{H}_j) \right] \exp(-2\pi i \vec{H}_j \cdot \vec{r}_k) \right\} \quad (2.40)$$

This is - up to a factor of  $2m_k/N_G$  - just the real part of an inverse Fourier Transform of the quantity in the square brackets.

## 2.6 Two-channel entropy

The concept of the two-channel entropy was first introduced for reconstructions of the nuclear density from non-polarized neutron scattering data (Papoular & Gillon, 1990). The same formalism can be used to reconstruct a difference electron density, that can have both positive and negative values (Papoular et al., 1996). The difference density must be separated into two parts that are positive in all points:

$$\Delta\rho = \rho^+ - \rho^- \quad (2.41)$$

The entropy of the difference density is then defined as sum of the entropies of  $\rho^+$  and  $\rho^-$ :

$$S_{\Delta\rho} = S_{\rho^+} + S_{\rho^-} = - \sum_{i=1}^{N_{pix}} \rho_i^+ \ln \frac{\rho_i^+}{\tau_i^+} - \sum_{i=1}^{N_{pix}} \rho_i^- \ln \frac{\rho_i^-}{\tau_i^-} \quad (2.42)$$

This entropy is maximized to obtain  $\Delta\rho_{MEM}$ . The input data consist of the difference structure factors  $\Delta F = F_{obs} - F_{model}$ . The advantage of this approach is, that by optimizing only the difference map, the dynamic ratio of the density ( $|\rho_{max}|/|\rho_{min}|$ ) is extremely reduced compared to maximization of the whole  $\rho_{MEM}$ . The disadvantage of this formalism is that it removes the constraint of an everywhere positive image, that is intrinsic to the basic MaxEnt formalism and that is so suitable for reconstructions of the electron densities. Moreover, the two-channel entropy often suppresses fine details in the reconstructed difference density. This problem can be partially solved by decreasing the stopping value of the constraint (Papoular et al., 2002).

## 2.7 Prior-derived F-constraints

MaxEnt reconstructions of electron densities suffer from occurrence of artifacts. Major artifacts stem from the series termination errors, that occur, if a flat prior density is used. A sufficiently informative, non-uniform prior electron density can suppress these artifacts almost completely (De Vries et al., 1996; Papoular et al., 2002; Palatinus & van Smaalen, 2002). But even a very informative prior density does not suppress another type of artifacts. They occur due to the fact, that the structure factors, that are not included in the input dataset, can assume any value, as far as it decreases the entropy of the image. This ability of the MEM to extrapolate the values of non-measured structure factors is very favorable for density reconstructions from a flat prior density, because this is the best available estimate for the missing structure factor. But if a procrystal prior electron density is available, it turns out, that the MaxEnt estimate is often worse than the information, that can be obtained from the structure factors of the prior electron density. Thus, the electron-density reconstruction can be significantly

improved, if the structure factors of the prior are used as a constraint for the structure factors that were not measured, especially in the high-angle diffraction region, where the contribution of the bonding electrons to the scattering is negligible. The method of the prior-derived F-constraints is described in detail in Chapter 4.

## 2.8 Prior electron density - program PRIOR

The prior electron density (prior) is an essential part of the MaxEnt formalism. Only the MEM with a sufficiently informative prior can be used for studies of fine features of the electron density, like the atomic charges or the distribution of bonding electrons (De Vries et al., 1996; Papoular et al., 2002; Palatinus & van Smaalen, 2002). The best prior that can be obtained from standard structure refinements is the Independent Atom Model (IAM). In this model, the electron density is modelled as a superposition of electron densities of free, non-interacting atoms placed at their refined positions and convoluted with the refined thermal motion. An electron density constructed in this way is called procrystal electron density ( $\rho_{pro}$ ). Such a model describes the major part of the electron density very well, but it does not account fully for the effects of bonding on the electron density. Therefore, the difference density  $\rho_{MEM} - \rho_{pro}$  can be successfully used to determine the deformations of the electron density due to the bonding.

The easiest way to construct the procrystal prior is to calculate the structure factors corresponding to the model, using the well known formulas involving the atomic form factors and tensors of temperature parameters (Shmueli, 1996). The electron density can be then simply calculated as an inverse Fourier transform of the structure factors. Unfortunately, this method cannot be used but for the lightest elements. By heavier elements, the series termination errors become too pronounced and even calculation of all structure factors up to  $\sin(\theta)/\lambda \leq 6.0$  does not avoid termination ripples of such an amplitude that makes the electron density unusable as a prior in the MEM calculations. Therefore, an alternative method must be used. The method is based on evaluation of the electron density by means of an analytical Fourier transform, using the analytical approximation to the atomic form factors<sup>3</sup>. The atomic form factors are usually analytically approximated by a sum of exponentials:

$$f_a(\sin(\theta)/\lambda) = \sum_{i=1}^n a_i \exp\left(-b_i \frac{\sin^2(\theta)}{\lambda^2}\right) \quad (2.43)$$

The International Tables for Crystallography (Wilson & Prince, 1999) use  $n = 5$  and  $b_5 = 0$ , the atomic form factors published by Su & Coppens (1997) use  $n = 6$ .

---

<sup>3</sup>The method described here was inspired by personal communication with Robert Papoular and later published in Papoular et al. (2002).

It is more convenient to express the atomic form factor as a function of the diffraction vector  $\vec{H}$  in reciprocal crystal coordinates:

$$f_a(\vec{H}) = \sum_{i=1}^n a_i \exp\left(\frac{b_i}{4} |\vec{H}|^2\right) = \sum_{i=1}^n a_i \exp\left(\frac{b_i}{4} \vec{H}^T \mathbf{G}^* \vec{H}\right) \quad (2.44)$$

Here  $\mathbf{G}^*$  denotes the reciprocal metric tensor  $G_{ij}^* = \vec{a}_i^* \cdot \vec{a}_j^*$

Convolution of the static atomic electron density with the anisotropic harmonic thermal motion of the atom is expressed in reciprocal space by multiplying the atomic form factor by corresponding displacement term that involves the displacement tensor  $\mathbf{U}$  (Shmueli, 1996). This yields the anisotropic dynamic atomic form factor  $d_a$ :

$$d_a(\vec{H}) = \sum_{i=1}^n a_i \exp\left(\frac{b_i}{4} \vec{H}^T \mathbf{G}^* \vec{H}\right) \exp(2\pi^2 \vec{H}^T \mathbf{A}^* \mathbf{U} \mathbf{A}^* \vec{H}) \quad (2.45)$$

The matrix  $\mathbf{A}^*$  is a diagonal matrix of the lengths of the reciprocal-space basic vectors:  $A_{ii}^* = |\vec{a}_i^*|^2$ ;  $A_{ij}^* = 0$ ,  $i \neq j$ .

After some reordering, Eq. 2.45 becomes:

$$d_a(\vec{H}) = \sum_{i=1}^n a_i \exp\left(-\vec{H}^T \underbrace{\left[\frac{b_i}{4} \mathbf{G}^* + 2\pi^2 \mathbf{A}^* \mathbf{U} \mathbf{A}^*\right]}_{\mathbf{M}_i} \vec{H}\right) = \sum_{i=1}^n a_i \exp\left(\vec{H}^T \mathbf{M}_i \vec{H}\right) \quad (2.46)$$

The dynamic electron density of an atom  $a$  is given by a Fourier transform of  $d_a$ . Since  $d_a$  is expressed as a three-dimensional Gaussian, its Fourier Transform can be calculated analytically. The result is:

$$\rho_a(\vec{r}) = |\mathbf{G}^*|^{\frac{1}{2}} \sum_{i=1}^n a_i \frac{|\mathbf{M}_i^{-1}|}{(2\pi)^{\frac{3}{2}}} \exp\left(-\vec{r}^T \mathbf{M}_i^{-1} \vec{r}\right) \quad (2.47)$$

The prefactor  $|\mathbf{G}^*|^{\frac{1}{2}}$  transforms  $\rho_a$  from units of the crystal coordinate system to  $e/\text{\AA}^3$ .

Eq. 2.47 provides a convenient way of calculating the electron density of an atom  $a$ . The atom is centered in the origin of the coordinate system and the density is a function of coefficients of the analytical approximation of the atomic form factors, and of the coefficients of the atomic tensor of displacement parameters. The formula does not involve any numerical Fourier Transform and therefore does not lead to series termination error. The analytical approximation becomes relatively inaccurate at high values of  $\sin(\theta)/\lambda$  (Wilson & Prince, 1999; Su & Coppens, 1997). However, these values influence mostly the density close to atomic nuclei. The experimental data provide almost no information about this electron

density, and the exact form of the electron density in the vicinity of atomic nuclei is therefore not crucial for the fit to the experimental data.

The method described in previous paragraphs was implemented in a computer program PRIOR. The input to PRIOR is the standard crystallographic information in a format common with BAYMEM (Appendix A) and the list of coordinates and thermal parameters of all independent atoms in the unit cell. The output is the procrystal electron density in .m81 format of JANA2000 (Section A.6.1). The prior density is calculated on the same grid that will be used for the MEM calculation. For a calculation with the same input data, but with different grid, a new prior on the new grid must be calculated. The input file for BAYMEM can be used as an input file for PRIOR, provided two specific keywords are added. These keywords are `outputprior filename`, that defines the name of the output electron density, and a pair of keywords `atoms - endatoms`. This keyword defines the parameters of the atoms in the structure and its format is:

```

small

atoms
name1 type occupancy x y z U11 U22 U33 U12 U13 U23
name2 type occupancy x y z U11 U22 U33 U12 U13 U23
.
.
.
endatoms

```

Each line defines one atom. The name is an arbitrary identifier without spaces. Type is the elemental symbol of the atom and is used to identify the parameters of the analytical approximation to the form factors of that atom in the table. Occupancy includes the site multiplicity of the atom. For example, if the multiplicity of the position of an atom is 4, and the position is fully occupied, then the value of occupancy must be 0.25. Next values are the fractional coordinates of the atom and the harmonic displacement parameters.

## 2.9 Analysis of $\rho_{MEM}$ - program EDMA

The main output from the MEM calculation is the MEM-optimized electron density distribution  $\rho_{MEM}$ .  $\rho_{MEM}$  can be viewed in form of two-dimensional sections or projections using special programs. However, there is a large amount of information that cannot be inferred by only observing the images. Quantitative tools have to be used to extract all information contained in  $\rho_{MEM}$ . This concerns at first place the exact position of the atoms and also other characteristics, like the atomic charge.

The accurate analysis of  $\rho_{MEM}$  becomes even more important in case of higher-dimensional electron densities, where the graphical representation becomes difficult and where the modulation of the atomic positions is the output of major interest.

The principles of the map analysis described in this section were implemented in a computer program EDMA. This program is capable of analysis of both ordinary (3D) and higher-dimensional structures. The user manual to this program is given in Appendix B.

### 2.9.1 Interpolation

The positions of the maxima of the electron density cannot be considered equal to the coordinates of the pixel with maximum electron density, because the resolution of the grid is not sufficient (usually about 0.05 Å). An interpolation method must be used to locate the position of the maximum of the density more accurately. In addition to that, the t-sections of the superspace electron density have a general orientation with respect to the grid and their accurate extraction also demands interpolation of the density values between the grid points.

The basis of the interpolation method used in EDMA is a cubic spline interpolation in one dimension (Press et al., 1996). The method has been generalized to arbitrary dimension using the philosophy of bicubic spline interpolation (Press et al., 1996). The principle of the method is illustrated in Fig. 2.4. The interpolation of a  $n$ -dimensional electron density runs in  $n$  cycles. In every cycle, one-dimensional cubic spline interpolation is used to calculate a  $(k-1)$ D section of the  $k$ D density. This section contains the point, in which the density is to be determined. In the next cycle the newly calculated  $(k-1)$ D density is used as input and the dimension is further reduced. Ultimately, this leads the interpolated density of the point in question.

The result of the interpolation is independent of the order of axes, in which the density is interpolated. To prove this statement, we first construct a general formula for spline interpolation in one dimension. We have a function  $y(x)$  given by its tabulated values  $(x_i, y_i), i = 0 \dots u-1$ , or, in short, by  $u$ -dimensional vectors  $\vec{x}, \vec{y}$ . For a general point  $x_p$  lying in an interval  $\langle x_j, x_{j+1} \rangle$  we have (Press et al., 1996):

$$y(x_p) = Ay_j + By_{j+1} + Cy_j'' + Dy_{j+1}'' \quad (2.48)$$

where

$$\begin{aligned} A &= \frac{x_{j+1} - x_p}{x_{j+1} - x_j} \\ B &= 1 - A \\ C &= \frac{1}{6}(A^3 - A)(x_{j+1} - x_j)^2 \\ D &= \frac{1}{6}(B^3 - B)(x_{j+1} - x_j)^2 \end{aligned} \quad (2.49)$$

The values of the second derivatives  $y_k'', k = 0 \dots u-1$  can be calculated from

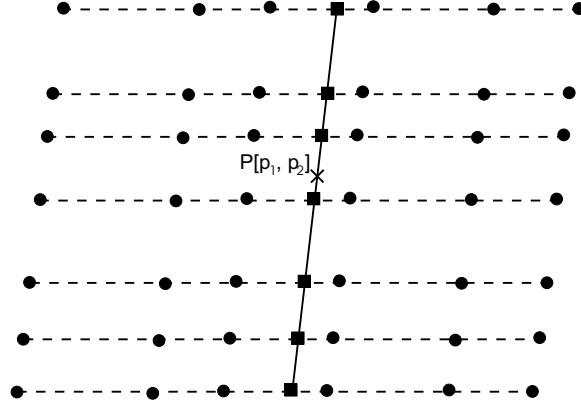


Figure 2.4: Interpolation process in two dimensions. In first step, the rows of points  $x_{ij}, y_{ij}$  (circles) are interpolated along the dashed lines to obtain points of the vector  $\vec{y}_{p_1}$  (squares). This column is then interpolated along the full line to obtain the density at the point P (cross).

a set of  $n - 2$  linear equations of the form:

$$\frac{x_k - x_{k-1}}{6} y''_{k-1} + \frac{x_{k+1} - x_{k-1}}{3} y''_k + \frac{x_{k+1} - x_k}{6} y''_{k+1} = \frac{y_{k+1} - y_k}{x_{k+1} - x_k} - \frac{y_k - y_{k-1}}{x_k - x_{k-1}} \quad k = 1 \dots u - 2 \quad (2.50)$$

In addition to that, two more equations have to be supplied to obtain a unique solution. The most usual choice is  $y''_0 = y''_{u-1} = 0$  to produce so called natural splines, but any other choice is possible. This set of linear equations can be compactly written in matrix form:

$$\begin{aligned} \mathbf{M}\vec{y}'' &= \mathbf{N}\vec{y} \\ \vec{y}'' &= \mathbf{M}^{-1}\mathbf{N}\vec{y} = \mathbf{S}\vec{y} \end{aligned} \quad (2.51)$$

The matrix  $\mathbf{S}$  is independent of the functional values  $y_i$  and depends only on the values  $x_i$ . In next step, we construct vectors  $\vec{A}, \vec{B}, \vec{C}, \vec{D}$  of dimension  $u$  from the functions  $A, B, C, D$  so that

$$\begin{aligned} \vec{A} \cdot \vec{y} &= Ay_j \\ \vec{B} \cdot \vec{y} &= By_{j+1} \\ \vec{C} \cdot \vec{y} &= Cy''_j \\ \vec{D} \cdot \vec{y} &= Dy''_{j+1} \end{aligned} \quad (2.52)$$

This is readily achieved by

$$A_k = \begin{cases} 0 & : k \neq j \\ A & : k = j \end{cases} \quad (2.53)$$

and analogously for  $\vec{B}$ ,  $\vec{C}$  and  $\vec{D}$ . With this notation, the interpolation formula can be written in a concise form as (compare Eqs. 2.48 and 2.51):

$$y_p = \vec{A} \cdot \vec{y} + \vec{B} \cdot \vec{y} + \vec{C}^T \mathbf{S} \vec{y} + \vec{D}^T \mathbf{S} \vec{y} \quad (2.54)$$

or

$$y_p = \vec{s} \cdot \vec{y} \quad (2.55)$$

The vector  $\vec{s}$  depends only on the values  $x_i$  and  $x_p$ .

Having obtained the general formula for the one-dimensional cubic splines we can turn to the higher-dimensional case. We will first explicitly consider the two dimensional case for the sake of simplicity. The generalization to the general  $nD$  case is then straightforward.

The 2D function is defined by its tabulated values  $x_{ij}$ ,  $y_{ij}$ ,  $i = 0 \dots u - 1$ ,  $j = 0 \dots v - 1$ . We suppose that the values  $x_{ij}$  lie on a straight line, if one index is fixed and the other varies. This is equivalent to following condition: every four values  $x_{ij}$ ,  $x_{(i+1)j}$ ,  $x_{i(j+1)}$ ,  $x_{(i+1)(j+1)}$  must form corners of a parallelogram. (Fig. 2.4).

To interpolate a value  $y_{p_1 p_2}$  of the function  $y(x_1, x_2)$  at point  $P[p_1, p_2]$ , we first calculate a one-dimensional section of the two-dimensional density by interpolation along every row of points  $x_{ij}$  with the first index fixed. As a result, we obtain  $v$  pairs  $x_{pj}$ ,  $y_{pj}$ ,  $j = 0 \dots v - 1$ , where  $p$  denotes the first coordinate is equal to the coordinate  $p_1$  of the point  $P$ . Using previous results (Eq. 2.55), we can write:

$$y_{pj} = \vec{s}_1 \cdot \vec{y}_j, \quad j = 0 \dots v - 1 \quad (2.56)$$

Notation  $\vec{y}_j$  denotes a column vector of dimension  $u$  corresponding to the row of  $y_{ij}$  with  $j$  constant and  $i = 0 \dots u - 1$ . The symbol  $\vec{s}_1$  stands for the vector  $\vec{s}$  from Eq. 2.55 related to the rows of  $x_{ij}$  with the second index constant. Because of the condition on the regularity of the grid the vector  $\vec{s}_1$  is independent of the index  $j$ .

We form a one-dimensional vector  $\vec{y}_{p_1}$  from the values  $y_{pj}$  and  $j$  Eqs. 2.56 can be written in a matrix form

$$\vec{y}_{p_1} = \mathbf{Y} \vec{s}_1 \quad (2.57)$$

where  $\mathbf{Y}$  is the matrix of the values  $y_{ij}$ .

The final value  $y_{p_1 p_2}$  is obtained using Eq. 2.55 again:

$$y_{p_1 p_2} = \vec{s}_2^T \cdot \vec{y}_{p_1} \quad (2.58)$$

Combining Eqs. 2.56 and 2.57, we obtain the final result:

$$y_{p_1 p_2} = \vec{s}_2^T \mathbf{Y} \vec{s}_1 \quad (2.59)$$

The proof follows immediately from Eq. 2.59. If the interpolation is independent of the order of the axes, the resulting formula must be invariant to the

transposition of the matrix  $\mathbf{Y}$  and simultaneous exchange of the indices 1 and 2 of the vectors  $\vec{s}$ . Eq. 2.59 fulfills this requirement.

The matrix notation becomes impractical for more-dimensional cases. Therefore we turn to the tensor notation. Eq. 2.59 becomes (using the standard convention for summation over repeated indices):

$$y_{p_1 p_2} = s_{1i} s_{2j} y_{ij} \quad (2.60)$$

The general  $n$ -dimensional case follows immediately from the considerations in the previous paragraphs (and by analogy to Eq. 2.60):

$$y_{p_1 p_2 \dots p_n} = s_{1i_1} s_{2i_2} \dots s_{ni_n} y_{i_1 i_2 \dots i_n} \quad (2.61)$$

This equation is invariant to any permutation of the indices  $i_k$  combined with corresponding permutation of the first indices of the numbers  $s_{ki_k}$ .

The interpolated value by the cubic-spline method is theoretically dependent on all values of the grid. In practice, the dependence strongly decreases with the distance from the central point. Therefore, in EDMA, every point is calculated from the pixels lying in some (user-definable) neighborhood of that pixel. This simplification does not introduce any detectable errors and saves computational time.

## 2.9.2 Charge partitioning

A large number of charge-partitioning systems have proposed in past (Hirshfeld, 1977; Bader, 1990; Coppens, 1997; and references therein). The most widely used and acknowledged system is the concept ‘‘Atoms in molecules’’ (Bader, 1990). The concept partitions the whole electron density of a molecule (or crystal) into a set of non-overlapping, space-filling regions, so called atomic basins. The points  $\vec{r}$  of the boundary between the basins are defined as the points of zero flux of charge:

$$\nabla \rho(\vec{r}) \vec{n}(\vec{r}) = 0 \quad (2.62)$$

where  $\vec{n}(\vec{r})$  is the normal to the boundary at point  $\vec{r}$ . In words, the interatomic surface is such an area, that is not crossed by any gradient path of the electron density.

This definition allows for charge partitioning that is based solely on the electron density, while it bears close relations to the quantum-mechanical approach to assemblies of atoms (Bader, 1990). Two basic properties of this partitioning are of both theoretical and practical importance: The sum of the charges assigned to individual atoms corresponds to the total charge in the crystal and at each point of space the entire electron density is assigned to one and only one atom.

Based on the Bader’s charge-partitioning system, many properties of the electron density can be directly evaluated, including:

- The total charge of the atom: defined as the integral of the charge density over the volume of the atomic basin.
- The atomic volume: the volume of the atomic basin.
- The dipole moment of a molecule or the total dipole moment of an acentric crystal structure: The dipole moment can be determined from the difference between position of the center of negative charge of the atomic basin and the position of the positive charge, that coincides with the atomic position (see Section 2.9.3).

EDMA uses Bader's space- and charge-partitioning to calculate the charge of the atom and the center of the atomic charge. The theory has been adapted to discretized electron density and simplified to allow reasonably fast calculation (Fig. 2.5). The charge of each pixel is assigned to the corresponding local maximum fully. This is not a problem except for the pixels on the border of two atomic basins. The border would probably divide the pixel in two parts, assigning each part to different maximum. Thus, small inaccuracies in the charges can be expected. In particular, two symmetrically equivalent atoms, which share a common border, will have slightly different charges, because the pixels on their border are assigned arbitrarily to one of them. This problem can be overcome by prior resampling of the electron density to a better resolution. However, this will naturally increase the computational time. In practice, the inaccuracies introduced by the discrete nature of the MEM electron density are usually much lower than the inaccuracy resulting from other sources.

### 2.9.3 Definition of atomic position

The position of an atom in a crystal is best defined as a time-averaged position of its nucleus. The electron-density provides only indirect evidence on the position of the atoms. One way to estimate the position of the atom is to determine the point with highest electron density. If the thermal movement of the atom is perfectly harmonic, then the position of the highest electron density in an atomic basin coincides with the position of the atom. This statement is based on the widely accepted approximation, that the electrons follow the movement of the atomic nucleus exactly. However, if the thermal movement is not purely harmonic, then the point of the highest electron density does not coincide with the time-averaged position of the nucleus.

An alternative way to estimate the atomic position is to determine the center of charge of the electron distribution in the atomic basin. This estimate is very close to that used implicitly in the standard structure refinements. In case of a discrete-boundary charge partitioning, the center of charge of an atomic basin  $\Omega$

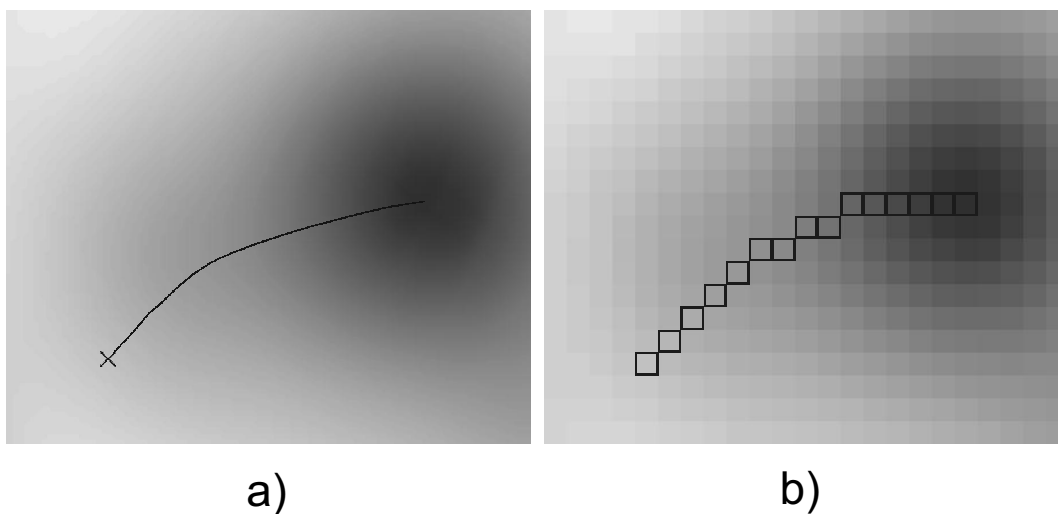


Figure 2.5: The assignment of a point to a local maximum a) in a continuous density according to the theory and b) in a discrete density by choosing the neighboring pixel of the highest density until the maximum is reached.

of an atom  $a$  is given by:

$$\vec{r}_a = \frac{1}{\int_{\Omega_a} \rho(\vec{r}) d\vec{r}} \int_{\Omega_a} \vec{r} \rho(\vec{r}) d\vec{r} \quad (2.63)$$

In the discrete case, the integrals must be replaced by summations and the summation runs over all pixels  $i$  belonging to the atomic basin  $\Omega_a$ :

$$\vec{r}_a = \frac{1}{\sum_{\Omega_a} \rho_i} \sum_{\Omega_a} \vec{r}_i \rho_i \quad (2.64)$$

In practice, not all density of an atomic basin can be included in the calculation of the center of charge. First, the deformation of the electron density due to the interaction with neighboring atoms should not be taken into account for the determination of the center of charge, if the center of charge is to be used as an estimate of the atomic position. Second, the low density regions far from the atomic positions can contain relatively large amount of noise compared to the values of the density. Including these low-density regions would introduce unnecessary inaccuracy in the determination of the center of charge. For both these reasons, the center of charge is in practice determined only from pixels, whose  $\rho_i$  exceeds some (user-definable) limit. If the center of charge is calculated as an input for the determination of the dipole moment, then it is necessary to include all pixels within the atomic basin in the calculation.

### 2.9.4 Positions of atoms in higher-dimensional electron density

The positions of atoms in a  $(3 + d)$ D electron density are not given by one point, but by  $d$ D atomic domains. The 3D structure is obtained as a 3D section of the  $(3 + d)$  electron density perpendicular to the internal coordinate axes  $\vec{a}_i, i = 4, \dots, 3 + d$ . The position of the 3D section along the internal dimension is described by a vector  $\vec{t}$  (Section 1.1.3). Such 3D sections are called t-sections. The t-sections represent the real-space electron density, that can be analyzed with the same methods as used for ordinary electron density with the exception, that the t-sections are not periodic. Therefore, the atomic properties, that are not defined purely in the reference basic unit cell (atomic basins of atoms lying close to the border of the basic unit cell), cannot be determined from the periodicity and the electron density of the neighboring basic unit cells must be calculated explicitly.

The analysis of the higher-dimensional electron density thus proceeds in two steps: First, t-sections at some user-defined interval of  $\vec{t}$  of one basic unit cell plus necessary neighborhood is extracted from the  $(3 + d)$ D electron density. The interval in  $\vec{t}$  between successive sections determines the sampling of the modulation functions. Second, the t-section is analyzed to obtain the properties of the electron density, i.e. positions of the atoms, atomic volumes, atomic charges and centers of atomic charges. The values of the atomic properties as a function of  $\vec{t}$  then give the modulation functions of the atomic properties.



# Chapter 3

## The Generalized F-constraint in the Maximum Entropy Method — a study on simulated data

### Abstract

One of the classical problems in the application of the Maximum Entropy Method (MEM) to electron density reconstructions is the uneven distribution of the normalized residuals of the structure factors  $(|F_{obs}(\vec{H})| - |F_{MEM}(\vec{H})|)/\sigma(\vec{H})$  of the resulting electron density. This distribution does not correspond to the expected Gaussian distribution and it leads to erroneous features in the MEM reconstructions. It is shown that the classical  $\chi^2$ -constraint is only one of many possible constraints, and that it is too weak to restrict the resulting distribution to the expected Gaussian shape. It is proposed that constraints should be used that are based on the higher-order central moments of the distribution of the structure factor residuals. In this work the influence of different constraints on the quality of the MEM reconstruction is investigated. It is proposed that the use of a combined constraint on more than one central moment simultaneously would lead to again improved results. Oxalic acid dihydrate was chosen as model structure, from which several datasets with different resolutions and different levels of noise were calculated and subsequently used in the MEM. The results clearly show that the use of different constraints leads to significantly improved results.

### 3.1 Introduction

The Maximum Entropy Method (MEM) is used as a powerful tool for a model-free image reconstruction in many scientific applications (von der Linden et al., 1998). In crystallography, one particular application is the investigation of the electron

density in the crystal structure. After the first promising applications in this field (Collins, 1982; Sakata & Sato, 1990), several warnings concerning the reliability and possible pathologies of the method appeared (Jauch, 1994; De Vries et al., 1996). One of the obvious problems was that the distribution of the normalized residuals of the structure factors  $\Delta F(\vec{H})/\sigma(\vec{H}) = (|F_{obs}(\vec{H})| - |F_{calc}(\vec{H})|)/\sigma(\vec{H})$  was strongly deviated from the expected Gaussian distribution. Some of the reflections – usually strong reflections at low angles – had very large  $\Delta F(\vec{H})/\sigma(\vec{H})$ , while the rest was fitted almost exactly. The large deviation of the histogram of  $\Delta F(\vec{H})/\sigma(\vec{H})$  from the Gaussian distribution was responsible for unphysical features in the corresponding electron density. A solution to this problem was proposed by De Vries et al. (1994), who employed an *ad hoc* weighting scheme within the classical  $\chi^2$ -constraint. However, a theoretical basis for this weighting scheme does not exist.

Here we propose new constraints based on the higher-order central moments of the distribution of  $\Delta F(\vec{H})/\sigma(\vec{H})$ . We show that the use of these constraints produces results with better distributions of  $\Delta F(\vec{H})/\sigma(\vec{H})$  and with less artifacts in the reconstructed electron density than the classical  $\chi^2$ -constraint.

The method is tested against datasets of various resolutions and with various noise levels, that were computed for a known electron density of oxalic acid dihydrate.

## 3.2 The Method

The basic principle of the MEM is that the optimal image is defined to be the image with the maximum value of the entropy functional  $S$ , while one or more constraints of the type  $C_j = 0$  ( $j = 1, \dots, N_c$ ) are fulfilled. For our purposes the image is the electron density ( $\rho$ ) in the unit cell, that is defined by its values  $\rho_i$  on a grid of  $N_p = N_1 \times N_2 \times N_3$  points. The entropy is defined as

$$S = - \sum_{i=1}^{N_p} \rho_i \log \frac{\rho_i}{\tau_i} \quad (3.1)$$

where the values  $\tau_i$  define the prior or reference electron density. For an overview of the crystallographic applications of the MEM see Gilmore (1996).

The constraints should be selected so as to define, which image is in agreement with the observed data. The first reasonable constraint is the normalization of  $\rho$  to the expected number of electrons per unit cell volume:

$$\int_V \rho dV - N_{el} = 0 \quad (3.2)$$

Traditionally, the constraint to the scattering data is the least squares likelihood

criterion  $\chi^2 - 1 = 0$ , with

$$\chi^2 = \frac{1}{N_F} \sum_{i=1}^{N_F} \left( \frac{|F_{obs}(\vec{H}_i)| - |F_{MEM}(\vec{H}_i)|}{\sigma(F_{obs}(\vec{H}_i))} \right)^2 \quad (3.3)$$

where the summation runs over all measured structure factors  $N_F$ . This definition of the constraint cannot be used directly, since it does not contain the information about the phases of the structure factors and does not lead to convergence. Therefore, the so called F-constraint is usually employed:

$$C_F = -1 + \frac{1}{N_F} \sum_{i=1}^{N_F} \left( \frac{|F_{obs}(\vec{H}_i) - F_{MEM}(\vec{H}_i)|}{\sigma(F_{obs}(\vec{H}_i))} \right)^2 \quad (3.4)$$

The value of  $C_F$  depends both on the amplitudes and phases of  $F_{obs}(\vec{H})$  and  $F_{MEM}(\vec{H})$ .  $C_F$  is minimal, if the phases of all  $F_{obs}(\vec{H}_i)$  are equal to the corresponding  $F_{MEM}(\vec{H}_i)$ . In that case  $C_F = \chi^2 - 1$ .

The use of the  $\chi^2$  statistics (and its phased modification in the  $C_F$ -constraint) is based upon an assumption that the experimental errors on  $|F_{obs}(\vec{H})|$  are random with a Gaussian distribution:

$$\frac{|F_{obs}(\vec{H})| - |F_{true}(\vec{H})|}{\sigma(F_{obs}(\vec{H}_i))} = \varepsilon_{Gauss} \quad (3.5)$$

where  $\varepsilon_{Gauss}$  is a sample of the random variable with normalized Gaussian distribution. Since the resulting electron density  $\rho_{MEM}$  should be the best estimate of the true density, the corresponding calculated structure factors  $F_{MEM}$  should be the best estimate of  $F_{true}$  and the distribution of the normalized residuals should be Gaussian too.

It is obvious that the Gaussian distribution of errors does imply the validity of the  $\chi^2$ - (or  $C_F$ -) constraint, but not *vice versa*. Constraining only  $\chi^2$  is not sufficient to assure the proper Gaussian form of the resulting error distribution.

A probability distribution of a random variable  $x$  is characterized by the values of its central moments  $m_n$ . For the normalized Gaussian distribution the central moments are

$$m_n(Gauss) = \int_{-\infty}^{\infty} x^n \frac{1}{\sqrt{2\pi}} \exp\left(-\frac{x^2}{2}\right) dx \quad (3.6)$$

The values of the moments of odd order are all zero and the moments of even order are:

$$m_{2k}(Gauss) = \prod_{i=1}^k (2i - 1) \quad (3.7)$$

In case of  $N$  samples of the variable  $x$  the central moments  $m_n$  can be computed from

$$m_n = \frac{1}{N} \sum_N x_i^n \quad (3.8)$$

It follows from Eqs. 3.3 and 3.8 that  $\chi^2$  is the  $m_2$  central moment of the distribution of  $\Delta F(\vec{H})/\sigma(\vec{H})$ . Thus, the concept of generalized F-constraint can be introduced, with  $F_2$  referring to the classical constraint on the second-order moment, and with  $F_n$  defining a constraint based on the moment of order  $n$ :

$$C_{F_n} = -1 + \frac{1}{m_n(Gauss)} \frac{1}{N_F} \sum_{i=1}^{N_F} \left( \frac{|F_{obs}(\vec{H}_i) - F_{MEM}(\vec{H}_i)|}{\sigma(F_{obs}(\vec{H}_i))} \right)^n \quad (3.9)$$

Only the constraints with  $n$  even restrict the width of the histogram, constraints with  $n$  odd are sensitive only to the symmetry of the distribution with respect to the origin. Therefore, only the constraints with  $n$  even are used in this work.

It has been suggested that more simultaneous constraints (up to the number of independent observations) of the form  $(|F_{obs}(\vec{H})| - |F_{calc}(\vec{H})|)/\sigma(F_{obs}(\vec{H}))$  could be used instead of the single  $\chi^2$ -constraint (Carvalho et al., 1996). This requires some additional criterion for defining the point of convergence and strongly restricts the role of the MEM as the noise filter. We suggest that the use of several  $F_n$ -constraints simultaneously is the proper way to handle noisy data, since the expected shape of the histogram is the only information about the noise that is available. However, the available algorithms do not allow such a generalization. Therefore, in the present stage of work, the influence of different choices of a single constraint based on Eq. 3.9 on the result of MEM was investigated.

### 3.3 Computational details

The method was tested on the structure of the oxalic acid dihydrate. The main reason for this choice was that this compound became a kind of standard for charge density studies. In addition to that, the structure of oxalic acid dihydrate is very suitable for this type of work, since it is centrosymmetric and the central molecule is planar. That allows an easy interpretation of the majority of the features using only one section of the electron density. The basic characteristics of the structure are summarized in Table 3.1.

At first, the electron density of the procrystal structure (superposition of independent atoms,  $\rho_{pro}$ ) was created. This was done by a method due to Papoular et al. (2002). The analytical approximation to spherical atomic scattering factors (Su & Coppens, 1997) for each atom of the structure was multiplied by the anisotropic displacement factor of that atom. The resulting 3-dimensional distribution in reciprocal space was then transformed by means of the analytical

Table 3.1: Basic characteristics of the structure of the oxalic acid dihydrate

Chemical formula	HOOC-COOH.2H <sub>2</sub> O
Chemical formula weight	126.06
Cell setting, space group	Monoclinic, unique axis b, P2 <sub>1</sub> /n
a, b, c [Å]	6.101, 3.500, 11.955
$\beta$ [°]	105.78
V [Å <sup>3</sup> ]	245.64
Z	2

Fourier transform to obtain the electron density of that atom. The density was sampled on the  $64 \times 32 \times 128$  pixel grid, which corresponds to pixel size of approximately  $0.1 \times 0.1 \times 0.1 \text{ \AA}^3$ . The positional and displacement parameters from the refinement due to Šlouf (2001) were used. The electron densities of the individual atoms were then summed up to obtain  $\rho_{pro}$ . The “true” electron density  $\rho_{true}$  was then constructed by summing  $\rho_{pro}$  with the dynamic deformation density  $\rho_{def}$ , as determined by the multipole refinement of Šlouf (2001) (Fig. 3.1a). This caused 1.65% of the pixels of the resulting electron density to be negative. The lowest density was  $-0.021e/\text{\AA}^3$ . The negative areas were located in the low-density intermolecular regions. This unphysical feature probably originates from the inaccuracy of the multipole expansion in these very low density regions. The MEM cannot handle these negative regions and very low density regions increase the dynamic ratio of the electron density inadequately. Therefore, the pixels with  $\rho < 0.005e/\text{\AA}^3$  were set to  $0.005e/\text{\AA}^3$ . 2.45% of the pixels were corrected.

The electron density obtained by this procedure is certainly not the true electron density of oxalic acid dihydrate. The analytical approximation used in the first step is not absolutely accurate and the structure parameters and multipole deformation density can contain substantial degree of inaccuracy, too. However, this model of electron density is good enough to be used as the reference electron density for MaxEnt calculations and will be denoted as  $\rho_{true}$  (Fig. 3.1b).

The structure factors corresponding to the original map were calculated by means of a numerical Fourier transform. To investigate the influence of noise and resolution on the quality of the MEM reconstruction, 16 different datasets were created. The value  $(\frac{\sin(\theta)}{\lambda})_{max}$  is used as a measure of resolution in this paper. It was chosen to be 0.5, 0.75, 1.0 and 1.25 for the respective datasets, and for each resolution four different levels of Gaussian noise were added to the calculated structure factors. To simulate the error distribution in real experimental data,  $\sigma(F_{obs})$  were calculated from:

$$\sigma(F_{obs}) = \nu \sqrt{p|F_{obs}|^2 + \frac{\beta + |F_{obs}|^2}{|F_{obs}|^2}} \quad (3.10)$$

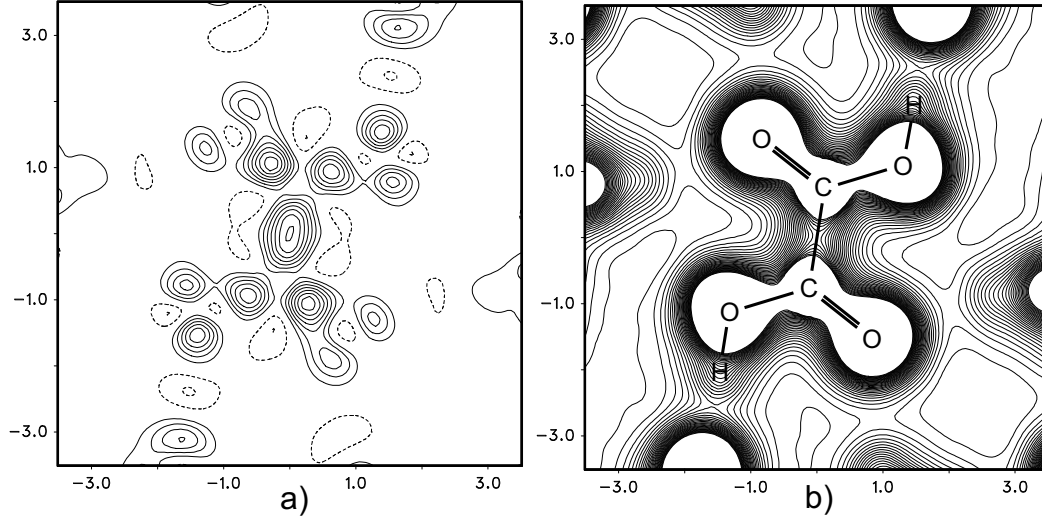


Figure 3.1: The sections of the true electron density showing the oxalic acid molecule. a) The dynamic deformation density  $\rho_{def}$  obtained by the multipole refinement (Šlouf, 2001). b) The total electron density  $\rho_{true}$ . Scale in Å, contours  $0.07 \text{ e}/\text{Å}^3$ , cut-off  $2.0 \text{ e}/\text{Å}^3$ , zero contour omitted. Maximum of the deformation density  $0.56 \text{ e}/\text{Å}^3$ , maximum of the total density  $56.79 \text{ e}/\text{Å}^3$ .

where  $\nu$  defines the noise level,  $\beta$  simulates the influence of nonzero background and  $p$  is the commonly used instability factor. The noisy “observed” structure factors were then calculated to fulfill the equation:

$$F_{obs} = F_{true} + \sigma(F_{obs}) \cdot \varepsilon_{Gauss} \quad (3.11)$$

Here  $\varepsilon_{Gauss}$  is the random variable with normalized Gaussian probability distribution. Three different non-zero noise levels were created this way. The noiseless datasets at each resolution were included for checking purposes. Although the structure factors in the noiseless datasets were exact, which means they should be assigned a zero standard deviation, this is not possible due to the nature of the constraints (Eq. 3.9). Therefore, the value of  $\sigma(F_{obs})$  was set to 0.005 for all structure factors, so as to be low enough and to allow the computations to finish in a reasonable time. The parameters of different noise levels and resolutions are summarized in Table 3.2 and Fig. 3.2.

It is interesting to compare the phases of structure factors corresponding to  $\rho_{true}$  with the phases corresponding to  $\rho_{pro}$ . In the present case, which is representative for investigations of accurate electron densities, the amount of the unknown structure is minute and the phases of the true structure factors are very well estimated by the phases of the structure factors of  $\rho_{pro}$ . Among all 4029 structure factors up to  $(\frac{\sin(\theta)}{\lambda})_{max} = 1.25$ , only 9 have different phases for  $\rho_{true}$  and  $\rho_{pro}$ . Moreover, Eq. 3.11 allows for changes of phases between  $F_{obs}$  and  $F_{true}$ .

Table 3.2: Parameters of the datasets. Reflections with  $|F_{obs}| < 5\sigma(F_{obs})$ , (which corresponds to  $I < 2.5\sigma(I)$ ) are considered unobserved. The shorthand notation used in text and figures for given dataset consists of the letter "n" and the noise level followed by the letter "r" and the value of  $(\frac{\sin(\theta)}{\lambda})_{\max}$  of the resolution. For example, n1r0.75 denotes dataset with noise level 1 and resolution  $(\frac{\sin(\theta)}{\lambda})_{\max} = 0.75$ . For definitions of  $\nu$ ,  $\beta$  and  $p$  see Eq. 3.10.

noise levels				
	level 0	level 1	level 2	level 3
$\nu$	0.005	0.025	0.1	0.25
$\beta$	0	1	10	15
$p$	0	0.0001	0.0001	0.0001

resolution				
shells in	independent	observed/unobserved		
$\frac{\sin(\theta)}{\lambda}$	reflections	level 1	level 2	level 3
$< 0, 0.5 >$	258	253/ 5	235/ 23	217/ 41
$(0.5, 0.75 >$	608	574/ 34	468/ 140	358/ 250
$(0.75, 1.00 >$	1182	1042/140	714/ 468	425/ 757
$(1.00, 1.25 >$	1981	1480/501	604/1377	165/1816

As the consequence of the introduction of the noise, there have been many more phases changed in each noisy dataset than nine. Thus, the results presented here are not influenced by the preliminary multipole refinement and can be regarded as being obtained using just the standard refinement.

We have developed our own computer program BAYMEM for the applications of the MEM in charge density analysis (first version Schneider, 2001). This program is designed to work in general n-dimensional space to allow computations of the MEM electron density of incommensurately modulated structures, but can be used for standard 3D structures too without any restrictions. BAYMEM can use both the algorithm of Sakata & Sato (1990) and the MEMSys5 package (Gull & Skilling, 1999a). The program was extended to deal with the generalized F-constraint. For the present study the algorithm by Sakata & Sato (1990) was used.

The following characteristics are used to compare the quality of the MaxEnt reconstructions:

- The values of the even central moments of the distribution of normalized residuals
- The overall shape of the histogram
- The section through  $\rho_{MEM}$  in the plane of the HOOC-COOH molecule

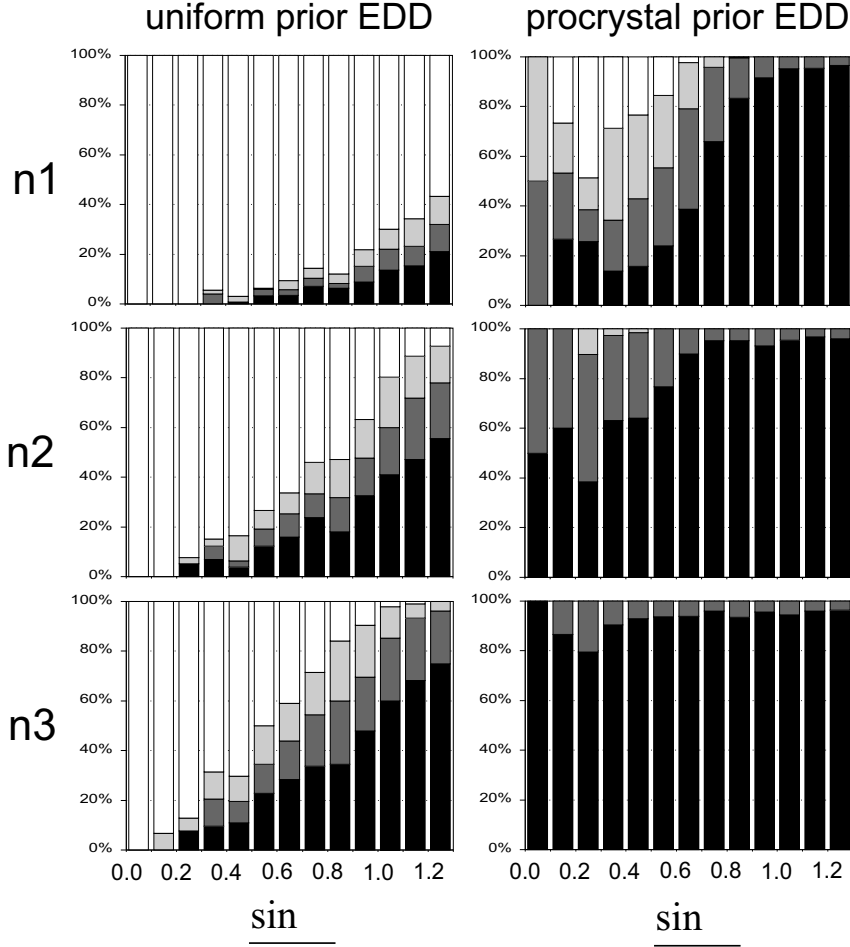


Figure 3.2: Distribution of  $|F_{obs} - F_{prior}|/\sigma(F_{obs})$  as function of the resolution for different noise levels. Note that for uniform prior  $F_{prior}=0$  for all structure factors except  $F(000)$ . Black:  $\Delta F < 2\sigma$ , dark gray:  $2\sigma < \Delta F < 5\sigma$ , light gray:  $5\sigma < \Delta F < 10\sigma$ , white:  $10\sigma < \Delta F$ .

- The section through the difference map  $\rho_{diff} = \rho_{MEM} - \rho_{true}$  in the plane of HOOC-COOH molecule
- The MEM deformation density  $\rho_{MEM-pro} = \rho_{MEM} - \rho_{pro}$  in the plane of HOOC-COOH molecule
- The coincidence factor C, which allows for an easy comparison among dif-

ferent reconstructions by one number:

$$C = \frac{\sum_{i=1}^{N_{pix}} |\rho_{MEM}^i - \rho_{true}^i|}{\sum_{i=1}^{N_{pix}} \rho_{true}^i} \quad (3.12)$$

For all n1, n2 and n3 datasets the computations using the  $F_n$ -constraints of order 2 to 8 were performed, for the n0 dataset only the orders 2 to 6 were used, since there was no visible influence of the constraint on the results. For comparison the computations using the *ad hoc* weighting (De Vries et al., 1996; referred to as static weighting hereafter) were performed on the noisy datasets. The F-constraint with additional static weighting is defined as:

$$C_w = -1 + \frac{1}{N_F} \sum_{i=1}^{N_F} w(F_{obs}(\vec{H}_i)) \left( \frac{|F_{obs}(\vec{H}_i) - F_{MEM}(\vec{H}_i)|}{\sigma(F_{obs}(\vec{H}_i))} \right)^2 \quad (3.13)$$

Weights  $w(F_{obs}(\vec{H})) = 1/|\vec{H}|^n$  ( $|\vec{H}|$  is the length of the diffraction vector) with  $n$  equal 3, 4 and 5 were used in this work. To investigate the influence of the prior electron density, two series of calculations were performed. The first series was made with the uniform prior, the second series with the procrystal prior  $\rho_{pro}$ .

The quality of the MEM reconstructions can be compared with Fourier maps. The Fourier transform the observed structure factors with calculated phases results in an electron density ( $\rho_{fou}$ ) that can be compared with  $\rho_{MEM}$  as obtained with the uniform prior. Inspection of  $\rho_{fou}$  shows that the noise is much larger than in  $\rho_{MEM}$ . This is quantified by the C-values (Table 3.3).

The classical method to derive information about electron densities beyond the model is the difference Fourier. We have computed the difference Fourier for  $F_{obs} - F_{pro}$  ( $\rho_{df}$ ). To be able to compare the result with  $\rho_{MEM}$ , we have added  $\rho_{pro}$  to  $\rho_{df}$ . Again, the noise in  $\rho_{fou} + \rho_{df}$  is significantly larger than in  $\rho_{MEM}$  (Table 3.4).

## 3.4 Results and Discussion

### 3.4.1 The uniform prior

In the first series of calculations a uniform electron density was used as prior. The dominating structure of  $\rho_{diff}$  is the oscillatory electron density around each atomic position (Fig. 3.3). Its presence is independent of the constraint and of the noise level. However, at the high noise levels these features are partly camouflaged by the noise of  $\rho_{MEM}$  itself. The oscillations are most pronounced at the zero noise level. Clearly, this effect is a demonstration of the series termination

Table 3.3: The coincidence factors  $C = \frac{\sum_{i=1}^{N_p} |\rho_{MEM}^i - \rho_{true}^i|}{\sum_{i=1}^{N_p} \rho_{true}^i}$  for MaxEnt calculations using the uniform prior and  $\rho_{fou}$ .  $F_n$  denotes the generalized  $F$ -constraint of order  $n$ ,  $sw_n$  denotes the static weighting with weight  $w = |H|^n$  (for definition see Eq. 3.13, for definition of shorthand notation of different datasets see Table 3.2) Note: Some calculations could not be finished using the algorithm of Sakata & Sato due to convergence problems. For static weighting computations this could be overcome by using the MEMSys5 package (Gull & Skilling, 1999a). Those results are printed in italic. Generally, the differences between the results of the two algorithms are not very large, but the results of the latter algorithm seem to be slightly better. The calculation with  $F_6$ -constraint on n0r0.50 dataset did not converge (denoted by n.c.).

Dataset	$F_2$	$F_4$	$F_6$	$F_8$	sw3	sw4	sw5	$\rho_{fou}$
n3r0.50	0.3515	0.2971	0.2942	0.2961	0.2884	0.2631	0.2548	1.3375
n3r0.75	0.3455	0.2237	0.2180	0.2230	0.1836	0.1546	0.1567	1.2187
n3r1.00	0.4137	0.2021	0.1873	0.1885	0.1569	0.1119	0.1179	1.1329
n3r1.25	0.4880	0.2316	0.1976	0.1970	0.1709	0.1073	0.1046	1.1434
n2r0.50	0.2730	0.2498	0.2515	0.2539	0.2447	0.2353	0.2326	1.3323
n2r0.75	0.2126	0.1476	0.1469	0.1502	0.1359	0.1212	<i>0.1209</i>	1.2073
n2r1.00	0.2250	0.1059	0.1010	0.1033	0.0935	0.0661	<i>0.0685</i>	1.1000
n2r1.25	0.2755	0.1063	0.0967	0.0969	0.1018	0.0632	0.0629	1.0440
n1r0.50	0.2287	0.2250	0.2254	0.2260	0.2233	0.2221	0.2457	1.3290
n1r0.75	0.1186	0.1026	0.1026	0.1033	0.1017	0.0998	0.1303	1.2061
n1r1.00	0.0815	0.0458	0.0448	0.0456	0.0451	0.0382	0.0708	1.0977
n1r1.25	0.0952	0.0365	0.0343	0.0353	0.0355	0.0255	0.0247	1.0339
n0r0.50	0.2199	0.2199	n.c.					
n0r0.75	0.0949	0.0949	0.0950					
n0r1.00	0.0286	0.0289	0.0290					
n0r1.25	0.0147	0.0151	0.0155					

error intrinsically present in the method, as pointed out already by Jauch (1994) and later discussed in detail by Roversi et al. (1998). The present results show the extent of this effect and its dependence on the resolution of the dataset. The amplitude of the artifacts ( $\rho_{diff}^{\max} - \rho_{diff}^{\min}$ ) decreases with resolution, but even at resolution 1.25 remains significant (Fig. 3.3, Table 3.5). Further lowering of the artifacts by increasing the resolution is in practice not possible due to the experimental limitations. Possible ways to overcome this problem are summarized in Section 3.5.

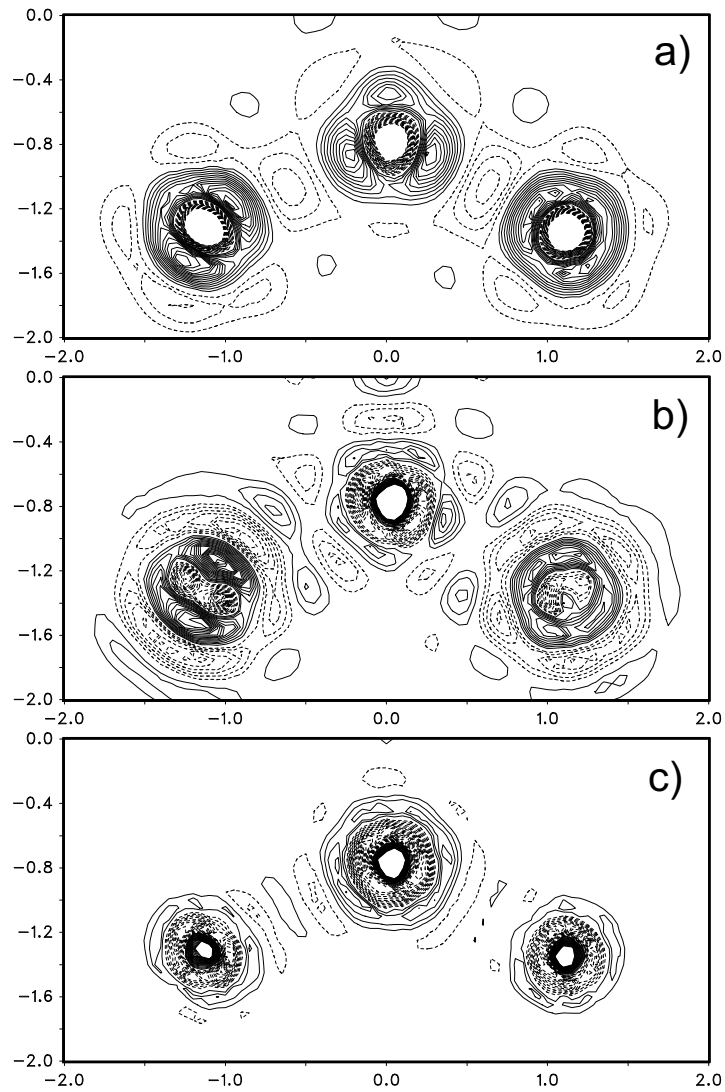


Figure 3.3: Sections through the difference electron density map  $\rho_{diff}$  showing one COOH group. Uniform prior. a)  $n\sigma=0.75$ , contours  $0.2 \text{ e}/\text{\AA}^3$ , cut-off  $3.0 \text{ e}/\text{\AA}^3$ . b)  $n\sigma=1.00$ , contours  $0.05 \text{ e}/\text{\AA}^3$ , cut-off  $1.0 \text{ e}/\text{\AA}^3$ . c)  $n\sigma=1.25$ , contours like in b). The decreasing width of the waves of the difference density with increasing resolution and the interference of the waves is clearly visible.

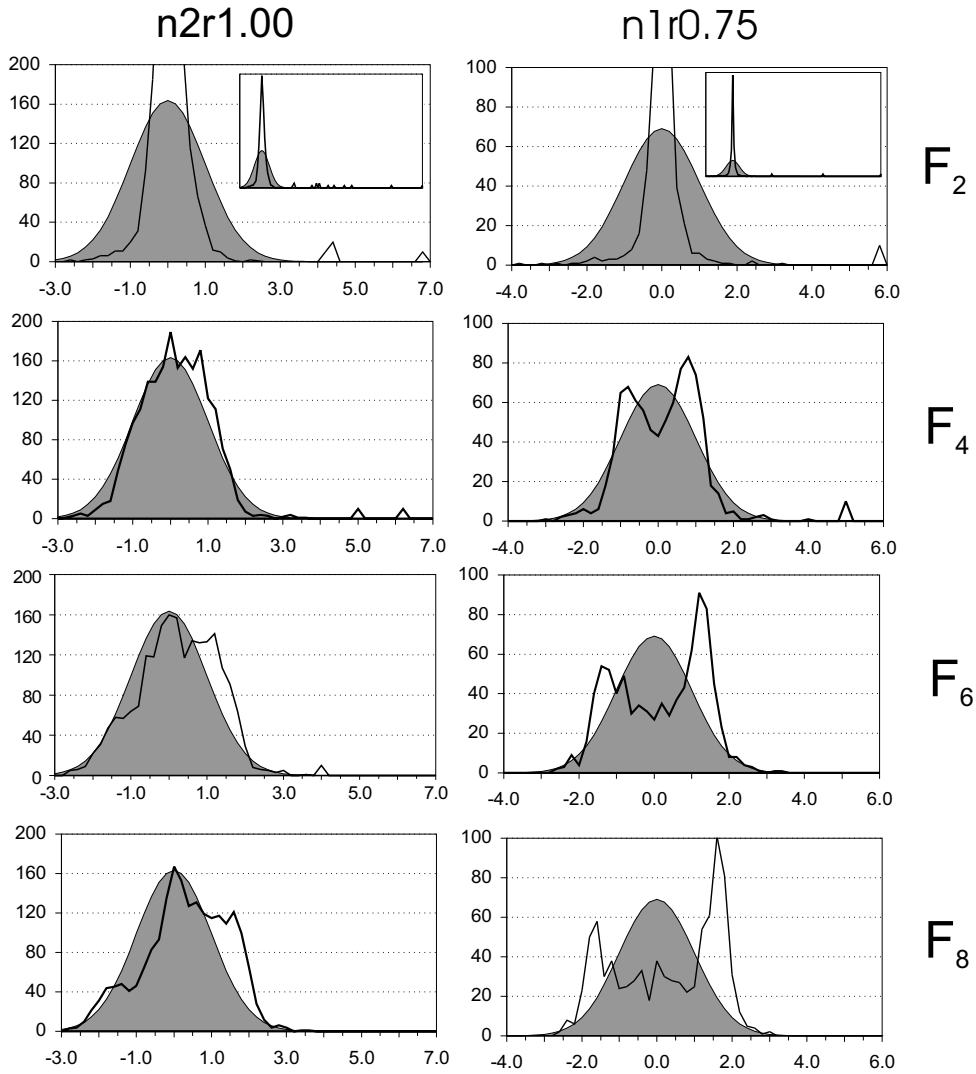


Figure 3.4: The histograms of  $\Delta F(\vec{H})/\sigma(\vec{H})$  for different constraints. Uniform prior. For the  $F_2$  histograms only the central section is shown for good comparability, the full histogram is shown in the inset. The ideal Gaussian shape is shown as the grey area in each histogram. The counts of normalized residuals in classes higher than 4.0 are multiplied by 10.

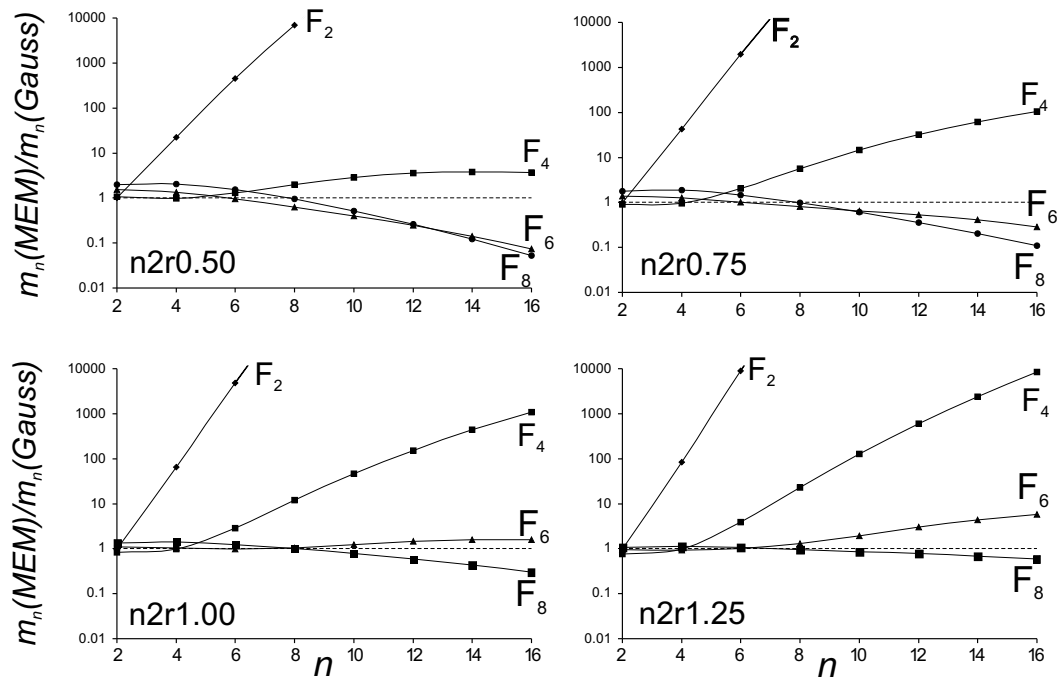


Figure 3.5: The even central moments  $m_2$  to  $m_{16}$  of the histograms of all MEM-runs on the  $n2$  datasets. Uniform prior. Horizontal axis = order of the moment, vertical axis = normalized values of the moments  $m_n(MEM)/m_n(Gauss)$  on a logarithmic scale. Each curve corresponds to one histogram and is labeled with the constraint used for the MaxEnt calculation.

Table 3.4: The coincidence factors  $C = \frac{\sum_{i=1}^{N_p} |\rho_{MEM}^i - \rho_{true}^i|}{\sum_{i=1}^{N_p} \rho_{true}^i}$  for MaxEnt calculations using the procrystal prior and  $\rho_{pro} + \rho_{df}$ . For explanation of the symbols see table 3.3. The C-value of the procrystal prior is 0.0598.

Dataset	F <sub>2</sub>	F <sub>4</sub>	F <sub>6</sub>	F <sub>8</sub>	sw3	sw4	sw5	$\rho_{pro} + \rho_{df}$
n3r0.50	0.0538	0.0560	0.0589	0.0585	0.0554	0.0574	<i>0.0575</i>	0.1015
n3r0.75	0.0554	0.0552	0.0580	0.0574	0.0534	<i>0.0513</i>	<i>0.0533</i>	0.2023
n3r1.00	0.0598	0.0597	0.0590	0.0592	0.0598	0.0598	<i>0.0545</i>	0.3308
n3r1.25	0.0598	0.0598	0.0598	0.0598	0.0598	0.0598	<i>0.0555</i>	0.4856
n2r0.50	0.0421	0.0423	0.0443	0.0458	0.0400	0.0403	<i>0.0386</i>	0.0598
n2r0.75	0.0434	0.0404	0.0414	0.0433	0.0361	0.0353	<i>0.0328</i>	0.1016
n2r1.00	0.0496	0.0447	0.0453	0.0466	0.0420	<i>0.0358</i>	<i>0.0372</i>	0.1744
n2r1.25	0.0545	0.0491	0.0486	0.0496	0.0483	0.0473	<i>0.0350</i>	0.2702
n1r0.50	0.0285	0.0259	0.0258	0.0262	0.0253	0.0248	<i>0.0236</i>	0.0340
n1r0.75	0.0275	0.0233	0.0219	0.0224	0.0209	0.0184	<i>0.0172</i>	0.0206
n1r1.00	0.0290	0.0220	0.0208	0.0211	0.0205	<i>0.0170</i>	<i>0.0157</i>	0.0339
n1r1.25	0.0321	0.0245	0.0229	0.0229	0.0218	<i>0.0174</i>	<i>0.0150</i>	0.0563
n0r0.50	0.0224	0.0223	0.0223					
n0r0.75	0.0106	0.0105	0.0104					
n0r1.00	0.0057	0.0056	0.0057					
n0r1.25	0.0038	0.0041	0.0045					

$\rho_{MEM}$  obtained for different noise levels and different resolutions is characterized by the C-values (Table 3.3), by the shapes of the histograms of  $\Delta F(\vec{H})/\sigma(\vec{H})$  (Fig. 3.4), and by the values of the central moments of the distribution of  $\Delta F(\vec{H})/\sigma(\vec{H})$  (Fig. 3.5). Following conclusions can be made based upon the table and the figures:

- The use of the higher order constraints significantly improves the quality of  $\rho_{MEM}$ . The improvement is the largest between the F<sub>2</sub>- and F<sub>4</sub>-constraint. Only for the noiseless datasets the use of different constraints does not have any effect on the resulting C-value, although the effect on the histogram is large. This is due to the fact that at this noise level the C-value is determined mainly by the series termination artifacts, which are almost independent on the particular constraint. The improvement is generally better with increasing resolution. The probable reason for this is not the higher resolution itself, but rather the higher number of reflections in the dataset.

- The histograms of the higher order constraints are much closer to the ideal Gaussian distribution than the  $F_2$ -histograms and the number of very large normalized residuals is reduced (Fig. 3.4). On the other hand, these histograms are not free of systematic errors either. The histograms of the higher-order constraints tend to be slightly asymmetric towards positive differences. For a smaller number of reflections and/or lower noise level the histograms tend to have flatter peak with respect to the ideal shape and in the extreme case split into two distinct peaks (Fig. 3.4). The two peaks tend to be at the positions  $\pm \sqrt[n]{m_n(Gauss)}$ , which correspond to the average value of normalized residual necessary to fulfill the given constraint. This is not the exclusive property of higher order constraints, similar splitting can appear in the  $F_2$  histograms, too, although only in very extreme case (n0r0.50).
- The quality of the result (measured by the C-value) is perfectly correlated with the quality of the histogram expressed by the values of its central moments. The best results are obtained with that constraint, which produces a histogram closest to the expected normalized Gaussian (compare Table 3.3 and Fig. 3.5). With increasing order of the constraint the resulting histograms get better first (the large positive slope of the curve in Fig. 3.5 gets smaller) and then the high-order central moments of the histograms become overestimated (the slope of the curves in Fig. 3.5 becomes negative). The best result is obtained, when the slope of the curve is close to zero. We suggest that if there are two constraints close to the optimal slope, the one with positive slope should be preferred. This can be understood to be a choice between slight underestimating and slight overestimating of the data. Using the constraint with positive slope means possibly losing some information present in the data, using the one with negative slope means letting the MEM fit some noise and thus introducing some false features in the resulting  $\rho_{MEM}$ . But in practice the difference between the two results is negligible.

The improvement of  $\rho_{MEM}$  is visible both in the total and difference electron density maps  $\rho_{MEM}$  and  $\rho_{diff}$  (Fig. 3.6). The waviness of the low-density contours in  $\rho_{MEM}$  is suppressed, the overall amount of the residual structure in  $\rho_{diff}$  decreases. It should be noted that the total density maps do not give sufficient insight into the accuracy of the result and cannot be used as a single criterion of the quality of the MaxEnt reconstruction. This can be seen from the comparison of the total and difference maps (Fig. 3.6). The largest errors occur in the medium and high density levels, where the total density map seems to be smooth and well behaved. This is especially true for the low resolution maps, which seem to be smooth at the first sight, but which exhibit large differences in comparison to the original map.

Table 3.5: Extremals of the artifacts at different resolutions for noise level  $n_0$  and  $F_2$ -constraint.

	max	min
r0.50	4.36	-28.62
r0.75	3.32	-10.87
r1.00	4.94	-1.84
r1.25	3.42	-0.95

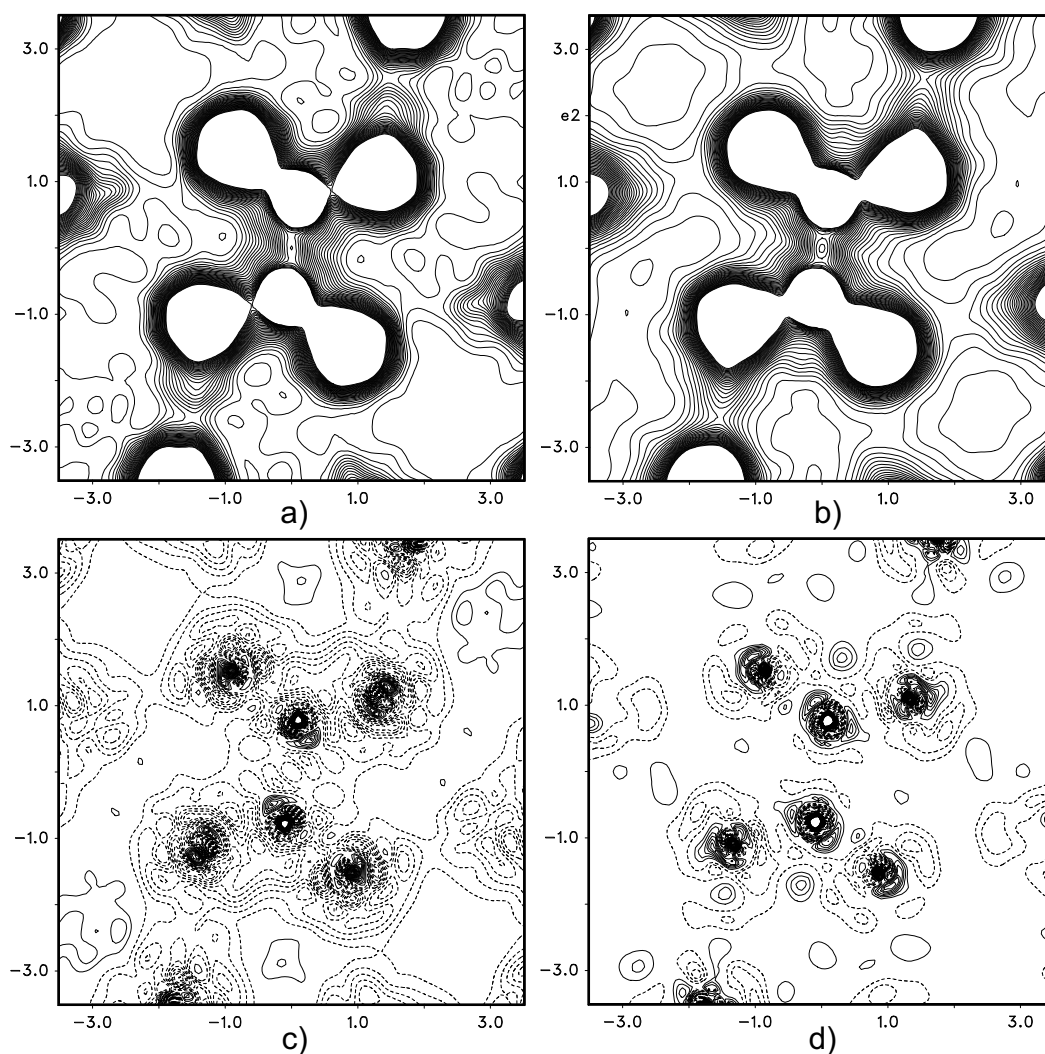


Figure 3.6:  $\rho_{MEM}$  and  $\rho_{diff}$  obtained with the n2r1.00 dataset and with the uniform prior. a)  $\rho_{MEM}$ ,  $F_2$ -constraint. b)  $\rho_{MEM}$ ,  $F_6$ -constraint. c)  $\rho_{diff}$ ,  $F_2$ -constraint. d)  $\rho_{diff}$ ,  $F_6$ -constraint. All contours like in Fig. 3.1.

Despite the significant improvement of the MEM reconstructions obtained with the constraints on the higher-order moments, the quality of the reconstructions using the static weighting was in our case even better (Table 3.3). This surprising effectiveness of the idea of the static weighting suggests that there might exist some fundamental reason for it. A closer investigation of possible theoretical foundations of this type of weighting is desirable.

The systematic investigation of the large number of different datasets allows to make some general conclusions about the influence of the noise and the resolution on the quality of the result. The expected improvement of the C-values with decreasing noise level is clearly visible. The improvement with the increasing resolution is visible, too, but not as an absolute rule (compare C-values of n3r1.00 and n3r1.25, n2r1.00 and n2r1.25, Table 3.3). This can be correlated with the Fig. 3.2. The larger fraction of unobserved reflections is present in the outer shell, the smaller amount of information it contains. In the datasets with the high level almost all reflections in the outer shells are less-than's, and they cannot contribute to the improvement of the MEM reconstruction.

### 3.4.2 The procrystal prior

In the second series of calculations the procrystal electron density  $\rho_{pro}$  was used as prior. The summary of the resulting C-values is given in the Table 3.4. The deformation density  $\rho_{MEM} - \rho_{pro}$  obtained with datasets n2r1.00 and n1r0.75 is shown in the Fig. 3.7. We believe that these examples are quite close to the datasets obtainable in practice.

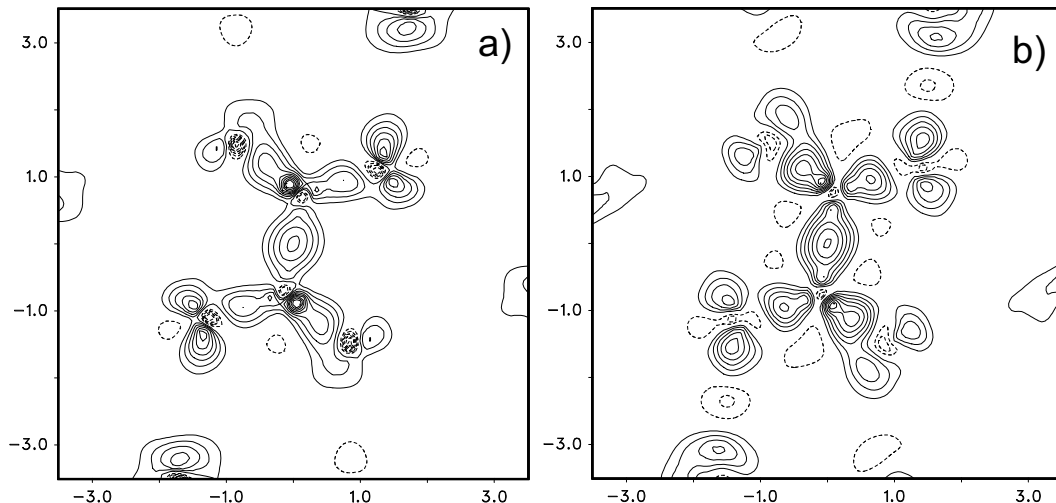


Figure 3.7: MEM deformation electron density,  $\rho_{MEM} - \rho_{pro}$ . Calculations with  $\rho_{pro}$  prior. a) n2r0.75 dataset,  $F_4$ -constraint. b) n1r1.00 dataset,  $F_6$ -constraint. All contours like in Fig. 3.1.

As expected, the artifacts are strongly reduced and visible only in the vicinity of the atomic center. The deformation density resembles the true deformation density quite well even for the medium noise level. The differences in C-values among the different  $F_n$ -constraints and the different static weighting are much smaller than in the case of the uniform prior, but they are still significant, especially for the low noise levels.

With increasing noise level, outer shells of structure factors contain so much noise that it masks their statistical difference from the prior structure factors. Such reflections do not improve the result and can even lead to a slightly worse  $\rho_{MEM}$  (compare Table 3.4 and Fig. 3.2). In an extreme case — noise level 3 — the reflections do not provide any additional information at all and  $\rho_{MEM}$  is almost identical with the prior. In other words, the MEM indicates, that the data do not contain any evidence for deviation from the prior.

The results confirm that with procrystal prior information, the MEM is able to reveal the deformation electron density even from the medium resolution data, provided they are sufficiently accurate.

### 3.5 Conclusions

The intrinsic presence of series termination effect in the crystallographic applications of the MEM is demonstrated. The extent of this effect depends on the resolution of the dataset and on the kind of the prior electron density. For the uniform prior, the artifacts are significantly higher than the bonding electron density level and make this version of the MEM unsuitable for investigation of fine features in the electron density. Nevertheless, it is still a useful method for investigation of more robust features like anharmonic atomic movement or disorder (Bagautdinov et al., 1998; Dinnebier et al., 1999; Wang et al., 2001).

The procrystal prior electron density lowers the artifacts and the reconstructions with this prior contain the information about the fine features of the electron density. Further lowering of the artifacts could be probably achieved with the two-channel MEM (Papoular et al., 1996) or with the valence-only MEM proposed by Roversi et al. (1998). The latter method uses the refined structure parameters to create a core electron density fragment, which is then considered to be known and is not included in the MaxEnt optimization. Only the valence electron density is modified. However, this method is of practical use only for extremely accurate data of simple structures, since it relies on the knowledge of the temperature parameters, which are often inaccurate and correlated with systematic errors in the datasets.

The use of the generalized F-constraint dramatically improves the quality of the MEM results. The selection criterion for the proper order is the best coincidence of the histogram with the expected Gaussian distribution. From our

experience the order 4 or 6 gives the best result.

The static weighting still gives better results than the non-weighted  $F_n$ -constraints. But this type of weighting lacks any theoretical foundation, and the choice of the best weighting is very dataset-dependent (Yamamoto et al., 1996). On the other hand, the constraints based on the expected moments of the distribution of  $\Delta F(\vec{H})/\sigma(\vec{H})$  have a clear interpretation. One can expect that the new algorithms that will allow the simultaneous use of several constraints in the MEM will again lead to improved results.

One more advantage of the higher-order F-constraints in comparison to the classical  $F_2$ -constraint or static weighting is the faster convergence, which makes the computation time significantly shorter.



# Chapter 4

## The Prior-derived F-constraints in the Maximum Entropy Method

### 4.1 Introduction

It has been pointed out (Jauch & Palmer, 1993; Jauch, 1994; De Vries et al., 1996; Roversi et al., 1998; Palatinus & van Smaalen, 2002), that the use of the MEM can lead to features in the reconstructed electron densities that are not reliable and that can lead to misinterpretation of the reconstructed features, like in the most well known example of silicon (Sakata & Sato, 1990; De Vries et al., 1996). Several methods have been proposed, that aim to suppress the various types of artifacts. These methods either try to reduce the dynamic ratio of the optimized electron density (Papoular et al., 1996; Roversi et al., 1998) or improve the statistic distribution of the normalized residuals of the structure factors (De Vries et al., 1994; Chapter 3).

This chapter presents a method to suppress another type of artifacts in the MEM calculations. These artifacts arise due to the fact, that MEM sometimes incorrectly estimates the values of the structure factors that were not experimentally determined. The problem and its solution is first described and demonstrated on a simple one-dimensional example. Its justification for the realistic problems is demonstrated on the simulated data of the oxalic acid dihydrate.

### 4.2 Theory

One source of the artifacts in the MEM electron densities is the occurrence of a truncated Fourier series in the derivative of the constraints. These artifacts can be strongly suppressed by decreasing the dynamic ratio of the optimized

distribution. The concepts of the two-channel MEM (Papoular et al., 1996) and the valence-only MEM (Roversi et al., 1998) have been proposed for this purpose. Alternatively, the series termination error can be significantly reduced by using sufficiently informative prior electron density (De Vries et al., 1996; Papoular et al., 2002; Chapter 3). The second main source of artifacts is related to the very nature of the MEM - the search for the electron density with the maximum entropy. The algorithm tends to estimate incorrectly values of the structure factors, that are most sensitive to the changes of the entropy, in order to decrease the entropy as much as possible. These structure factors are known as the outliers. One or two of these outliers often account for substantial part of the total  $\chi^2$  (Jauch & Palmer, 1993; De Vries et al., 1994; Iversen et al., 1997). This effect can be effectively suppressed by devising different constraints than the classical  $\chi^2$  (De Vries et al., 1994; Chapter 3). However, the constraints apply only to the experimentally observed reflections. The structure factors that were not measured are extrapolated by the MEM formalism to obtain the MEM solution with the lowest entropy. These structure factors are not subject to any constraint. If the MEM estimates the non-measured structure factors incorrectly, errors occur in the reconstructed  $\rho_{MEM}$ .

If no prior information on the electron density is available, then the errors from this source are unavoidable. Indeed, the MEM-estimated values of the missing structure factors are the best available guesses. It is sufficiently accurate to reveal the basic features of the electron density (Bagautdinov et al., 1998; Dinnebier et al., 1999; Wang et al., 2001). On the other hand, if the prior information in the form of a procrystal electron density is available, then good estimates of the high-angle structure factors are readily available. They are the structure factors corresponding to the prior electron density ( $F_{prior}$ ). It will be shown that the values of  $F_{prior}$  are indeed much closer to the true structure factors than the MEM-estimated  $F_{MEM}$  (Section 4.3). Thus, it is advisable to include these structure factors as additional constraints in the MEM optimization. This procedure assures, that the structure factors that are not known from the experiment will be constrained to the values close to  $F_{prior}$ , which is the best available estimate. The structure factors that have been experimentally measured are optimized in the usual way. The prior structure factors included in the constraint list (called “the prior-derived F-constraints” or PDC hereafter) behave exactly like the ordinary experimental structure factors in the entropy maximization. However, they are not included in the calculation of the value of  $\chi^2$ , that used to determine the stopping point of the iteration. The stopping criterion  $\chi^2 = N_{data}$  bases on the statistical distribution of the noise in the experimental data. Thus, the convergence of the MEM calculation is stopped when the  $\chi^2$  of the experimental structure factors (without the prior-derived F-constraints) is equal to  $N_{data}$ .

Each constraint has to be assigned a non-zero standard deviation. Standard deviations are not available for the prior-derived F-constraints. In the present

applications, all PDC have assigned uniform standard uncertainty, that is approximately equal to the lowest standard uncertainty of the experimental structure factors.

The method of the prior-derived F-constraints is based on the fact, that the good-quality datasets are complete in the low-angle region (up to  $\sin(\theta)/\lambda = 0.9$  or more) and only the high-angle reflections are missing. The intensities of the high-angle reflections are most sensitive to sharp features of the electron density in the vicinity of the atomic cores. The inner electron shells are not deformed by the bonding interactions between the atoms and they have therefore the same form in the procrystal electron density and in the real electron density. For this reason, the intensities of the high-angle reflections are very similar in the procrystal electron density and in the real density.

This property of the electron densities and of the structure factors is sometimes also used in the multipole refinements (Benabicha et al., 2000; Pichon-Pesme et al., 2000). Prior to the refinement of the multipole parameters the positional and displacement parameters are refined using only the high-angle reflections. Then the displacement parameters are fixed and the multipolar parameters are refined. Thus, the deformation of the electron density due to the bonding is refined under the assumption that the displacement parameters can be successfully determined from the standard model of independent atoms by using only the high-angle reflections.

The concept of the prior-derived F-constraints will be demonstrated on a simple example in following section. It will be demonstrated that the incorrect estimates of the structure factors not included in the dataset are the major source of artifacts in the MEM calculations with informative prior electron density and that the method of the prior-derived F-constraints removes these artifacts successfully.

### 4.3 A simple one-dimensional example

In this section, a simple one-dimensional example is used to demonstrate the basic properties of the prior-derived F-constraints. One unit cell of the one-dimensional (1D) density  $\rho_{true}$  was constructed by superposing five Gaussian functions (Table 4.1). Three of them simulate the 1D analogs of atoms and two further Gaussians simulate the bonds between the atoms (Fig. 4.1a). The “procrystal” prior density  $\rho_{pro}$  was constructed in a similar way, but without the “bonds”. The widths of the atoms in the prior were increased in order to maintain the integral over the unit cell equal in both cases (Table 4.1, Fig. 4.1b). A center of inversion was put in the origin of the unit cell. The densities are sampled on a grid with 128 points.

$\rho_{prior}$  is very close to  $\rho_{true}$ . It is the task of the MEM to reconstruct the

Table 4.1: Parameters of the Gaussians  $G = A \exp\left(\frac{-(x-c)^2}{2\sigma^2}\right)$  used to construct the prior and true 1D densities. The scale of  $x$ ,  $c$  and  $\sigma$  is pixels, the scale of  $A$  is arbitrary. The width of the unit cell is 128 pixels, numbered from 0 in the origin to 127.

	prior density			true density		
	$A$	$\sigma$	$c$	$A$	$\sigma$	$c$
A1	60	3.20	0	60	3.12	0
A2	50	3.20	64	50	3.12	64
A3	30	4.66	36	30	4.52	36
B1	0	-	-	0.5	11.31	15
B2	0	-	-	0.5	5.66	51

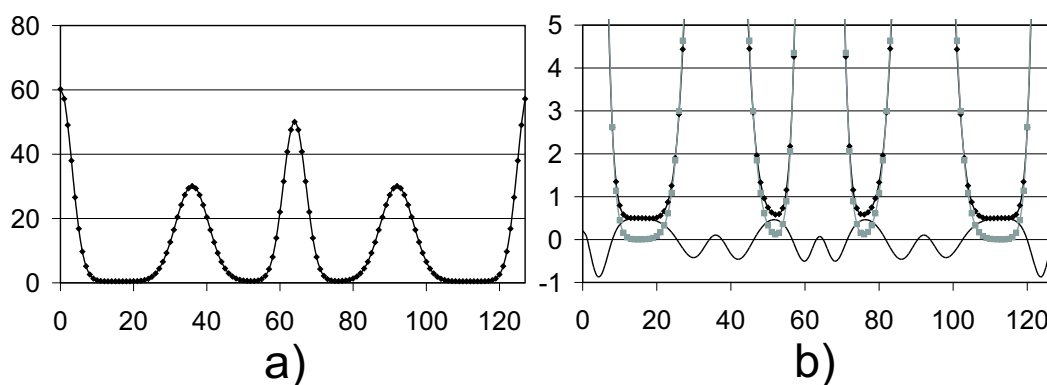


Figure 4.1: a) One unit cell of the true 1D density sampled on the grid with 128 pixels. b) The exaggerated low-density region of the densities. Black diamonds:  $\rho_{true}$ ; grey squares:  $\rho_{pro}$ ; bold line:  $\rho_{true} - \rho_{pro}$ .

small differences of order of percent of the total density. This is analogical to the realistic case, where the procrystal prior density is available and only the deformations due to the bonding remain to be inferred.

Nine MaxEnt optimizations were performed with BAYMEM using the Cambridge algorithm (Skilling & Bryan, 1984) and with the  $\rho_{pro}$  as the prior density. Three different input datasets were created with low-order structure factors with indices up to 12, 20 and 28 as observed data. The exact values of the structure factors were used, without adding any noise. Uniform standard uncertainties  $\sigma = 0.01$  were assigned to all structure factors. Calculations without the prior-derived F-constraints were performed on each input dataset as well as calculations with the prior-derived F-constraints up to F(32) and up to F(48). The calculations are denoted with letter f followed by the number of structure factors in the input dataset and letter p followed by the highest index of the added PDC. For example, f20p48 denotes a calculation with low-order structure factors up to F(20) included as observed data and the remaining structure factors up to F(48) added as PDC.

The resulting difference densities  $\rho_{diff} = \rho_{MEM} - \rho_{true}$  are shown in Fig. 4.2, 4.4 and 4.6. The corresponding MEM structure factors  $F_{MEM}$  are shown in Fig. 4.3, 4.5 and 4.7.

$\rho_{diff}$  obtained without the prior-derived F-constraints shows large wavy structures, that are comparable in amplitude to the difference between the prior and true density. The difference densities are dominated by a few frequencies. These frequencies correspond to the structure factors not included as the observed data that have been most badly estimated. The difference between the values  $F_{true}(H)$  and  $F_{MEM}(H)$  of these structure factors is responsible for occurrence of waves in the difference density with periodicity  $1/H$  in the unit cell and with amplitude proportional to  $|F_{true}(H)| - |F_{MEM}(H)|$ . As an example, the most prominent structure in  $\rho_{diff}$  of the calculation f20p0 (Fig. 4.4a) is the wave with frequency 21, which corresponds to the overestimated value of F(21) (Fig. 4.5a). The incorrect estimates of the values of F(21) and other structure factors are produced by MEM, because they increase the entropy of  $\rho_{MEM}$  compared to the entropy of the map with correct values of the structure factors. That can be seen by comparing the entropy of  $\rho_{MEM}$  with unconstrained high-order structure factors and the entropy of  $\rho_{MEM}$  with high-order structure factors constrained via PDC (Table 4.2). The entropy of the former is always higher than the entropy of the latter.

Calculations with PDC and with 20 and 28 observed structure factors produce results with much lower values of  $\rho_{diff}$ , because the high-order structure factors are constrained to  $F_{prior}$ , that are very close to  $F_{true}$  (Fig. 4.3, 4.5, 4.7). The calculations with the PDC up to F(32) still show a high-frequency noise, which can be correlated with the overestimated values of the unconstrained structure factors above F(32) (Fig. 4.5b, 4.7b). If PDC up to F(48) are added, the resul-

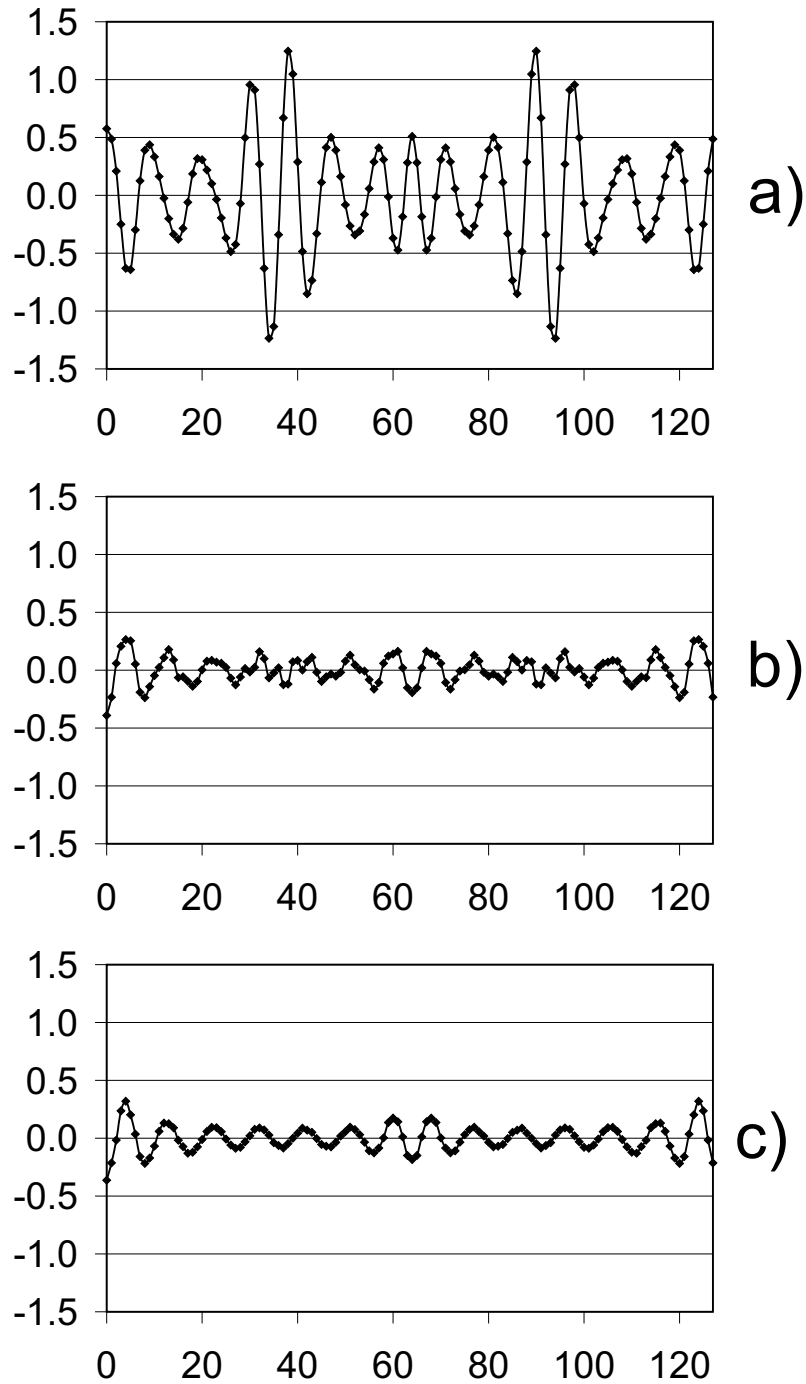


Figure 4.2: The difference densities  $\rho_{diff} = \rho_{MEM} - \rho_{true}$  from the calculations a) f12p0, b) f12p32, c) f12p48. The lines connecting the points serve as guide for eye.

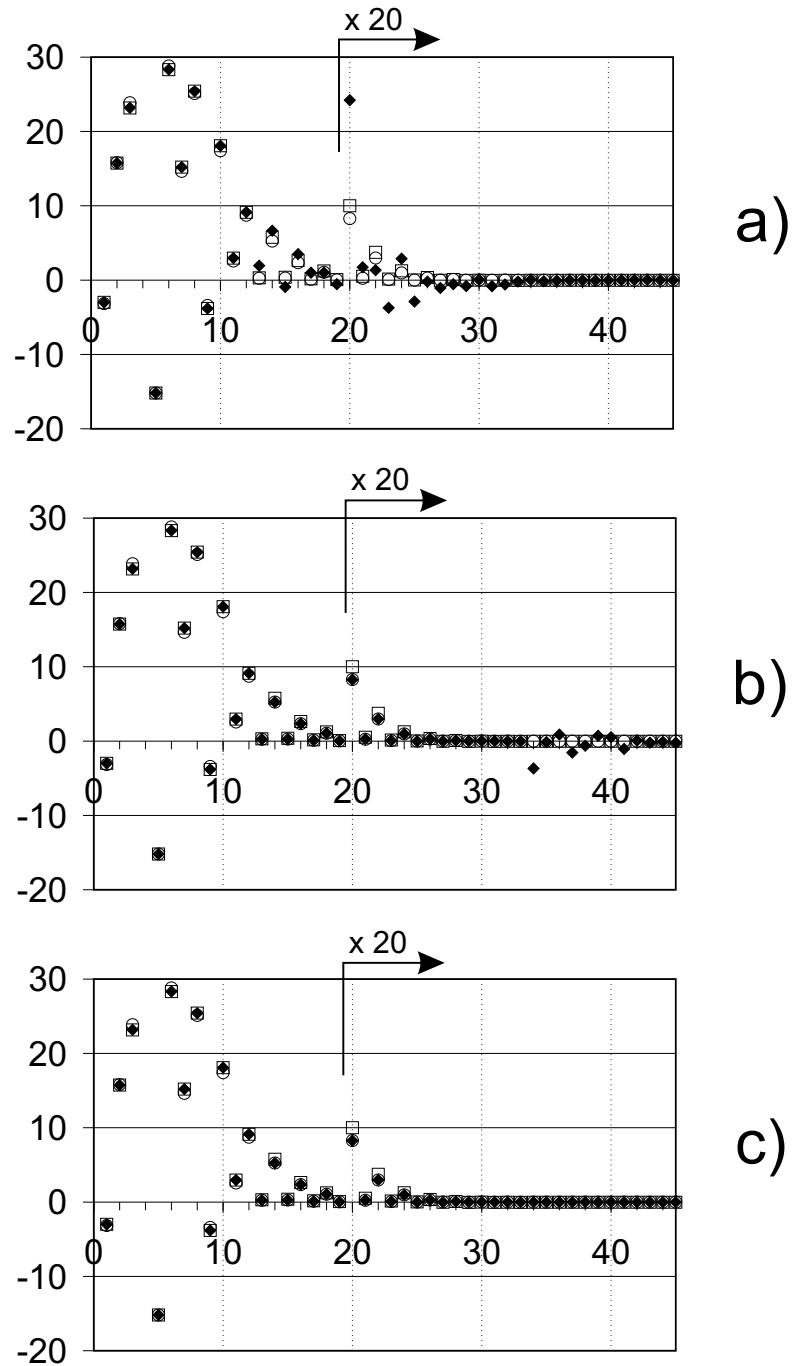


Figure 4.3: The structure factors  $F_{MEM}$  (filled diamonds) corresponding to  $\rho_{MEM}$  from calculations a) f12p0, b) f12p32, c) f12p48.  $F_{true}$  (open squares) and  $F_{pro}$  (open circles) are shown in each plot for comparison. Values of structure factors with indices higher than 19 are multiplied by 20. Structure factor  $F(4)$  has a value of approximately 64 and is not shown in the plots.

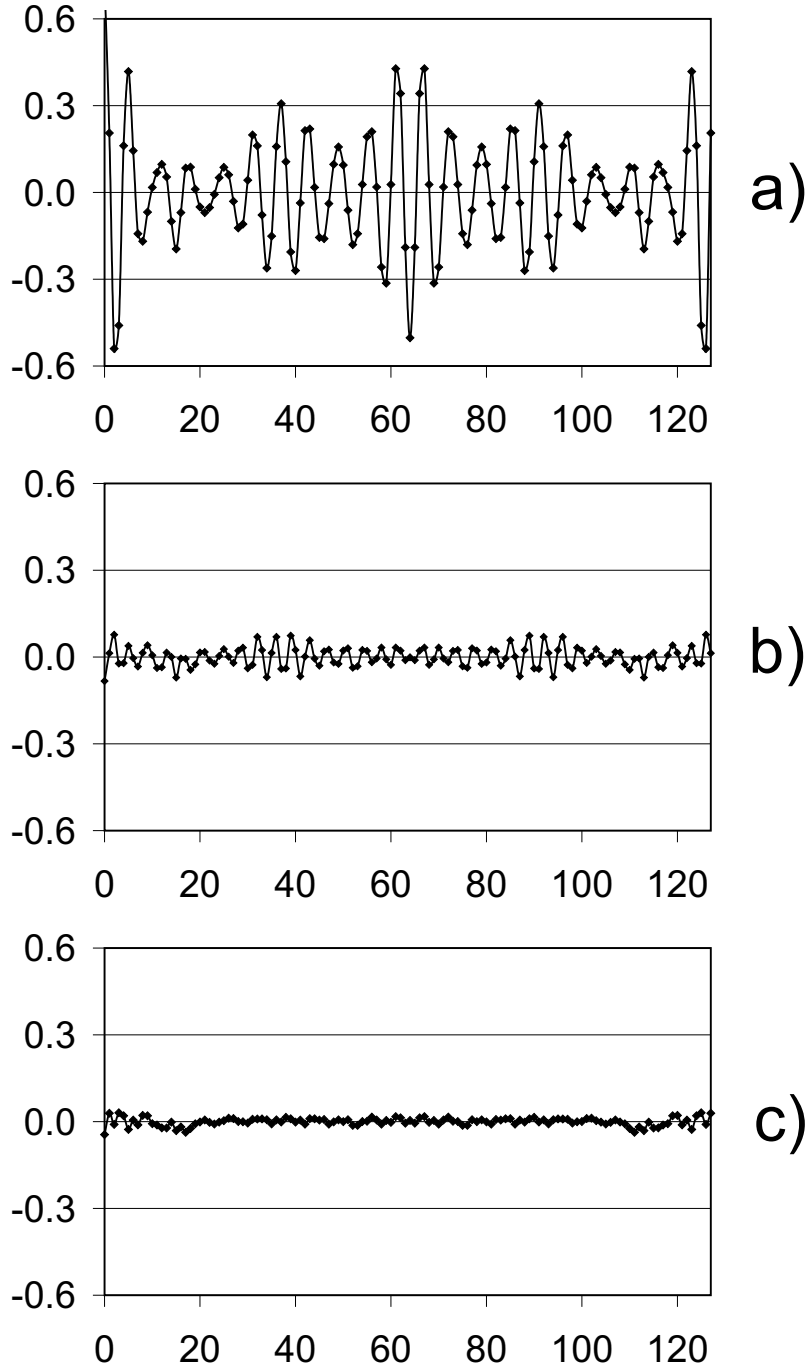


Figure 4.4: The difference densities  $\rho_{diff} = \rho_{MEM} - \rho_{true}$  from the calculations a) f20p0, b) f20p32, c) f20p48. The lines connecting the points serve as a guide for eye.

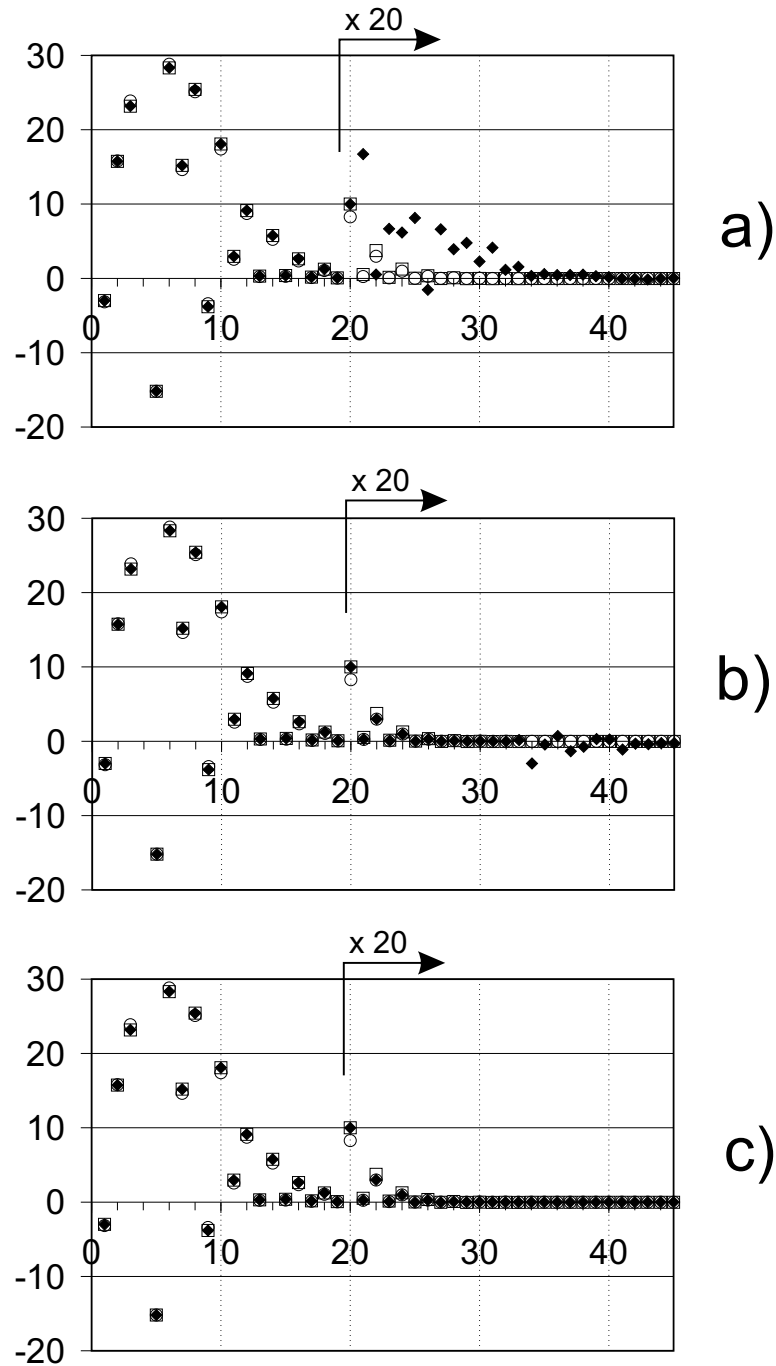


Figure 4.5: The structure factors  $F_{MEM}$  (filled diamonds) corresponding to  $\rho_{MEM}$  from calculations a) f20p0, b) f20p32, c) f20p48. Other description as in Fig. 4.3.

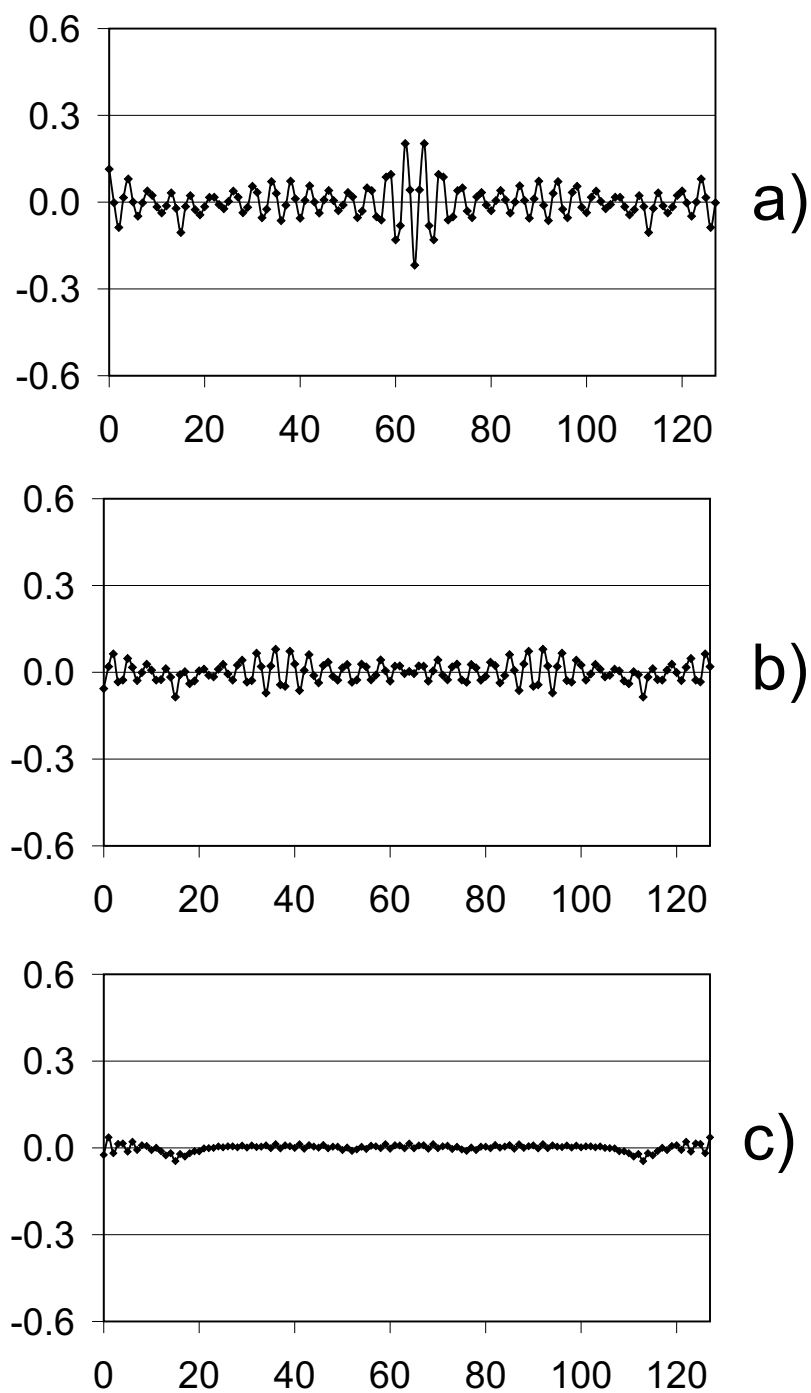


Figure 4.6: The difference densities  $\rho_{diff} = \rho_{MEM} - \rho_{true}$  from the calculations a) f28p0, b) f28p32, c) f28p48. The lines connecting the points serve as a guide for eye.

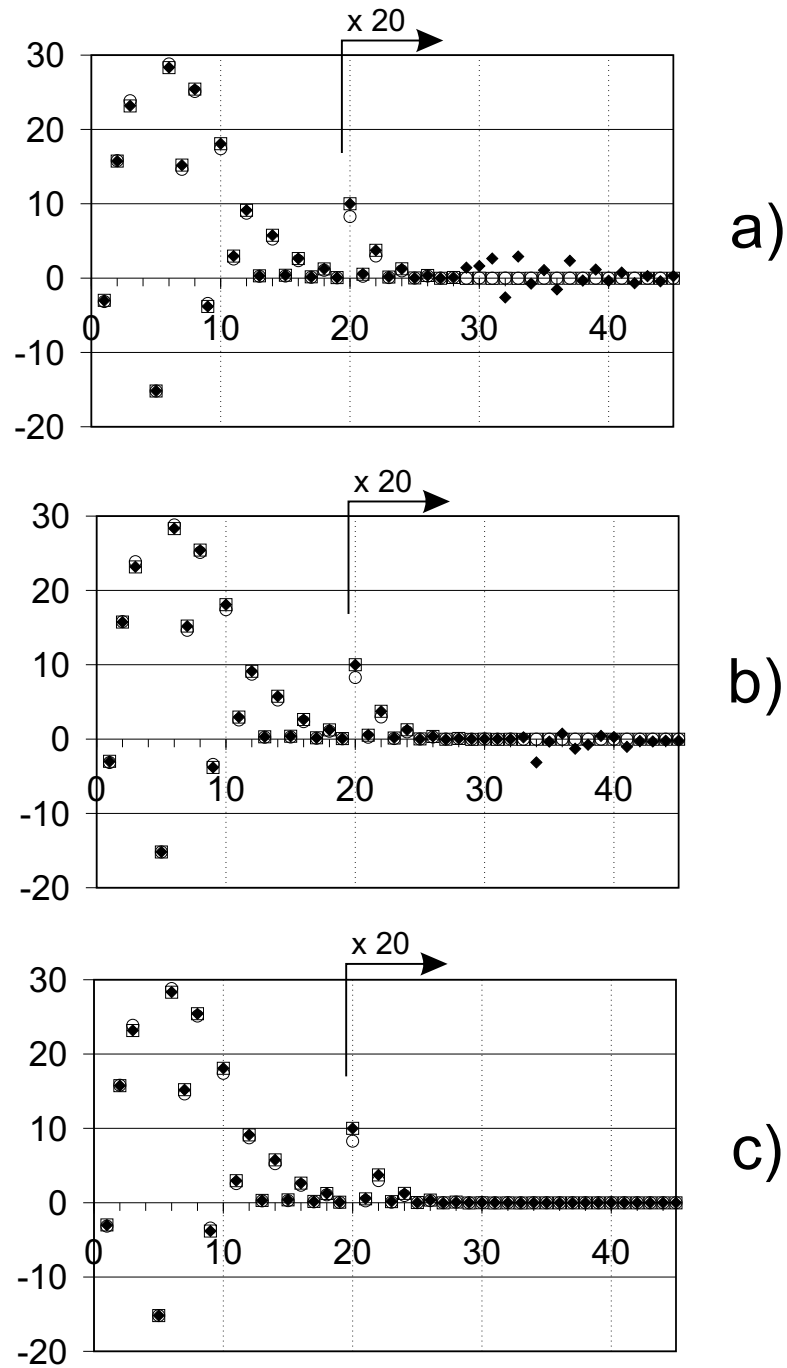


Figure 4.7: The structure factors  $F_{MEM}$  (filled diamonds) corresponding to  $\rho_{MEM}$  from calculations a) f28p0, b) f28p32, c) f28p48. Other description as in Fig. 4.3.

Table 4.2: Entropy of  $\rho_{MEM}$  from different calculations

observed data up to:	PDC up to:		
	0	F(32)	F(48)
F(12)	-1.53815	-1.88067	-1.88290
F(20)	-1.74731	-1.78002	-1.78153
F(28)	-1.76185	-1.76343	-1.76498

ting  $\rho_{MEM}$  is virtually error-free (Fig. 4.4c, 4.6c). The remaining discrepancies are due to the fact, that the MEM does not fit the low-order structure factors exactly. Nevertheless, the remaining errors in  $\rho_{diff}$  from the calculations f20p48 and f28p48 are smaller than 0.05 in absolute value, while the difference density  $\rho_{true} - \rho_{pro}$  has minimum  $-0.86$  and maximum  $0.50$ . Thus the MEM with PDC is able to reconstruct the difference between the  $\rho_{true}$  and  $\rho_{pro}$  with an average accuracy of few percent of the values of  $\rho_{true} - \rho_{pro}$ .

The calculations f12p32 and f12p48 demonstrate the limitations of the method of the prior-derived F-constraints. The structure factors above F(12) are replaced by  $F_{prior}$ . The resulting difference densities show errors with a dominant frequency of 14 (Fig. 4.3b, 4.3c). This is caused by the fact, that  $F_{prior}(14) = 5.25$ , which is significantly different from  $F_{true}(14) = 5.76$ . The value of  $F_{MEM}(14)$  is constrained to the value of  $F_{prior}(14)$  and the difference between  $F_{prior}$  and  $F_{true}$  is responsible for the artifacts in  $\rho_{diff}$ . This error is induced by the incompleteness of the data and cannot be avoided by data processing. Such a limited dataset is not suitable for accurate reconstructions of the density.

## 4.4 Simulated data of oxalic acid dihydrate

To investigate the effect of the prior-derived F-constraints on a realistic problem, the method was applied to the simulated data of the oxalic acid dihydrate. The simulated model has been extensively described in Chapter 3. It was shown there, that the use of the procrystal prior density enhances the performance of the MEM strongly compared to MEM with uniform density, but the resulting maps are not artifact-free either. To demonstrate the benefits of the prior-derived F-constraints, the method was applied to the dataset n1r100 (for explanation see Chapter 3). Two calculations were performed on this dataset. The first calculation was performed using the classical MEM formalism with the procrystal prior, with the Cambridge algorithm and with the static weighting with weights  $w = 1/|\vec{H}|^5$  (Eq. 2.27). This setting produced the best result, if measured by the C-value of the resulting  $\rho_{MEM}$  (Eq. 3.12, Table 3.4). The second calculation was performed with the same algorithm and static weighting and with the prior-derived F-constraints added to the experimental data up to  $\sin(\theta)/\lambda = 2.5$ . A

uniform standard uncertainty of  $\sigma_{PDC} = 0.02$  was assigned to all prior-derived F-constraints.

The results of both calculations are shown in Fig. 4.8. The maximum difference density  $|\rho_{MEM} - \rho_{true}|_{max}$  is  $0.447 e/\text{\AA}^3$  in the calculation without the PDC. The difference density contains sharp peaks around the atomic positions. In the calculation with the PDC, the maximum difference density has decreased to  $0.061 e/\text{\AA}^3$ . The C-value has decreased from 0.0157 in the calculation without the PDC to 0.0138 in the calculation with the PDC. The noise is distributed much more uniformly in  $\rho_{MEM}$  obtained with PDC and does not form sharp spikes.

## 4.5 Conclusions

The method of prior-derived F-constraints has been introduced. It has been demonstrated on two examples that the method leads to significantly improved MEM reconstructions, if sufficiently informative prior density is used. The simple 1D example allows to reveal the origin of the artifacts in the MEM reconstructions and to investigate the properties of the new method. It has been shown that the amplitude of the remaining artifacts critically depends on the maximal difference between  $F_{true}$  and  $F_{prior}$ . If experimental data with sufficient resolution are available, then the method of prior-derived F-constraints leads to the MEM reconstructions that are virtually artifact-free.

The applicability of the method to realistic problems is demonstrated for the simulated dataset of oxalic acid dihydrate. The dataset n1r100 corresponds to high-quality experimental data. It is shown that the prior-derived F-constraints improve significantly the quality of the MEM reconstruction. The errors in the reconstruction are of order of  $10^{-2} e/\text{\AA}^3$ , which is comparable to or even smaller than the errors reported from the multipole refinements of the electron density (Pillet et al., 2000). Based on this observation it is concluded that the MEM with the prior-derived F-constraints can be successfully used for accurate charge density studies.

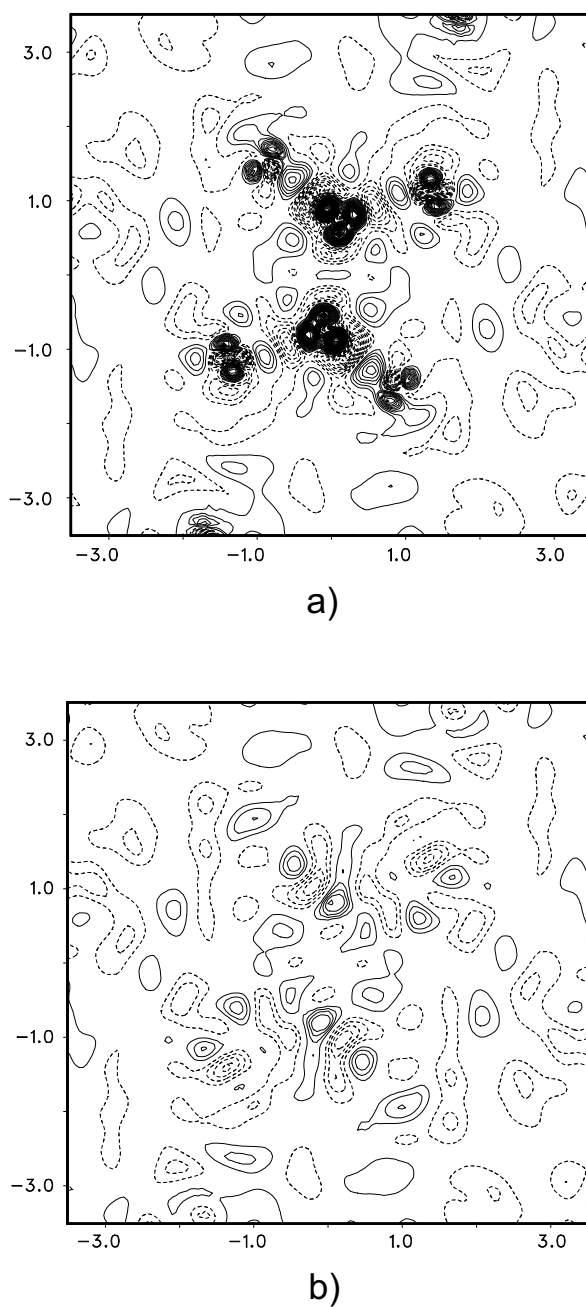


Figure 4.8: Sections of the  $\rho_{MEM}$  of the oxalic acid dihydrate in the plane of the oxalic acid molecule. a) calculation without the prior-derived F-constraints.  $\rho_{\min} = -0.144 e/\text{\AA}^3$ ,  $\rho_{\max} = 0.392 e/\text{\AA}^3$ . b) calculation with the prior-derived F-constraints up to  $\sin(\theta)/\lambda = 2.5$ .  $\rho_{\min} = -0.048 e/\text{\AA}^3$ ,  $\rho_{\max} = 0.051 e/\text{\AA}^3$ . Cambridge algorithm, static weighting  $w(\vec{H}) = 1/|\vec{H}|^5$ . Contours in both maps are drawn in intervals of  $0.01 e/\text{\AA}^3$ .

# Chapter 5

## The inorganic misfit layer compound $(\text{LaS})_{1.14}\text{NbS}_2$

Inorganic misfit layer compounds belong to the class of incommensurate composite crystals (van Smaalen, 1995; Wiegers, 1996). We have performed MaxEnt calculations on the two isostructural misfit layer compounds  $(\text{LaS})_{1.14}\text{NbS}_2$  and  $(\text{LaS})_{1.13}\text{TaS}_2$ , employing the computer program BAYMEM. The results for both compounds turned out to be similar in every way. Therefore, we present here in detail only the results for  $(\text{LaS})_{1.14}\text{NbS}_2$ .

### 5.1 The structure model and experimental data

The structure has been solved and refined using conventional crystallographic methods (van Smaalen, 1991*a*; Jobst & van Smaalen, 2002). The data and model published in Jobst & van Smaalen (2002) were used in the present work, and we refer to Jobst & van Smaalen (2002) for experimental details and structural parameters (Fig. 5.1).

Important for the present analysis is that a complete dataset is available up to  $\sin(\theta)/\lambda = 1.01$ . Almost all (98%) of the main reflections are of the type observed (they have  $I > 3\sigma(I)$ ), whereas about half of the first- and second-order satellites are observed. The model included the Fourier components up to second harmonics for the modulation functions for the displacements and the temperature factors. Furthermore the average occupation of La was refined towards 0.949(2), and the modulation function for this occupancy was included in the model.

The phases of the reflections were taken from the calculated structure factors of the final structure model (model D in Jobst & van Smaalen, 2002). Together with the observed structure factor amplitudes they formed the observed data (subscript *obs*), that were used in the MaxEnt calculations. Standard uncertainties are based on counting statistics. The scaling towards the scattering of the

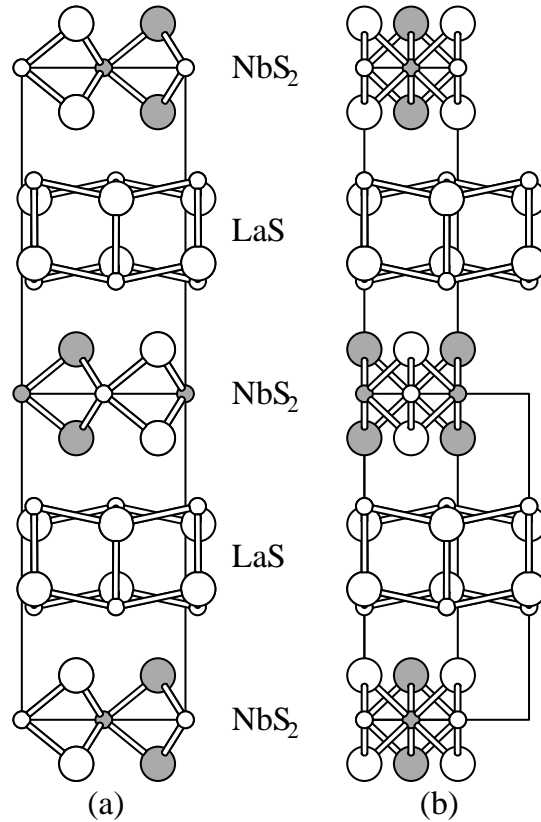


Figure 5.1: The average structure of  $(\text{LaS})_{1.14}\text{NbS}_2$ . (a) Projection along the incommensurate  $a$ -axis, (b) Projection along the common  $b$ -axis. Large circles denote S atoms, small circles represent the metal atoms. Shaded and white circles represent atoms at different positions of the projected coordinate. Lattice constants at  $T = 115$  K are:  $a_1 = 3.3065$ ,  $a_2 = 5.7983$ ,  $b = 5.7960$  and  $c = 22.957$  Å.

unit cell and the corrections for the anomalous scattering were obtained by a procedure described elsewhere (Bagautdinov et al., 1998).

A second dataset was formed by the structure factors computed for the final structure model, albeit without the contributions of the anomalous scattering factors. They were denoted as calculated data (subscript *calc*). To be able to apply the MaxEnt procedure, non-zero standard uncertainties must be assigned to each reflection. Standard uncertainties of the calculated data were set equal to the standard uncertainties of the observed data. The calculated data correspond to the Fourier transform of the model electron density. Their use as “observed” data in the MEM (Eq. 1.20) thus allows to quantitatively estimate the quality of the MaxEnt reconstruction of the electron density for a model that is as close as possible to the real electron density.

## 5.2 Details of the computations

The electron density was calculated on a grid of  $32 \times 64 \times 256 \times 32$  pixels. This corresponds to a resolution of  $0.103 \times 0.092 \times 0.090 \times 0.181 \text{ \AA}^4$ . A finer grid might be desirable, but then the calculations would have been too time consuming. A flat prior was used throughout the whole analysis.

$\rho_{obs}^{MEM}$  was obtained from a run of BAYMEM using the observed data and the Cambridge algorithm (Fig. 5.2). In a similar way  $\rho_{calc}^{MEM}$  was obtained from the calculated data. Calculations with the Sakata-Sato algorithm and the  $F_4$ -constraint did not converge within a reasonable time, and the iteration had to be stopped before the  $F_4$ -criterion was fulfilled. Therefore we have only used the results obtained with the Cambridge algorithm in the present analysis. Details

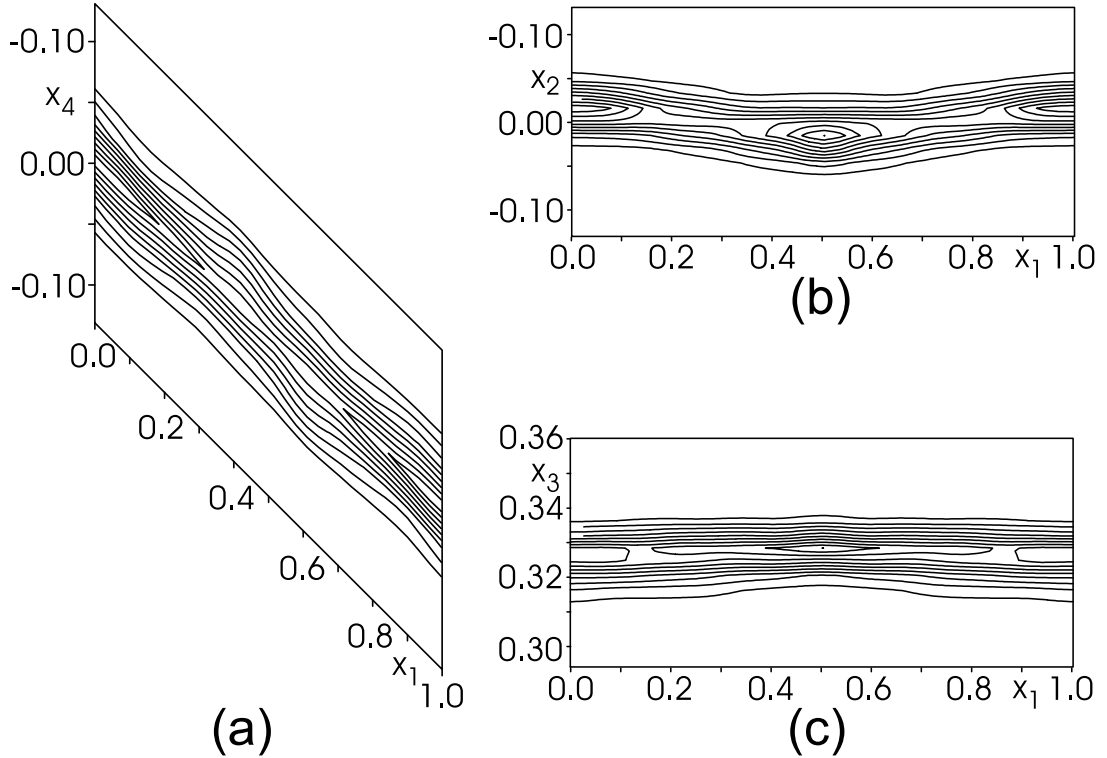


Figure 5.2: Sections of the electron density  $\rho_{obs}^{MEM}$  at the position of La. a)  $x_1$ - $x_4$  section with  $\rho_{max} = 961.1 \text{ e/\AA}^4$ ; b)  $x_2$ - $x_4$  section with  $\rho_{max} = 1409.9 \text{ e/\AA}^4$ ; c)  $x_3$ - $x_4$  section with  $\rho_{max} = 1161.4 \text{ e/\AA}^4$ . Contour lines are shown at intervals of 10 % of the maximum value  $\rho_{max}$  of the electron density in the corresponding sections.

Table 5.1: Computational details and results for the MEM calculations on LaS<sub>1.14</sub>NbS<sub>2</sub>.

	observed data		calculated data	
	Cambridge algorithm	Sakata- Sato algorithm	Cambridge algorithm	Sakata- Sato algorithm
No. of reflections		10237		
$N_{pix}$		16777216		
$N_{pix}^{au}$		1052736		
RAM [MB]		678		
Computation time [hours]	76.8	73.9	11.4	4.4
Constraint (Eq. 3.9)	F <sub>2</sub>	F <sub>4</sub>	F <sub>2</sub>	F <sub>4</sub>
Final value of constraint	1.0	58.4	1.0	1.0
$R$ -values obs/all [%]:				
all reflections	2.1/4.1	2.8/6.4	3.2/3.1	2.7/3.4
main reflections	1.6/1.7	2.2/2.3	3.9/3.9	2.7/2.8
1 <sup>st</sup> order sat.	3.7/8.6	4.8/14.1	0.6/0.8	2.4/3.4
2 <sup>nd</sup> order sat.	3.8/16.8	6.2/28.7	0.6/1.6	3.3/8.7

about the MaxEnt computations are summarized in Table 5.1.

BAYMEM can save the electron densities in several formats. An internal format is used to store all independent density values in the full double precision that is necessary to maintain the accuracy of the calculations. The computer program JANA2000 (Petříček & Dušek, 2000) is used for the visualization of the electron density, and BAYMEM can save the electron density in the format suitable for JANA2000.

A principal task of the analysis of the  $\rho^{MEM}$  is to extract the modulation functions for the displacive modulation of the atoms from it. This involves:

- The computation of the electron densities in 3D sections of superspace from  $\rho^{MEM}$  for a series of  $t$ -values ( $t$ -maps), each of them representing the electron density in physical space.
- Determination of the maxima in each  $t$ -map. The maxima of the electron density in physical space are then identified with the atomic positions in this particular section.

For each step it is necessary to be able to compute the electron density for arbitrary values of the coordinates. Because  $\rho^{MEM}$  is defined on a grid only, an interpolation method is required. We have used the bicubic spline method (Press et al., 1996), generalized to arbitrary dimensions.

Using this two-step procedure, it is possible to extract the positions of the individual atoms from the  $\rho^{MEM}$  as a function of the parameter  $t$  with arbitrary

dense sampling in  $t$ . The difference between the modulated and the average positions then defines the modulation function. For all four crystallographically independent atoms of  $(\text{LaS})_{1.14}\text{NbS}_2$  we have extracted the modulation functions from  $\rho_{calc}^{MEM}$  and  $\rho_{obs}^{MEM}$  accordingly, employing 50 equally spaced points on the interval  $0 \leq t < 1$  (Fig. 5.3).

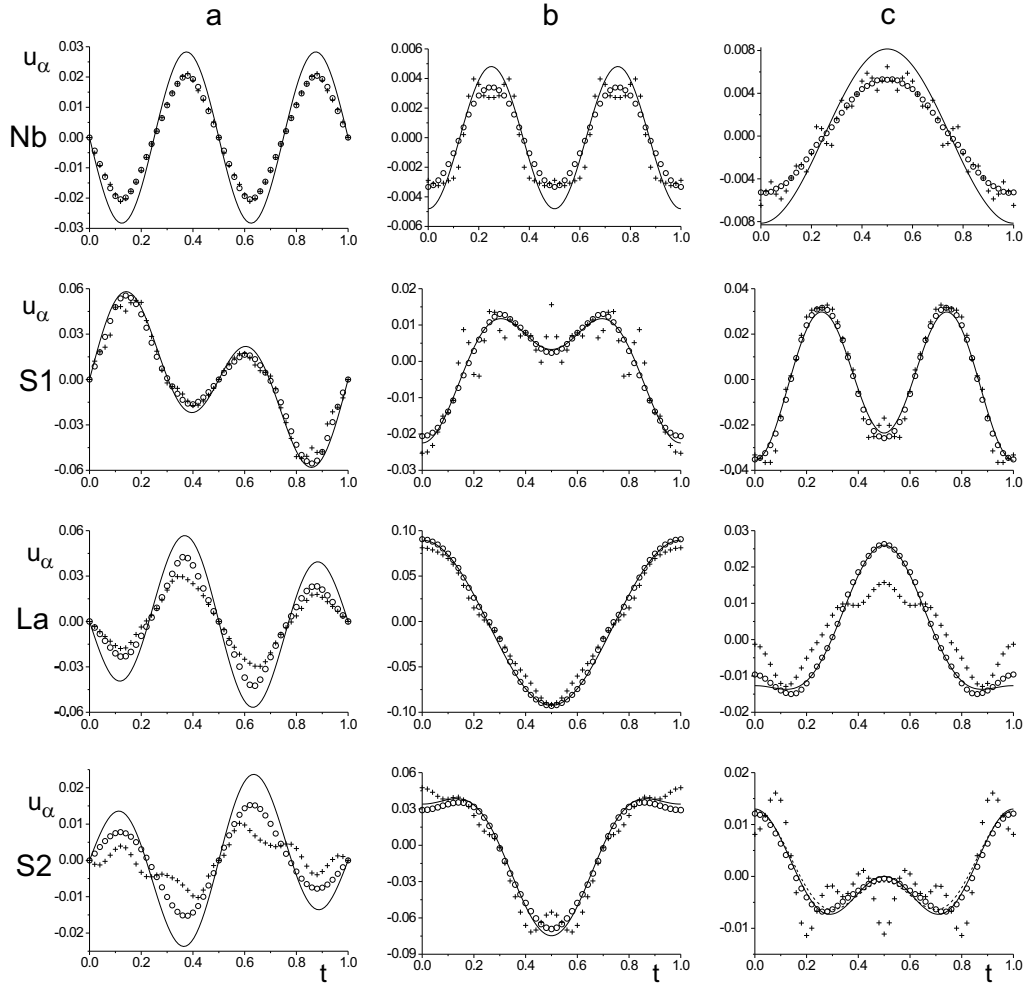


Figure 5.3: Overview of the modulation functions of the independent atoms of  $\text{LaS}_{1.14}\text{NbS}_2$ . Full lines: Model modulation functions, open circles: modulation extracted from  $\rho_{calc}^{MEM}$ , crosses: modulation extracted from  $\rho_{obs}^{MEM}$ , dashed line for  $u_c$  of S2: best harmonic fit to  $\rho_{obs}^{MEM}$ . Horizontal scale:  $t$ , vertical scale: deviation from the average position along the respective directions  $\vec{a}$ ,  $\vec{b}$ ,  $\vec{c}$  in Å.

### 5.3 Discussion

With the calculated data as “observed” data (Eq. 3.4, 3.9), BAYMEM should reproduce the electron density of the model that was used to generate the calculated structure factors. Fig. 5.3 shows that the modulation functions that are determined from  $\rho_{calc}^{MEM}$  indeed follow the modulation functions of the structure model quite well. For some modulation functions the match is almost perfect (e.g. the modulation of La along  $y$ ), while for other modulation functions differences between the model and  $\rho_{calc}^{MEM}$  are found (e.g. the modulation of Nb along  $x$ ).

A number of reasons exist why  $\rho_{calc}^{MEM}$  will not reproduce the electron density of the model exactly (see below). However, the major source of the difference between the reconstructed modulation functions and the model is the finite resolution of the grid that is used to define the electron density in the MaxEnt calculations. First of all it is noted that the sizes of the modulation functions are of the same order as the grid size of about 0.1 Å. It then becomes apparent that the differences between the model and the modulation functions extracted from  $\rho_{calc}^{MEM}$  are only a few percent of the pixel size, with the largest deviation being less than 10% of the pixel size. Indeed it cannot be expected to obtain a more accurate estimate of the positions of the maxima in  $\rho^{MEM}$  than a few percent of the pixel size that was used to discretize this function.

In order to test the effects of the sizes of the pixels on the reconstructed density we have performed an additional computation with a double number of pixels along  $x_1$  and  $x_4$ . That is, the additional computation used a grid of  $64 \times 64 \times 256 \times 64$  pixels, and the resulting density is denoted by  $\rho'_{calc}^{MEM}$ . Modulation functions were derived from  $\rho'_{calc}^{MEM}$  by the procedure as described above. The result showed that the agreement between the model and the reconstructed modulation functions along  $x_1$  ( $x$  of the first subsystem) and  $x_4$  ( $x$  of the second subsystem) has improved considerably (Table 5.2). In fact the difference between these two has become less than half the value it was before (Table 5.3), in accordance with the double resolution along these directions.

We have thus shown that the major part of the discrepancies between the reconstructed density and the model is due to the discrete nature of  $\rho^{MEM}$ , and that the accuracy of the modulation functions is limited to a fraction less than about 10% of the size of the pixels. Nevertheless, this finding still leaves several possibilities for the dependence of the result on the pixel size. It can be due to the fact that  $\rho^{MEM}$  does not represent the values of the electron density on the grid points, but that it represents some type of average density, where the average involves all values of  $\rho$  within the space around the grid point. Alternatively, the problem can lie in the method of interpolation that was used to obtain the values of  $\rho^{MEM}$  in between the grid points.

Table 5.2: The difference between the modulation functions extracted from  $\rho_{calc}^{MEM}$  and those contained in the model. Given is the value of the difference averaged over  $t$ , both in units of length ( $\text{\AA}$ ) and as fraction of the pixel size (in percent). Only values for the modulation along the a-axis are given.  $\rho_{calc}^{MEM}$  was obtained with a grid of  $64 \times 64 \times 256 \times 64$  pixels. The values are given for both the Cambridge and Sakata-Sato algorithms.

Atom	Cambridge algorithm		Sakata-Sato algorithm	
	$\text{\AA}$	%	$\text{\AA}$	%
Nb	0.0010	2.1	0.0028	5.6
S1	0.0017	3.3	0.0023	4.7
La	0.0026	2.9	0.0027	3.0
S2	0.0010	1.1	0.0016	1.8

Table 5.3: The difference between the modulation functions extracted from  $\rho_{calc}^{MEM}$  and those contained in the model. Given is the value of the difference averaged over  $t$ , both in units of length ( $\text{\AA}$ ) and as fraction of the pixel size (in percent). The values are given for  $\rho_{calc}^{MEM}$  obtained with the Cambridge algorithm and for  $\rho_{calc}^{MEM}$  obtained with the Sakata-Sato algorithm. Note that both algorithms lead to results of comparable quality.

Atom	axis	Cambridge algorithm		Sakata-Sato algorithm	
		$\text{\AA}$	%	$\text{\AA}$	%
Nb	a	0.0057	5.6	0.0065	6.4
	b	0.0028	3.0	0.0019	2.1
	c	0.0018	2.0	0.0023	2.5
S1	a	0.0043	4.2	0.0041	3.9
	b	0.0024	2.6	0.0023	2.5
	c	0.0018	2.0	0.0019	2.2
La	a	0.0120	6.7	0.0114	6.3
	b	0.0020	2.2	0.0012	1.3
	c	0.0009	1.0	0.0015	1.7
S2	a	0.0049	2.7	0.0046	2.5
	b	0.0025	2.8	0.0023	2.5
	c	0.0031	3.5	0.0023	2.5

Even if a sufficiently fine grid would have been selected, sources of error remain. They include

- i. An inaccuracy of the MaxEnt algorithm resulting in an electron density that is not the density with the maximum value of the entropy.
- ii. An inaccuracy that is intrinsic to the method. Only a finite number of reflections can be used. This causes series termination effects and the so-called aliasing effect, resulting in artifacts and noise in  $\rho^{MEM}$  (Jauch, 1994; Roversi et al., 1998; Palatinus & van Smaalen, 2002).
- iii. Problems related to the estimated standard uncertainties. Although the calculated data are noise-free, the MEM requires that non-zero standard uncertainties be assigned to them. Therefore the MEM will never converge to a perfect fit to the data.

At present we do not have a quantitative estimate of the importance of these different effects. However, for the case of (LaS)<sub>1.14</sub>NbS<sub>2</sub> with the extensive dataset that was available to us, the sources of error listed above apparently are less important than the effects of the limited resolution.

The reconstructed electron density  $\rho_{obs}^{MEM}$  may show features that are not described by the model. The analysis shows that the modulation functions derived from  $\rho_{obs}^{MEM}$  follow the model quite well, and in particular they match the modulation functions derived from  $\rho_{calc}^{MEM}$  very good (Fig. 5.3). The differences between  $\rho_{obs}^{MEM}$  and the model are larger than the differences between  $\rho_{calc}^{MEM}$  and the model, but they still represent a small fraction of the pixel size only. In this respect it should be noted that additional sources of error are present when the MEM is applied to the experimental data instead of the calculated data. They include the following points.

- iv. The data contain noise. Although it is known that the MEM operates as a noise filter (Skilling & Bryan, 1984), the optimized density might still be different from the one obtained with noiseless data.
- v. The standard uncertainties of the data contain noise.
- vi. Both the standard uncertainties and the measured amplitudes may contain systematic deviations from their true values, because of systematic errors, like an absorption correction or extinction correction that is not perfect.

Point iv particularly applies to the satellite reflections. About half of them are less than's, and the MEM cannot fit their noisy values (Table 5.1). On the other hand, all of these reflections do have correct values in the calculated data. The discrepancies between the modulation functions derived from the calculated data and those derived from the observed data will thus be heavily affected by the

many satellites for which significant intensity values are missing. Although these sources of error may also affect the values of the parameters in the model that has been refined, the two methods are affected in different ways by errors in the data, and differences between the two are expected accordingly.

In view of (i–vi) and the pixel-size effect we believe that the major part of the differences between the model and the reconstructed modulation functions is artifacts and noise. However, in estimating the reliability of the reconstructed modulation functions one also needs to take into account the scattering powers of the individual atoms. For the weaker scatterers S1 and S2 we believe that the differences between the modulations functions derived from  $\rho_{obs}^{MEM}$  and  $\rho_{calc}^{MEM}$  are artifacts and noise indeed. But for Nb it is found that modulation functions of the model are followed by the reconstructed functions much better than for the sulfur atoms, although the displacements of Nb are smaller than for S1 and S2. Noise is visible, but it is an order of magnitude smaller than for S1 and S2. Lanthanum is the strongest scatterer, and it is thus tempting to interpret the deviations between model and reconstructed functions as a true structural effect. This is especially so for the displacements along  $x_3$ . Although we believe that the reconstructed modulation does indicate that there are deviations from the harmonic model, we refrain from a detailed analysis. We maintain our interpretation, that the modulations in  $(\text{LaS})_{1.14}\text{NbS}_2$  are described well by modulation functions based on the combinations of two harmonics (Fig. 5.3).

We have identified the positions of the atoms with the maxima in the electron density. In the case of anharmonic temperature movements, the electron density is asymmetric and its maximum does not need to coincide with the position of the atom. For  $(\text{LaS})_{1.14}\text{NbS}_2$  both the refinements and the reconstructed electron density do not give any indication for anharmonic temperature factors, and we believe that this source of error in deriving the displacement modulations is not important here.

Other effects that were important for the successful modelling of the structure were the modulations of the harmonic temperature factors and the occupancy of the La site (Jobst & van Smaalen, 2002). Both modulations lead to a modulation of the value of the electron density along the trace of its maximum as a function of  $t$ . Both for  $\rho_{calc}^{MEM}$  and  $\rho_{obs}^{MEM}$  the values of the electron density at the positions of La indeed exhibit a variation with  $t$ , that matches with the modulations of the temperature factors and the occupancy (Fig. 5.4). It can be concluded that the MEM is able to reconstruct these aspects of the modulations too.

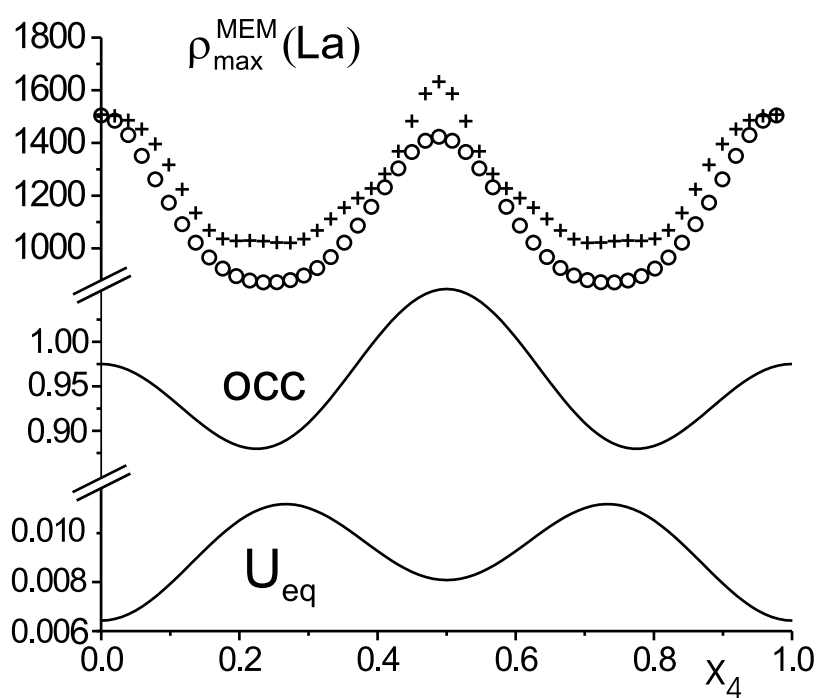


Figure 5.4: Modulation of the temperature factor ( $U_{\text{eq}}$ ) and the occupancy of La (occ) compared to the values of  $\rho_{\text{calc}}^{\text{MEM}}$  (circles) and  $\rho_{\text{obs}}^{\text{MEM}}$  (crosses) at the positions of the La atoms ( $\rho_{\max}^{\text{MEM}}(\text{La})$ ).

# Chapter 6

## Origin of the incommensurability of the crystal structure of the high-pressure phase III of Bi

### Abstract

In-situ single-crystal X-ray diffraction experiments have been performed on the high-pressure phase III of the element bismuth at  $p = 5.5$  GPa. The incommensurately modulated structure of the composite crystal type of Bi-III has been determined by structure refinements in combination with the Maximum Entropy Method (MEM) in superspace. Bi-III is tetragonal with superspace group  $I'4/mcm(00\gamma)$  with  $\gamma = 1.309$  (1). The first subsystem or host comprises a 3-dimensionally connected net of Bi atoms. Channels in this framework are filled by the atoms of the guest, that are equidistant in the basic structure of interpenetrating, periodic host and guest subsystems. The modulation is found to give rise to the formation of quasi-pairs within guest, in accordance with theoretical calculations. A good supercell approximation is found with  $c_s = 12.603$  Å  $\approx 3c_h \approx 4c_g$  and space group P4/ncc. The pairing of atoms is found to be responsible for the incommensurability of this structure as compared to the approximate superstructure. A second effect of the modulation is the presence of an increased inter-subsystem bonding. A peculiar feature of the structure of Bi-III is the presence of modulated 3<sup>rd</sup> order anharmonic temperature tensors, while their average values are zero. This is explained by the varying environments of the atoms in the incommensurate structure.

### 6.1 Introduction

Many metallic elements have been found to form complicated crystal structures at high pressures (Schwarz et al., 1998; Nelmes et al., 1999). The unit cells are large

and the environments of the atoms deviate strongly from the highly symmetric coordination polyhedra, as they are found in the simple closed packed structures that exist at ambient conditions.

Surprisingly, similar structures are found for elements in different groups of the periodic system. For the alkali metals, the driving force for the formation of the superstructures has been identified as the transfer of the valence electrons towards  $d$  orbitals. This results in deviations from spherical symmetry of the atoms, and it is thus responsible for the formation of complicated crystal structures at high pressures (Neaton & Ashcroft, 1999). For the elements belonging to other groups of the periodic system, the situation is less clear. Recent band structure calculations for the group VI elements suggest that the complicated superstructures are the result of a competition between band energy and electrostatic contributions to the total energy (Haussermann et al., 2002).

A particularly complicated structure is assumed by the phase III of bismuth: it belongs to the class of incommensurate composite crystals, that lack 3-dimensional (3D) translation symmetry (McMahon et al., 2000). Phase III of bismuth is stable at pressures between 2.8 and 7.7 GPa. Its structure comprises two subsystems, each of which has a periodic atomic structure in first approximation (Fig. 6.1).

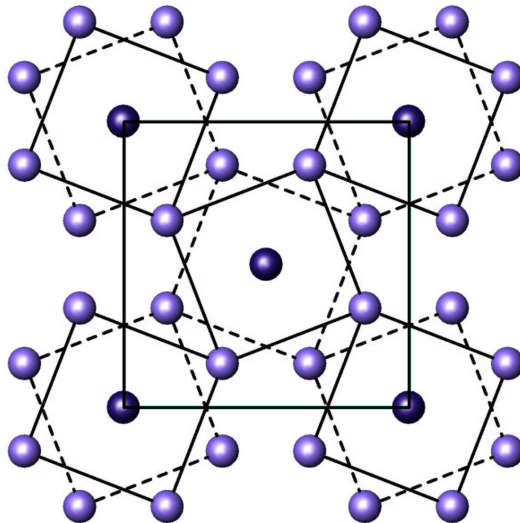


Figure 6.1: The basic structure of Bi-III projected along the tetragonal  $c$ -axis. Host atoms are represented by light circles. Dark circles stand for the guest atoms. The projected unit cell is indicated. Dashed and full lines connect atoms that are shifted over one half along  $\vec{c}$ .

The first subsystem or host consists of Bi atoms arranged in a 3-dimensionally connected network, in which channels exist parallel to the tetragonal axis. These

channels are filled by chains of atoms, that form the guest or second subsystem. The periodicity along the channel direction is different for the host and the guest, resulting in two independent, mutually incommensurate lattice constants  $c_h = 4.1817 \text{ \AA}$  and  $c_g = 3.1950 \text{ \AA}$  at  $p = 5.5 \text{ GPa}$  (McMahon et al., 2000).

The incommensurate structure type that is adopted by Bi-III has been described for the first time for Ba-IV (Nelmes et al., 1999). The same structure type has been found for Sb-II and Rb-IV (McMahon et al., 2001). Conclusive evidence for the incommensurate character of the structures is provided by the positions of the reflections in X-ray powder diffraction (McMahon et al., 2000; McMahon et al., 2001). The diffraction profiles could not be indexed by either  $c_g$  or  $c_h$  nor by a simple superlattice. The additional weak reflections that have been reported to occur in the powder diffraction of Sb-II and Bi-III could be indexed with 4 integers on the basis of the  $(3+1)\text{D}$  superspace description, again showing that the description as an incommensurate composite crystal is appropriate (McMahon et al., 2003).

The true crystal structures of incommensurate composite crystals consist of modulated subsystems (van Smaalen, 1995). Each subsystem has an incommensurately modulated structure, with a period of the modulation that is given by the basic-structure period of the other subsystem. The determination of the modulation functions of the Bi atoms is the subject of the present paper. The modulations will be shown to have a profound effect on the coordinations of the atoms, and thus they are necessary to understand the chemical bonding in these crystals as well as their stability. The comparison of the true incommensurately modulated structure with an approximate superstructure ( $c_s = 12.6030 \text{ \AA} \approx 3c_h \approx 4c_g$ ) then reveals the origin of the incommensurateness as the formation of Bi–Bi quasi-dimers within the guest.

The superspace formalism (de Wolff et al., 1981; Janssen et al., 1992) gives the positions of the atoms in incommensurately modulated structures as the sum of a periodic average position and a shift. The shifts are obtained as the values of modulation functions taken at the appropriate values of their arguments. Modulation functions can assume any form, and thus they are described by an infinite number of independent parameters. However, the experiment allows only a finite number of parameters to be determined. Usually only the first or the first two harmonics of the Fourier series are determined for each modulation function (van Smaalen, 1995). Sometimes the data are better described by a block-wave or saw-tooth shaped modulation function (Petříček et al., 1990), but a general shape is not easily modelled.

The Maximum Entropy Method (MEM) allows for a model-independent reconstruction of the electron density (Gilmore, 1996). We have extended this method to determine the electron density in superspace ( $\rho^{MEM}(\vec{x}_s)$ ) from the scattering data of an aperiodic crystal (van Smaalen et al., 2003). The modulation functions are then derived from  $\rho^{MEM}(\vec{x}_s)$  in a straightforward way. These

functions are independent of a model and they can assume any shape. Consequently, those shapes are recovered that provide the best fit to the data (van Smaalen et al., 2003).

In this paper we show that modulation functions comprising a sum of a few harmonics do not give a satisfactory fit to the scattering data of Bi-III. Employing the MEM in superspace, the modulation functions are shown to have shapes that are between that of a simple sum of harmonics and that of a block-wave or saw-tooth function. Furthermore  $\rho^{MEM}(\vec{x}_s)$  shows that the temperature factors are modulated, as it can be described by a modulation for the third-order anharmonic temperature factor tensors. Substitution of an idealized model based on these features then leads to an acceptable fit of the refinement to the data.

It is noticed that the modulation functions based on  $\rho^{MEM}(\vec{x}_s)$  cannot be modelled in all aspects by existing refinement software. Therefore we analyze the incommensurate crystal structure of Bi-III employing modulation functions that are derived directly from  $\rho^{MEM}(\vec{x}_s)$ . A preliminary account of this work has been given elsewhere (McMahon et al., 2003).

## 6.2 Experimental

A single crystal of Bi-III was grown at a pressure of 5.5 GPa inside a diamond anvil cell, following procedures reported earlier (McMahon et al., 2000; McMahon et al., 2003). Single-crystal X-ray diffraction was measured at station 9.8 of the Synchrotron Radiation Source (SRS) at Daresbury Laboratory. Diffracted intensities were measured in a series of rotation images on a Bruker diffractometer equipped with a SMART CCD detector. The determination of the integrated intensities of the Bragg reflections and further data processing were performed with the SMART and SAINT suite of programs. An empirical absorption correction was applied using SADABS (Sheldrick, 1997). Further details of the experimental procedures are given in Table 6.1.

All Bragg reflections could be indexed with four integers  $(h k l_1 l_2)$  according to (de Wolff et al., 1981)

$$\vec{H} = h\vec{a}^* + k\vec{b}^* + l_1\vec{c}_h^* + l_2\vec{c}_g^* \quad (6.1)$$

where the reciprocal lattice of the host is defined by  $\{\vec{a}^*, \vec{b}^*, \vec{c}_h^*\}$  and that of the guest by  $\{\vec{a}^*, \vec{b}^*, \vec{c}_g^*\}$ . The collinear vectors  $\vec{c}_h^*$  and  $\vec{c}_g^*$  have an incommensurate length ratio, that has been determined as  $\gamma = \frac{c_h}{c_g} = 1.309(1)$ . Different classes of reflections can be recognized in this notation. The reflections  $(h k l_1 0)$  are the main reflections of the host, while  $(h k 0 l_2)$  describe the main reflections of the guest. The reflections  $(h k 0 0)$  are common to host and guest. Reflections  $(h k l_1 l_2)$  with both  $l_1$  and  $l_2$  nonzero are satellite reflections. They are present due to the modulations, and they would have zero intensities if the structure

Table 6.1: Experimental data

Pressure (GPa)	5.5
Temperature (K)	295
Chemical formula	Bi
Chemical formula weight	277.42
Superspace group	$I'4/mcc(00\gamma)$
Centering in superspace $I'$	$\frac{1}{2}, \frac{1}{2}, \frac{1}{2}, \frac{1}{2}$
Subsystem space group (host, guest)	$I4/mcm, I4/mmm$
Lattice parameters $a, c_h, c_g$ (Å)	8.5562(4), 4.1817(3), 3.1950(2)
Volume (host, guest, Å <sup>3</sup> )	306.14, 233.90
Z (host, guest)	8, 2
Crystal form	circular disk
Crystal size (mm <sup>3</sup> )	0.1 × 0.1 × 0.1
Crystal colour	silver lustre
Radiation type	Synchrotron
Wavelength (Å)	0.4815 (1)
Diffractometer	Bruker
Detector	SMART 1K CCD
Method of measurement	rotation images
$\Delta\omega$ (deg.)	0.1
$(2\theta)_{max}$ (deg.)	42
Absorption correction	sadabs (Sheldrick, 1997)
No. of measured refl.	1309
No of independent refl.	497
No. of observed refl. (all/indep.)	983/389
Criterion for observed reflections	$I > 5.0\sigma(I)$
$R_{int}$ (all reflections)	0.059
$R_{int}$ (observed reflections)	0.060
Maximum of $\sin(\theta)/\lambda$ (Å <sup>-1</sup> )	0.769
Range of $h, k, l, m$	-11 → $h$ → 11 -12 → $k$ → 12 -6 → $l$ → 6 -4 → $m$ → 4
Refinement Refinement on	$F$
Weighting scheme	$(\sigma^2(F) + (0.03F)^2)^{-1}$
$R$ (observed reflections)	0.067
$wR$ (observed reflections)	0.142
Goodness of Fit (obs)	4.39
No. of parameters	24
Extinction correction	Isotropic type I (Becker & Coppens, 1974)
Extinction coefficient	0.04 (2)
Source of atomic scattering factors	Int. Tables for Crystallography, Vol. A

would be composed of periodic host and guest structures. We have observed only first-order ( $m = \min\{|l_1|, |l_2|\} = 1$ ) and second-order ( $m = 2$ ) satellites.

The SAINT program can only integrate Bragg reflections belonging to a single reciprocal lattice. In order to overcome the problems related to the incommensurate composite character of the present data, the integration was performed separately for the host and guest main reflections. The intensities of the satellites have been obtained by separate integrations using effective lattices. For example, the  $(hk\bar{1}2)$  and  $(hk\bar{2}4)$  reflections have been obtained as the first and second layers of a lattice with  $c_{eff}^* = -c_h^* + 2c_g^*$ . In this way satellite reflections are obtained with  $(l_1, l_2)$  equal to  $(\bar{1}, 1)$ ,  $(\bar{1}, 2)$ ,  $(2, \bar{1})$ ,  $(3, \bar{1})$ ,  $(1, 1)$ ,  $(4, \bar{1})$ ,  $(2, 1)$ ,  $(3, 1)$ ,  $(\bar{2}, 2)$ ,  $(\bar{2}, 4)$ ,  $(3, \bar{2})$ ,  $(4, \bar{2})$  and  $(2, 2)$ . All subsets of data contain the  $(hk00)$  reflections, that have been used for scaling.

The integration was complicated by the presence of scattered intensity originating in the diamonds, the wolfram gasket and the beryllium windows. The powder-like scattering of the gasket and the beryllium windows could not be eliminated perfectly, resulting in unwanted contributions to the intensities of some reflections. Obviously, weak reflections are affected more than strong reflections. Therefore, it was decided to use only observed reflections in the refinements, and to set the criterion of observed reflections to  $I > 5\sigma(I)$ . Furthermore 8 reflections were eliminated, for which  $F_{obs} > 10F_{calc}$  was found in the final stages of refinement.

After averaging in Laue symmetry  $4/mmm$ , a dataset was obtained with a total of 380 observed reflections, containing 238 main reflections, 111 first-order ( $m = 1$ ) and 31 second-order ( $m = 2$ ) satellites. These intensity data were used in the refinements and MEM calculations.

For the indexing of the reflections according to Eq. 6.1, reflection conditions were found as  $(hkl_1l_2)$ :  $h+k+l_1+l_2 = 2n$ ,  $(h0l_1l_2)$ :  $h+l_1+l_2 = 2n$  and  $(hhl_1l_2)$ :  $l_1+l_2 = 2n$ . This lead to the superspace group  $I'4/mcc(00\gamma)$  (Table 6.1). This superspace group is in accordance with the space groups of the average structures of the host and guest, as they were previously reported (McMahon et al., 2000).

## 6.3 Structure refinements

### 6.3.1 The basic structure

The first step was the refinement of the basic structure against the main reflections. A reasonably good fit was obtained with  $R(main) = 0.090$ . ( $R(host) = 0.073$  for 110 main reflections of the host and  $R(guest) = 0.134$  for 92 main reflections of the guest and  $R(comm) = 0.070$  for 36 common  $(h, k, 0, 0)$  reflections.) The previously reported structure was confirmed (McMahon et al., 2000), with one independent atom for the host (Bi1) at  $(0.1532(2), x + 0.5, 0)$  and one independent atom for the guest (Bi2) at  $(0, 0, 0)$ . The  $x$  coordinate of Bi1 was found

to have essentially the same value for all refinements, employing different models for the modulation functions. It is noticed that in the superspace approach, the coordinates of the atoms are referred to the lattice of the subsystem to which this atom belongs (Janssen et al., 1992; van Smaalen, 1995). Accordingly, the coordinates of Bi1 refer to the host lattice and the coordinates of Bi2 refer to the guest lattice. All refinements were performed with the computer program JANA2000 (Petříček & Dušek, 2000).

### 6.3.2 The modulated structure

The first model for the modulated structure consists of harmonic modulation functions for the positions of the two crystallographically independent atoms (Model 1).

$$u_i(\bar{x}_{s4}) = \sum_{n=1}^4 A_i^n \sin(2\pi n \bar{x}_{s4}) + B_i^n \cos(2\pi n \bar{x}_{s4}) \quad (6.2)$$

for  $i = x, y, z$  and with  $\bar{x}_{s4} = t + \vec{q} \cdot \vec{x}$  (van Smaalen, 1995). The parameter  $t$  represents the initial phase of the modulation. For Bi1 only  $n = 1, 2$  have been used, while for Bi2 the terms with  $n = \text{odd}$  are zero by symmetry. Similarly, modulation amplitudes for the temperature parameters were included into Model 1. A considerable reduction of the number of independent modulation parameters was obtained by the symmetry restrictions according to the superspace group. Most notably the modulation of Bi2 is restricted to displacements parallel to the  $c$ -axis. Refinements were performed of all independent parameters of Model 1 against the complete dataset, employing arbitrary but small starting values for the modulation parameters. Convergence was obtained at  $R = 0.068$  (Table 6.2). The final model was independent of the starting values of the parameters (Table 6.3). The improvement of the fit to the main reflections from 0.090 towards 0.063 shows that the refined modulation functions contain at least part of the truth. However, the fit to the satellite reflections is not satisfactory, in particular with respect to the second-order satellites (Table 6.2). Part of this could be

Table 6.2:  $R$ -values for the refinements of the basic structure and three different models for the modulation. Partial  $R$ -values are given for different groups of reflections.  $N_{par}$  is the number of independent parameters.

	Basic structure	Model 1	Model 2	Model 3
$N_{par}$	8	17	17	24
$R(all)$	0.090	0.068	0.067	0.067
$R(main)$	0.090	0.063	0.063	0.064
$R(m = 1)$		0.105	0.103	0.093
$R(m = 2)$		0.249	0.231	0.161

Table 6.3: Values of the parameters after the refinements of Models 1, 2 and 3. Bi1 is at the special position  $(x, 0.5 + x, 0)$  with  $U_{22} = U_{11}$ ,  $B_y^1 = -B_x^1$ ,  $B_y^2 = B_x^2$ ,  $U_{23}^{sin1} = -U_{13}^{sin1}$  and  $U_{22}^{cos1} = -U_{11}^{cos1}$ . Bi2 is at the special position  $(0, 0, 0)$  with  $U_{22} = U_{11}$  and  $U_{22}^{cos2} = U_{11}^{cos2}$ . All other parameters that are not listed in this table are zero by symmetry. The parameter  $U_{33}^{sin1}$  of Bi2 in Model 3 assumed insignificant values in the initial refinements. It was set to zero in the final refinements, in order to avoid correlations with the ADP parameters.

	Model 1	Model 2	Model 3
Bi1			
x	0.1532(1)	0.1532(1)	0.1532(1)
$U_{11}$	0.0146(8)	0.0146(8)	0.0149(8)
$U_{33}$	0.0167(15)	0.0168(15)	0.0171(15)
$U_{12}$	-0.0027(4)	-0.0027(4)	-0.0028(3)
$B_x^1$	-0.0047(1)	-0.0048(1)	-0.0048(1)
$B_x^2$	-0.0008(1)	-0.0008(1)	-0.0003(2)
$A_z^2$	0.0001(4)	0.0001(4)	0.0011(7)
$U_{13}^{sin1}$	0.0012(2)	0.0013(2)	0.0013(2)
$U_{11}^{cos1}$	0.0010(3)	0.0010(3)	0.0008(3)
Bi2			
$U_{11}$	0.0163(10)	0.0133(13)	0.0133(14)
$U_{33}$	0.0369(21)	0.0470(51)	0.0350(18)
$B_z^1$	0	0.0387(25)	0.0348(26)
$A_z^2$	0.0203(14)	-0.0124(24)	-0.0109(23)
$A_z^4$	0.0152(11)	0	0
$U_{11}^{sin1}$	0	0.0048(14)	0.0050(15)
$U_{33}^{sin1}$	0	-0.017(7)	0
$U_{11}^{cos2}$	-0.0021(6)	0	0
$U_{33}^{cos2}$	0.0111(29)	0	0

explained by the fact that the (weaker) satellites are much more affected by the problems of the data collection than the (stronger) main reflections (Section 6.2). However, the fit is much poorer than it is expected from the data quality, thus indicating that the modulation functions cannot be described as a sum of a few harmonics. The introduction of additional harmonics lead to unstable refinements, because of nearly dependent parameters. Therefore, we decided to study the structure of Bi-III by the MEM (Section 6.4).

Based on the analysis of  $\rho^{MEM}(\vec{x}_s)$  more appropriate models for the modulation were developed (Section 6.4). The atom Bi1 is better described by a combination of block-wave and saw-tooth shaped functions, but we retained the function of two harmonics in the refinement as a reasonable approximation. For the Bi2 atom a saw-tooth shaped function of double period describes the true shape of the modulation function better than a harmonic function does. This function was modelled by a sum of two harmonics defined for half of the period and the same sum of two harmonics shifted by half a period for the second half of the period in  $\bar{x}_{s4}$  (Model 2):

$$\begin{aligned} u_z(\bar{x}_{s4}) &= \sum_{n=1}^2 A_z^n \sin(2\pi n \bar{x}_{s4}) + B_z^n \cos(2\pi n \bar{x}_{s4}) \text{ for } 0 < \bar{x}_{s4} < \frac{1}{2} \\ u_z(\bar{x}_{s4}) &= \sum_{n=1}^2 A_z^n \sin(2\pi n (\bar{x}_{s4} - \frac{1}{2})) + B_z^n \cos(2\pi n (\bar{x}_{s4} - \frac{1}{2})) \text{ for } \frac{1}{2} < \bar{x}_{s4} < 1 \end{aligned} \quad (6.3)$$

A slightly better fit to the data was obtained than in Model 1 (Table 6.2).

Inspection of  $\rho^{MEM}(\vec{x}_s)$  showed that the atoms have a strongly asymmetric shape. This could be described by anharmonic displacement parameters (ADPs) of the third order (Kuhs, 1992), and they were included in the refinement (Model 3). A considerable improvement of the fit to the data was obtained (Table 6.2). Most notable is, that the ADPs of the average structure are zero, while significantly non-zero values are only obtained for the modulation parameters of the ADPs. This feature is readily understood from inspection of  $\rho^{MEM}(\vec{x}_s)$ . For half of the atoms in the crystal the skewness is to one side, while for the other half of the atoms the skewness is to the opposite direction (Section 6.4).

Model 3 is considered to be our best refinement model. The improvements of the fits to the data on the introduction of modulation features derived from  $\rho^{MEM}(\vec{x}_s)$  provide evidence for the meaningfulness of the results of the MEM. However, the shapes of the refined functions still show significant differences from the modulations as derived from  $\rho^{MEM}(\vec{x}_s)$ , that we were not able to describe by a simple, parameterized model. Therefore, the structure of Bi-III was analyzed employing the modulation functions as they were derived directly from  $\rho^{MEM}(\vec{x}_s)$  instead of using the refined model.

### 6.3.3 The commensurate approximation

The value of 1.309 for  $\gamma$  is close to the  $\frac{4}{3}$ . This suggests that the structure of Bi-III might be approximately described in a supercell, that is a 3-fold superstructure of the host and a 4-fold superstructure of the guest. Substitution of  $\gamma = \frac{4}{3}$  into the superspace group leads to different possibilities for the symmetry of the supercell. They are  $P4cc$ ,  $P4/mcc$  and  $P4/ncc$ . A good fit to the data could only be obtained in the space group  $P4/ncc$ . The fit to the data is equally good as the fit of the best incommensurate structure model. The lattice parameters  $a = b$  of the supercell are equal to the corresponding parameters of the host and guest. The fit to the data is independent of the precise value of the  $c_s$  lattice parameter of the supercell. Reasonable choices are within the range  $3c_h < c_s < 4c_g$ . We have chosen  $c_s = 12.6030 \text{ \AA}$ , such that the density of the approximate supercell is equal to the experimental density of the true incommensurate structure.

The approximate superstructure belongs to the  $\text{Ba}_5\text{Si}_3$  structure type, albeit with shifts of the atoms up to  $0.7 \text{ \AA}$  as compared to the published structure of  $\text{Ba}_5\text{Si}_3$  (Villars & Calvert, 1996). There are 4 crystallographically independent atoms in this supercell. (Table 6.4, Fig. 6.2).

Table 6.4: Atomic parameters for the approximate superstructure model. The space group is  $P4/ncc$  with the origin defined by the inversion operator  $(0.5 - x, 0.5 - y, -z)$ . Lattice parameters are  $a_s = 8.5562$  and  $c_s = 12.6030 \text{ \AA}$ .

Atom	$x$	$y$	$z$	$U_{iso}$
Bi1a	0.1492 (3)	0.1579 (3)	0.0837 (2)	0.0148 (7)
Bi1b	0.3459 (3)	$x$	0.25	0.0150 (8)
Bi2a	0	0.5	0.0578 (4)	0.0229 (16)
Bi2b	0	0.5	0.3144 (3)	0.0225 (11)

## 6.4 Application of the MEM

The MEM was used to determine the modulation functions, independent of any parameterization. The experimental data ( $F_e$ ) as used in the MEM were obtained from  $F_{obs}$  following a procedure described previously (Bagautdinov et al., 1998). The magnitude of  $F_e(\vec{H})$  is set equal to the magnitude of  $F_{obs}(\vec{H})$ , scaled towards the scattering of one unit cell and corrected for extinction and anomalous scattering. The phase of  $F_e(\vec{H})$  is made equal to the phase of  $F_{calc}(\vec{H})$ . We have used the refinement of Model 3 to derive  $F_e$ . However, it is noticed, that all reflections have identical phases in the three models that were considered in the refinements (Section 6.3.2). The MEM is therefore independent of the model that is used to derive  $F_e$  from the measured structure factor amplitudes  $F_{obs}$ .

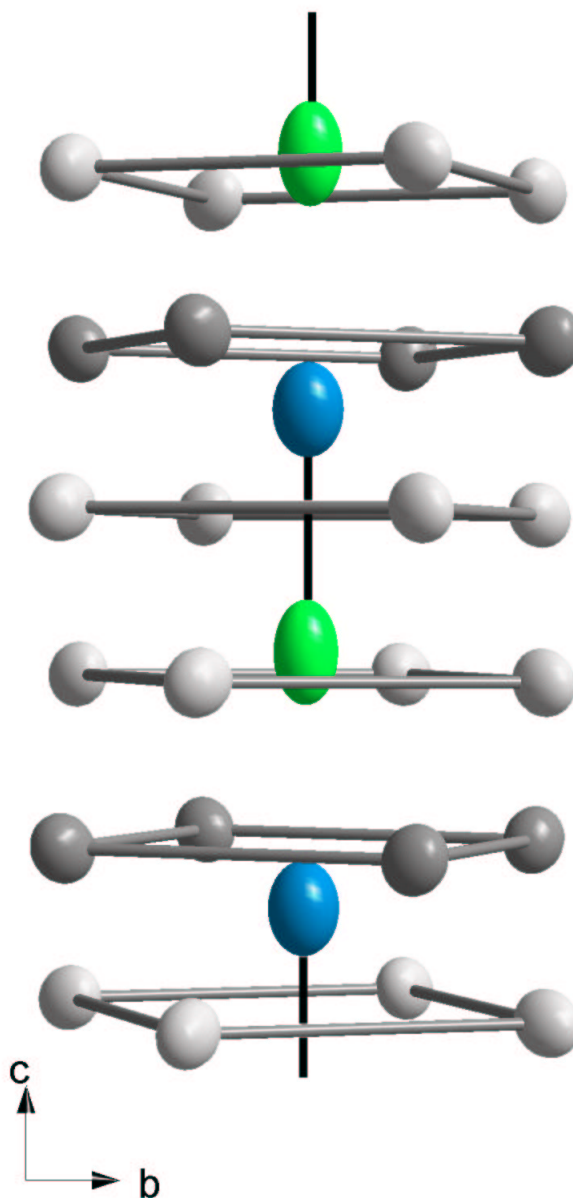


Figure 6.2: Perspective view of the supercell. One period along  $\vec{c}$  is given for one chain of guest atoms and the surrounding host atoms. Vertical lines connect the pairs of the guest atoms.

Three different Maximum Entropy (MaxEnt) optimizations were performed with the computer program BAYMEM (van Smaalen et al., 2003), employing alternatively the Sakata-Sato algorithm (Sakata & Takata, 1996) with the F<sub>2</sub>- or the F<sub>4</sub>-constraint (Palatinus & van Smaalen, 2002) and the MEMSys algorithm (Skilling & Bryan, 1984). An overview of the parameters and resulting  $R$ -values is given in Table 6.5. The result of the MEM is an electron density map  $\rho^{MEM}(\vec{x}_s)$

Table 6.5: Parameterization of the electron density and resulting  $R$ -values of the MEM calculations. S-S denotes the Sakata-Sato algorithm. F<sub>2</sub> and F<sub>4</sub> denote the type of constraint.

pixel division	128 × 128 × 32 × 32		
pixel size [Å]	0.067 × 0.067 × 0.131 × 0.100		
algorithm	S-S	S-S	MEMSys
constraint	F <sub>2</sub>	F <sub>4</sub>	F <sub>2</sub>
final value of the constraint	1.30	1.76	1.02
computation time [hours]	111.3	113.2	35.8
final $R$ -values			
all reflections	0.041	0.039	0.037
main reflections	0.044	0.041	0.039
1 <sup>st</sup> order satellites	0.004	0.026	0.004
2 <sup>nd</sup> order satellites	0.003	0.028	0.003

in (3 + 1)D superspace. These maps were analyzed by inspection of 2D sections, and by computational procedures to derive the modulation functions.

The MaxEnt computations with the F<sub>2</sub>-constraint result in unrealistically low partial  $R$ -values for satellites. This overfitting of the satellites is a direct consequence of the non-Gaussian distribution of the normalized residuals (De Vries et al., 1996; Palatinus & van Smaalen, 2002). MaxEnt computations with the F<sub>4</sub>-constraint (Table 6.5) give a much more evenly distribution of residuals. Therefore, we have used the results of the computation with the F<sub>4</sub>-constraint for a detailed analysis of the structure model. However, following similar procedures for the three different models as obtained with the MEM, it was found that all three electron density maps lead to similar results for the shapes of the modulation functions (Fig. 6.3). The positions of the atoms are not sensitive to the details of the method followed in the MaxEnt calculations, and it can be considered to be a robust result.

The modulation functions have been obtained from the positions of the centers of charge of  $\rho^{MEM}(\vec{x}_s)$  as a function of  $\bar{x}_{s4}$ . An interpolation method has been used to determine the values of the electron density at arbitrary  $\vec{x}_s$  (van Smaalen et al., 2003). The average positions are defined as the integral over one period, i.e. the integral over  $\bar{x}_{s4}$  from 0 to 1. The modulation functions then follow as the differences between the positions of the centers of charge and the corresponding

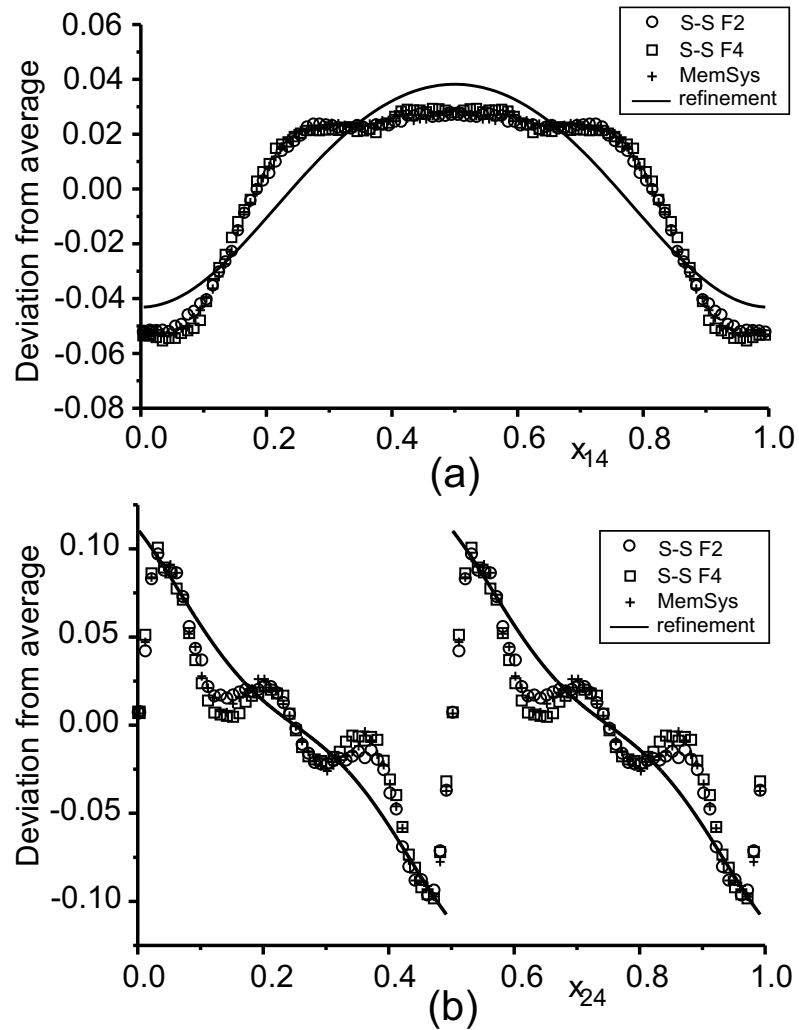


Figure 6.3: The modulation functions for displacements a) Modulation along  $x$  of Bi1, and b) Modulation along  $z$  of Bi2. The values in  $\text{\AA}$  are given as a function of  $x_{14}$  and  $x_{24}$ , respectively. The modulation functions derived from  $\rho^{MEM}(\vec{x}_s)$  for the 3 different MaxEnt calculations (Table 6.5) nearly coincide. The modulation functions derived from Model 3 are indicated by full lines (Table 6.3).

average positions. The results of these procedures for the two independent atoms are shown in Fig. 6.3.

The  $(x_{1s}, x_{s4})$ -section of  $\rho^{MEM}(\vec{x}_s)$  shows that the modulation of Bi1 along  $x$  is different from the modulation function in the refined model (Fig. 6.4). This is

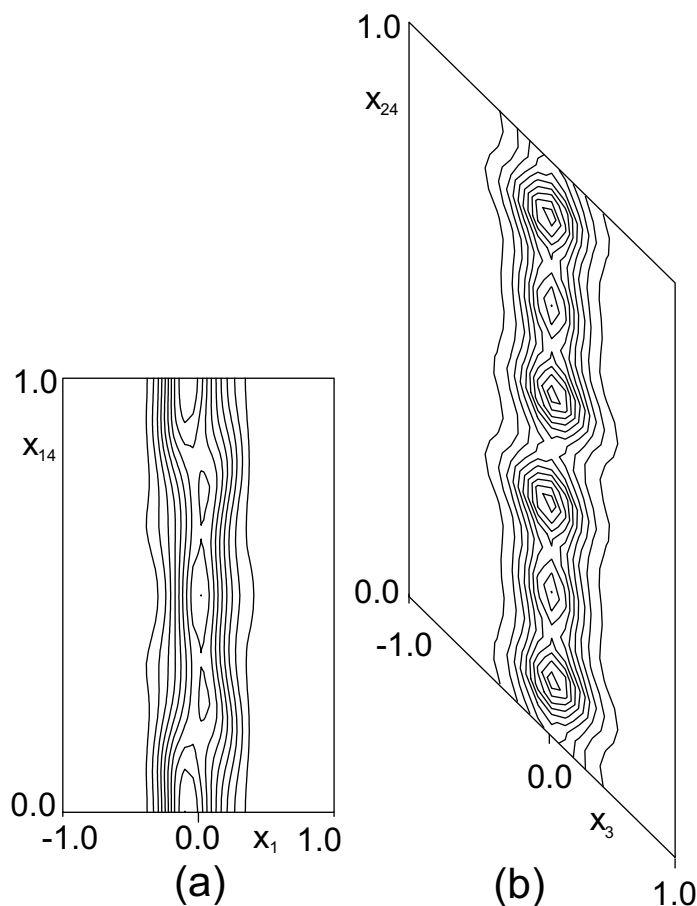


Figure 6.4: 2D sections of the electron density  $\rho^{MEM}(\vec{x}_s)$ . a)  $(x_1, x_{14})$ -Section centered at the position of Bi1. b)  $(x_3, x_{24})$ -Section centered at the position of Bi2. The scale of  $x_1$  and  $x_3$  is in  $\text{\AA}$ . The scale of  $x_4$  is in relative coordinates. Contour lines of equal density are drawn every 10% of the maximum density.

confirmed by the modulation function as determined by the procedure described above (Fig. 6.3). The modulation along  $y$  has the same shape as that along  $x$ , but it is shifted by  $\frac{1}{2}$  in the phase  $\bar{x}_{s4}$ . The analysis showed that the modulation of Bi1 is much smaller along  $z$  than it is along  $x$  and  $y$ . Values for the  $z$  modulation that deviate significantly from zero could not be found either in the MEM or in the structure refinements (Table 6.3). Fig. 6.4 also shows that the density is not symmetrical in  $x_{s1}$  around its maximum. This effect can be explained by anharmonic temperature tensors of odd orders. As presented in Section 6.3.2 the

introduction of  $3^{rd}$  order anharmonic temperature factors lead to a substantial improvement of the fit.

The modulation of Bi2 is restricted by symmetry to be parallel to  $\vec{c}$ . The function as derived from the MEM can be described as a modified saw-tooth function of a period that is half the fundamental period. The sum of two harmonics is a poor approximation. Instead, this function was modelled by a kind of saw-tooth function (Section 6.3.2). The fine structure on the modulation derived from  $\rho^{MEM}(\vec{x}_s)$  is not modelled in this way. Although this fine structure might be a realistic effect, that is related to the interactions between the two subsystems, it is the least reliable part of the modulation. Due to the limited resolution of the data along  $\vec{c}^*$ , the modulations parallel to  $\vec{c}$  are the least accurate. Therefore we refrain from a quantitative analysis of these details of the shapes of the modulation functions.

## 6.5 Discussion

The incommensurate composite character of the structure of Bi-III leads to the presence of an infinite number of different atomic environments. These environments can be summarized in  $t$ -plots (van Smaalen, 1995). Interatomic distances, bond angles and other properties can be computed as a function of  $t$  in the fourth superspace coordinate  $\bar{x}_{s4} = t + \vec{q} \cdot \vec{x}$  (Eq. 6.2). This plot is periodic, if it is calculated for a single central atom and its neighbors. Each value of  $t$  gives a possible environment of the central atom. The fraction of atoms with environments within a certain range is proportional to the fraction of  $t$  values that span this range. For both crystallographically independent atoms the  $t$ -plots show that the environments are within physically acceptable boundaries, with a minimum distance of about 3.07 Å and coordination numbers (CN) between 6 and 10 (Figs. 6.5 and 6.6).

The modulations of the atoms are responsible for the presence of the shortest distance of 3.07 Å instead of a shortest distance of 3.20 Å, as it is found in the hypothetical basic structure. The distance of about 3.07 Å is equal to the shortest Bi–Bi distance in the crystal structure of Bi at ambient conditions (Cucka & Barrett, 1962).

The coordination number of Bi1 is found to vary between 7 in points around  $B$  and  $C$  and 8 in points around  $A$  (Fig. 6.5). The nearest neighbors of Bi1 are two atoms of the same subsystem at distances of about 3.15 Å. The distances towards the four neighbors at about 3.34 Å switch between two values. The block-wave character of the modulation functions is responsible for this switching behavior. Thus the block-wave-like character seems to result from the strive towards a few stable environments of the Bi1 atoms, instead of a much broader range of environments, as it would result from harmonic modulations.

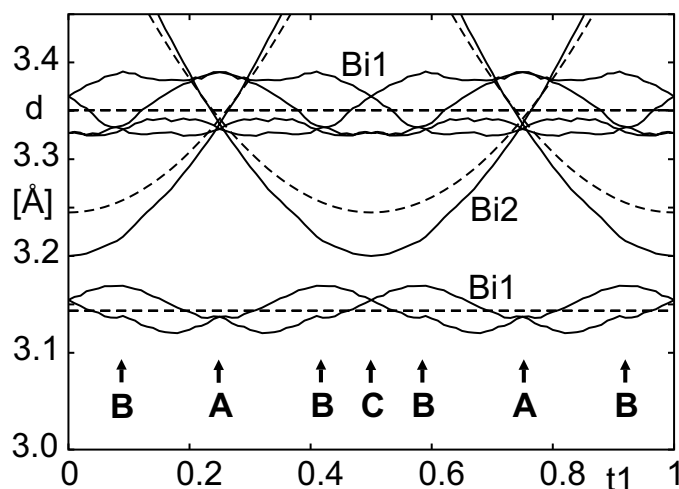


Figure 6.5: Distances between Bi1 and the neighboring atoms as a function of the fourth superspace coordinate. Full lines indicate the distances derived from  $\rho^{MEM}(\vec{x}_s)$ ; broken lines are distances in the hypothetical basic structure. Points A and B refer to the environments as they are realized in the commensurate approximation. Points A and C represent the positions of the superspace mirror planes.

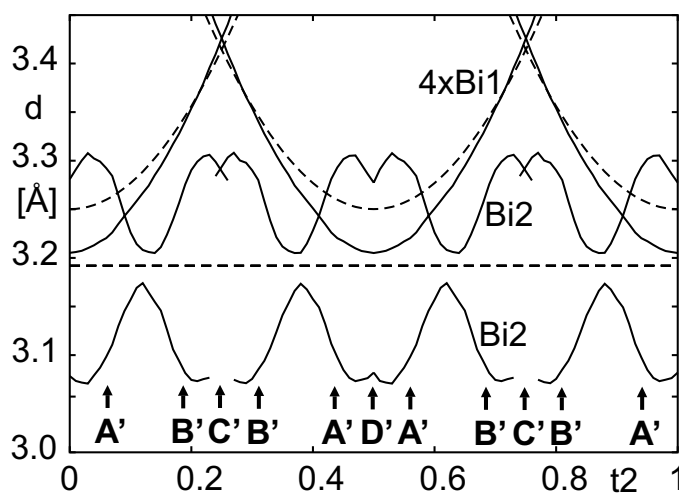


Figure 6.6: Distances between Bi2 and the neighboring atoms as a function of the fourth superspace coordinate. Full lines indicate the distances derived from  $\rho^{MEM}(\vec{x}_s)$ ; broken lines are distances in the hypothetical basic structure. Points A' and B' refer to the environments as they are realized in the commensurate approximation. Points C' and D' represent the positions of the superspace mirror planes.

Noteworthy is that the shortest Bi1–Bi2 contact is shorter in the modulated structure than in the basic structure, indicating increased inter-subsystem bonding as compared to the basic structure. The variations of this distance are mainly influenced by the modulations along  $x$  and  $y$  of the Bi1 atoms, and the driving force for this modulation is probably the generation of chemical bonds between Bi1 and Bi2. This feature is opposite to the observations for other incommensurate composite crystals, for which the modulations are responsible for a smoothed inter-subsystem contact (van Smaalen, 1995).

The coordination number of Bi2 is found to vary between 6 (points  $A'$ ,  $B'$  and  $D'$  in in Fig. 6.6) and 10 (points  $C'$  in Fig. 6.6). The most important feature of the modulation is a quasi-pairing of Bi2 with an intra-dimer distance varying between 3.07 and 3.16 Å and an inter-dimer distance varying between 3.21 and 3.31 Å. The quasi-pairing of the guest is reproduced by the approximate supercell structure. This approximate supercell structure was independently found in recent Density Functional Theory (DFT) calculations (Haussermann et al., 2002). These calculations also found quasi-pairing of the guest to occur in the approximate supercell. These calculations showed that the quasi-pairs form due to chemical bonding between the two atoms of the pairs.

We believe that the pairing is responsible for the incommensurate nature of the structure of Bi-III. First it is noticed that incommensurate composite structures can only be stable, if the most important interactions occur within the subsystems. This is the situation for the structure of Bi-III, as follows from the observation, that the shortest Bi–Bi contacts are between pairs of guest atoms (Fig. 6.5) and between pairs of host atoms (Fig. 6.6). The lattice parameters  $a$ ,  $b$  and  $c_h$  are determined by the strong bonds within the host, while the lattice parameter  $c_g$  is determined by the strong bonds along the chains of guest atoms. On the other hand, if the host-guest interactions would have been sufficiently strong, then the guest atoms would have adapted their positions to the host and the structure would have been periodic. For the observed composite-type structure the host–guest interactions are responsible for the incommensurate modulations of the atoms.

The origin of the incommensuration can be revealed by comparison of the true structure with the approximate supercell (Section 6.3.3). The supercell contains four crystallographically independent Bi atoms, that have coordinations approximately corresponding to the coordinations in the points  $A$ ,  $B$ ,  $A'$  and  $B'$  of the incommensurate structure (Figs. 6.5 and 6.6). The supercell thus represents a very good approximation to the incommensurate structure. However, both the supercell approximation refined against the experimental data and the DFT calculations (Haussermann et al., 2002) have smaller guest-guest distances than are found in the incommensurate structure. Apparently this compressed state is less stable than the true incommensurate structure. The average Bi–Bi distance along the chains in the guest is equal to  $c_g = 3.195$  Å. In the supercell this average dis-

tance is reduced towards 3.151 Å and 3.185 Å for the refined and DFT structures, respectively. This distance is longer than the shortest distances within the host and it is almost equal to the shortest host–guest distances. Therefore it does not provide an incentive to form an incommensurate composite structure. However, Bi–Bi quasi-pairs are present in the high-pressure structure. The average bonding distance in the incommensurate structure is 3.12 Å, while the average inter-pair distance is 3.26 Å. We noted that the actual ranges of distances in the incommensurate structure critically depend on the fine structure of the modulation function, that could not be determined with high accuracy (Section 6.3.2 and Fig. 6.3). But, independently of the accuracy, the Bi–Bi distance within the pairs is the shortest distance in the structure. Apparently, further shortening of this distance, that would be necessary to form the commensurate structure, cannot be tolerated and the structure is stabilized by an expansion of the guest towards the observed basic structure lattice parameter  $c_g$ .

Thus the bond alternation in the chains comprising the guest is responsible for an average  $c_g$  that is slightly longer than  $\frac{3}{4} \times c_h$ , and this effect stabilizes the incommensurate composite structure of Bi-III.

In the hypothetical supercell precisely 50% of the guest–guest nearest neighbor distances would be shorter than average, and all atoms of the guest participate in exactly one quasi-pair. In the incommensurate composite structure the fraction of short guest–guest distances depends on the incommensurability parameter. For  $\gamma = 1.309$  it is obtained as 48.7%. Accordingly, a fraction of 0.973 of the guest atoms are part of a quasi-pair. This leads to a disruption of the sequence of pairs, and the occasional presence of an isolated Bi atom in the guest (points  $C'$  in Fig. 6.6).

The formation of quasi-pairs in the guest competes with the bonding between the host and the guest. For Bi2 that are closest to the Bi1 atoms, the modulation of Bi2 along  $z$  is perpendicular to the directions of the Bi1–Bi2 bonds and it hardly affects their lengths (points  $D'$  in Fig. 6.6). Accordingly the Bi2 atoms around points  $D'$  have the largest shifts, while a minimum value of the shift is found for Bi2 atoms in between the squares of Bi1 atoms (points  $C'$  in Fig. 6.6). Both the inter-subsystem bonding and the formation of quasi-pairs appear to be important effects in this structure, and their competition is responsible for the complicated shape of the modulation of Bi2. Unfortunately, this part of the modulation is the least accurate part of the present analysis. Although we do believe that deviations from the simple saw-tooth shape are present, the deviations from this shape, as found in the present analysis, are not necessarily accurate. The variations of the distances within the quasi-pairs therefore should not be given a too detailed interpretation. (Notice that a simple saw-tooth function would lead to a constant distance within the quasi-pairs.)

## 6.6 Conclusions

The incommensurately modulated structure of Bi-III at  $p = 5.5$  GPa has been determined by a combination of structure refinements and the application of the MEM. The MEM has been found to be an indispensable tool to recover the true shapes of the modulation functions. Although the MEM has led to an improved model for the modulation functions, their shapes are too complicated to capture in a simple parameterized model. Even the best refinement cannot give the true shapes of the modulation functions, that we believe to have been recovered by the MEM. Furthermore, the MEM has provided the crucial information, that led to the idea of modulated temperature tensors.

The basic structure of Bi-III consists of the intergrowth of two periodic subsystems (McMahon et al., 2000). The displacement modulation functions of the two crystallographically independent Bi atoms give rise to structural features beyond the basic structure, that are essential for the understanding of the chemistry of this element. Principal effect is that Bi-III contains quasi-pairs of Bi atoms within the guest. DFT calculations indicated the formation of bonded quasi-pairs within the guest of the approximate supercell (Haussermann et al., 2002), in agreement with the experiment. It has been argued that the pairing is responsible for the incommensurate composite character of this structure, as opposed to the formation of a simple superstructure.



## Chapter 7

# The crystal structure of incommensurate ammonium tetrafluoroberyllate studied by structure refinements and the Maximum Entropy Method

### Abstract

Incommensurately modulated ammonium tetrafluoroberyllate (AFB) occurs in a narrow temperature interval between the paraelectric room-temperature phase with spacegroup  $Pnma$  ( $T_i = 178$  K) and the ferroelectric low temperature phase with space group  $Pna2_1$  ( $T_c = 173$  K). The structure is determined from accurate single-crystal X-ray diffraction data collected with synchrotron radiation at 175 K. The superspace group of the structure is  $Pnma(\alpha 00)0ss$  with  $\alpha=0.47956$ . Both structure refinements and the maximum entropy method lead to the same structure model, involving single harmonic modulation only. The building units of the structure are  $\text{BeF}_4^{2-}$  and  $\text{NH}_4^+$  complex ions with approximately tetrahedral point symmetry. They are relatively rigid and the modulations consist mainly of translations of the tetrahedra and their rotations around a fixed axis. The modulation is related to changes in the network of the hydrogen bonds. The low-temperature superstructure can be described as a commensurately modulated structure with the same superspace symmetry. The first harmonic modulations of the low-temperature and incommensurate phases are related by a scale factor with a value of approximately two. In addition, the low-temperature phase exhibits a second harmonic modulation, that is responsible for shifts along  $\vec{c}$  and the ferroelectricity in this phase. The absence of a second-order modulation in the incommensurate phase shows that the incommensurate phase does not involve a

modulation of local dipole moments, contrary to previous models for the phase transitions in AFB (Iizumi & Gesi, 1977).

## 7.1 Introduction

Ammonium tetrafluoroberyllate (AFB) is centrosymmetric with space group  $Pnma$  at room temperature. It undergoes two phase transitions at lower temperatures. After the first transition at  $T_i=182$  K (Strukov et al., 1973; Makita & Yuiko, 1974) the structure becomes incommensurate with the modulation wavevector close to  $0.5\bar{a}^*$  (Iizumi & Gesi, 1977). The second phase transition at  $T_c=175$ K leads to a non-centrosymmetric ferroelectric phase (Pepinsky & Jona, 1957). The crystal structures of the paraelectric and ferroelectric phases have been studied by X-ray diffraction (Onodera & Shiozaki, 1979; Garg & Srivastava, 1979) and neutron diffraction (Srivastava et al., 1999). O'Reilly et al. (1967) and Onodera & Shiozaki (1979) suggest that one of the ammonium ions is orientationally disordered in the paraelectric phase. O'Reilly et al. (1967) propose that the phase transition is of the order-disorder type. However, the structures by Garg & Srivastava (1979) and the most recent work by Srivastava et al. (1999) do not indicate any disorder in the room temperature structure. These authors conclude the phase transition is a result of changes in the hydrogen bonding scheme.

Iizumi & Gesi (1977) have proposed a model of the phase transitions similar to that proposed for potassium selenate (Iizumi et al., 1977). In this model, the spontaneous polarization would already be present in the modulated phase on a microscopic scale, but the incommensurateness of the modulation would cause the average spontaneous polarization to be zero. The incommensurate to commensurate phase transition would then correspond to ordering of the directions of the microscopic polarizations, resulting in a macroscopic spontaneous polarization.

None of the previous works have studied the crystal structure of the intermediate, incommensurate phase. Knowledge of the structure of this phase can give additional insight into the mechanism of the phase transitions in AFB and into the origin of the ferroelectricity of the low temperature phase. In particular, we will show that the model by Iizumi & Gesi (1977) is not correct, and that the microscopic polarizations are zero in the incommensurate phase within the experimental resolution.

Single-crystal diffraction data were collected with synchrotron radiation. The structural model was found by refinements in superspace. The structure was further studied by means of the Maximum Entropy Method (MEM). The Maximum Entropy Method (MEM) is a general tool for a model-free reconstructions of positive additive distributions. One of many applications in crystallography is a reconstruction of the electron density from phased structure factors

(Gilmore, 1996). The maximum entropy formalism can be extended to superspace (Steurer, 1991; van Smaalen et al., 2003). The MEM in superspace can give a non-parametric estimate of the shapes of the modulation functions. Thus, the MEM can be used to either independently confirm the refined model or to find a shape of modulation functions that differ from the parametrized model (van Smaalen et al., 2003; Chapter 6).

## 7.2 Experimental

Crystals of AFB were grown by slow evaporation at 5°C from an aqueous solution of a stoichiometric mixture of  $\text{NH}_4\text{F}$  (ACROS, ACS-Reagenz, purity  $\geq 98\%$ ) and  $\text{BeF}_2$  (Alfa Aesar, 99.9% purity of the metals basis). Several crystals were tested on a Nonius Mach3 diffractometer with a rotating anode generator and  $\text{MoK}\alpha$  radiation. A thick plate of dimensions  $0.20 \times 0.13 \times 0.08 \text{ mm}^3$  was selected for the data collection. The diffraction data were collected on a Huber four-circle diffractometer at beamline D3 at Hasylab, DESY, Hamburg. The beam was monochromated by a Si(111) double-crystal monochromator. The wavelength was set to 0.7100 Å. An Oxford Cryojet was used to cool the sample by a cold nitrogen gas flow. Incommensurate satellite reflections were observed in a temperature range between 173K and 178K; the data were collected at 175K. Three standard reflections were measured every two hours as a check of the stability of the experimental setup. Experimental details are given in Table 7.1.

The modulation wavevector was determined from the positions of 32 satellites. The value  $q = 0.49756(4) \bar{a}^*$  is very close to  $1/2$ . Thus, reflections of the type  $hklm$  are very close to reflections  $(h \pm 1)kl(m \mp 2)$ . This can result in overlaps of these reflections in the  $\omega$  scans. The value of the  $\psi$ -angle (rotation of the crystal around the scattering vector) was therefore optimized so, that the distance between the positions of the reflections in the  $\omega$ -scans was maximal. Even with this procedure the occurrence of the two neighboring reflections in one scan could not always be avoided, but the distances between the peaks became large enough to allow intensities of the individual reflections to be determined.

The critical problem in the determination of the integrated intensities was the determination of the background. The standard procedures for background determination could not be used due to the presence of more than one peak in some scans. Therefore, the following procedure was used. Every profile was first smoothed by calculating a thirteen-point sliding average. Then a least-squares line was fitted to every 16 points of the smoothed profile. As a result, a smooth first derivative of the scan profile was obtained. Starting from the expected peak position, the derivative was scanned to the left. The first negative point, that was not followed by any significantly positive point, was considered to be the border of the peak area. On the right side, the procedure was repeated symmetrically.

Table 7.1: Experimental data

Temperature (K)	175
Chemical formula	$(\text{NH}_4)_2\text{BeF}_4$
Chemical formula weight	121.08
Superspace group	$Pnma(\alpha 00)0ss$
q-vector	$0.47956(4) \vec{a}^*$
Lattice parameters $a, b, c$ (Å)	7.5284(14), 5.8848(11), 10.436(3)
Z	4
Crystal form	thick plate
Crystal size ( $\text{mm}^3$ )	$0.20 \times 0.13 \times 0.08$
Crystal colour	colourless, transparent
Radiation type	Synchrotron
Wavelength (Å)	0.7100
Absorption coefficient ( $\text{mm}^{-1}$ )	0.215
Diffractometer	Huber four-circle
Detector	NaI scintillation counter
Method of measurement	$\omega$ -scans
Scan width:	
$0 < \frac{\sin(\theta)}{\lambda} < 0.45$ (deg.)	0.700
$0.45 < \frac{\sin(\theta)}{\lambda} < 0.60$ (deg.)	0.550
$0.60 < \frac{\sin(\theta)}{\lambda} < 0.89$ (deg.)	0.500
Step width (deg.)	0.005
$(2\theta)_{max}$ (deg.)	78.4
Absorption correction	not performed
No. of measured refl.	4109
No of independent refl.	3969
No. of observed refl. (all/indep.)	2321/2260
Criterion for observed refl.	$I > 3\sigma(I)$
Range of $h, k, l, m$	$-13 \rightarrow h \rightarrow 0$ $0 \rightarrow k \rightarrow 10$ $0 \rightarrow l \rightarrow 18$ $-1 \rightarrow m \rightarrow 1$
No. of standard reflections	3
Frequency of standard reflections	every 2 hours
Refinement on	$F$
Weighting scheme	$(\sigma^2(F) + (0.006F)^2)^{-1}$
$R_{obs}/R_{all}/wR_{obs}/wR_{all}$ (%)	
all reflections:	3.41/6.22/3.84/3.99
main reflections:	2.76/3.16/3.66/3.68
1 <sup>st</sup> order satellites	6.62/17.91/5.43/6.46
Goodness of Fit (obs/all)	2.59/1.99
No. of parameters	175
Extinction correction	Isotropic type I (Becker & Coppens, 1974)
Extinction coefficient	0.05(3)
Source of atomic scattering factors	International Tables for Crystallography, Vol. C

The peak area was determined for each peak in the profile and the points lying outside the peak areas were considered to be the background points. At least ten points were always assigned to background at each side of the peak. The parameters of the method were selected empirically to produce the best results. In the case of present data the method proved to be very robust and to produce reliable estimates of the background.

The raw counts were corrected for the dead-time of the detector, the integrated intensities were corrected for the LP effect and for variation of the intensity of the primary beam. The absorption correction was not applied because of the very small absorption coefficient ( $\mu=0.215 \text{ mm}^{-1}$ ).

The classes of reflections ( $0kl0$ ) with  $k+l=2n+1$ , ( $hklm$ ) with  $h+m=2n+1$ , and ( $h0lm$ ) with  $m=2n+1$  were systematically extinct. No other extinction rule was observed. The unique superspace group corresponding to these extinction rules is  $Pnma(\alpha 00)0ss$ .

Second-order satellites ( $m=\pm 2$ ) were not observed in preliminary measurements. Therefore, these satellites were not measured during the data collection. However, due to the almost commensurate value of the q-vector the second-order satellites occur close to the main reflections. Analysis of the collected dataset showed, that profiles of 1131 main reflections (out of 1460) contained positions of the second-order satellites. All these 1131 profiles were visually checked and no peak was observed at the positions of the second-order satellite reflections.

### 7.3 Structure refinements

The structure was refined using the superspace approach (de Wolff et al., 1981; van Smaalen, 1995). All refinements were performed using the computer program JANA2000 (Petříček & Dušek, 2000). The coordinates of the room temperature structure (Srivastava et al., 1999) were used as a starting point for the refinement of the basic structure. The positional parameters of all atoms were refined together with isotropic temperature parameters of hydrogen atoms and anisotropic harmonic temperature parameters of all other atoms. The fit to main reflections converged to  $R_{main}(\text{obs})=4.25\%$ . In the next step, the modulation was introduced. The displacive modulations in the directions  $i = 1, 2, 3$  were described by Fourier series:

$$u_i(\bar{x}_{s4}) = \sum_{n=1}^{\infty} A_i^n \sin(2\pi n \bar{x}_{s4}) + B_i^n \cos(2\pi n \bar{x}_{s4}) \quad (7.1)$$

Functions with  $n = 1$  (first-order harmonic modulation) were refined for all atoms, starting from arbitrary but small values. The refinement with 97 parameters converged to  $R_{main}(\text{obs})=4.22\%$  and  $R_{sat}(\text{obs})=13.13\%$ . The difference Fourier maps showed significant structure around the positions of the fluorine atoms (Fig. 7.1a).

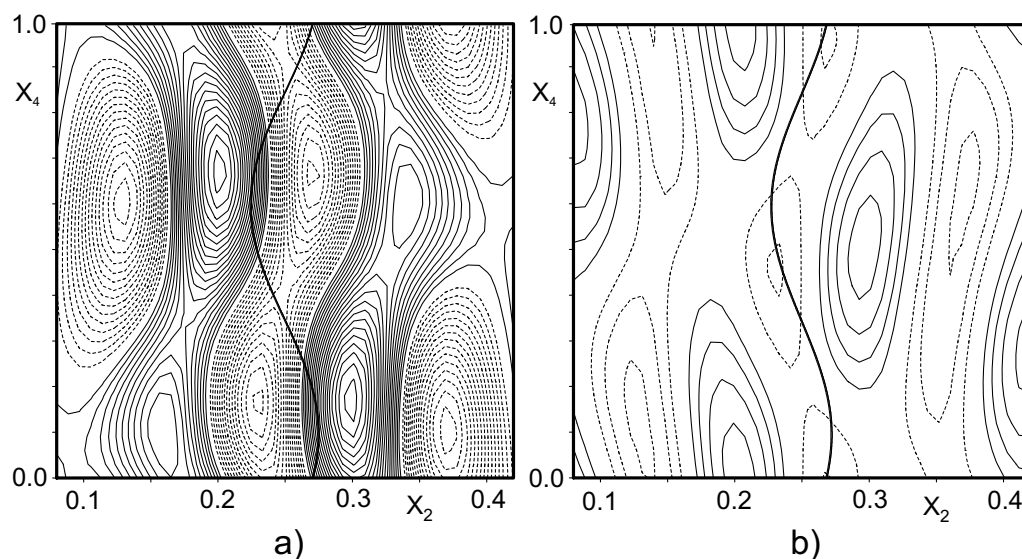


Figure 7.1:  $x_2 - x_4$  sections of the difference Fourier map at the position of the F(2) atom. a) without modulated ADP,  $\Delta\rho_{min} = -0.94\text{e}/\text{\AA}^3$ ,  $\Delta\rho_{max} = 0.90\text{e}/\text{\AA}^3$ . b) with modulated ADP,  $\Delta\rho_{min} = -0.18\text{e}/\text{\AA}^3$ ,  $\Delta\rho_{max} = 0.23\text{e}/\text{\AA}^3$ . Contours at  $0.05\text{e}/\text{\AA}^3$ , positive contours solid, negative contours dashed, the zero contour omitted. The thick line corresponds to the refined position of the F(2) atom.

It turned out, that the fit can be significantly improved by introducing anharmonic displacement parameters (ADP) of the 3<sup>rd</sup> order (Kuks, 1992) for the fluorine atoms as well as their first-order harmonic modulation. The R-values dropped to  $R_{main}(\text{obs}) = 2.76\%$  and  $R_{sat}(\text{obs}) = 6.62\%$  after introduction of the modulated ADP. This decrease is significant, although the number of refinable parameters increased to 175. The maxima in the difference electron density of all fluorine atoms decreased by a factor larger than three (Fig. 7.1b). There is no significant negative region of the probability density function at any of the three atoms. Moreover, the  $\text{BeF}_4$  tetrahedron becomes more regular in comparison with the refinement without ADPs. All these observations support the conclusion, that the ADP parameters are the appropriate way to describe the structure. The positional parameters of the basic structure are listed in Table 7.2; the parameters of the modulation functions are listed in Table 7.3.

As mentioned in Section 7.2, we did not observe any second-order satellites. This indicates that the harmonic modulation of second order is very weak or absent. Indeed, the introduction of the second-order harmonic modulation did not improve the fit and did not lead to significant amplitudes of the second-order modulation functions.

Table 7.2: Basic structure coordinates of the incommensurate structure corresponding to the final refined model.

	x	y	z
Be	0.25141(8)	0.25	0.41847(6)
F(1)	0.05442(9)	0.25	0.38015(8)
F(2)	0.27030(10)	0.25	0.56419(6)
F(3)	0.33820(7)	0.03489(9)	0.36575(5)
N(1)	0.18709(6)	0.25	0.09990(4)
N(2)	0.45778(6)	0.25	0.80326(4)
H(11)	0.3059(12)	0.25	0.1228(10)
H(12)	0.1075(16)	0.25	0.1586(12)
H(13)	0.1718(10)	0.1298(15)	0.0498(8)
H(21)	0.4876(13)	0.25	0.7213(10)
H(22)	0.5606(18)	0.25	0.8468(13)
H(23)	0.3946(12)	0.1227(17)	0.8194(8)

Table 7.3: Modulation functions of the displacive modulation. For definition see Eq. 7.1. Only first-order harmonic modulation functions were refined. Amplitudes are given in Å.

	$A_x^1$	$B_x^1$	$A_y^1$	$B_y^1$	$A_z^1$	$B_z^1$
Be	0	0	-0.0143(13)	0.0085(12)	0	0
F(1)	0	0	-0.0197(13)	-0.0829(12)	0	0
F(2)	0	0	0.0736(13)	0.1095(12)	0	0
F(3)	0.0251(9)	0.0243(8)	-0.0348(7)	-0.0071(7)	0.0828(8)	0.0653(9)
N(1)	0	0	-0.0133(9)	0.0254(9)	0	0
N(2)	0	0	0.0338(9)	-0.0067(9)	0	0
H(11)	0	0	-0.033(14)	0.110(14)	0	0
H(12)	0	0	-0.123(17)	0.040(16)	0	0
H(13)	-0.040(12)	0.018(11)	0.093(13)	-0.065(13)	-0.142(12)	0.103(13)
H(21)	0	0	0.029(15)	-0.020(13)	0	0
H(22)	0	0	0.003(19)	-0.125(17)	0	0
H(23)	0.018(13)	-0.128(13)	0.017(14)	0.061(14)	0.004(11)	-0.029(12)

## 7.4 The ferroelectric structure as commensurately modulated structure

The low-temperature phase can be described as a 2-fold superstructure of the room-temperature phase. Alternatively, it can be described in superspace as a commensurately modulated structure with  $q_c = 0.5\vec{a}^*$  and with the same superspace group as the incommensurate phase. For a given superspace group and modulation wavevector, the symmetry and structure of the supercell depend on the section  $t_0$  of superspace (Yamamoto, 1982; van Smaalen, 1995). For  $Pnma(\alpha 00)0ss$  Hogervorst (1986) has listed all possible space groups of the supercell for different values of  $t_0$  and different commensurate modulation wavevectors. The space group  $Pna2_1$  of the 2-fold supercell corresponds to the sections  $t_0 = 1/8 + n/4, n = 0, 1, 2, 3$ . Alternative values of  $n$  correspond to a shift of the phase of the modulation or a shift of the origin of the 3D space group. The proper value of  $t_0$  for the transformation between the LT structure reported by Srivastava et al. (1999) and the superspace model used in this work is  $t_0 = 7/8$ . Using this information, we have derived the modulation amplitudes of the superspace description for the LT structure (Tables 7.4 and 7.5). Both first- and second-order harmonics were necessary to fit the supercell coordinates. Because of the commensurateness of the modulation ( $q_c = 0.5\vec{a}^*$ ), the phase and amplitude of the second-order harmonic are correlated. We have chosen the phases so, that the modulation amplitudes are minimal.

The average N-H bond-length in the LT structure is 1.005 Å, while the presently determined incommensurate structure gives 0.900 Å. This difference is due to the different experimental techniques (neutron vs. X-ray scattering). In order to facilitate the comparison of the two structures, we have modified the positions of the hydrogen atoms in the LT structure in such a way, that the N-H bonds are shorter than the published values by a factor of 0.9.

## 7.5 The Maximum Entropy Method

The superspace electron density of AFB is discretized on a grid of  $128 \times 100 \times 162 \times 32$  pixels. That corresponds to a resolution of approximately 0.06 Å in each real-space direction. The modulation functions are sampled in 32 points, allowing, in principle, the determination of up to eight harmonics. The experimental amplitudes of the structure factors, corrected for anomalous scattering and extinction, were combined with the phases of the best refined model to produce the input for the MEM calculation (Bagautdinov et al., 1998). This input is called “observed data”. For checking purposes, the MEM calculations were performed with the structure factors derived directly from the refined model (“calculated data”). The computer program BAYMEM (van Smaalen et al., 2003) was used for two

Table 7.4: Basic structure coordinates of the superspace description of the low temperature structure, corresponding to the published coordinates of the structure at 163 K (Srivastava et al., 1999) with positions of hydrogen atoms corrected for differences between the neutron and X-ray positions (see text, Section 7.6). The inaccuracies in parentheses are combined inaccuracies of the average positions and modulation functions, because the inaccuracies of the separate parameters cannot be determined from the coordinates of the 3D model.

	x	y	z
Be	0.2517(2)	0.2500(3)	0.4188(4)
F(1)	0.0560(3)	0.2500(7)	0.3769(6)
F(2)	0.2668(3)	0.2500(6)	0.5645(4)
F(3)	0.3397(3)	0.0352(6)	0.3666(5)
N(1)	0.1879(2)	0.2500(3)	0.1006(1)
N(2)	0.4559(2)	0.2500(3)	0.8029(3)
H(11)	0.3034(5)	0.2500(16)	0.1244(10)
H(12)	0.1124(7)	0.2500(15)	0.1665(11)
H(13)	0.1690(5)	0.1278(12)	0.0554(9)
H(21)	0.4816(6)	0.2500(15)	0.7188(8)
H(22)	0.5544(6)	0.2500(15)	0.8512(10)
H(23)	0.3930(6)	0.1281(13)	0.8206(8)

MaxEnt calculations, with different algorithms and different constraints for each dataset (Table 7.6). Convergence was obtained for all four calculations.

The MaxEnt calculations result in optimized superspace electron densities  $\rho_{MEM}$ .  $\rho_{MEM}$  exhibits local maxima in the form of strings parallel to the fourth dimension of superspace at the positions of the atoms (Fig. 7.2). The positions of the atoms as a function of the fourth coordinate have been determined by the computation of the centers of charge around each local maximum for different real-space sections (different values of  $t$ ). The positions of the hydrogen atoms cannot not be determined with this method, because these atoms do not form separate maxima in the electron density. The determination of the hydrogen positions and the investigation of the bonding electron density will be a topic of future research.

The agreement of the modulation functions derived from  $\rho_{MEM}$  with the refined functions of the model is excellent (Fig. 7.3). The differences between the results by the MEM on the observed data and the refined functions are similar to or even smaller than the differences between the results by the MEM on calculated data and the refined functions. All differences in atomic positions are found to be below 10% of the pixel size. Thus, within the accuracy of the MEM calculations, the MEM shows perfect agreement with the refined model and the model is confirmed (van Smaalen et al., 2003). Inspection of  $\rho_{MEM}$  also provides

Table 7.5: Modulation functions of the superspace description of the low temperature structure, corresponding to the published coordinates of the structure at 163K (Srivastava et al., 1999) with positions of hydrogen atoms corrected for differences between the neutron and X-ray positions (see text, Section 7.4). For definition of the symbols see Eq. 7.1. Amplitudes are given in Å.

	$A_x^n$	$B_x^n$	$A_y^n$	$B_y^n$	$A_z^n$	$B_z^n$
$n = 1$						
Be	0	0	-0.0311	0.0212	0	0
F(1)	0	0	-0.0529	-0.1810	0	0
F(2)	0	0	0.1669	0.2074	0	0
F(3)	0.0675	0.0485	-0.0664	0.0018	0.1781	0.1125
N(1)	0	0	-0.0270	0.0546	0	0
N(2)	0	0	0.0670	-0.0047	0	0
H(11)	0	0	-0.0529	0.1974	0	0
H(12)	0	0	-0.2121	0.0993	0	0
H(13)	-0.0531	0.0478	0.1363	-0.0570	-0.2396	0.1625
H(21)	0	0	0.0905	0.0000	0	0
H(22)	0	0	-0.0147	0.2180	0	0
H(23)	0.0971	-0.2177	0.0118	0.1351	-0.0167	-0.0313
$n = 2$						
Be	0.0000	0.0008	0	0	0.0000	-0.0281
F(1)	-0.0061	0.0023	0	0	0.0000	0.0000
F(2)	0.0000	0.0000	0	0	-0.0031	-0.0292
F(3)	-0.0023	-0.0030	0.0029	0.0047	-0.0135	-0.0219
N(1)	0.0008	-0.0023	0	0	0.0063	-0.0156
N(2)	0.0068	0.0015	0	0	-0.0135	-0.0042
H(11)	-0.0053	-0.0144	0	0	0.0042	0.0115
H(12)	-0.0030	0.0023	0	0	0.0063	-0.0052
H(13)	-0.0061	0.0106	-0.0088	0.0153	0.0260	-0.0458
H(21)	0.0652	0.0076	0	0	0.0250	0.0031
H(22)	0.0190	-0.0068	0	0	-0.0479	0.0167
H(23)	-0.0372	-0.0296	0.0270	0.0212	0.0135	0.0104

Table 7.6: Parameters of the MEM calculations. S-S denotes the Sakata-Sato algorithm (Sakata & Sato, 1990), Cambridge denotes the Cambridge algorithm (Skilling & Bryan, 1984).  $F_6$  denotes the type of generalized F-constraint (Palatinus & van Smaalen, 2002), sw4 denotes the static weighting (De Vries et al., 1994) with weighting factor  $w = 1/|\vec{H}|^4$ ,  $|\vec{H}|$  is the length of the diffraction vector.

name of the calculation	calc1	calc2	obs1	obs2
pixel division		$128 \times 128 \times 32 \times 32$		
pixel size [ $\text{\AA}^3$ ]		$0.059 \times 0.059 \times 0.064$		
input data	calculated	calculated	observed	observed
algorithm	S-S	Cambridge	S-S	Cambridge
constraint	$F_6$	sw4	$F_6$	sw4

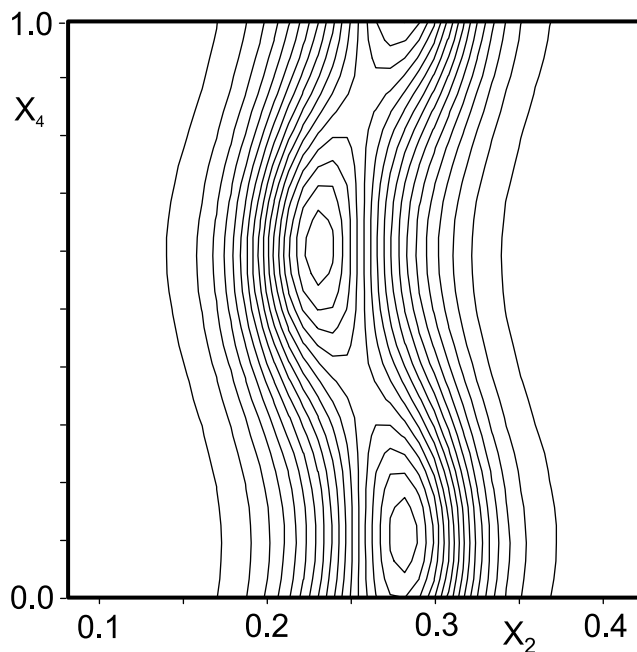


Figure 7.2: A  $x_2$ - $x_4$  section of the MEM electron density at the position of atom F(2) (calculation obs2, Table 7.6). Contours at  $2 \text{ e}/\text{\AA}^3$ . The anharmonicity of the thermal displacement is observable as the asymmetric shape of the sections parallel to  $x_2$ .

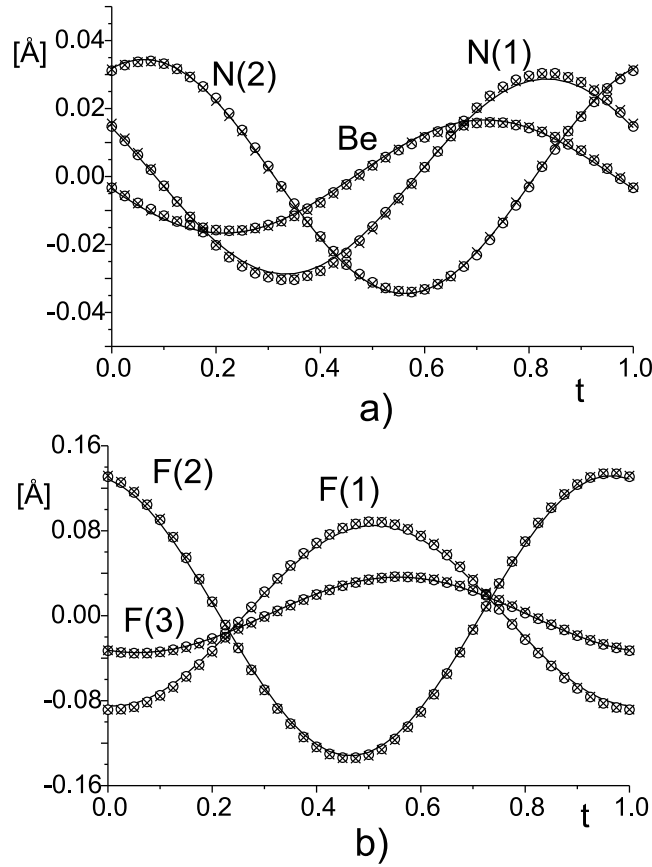


Figure 7.3: Modulation functions  $u_i^y$  of the non-hydrogen atoms. Full lines: refined modulation functions; crosses: modulation functions derived from  $\rho_{MEM}$  of the calculation obs1; circles: modulation functions derived from  $\rho_{MEM}$  of the calculation obs2 (see Table 7.6).

an independent indication of the modulated odd-order anharmonic temperature factors of the fluorine atoms (Fig. 7.2).

A possible displacement along  $\vec{c}$  of the atoms in the special positions is of particular importance, because they are responsible for the spontaneous polarization in the LT phase. In the superspace approach the  $z$ -displacements are described by the second harmonics. Any evidence for the presence of second harmonics in the incommensurate structure has not been found in the MaxEnt calculations. We have tested the sensitivity of the MEM for second harmonic modulations by two additional calculations on simulated data. The structure model of the incommensurate phase (Table 7.3) is combined with second-order harmonic modulation functions, as they were obtained by dividing the second harmonics of the LT structure by a factor of 2 (Table 7.5, Section 7.6.3). The structure factors calculated from this model were used as input in the MEM calculations.

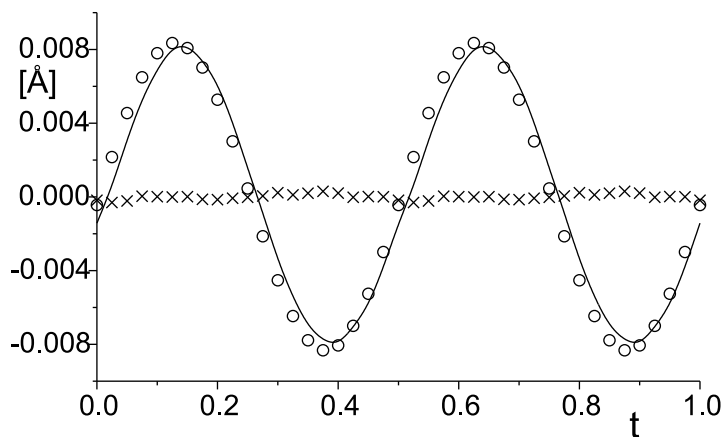


Figure 7.4: Modulation along  $z$  of atom N(1) in the hypothetical incommensurate structure, that includes second-order modulation functions (Section 7.5). Full line: modulation derived from the coordinates of the ferroelectric structure. Circles: MEM reconstruction from simulated data including second-order satellites. Crosses: MEM reconstruction from simulated data with second-order satellites excluded from the input dataset.

The first calculation contained main reflections, first- and second-order satellites, the second calculation only the main reflections and the first-order satellites. The results of the first calculation clearly reproduce the weak second-order modulations along  $x$  and  $z$ . However, the results of the second calculation do not show any such modulations (Fig. 7.4). It can be concluded, that it is not possible to detect the weak second-order modulations, if the corresponding satellites have not been measured and included in the dataset, because the main reflections and first-order satellites do not contain enough information about this modulation.

## 7.6 Discussion

### 7.6.1 Description of the modulated structure

Among the seven structures of AFB published previously (Section 7.1), the work by Srivastava et al. (1999) is the most recent one and it involves the most extensive datasets. The structures by Srivastava et al. (1999) basically confirm earlier refinements of the paraelectric and ferroelectric structures, but they are more accurate. Therefore, we compare the present structure of the incommensurate phase with the structures from Srivastava et al. (1999). If not otherwise stated, the expression “RT structure” refers to the room-temperature structure, while the “LT structure” indicates the two-fold superstructure at 163 K, as they were reported by Srivastava et al. (1999).

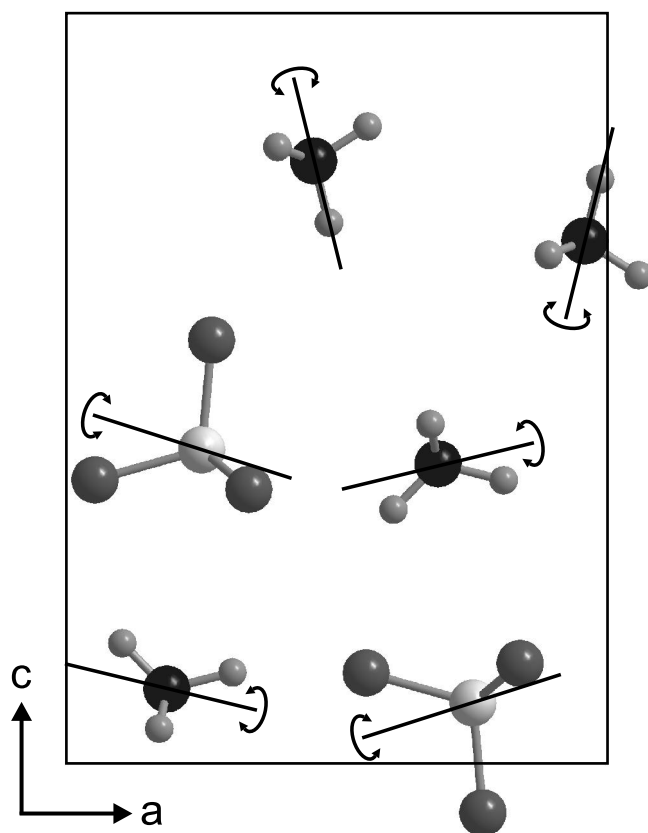


Figure 7.5: View of the basic structure of AFB along the  $b$ -axis with axes of rotation of individual ions. Only ions with central atoms at  $y=0.25$  are shown. Be atoms light gray, N atoms black.

The  $\text{BeF}_4^{2-}$  complex anion has nearly perfect tetrahedral geometry. The small deviations from this symmetry are of equal sizes for the RT and incommensurate structures, while LT structure exhibits slightly larger distortions (Table 7.7). The modulation hardly affects the geometry (Table 7.8). This implies that the modulation of the  $\text{BeF}_4^{2-}$  complex anion can be described as rigid-body translations and rotations in very good approximation.

A quantitative analysis shows that the modulation of  $\text{BeF}_4^{2-}$  can be described as the combined effect of small displacements along  $\vec{b}$  and rotations around an axis in the mirror plane. While the angle of rotation varies with the phase of the modulation, the direction of this axis is fixed and is not affected by the modulation (Table 7.9, Fig. 7.5).

The deviations from tetrahedral symmetry are larger for the  $\text{NH}_4^+$  cations than they are for the  $\text{BeF}_4^{2-}$  complex anions (Table 7.7). However, the variations of  $0.04 \text{ \AA}$  due to the modulations of the individual N-H bond lengths (Table 7.8) are

Table 7.7: Summary of the geometric parameters of the crystallographically independent complex ions in the incommensurate structure, room-temperature structure and low-temperature structure. The latter two structures are taken from Srivastava et al. (1999).  $d_{ave}$ ,  $d_{min}$  and  $d_{max}$  are the average, minimal and maximal distance between the central atom and the ligand atoms of the complex ions;  $\Delta_d = d_{max} - d_{min}$ .  $\alpha$  denotes the angles F-Be-F or H-N-H.

	ferroelectric phase	incommensurate phase	paraelectric phase
temperature	163K	175K	295K
BeF <sub>4</sub>			
$d_{ave}$	1.535	1.5315	1.528
$d_{min}$	1.524	1.5251	1.524
$d_{max}$	1.550	1.5381	1.535
$\Delta_d$	0.026	0.0130	0.011
$\alpha_{ave}$	109.5	109.47	109.5
$\alpha_{min}$	107.5	108.19	108.2
$\alpha_{max}$	112.2	112.15	111.9
$\Delta_\alpha$	4.7	3.96	3.7
N(1)H <sub>4</sub>			
$d_{ave}$	1.007	0.898	0.980
$d_{min}$	0.989	0.857	0.964
$d_{max}$	1.012	0.930	1.004
$\Delta_d$	0.044	0.073	0.040
$\alpha_{ave}$	109.5	109.3	109.5
$\alpha_{min}$	105.2	104.2	107.3
$\alpha_{max}$	115.4	119.5	115.4
$\Delta_\alpha$	10.2	15.3	8.1
N(2)H <sub>4</sub>			
$d_{ave}$	1.003	0.901	0.991
$d_{min}$	0.971	0.884	0.985
$d_{max}$	1.030	0.926	1.000
$\Delta_d$	0.059	0.042	0.015
$\alpha_{ave}$	109.5	109.4	109.4
$\alpha_{min}$	101.1	105.5	104.4
$\alpha_{max}$	118.6	113.1	112.8
$\Delta_\alpha$	17.5	7.7	8.4

Table 7.8: Selected interatomic distances ( $\text{\AA}$ ) and angles (deg.) in the refined structure of the incommensurate phase.

	average	min	max	$\Delta$
Be-F(1)	1.5370(9)	1.5359(9)	1.5381(9)	0.002
Be-F(2)	1.5302(9)	1.5273(9)	1.5331(9)	0.006
Be-F(3)	1.5294(14)	1.5251(14)	1.5334(14)	0.008
N(1)-H(11)	0.928(10)	0.926(9)	0.930(10)	0.004
N(1)-H(12)	0.860(12)	0.857(9)	0.864(12)	0.007
N(1)-H(13)	0.902(16)	0.878(16)	0.919(16)	0.041
N(2)-H(21)	0.884(11)	0.884(11)	0.884(11)	0.000
N(2)-H(22)	0.901(14)	0.898(14)	0.905(14)	0.007
N(2)-H(23)	0.909(16)	0.895(17)	0.926(16)	0.031
F(1)-Be-F(2)	110.52(5)	110.43(5)	110.61(5)	0.2
F(1)-Be-F(3)	108.55(8)	108.19(8)	108.81(8)	0.6
F(2)-Be-F(3)	108.58(8)	108.46(8)	108.73(8)	0.3
F(3)-Be-F(3)	112.06(6)	111.98(6)	112.15(6)	0.2
H(11)-N(1)-H(12)	118.9(11)	118.4(11)	119.5(10)	1.1
H(11)-N(1)-H(13)	106.2(12)	104.2(12)	108.1(12)	3.9
H(12)-N(1)-H(13)	109.4(14)	107.0(14)	111.6(14)	4.6
H(13)-N(1)-H(13)	105.7(14)	105.5(14)	105.8(14)	0.3
H(21)-N(2)-H(22)	105.6(11)	105.5(11)	105.7(11)	0.2
H(21)-N(2)-H(23)	108.2(13)	107.6(12)	108.8(13)	1.2
H(22)-N(2)-H(23)	111.1(14)	109.1(14)	113.1(14)	4.1
H(23)-N(2)-H(23)	112.3(14)	112.1(14)	112.5(24)	0.4

Table 7.9: Characteristics of the rotations of the complex ions. The rotation axes lie in the mirror plane. The orientations of the axes are given as the oriented angle between the rotation axis and the lattice vector  $\vec{a}$ , with positive angles corresponding to a rotation towards the positive direction of lattice vector  $\vec{c}$ .  $\rho(\text{A}(i))$  is the angle, that corresponds to the rotation of the atom  $\text{A}(i)$  around the axis between the two most displaced positions. Atoms  $\text{A}(i)$  correspond to atoms  $\text{F}(i)$ ,  $\text{H}(1i)$  and  $\text{H}(2i)$  for  $\text{BeF}_4$ ,  $\text{N}(1)\text{H}_4$  and  $\text{N}(2)\text{H}_4$  tetrahedron, respectively. The angle  $\rho(\text{H}(21))$  was not determined, because the atom  $\text{H}(21)$  lies almost on the axis of rotation.

	$\text{BeF}_4$		$\text{N}(1)\text{H}_4$		$\text{N}(2)\text{H}_4$	
	inc.	LT	inc.	LT	inc.	LT
position of the axis	$-17.7^\circ$	$-20.9^\circ$	$-13.6^\circ$	$-13.5^\circ$	$-76.1^\circ$	$-82.8^\circ$
$\rho(\text{A}(1))$	$11.3^\circ$	$17.5^\circ$	$22.2^\circ$	$30.3^\circ$	—	—
$\rho(\text{A}(2))$	$10.2^\circ$	$15.2^\circ$	$15.0^\circ$	$28.9^\circ$	$14.8^\circ$	$24.5^\circ$
$\rho(\text{A}(3))$	$10.1^\circ$	$15.5^\circ$	$28.9^\circ$	$34.2^\circ$	$19.3^\circ$	$27.1^\circ$

much smaller than the displacements up to 0.35 Å of the hydrogen atoms due to the modulation. Similarly, the variation of angles H-N-H due to the modulation (up to 4.6°) are much smaller than the rotations of the whole cations (Tables 7.8 and 7.9). The result is that the largest part of the modulations of the  $\text{NH}_4^+$  ions is described by rigid body modulations. The quantitative analysis again shows that the modulation is a combination of small displacements along  $\vec{b}$  and rotations about a single axis in the mirror plane (Table 7.9, Fig. 7.5).

The modulation of the  $\text{NH}_4^+$  cations affects the N(1)-H(13) and N(2)-H(23) bond lengths only, as well as a few bond angles involving either H(13) or H(23). The other bond lengths and angles are almost independent of the modulation (Table 7.8). The variation of deformations in the LT structure is slightly smaller for the N(1) $\text{H}_4^+$  cation, while it is much larger for the N(2) $\text{H}_4^+$  cation. Especially the N(2)-H(21) bond length does not vary in the incommensurate structure, while it results in two distances different by 0.059 Å in the LT structure. These differences are significant with respect to the standard uncertainties of the positions in both structures. We believe that the differences in distortions between the incommensurate and LT structures are related to the development of the spontaneous polarization in the latter phase.

The structure can be considered to consist of two alternating layers stacked along  $\vec{c}$  (Fig. 7.6). Layer I is centered on  $z=0$ , while layer II is centered on  $z=0.5$ . The translations and rotations of the complex ions within the same layer are so correlated, that the neighboring ions have approximately the same deviations from average position and orientation at the same value of  $t$ . The modulations of the ions of the second layer are shifted by about 0.25 in  $t$ . The result is such, that at the places of the structure, where the ions of one layer reach their maximal deviations, the ions of the other layer are in their average positions and *vice versa*. The ions in layer I have the largest deviations approximately at  $t = 0.25$  and  $t = 0.75$ ; the ions in layer II are most displaced around  $t = 0.0$  and  $t = 0.5$ . Because of the commensurateness of the LT structure, each ion adopts only four different orientations. The value  $t_0=0.875$  corresponds to intermediate deviations of the ions in both layers.

As we will discuss below, the dissection of the structure into layers is strongly correlated with the modulations of the hydrogen bonds.

### 7.6.2 Hydrogen bonding scheme

The interactions between the complex anions and cations are governed by ionic interactions and hydrogen bonds. Changes in the pattern of hydrogen bonds are believed to be responsible for the phase transitions in AFB (Onodera & Shiozaki, 1979; Garg & Srivastava, 1979; Srivastava et al., 1999).

The distances H...F as a function of  $t$  are shown in Fig. 7.7. We take 2.6 Å as a limit for the effective bonding interaction between H and F in the present

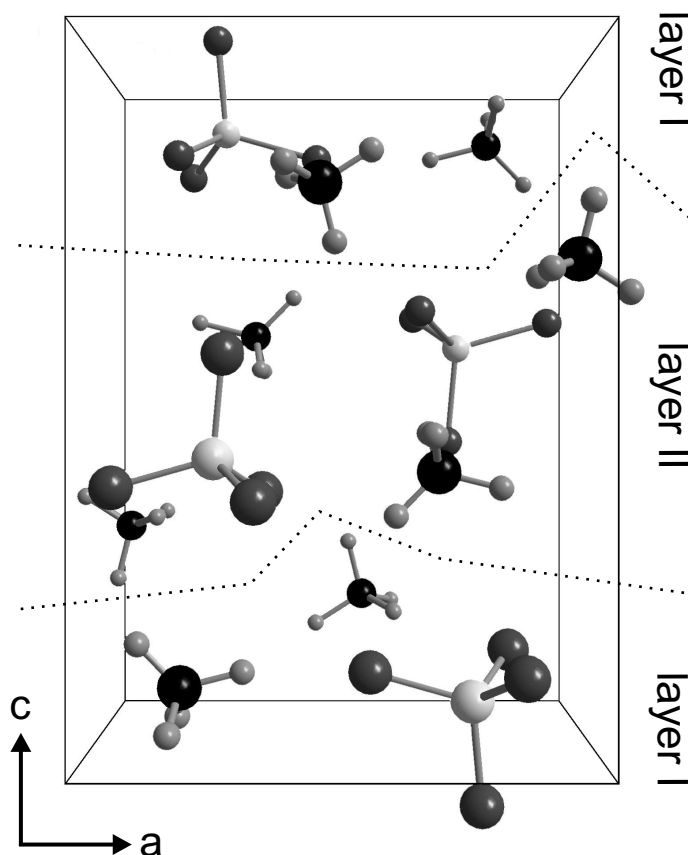


Figure 7.6: Perspective view of the basic structure along the  $b$ -axis. Dotted lines separate the layers with correlated modulations of the ions (Section 7.6). Be atoms are light gray, N atoms black.

structure. There is a gap between the distances below and above this limit. Inclusion of all distances below this limit is necessary and sufficient to fully connect the structural units in a 3D network of hydrogen bonds.

The H...F interactions can be roughly separated into two classes: “stable” and “instable” interactions. The “stable” interactions change only little with the phase of the modulation. They involve the atoms H(11), H(12), H(21) and H(22), that lie in the mirror plane. H(11) and H(22) have only one very short distance to a neighboring F atom. This distance is not influenced by the modulation at all. These distances represent the strongest hydrogen-bond interactions in the structure and they remain almost unchanged in all three phases of AFB. The atoms H(12) and H(21) have three almost equally long distances to fluorine atoms. These distances are considerably longer than the H(11)...F and H(22)...F distances and they can be considered weak, but the simultaneous occurrence of three such interactions in different directions stabilizes the position of the

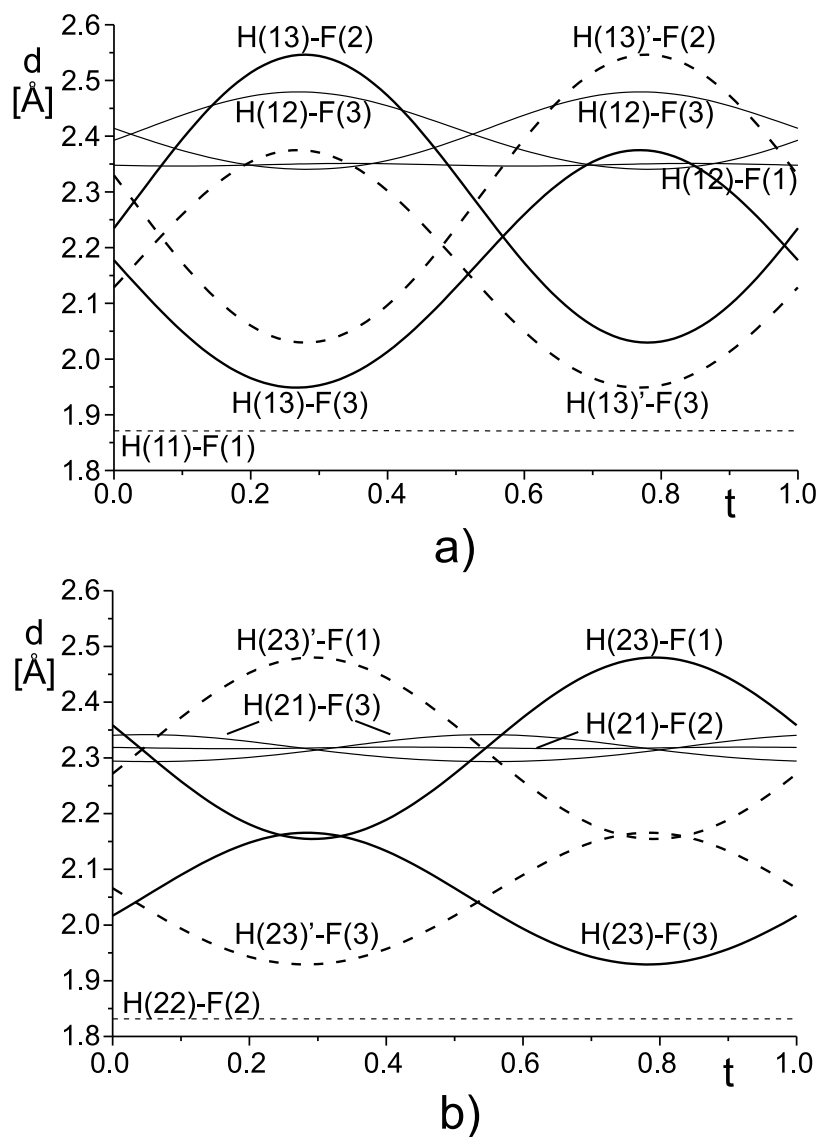


Figure 7.7: H...F distances shorter than 2.6 Å as a function of  $t$ . a) hydrogen atoms of the  $N(1)H_4^+$  ion, b) hydrogen atoms of the  $N(2)H_4^+$  ion. All hydrogen atoms belong to layer I. The primed hydrogen atoms have symmetry code  $x_1, 1/2-x_2, x_3, 1/2+x_4$ . Each curve represents distance to different fluorine atom. The symmetry codes of fluorine atoms are omitted for clarity.

hydrogen atoms and is probably responsible for the special behavior of these atoms. Note, that the H(12) atom rotates considerably less around the rotational axis of the N(1)H<sub>4</sub> tetrahedron than the other atoms, and H(21) lies almost exactly in the rotational axis of the N(2)H<sub>4</sub> tetrahedron (Table 7.9).

The “instable” interactions involving atoms H(13) and H(23) are subject to large changes of the H...F distance with the phase of the modulation. The result is that the H(13) and H(23) atoms of one NH<sub>4</sub><sup>+</sup> ion are alternatively bonded to F(2) or F(3) atoms of different BeF<sub>4</sub><sup>2-</sup> anions, depending on the phase of the modulation. The formation of one very short and one very long H...F distance for each of the hydrogen atoms H(13) and H(23) will have lower energy than all distances being of intermediate length, as it is found in the RT structure. The modulation of these bonds thus appears to be the driving force for the phase transition.

All the inter-layer hydrogen bonds belong to the “stable” interactions. The changes in the hydrogen bonding scheme occur only within the layers and the bonds between the layers are not influenced by the modulation.

In the LT structure, only four points from each curve representing the H...F distance are realized. In each “instable” interaction, two of the four points represent the stronger H...F interaction and two the weak or broken interaction. However, no general distance limit can be defined, that separates the stronger and weaker interactions within the modulated distances. The limit 2.1 Å used by Srivastava et al. (1999) yields 13 strong hydrogen bonds involving four crystallographically independent ammonium ions, but these bonds involve both stronger and weaker H...F bonds on the H(23)...F(3) curve, and neglect one of the shorter distances on the H(23)...F(1) curve. Obviously, it is inappropriate to reduce the description of the hydrogen-bond interactions in the LT structure of AFB to a simple categorization of the bonds to strong and weak based only on the distance limit.

### 7.6.3 The ferroelectric phase transition

The superspace description reveals a striking similarity between the incommensurate and the LT structures. The phases of the first harmonic modulation functions in the two structures are almost equal. The amplitudes of these modulation functions in the LT structure are approximately two times larger (Tables 7.3 and 7.5). The LT structure also contains second-order harmonic displacements, that are responsible for the ferroelectricity, as is demonstrated by following argument: All central atoms of the complex ions lie on special positions in superspace mirror planes. Symmetry restricts the first-order harmonic modulations of these atoms to shifts along the y-axis. The vectors representing the dipole moments of the NH<sub>4</sub><sup>+</sup> and BeF<sub>4</sub><sup>2-</sup> complex ions lie also in the mirror planes and they are subject to the same symmetry restrictions. As a consequence, the first-order modulation

cannot change the z-components of the dipole moments of the individual complex ions, nor can it create a z component of the dipole moment by relative shifts of the  $\text{NH}_4^+$  and  $\text{BeF}_4^{2-}$  ions. However, the small spontaneous polarization in the LT structure is along  $\vec{c}$ , because this is the polar axis of the space group of the LT structure. Consequently, second-order harmonic modulations, that include displacements along  $\vec{a}$  and  $\vec{c}$ , are necessary to describe the spontaneous polarization.

Second-order harmonic modulation amplitudes have not been found in the incommensurate structure, although neither the MEM nor the refinements could disprove the possibility of small second-order amplitudes. To analyze this further we have computed the intensities of second-order satellites for a model composed of the modulation functions of the incommensurate structure combined with second-order harmonic modulation functions derived from the LT structure by applying a factor of 0.5 (Table 7.5). The positions of the second-order satellites are close to the main reflections, and they are present in the scans made to measure the intensities of the main reflections. Inspection of all scans did not reveal any observable second-order satellite (Section 7.2), while for some of these reflections they should have been visible, if the second-order harmonic modulations corresponding to the extrapolation from the LT structure would have been present (Fig. 7.8). The absence of any second-order satellites in our experiment implies that the modulation of the incommensurate structure does not contain a second-order harmonic contribution, or at least that these amplitudes are much smaller than in the LT structure.

Any spontaneous polarization of the incommensurate phase is forbidden by the centrosymmetric superspace group. Furthermore, the absence of observable second-order harmonic modulation implies that even the z-components of the local dipole moment of the basic unit cells are very close to zero. This finding is in contradiction with the model proposed by Iizumi et al. (1977) for the phase transition in potassium selenate and applied to AFB by Iizumi & Gesi (1977). These authors propose, that the incommensurate phase contains a modulated local dipole moment, that, at the lock-in transition, orders to form the spontaneous polarization in the commensurate phase. Our analysis of the incommensurate structure indicates that the local dipole moments are extremely small or absent in the modulated structure and that the dipole moment responsible for the observed spontaneous polarization is formed at the lock-in transition.

If it is further considered that the first harmonics are sufficient to stabilize the pattern of hydrogen bonds (Section 7.6.2), we obtain following possibilities of the mechanisms the phase transitions: The transition at  $T_i$  is most probably governed by changes in the hydrogen bonding, in accordance with previous suggestions (Onodera & Shiozaki, 1979; Garg & Srivastava, 1979; Srivastava et al., 1999). The formation of the spontaneous polarization (forbidden in the incommensurate structure) might be the driving force for the transition at  $T_c$ . Alternatively, the rearrangements of the hydrogen bonds might also be responsible for the lock-in

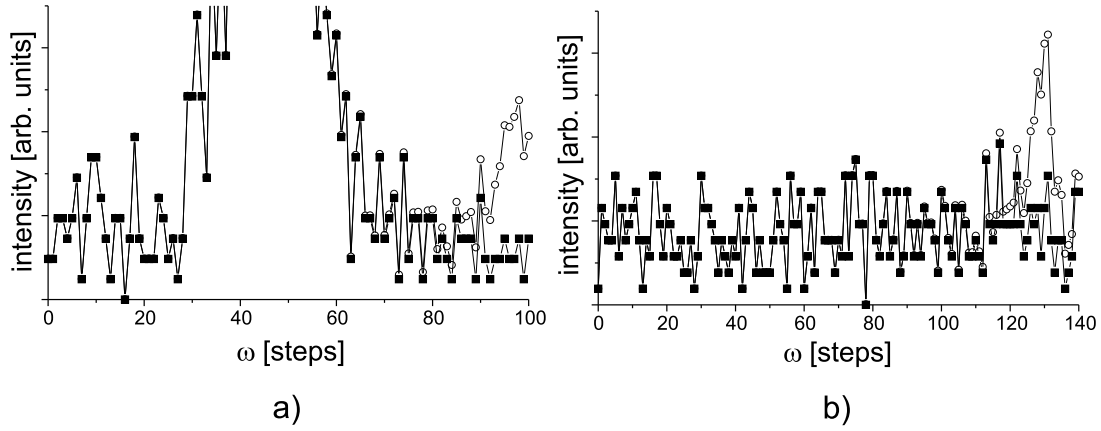


Figure 7.8: Experimental (filled squares) and simulated (open circles) profiles through the positions of the reflections a)  $-5\ 0\ 13\ 0$  and  $-6\ 0\ 13\ 2$  and b)  $-1\ 5\ 0\ 0$  and  $-2\ 5\ 0\ 2$ . Positions of the main reflections are located in the middle of the scans. Simulated profiles are calculated as a sum of the experimental profile and a Lorentzian curve centered at the position of the second-order satellite and with intensities predicted from hypothetical incommensurate structure model including  $2^{\text{nd}}$ -order harmonics (Section 7.6.3). The reflection  $-1\ 5\ 0\ 0$  is systematically extinct. The peaks corresponding to the second-order satellites are clearly visible in the simulated scans.

transition at  $T_c$ , and the spontaneous polarization would be a side-product of this rearrangement. However, the absence of significant local dipole moments in the incommensurate structure and the similarity of the overall pattern of the hydrogen bonding scheme in the incommensurate and LT structures suggest that the spontaneous polarization is important for the stabilization of the LT lock-in phase, thus making the first mechanism the most probable one.

## 7.7 Conclusions

The atomic structure of the incommensurately modulated phase of ammonium tetrafluoroberyllate has been determined at  $T=175$  K. The transition from the paraelectric phase to incommensurate phase is found to be due to rearrangements in the hydrogen bonding scheme. The structure of AFB can be described as an alternate stacking of two layers along  $\vec{c}$ . In the incommensurate structure, H...F distances between the layers remain constant at their values in the RT phase. Within the layers, some of the H...F distances strongly vary between values corresponding to strong and very weak hydrogen bonds. This change is the driving force for the phase transition at  $T_i$ .

A microscopic polarization is found to be correlated with the lock-in transition rather than to be an intrinsic property of the incommensurate phase. This finding

is in variance with the mechanism proposed by Iizumi & Gesi (1977). In this mechanism local dipole moments would already be present in the incommensurate structure. At  $T_c$  these dipoles would rearrange to form the LT structure with a spontaneous polarization. Instead, we do not find evidence for a local polarization in the incommensurate structure.

Two mechanisms can be envisaged for the transition at  $T_c$ . The first is further rearrangements in the hydrogen bonding scheme, with the spontaneous polarization as an “accidental” corollary. The second, more likely mechanism is that the development of the spontaneous polarization is the driving force for the lock-in transition.

Interesting questions pertaining to the mechanisms of the transitions remain. For example, it could be possible, that the second-order harmonic modulation (and consequently local dipole moments) develops in the incommensurate phase close to  $T_i$ , or that the second-order harmonics develop as critical fluctuations. Whether this is true or not can be investigated by high-resolution diffraction experiments towards measuring the temperature dependence of the second-order satellites, as it is possible at the third generation synchrotron sources.



# Chapter 8

## Conclusions

This thesis discusses several aspects of the combination of the Maximum Entropy Method (MEM) for the reconstructions of the electron density with the superspace approach to the description of structures of aperiodic crystals. The MEM in superspace provides a tool for a parameter-free reconstruction of the shapes of the modulation functions of the atoms in the aperiodic structures. It is shown that the MEM in superspace provides a parameter-free reconstruction of the modulation functions with sufficient accuracy. The opportunities offered by the new method as well as its limitations and possible shortcomings are investigated.

The MEM in superspace has been applied to diffraction data of several compounds. The computer program BAYMEM was developed for this purpose. The first version of BAYMEM was produced by Schneider (2001). BAYMEM allows electron densities of the ordinary 3D structures and the superspace electron densities of the aperiodic structures to be reconstructed using the same general principles. The program has been extended by adding features improving its versatility and accuracy of the results. The improvements include:

- Attaching of the set of subroutines MEMSYS5 to BayMEM (Gull & Skilling, 1999*a*; Section 2.2). BAYMEM with MEMSYS provides MEM reconstructions that are closer to the ideal MEM solutions than the Sakata-Sato algorithm (Section 2.2.4). Moreover, the convergence of MEMSYS5 is more reliable and more robust than the convergence of the Sakata-Sato algorithm.
- Implementation of the method of the Generalized F-constraints (Chapter 3) and the static weighting (Section 2.3). These methods suppress the occurrence of large “outliers” in the histograms of the normalized residuals  $|F_{obs} - F_{MEM}|/\sigma(F_{obs})$  and produce MEM densities with less artifacts.
- Implementation of the G-constraints (Section 2.5). G-constraints are constraints on structure-factor amplitudes or on groups of structure-factor amplitudes. Their use allows to include those intensities in the MEM opti-

mization, which can not be measured individually or for which phases are not available.

- Implementation of the method of the Prior-derived F-constraints (Chapter 4). This method produces accurate, virtually artifact-free MEM reconstructions provided a sufficiently informative prior electron density is used.
- Implementation of the two-channel entropy (Papoular et al., 1996). With this method, BayMEM is able to reconstruct densities that have both positive and negative regions, like the difference electron densities  $\rho_{obs} - \rho_{model}$ .

The second major computer program EDMA is a software tool for analysis of the electron densities in arbitrary dimension (Section 2.9; Appendix B). The program analyzes the MEM electron density and extracts quantitative information about the atoms according to Bader's formalism "Atoms in molecules" (Bader, 1990). This includes the positions of the atoms, atomic charges, atomic volumes and dipole moments. By the higher-dimensional electron densities, information provided by EDMA can be used for an accurate determination of the shapes of the atomic modulation functions.

Two new variants of the constraints in the MEM have been developed in order to solve the problems with artifacts in the MEM reconstructions. The two methods are the Generalized F-constraints (Chapter 3) and the Prior-derived F-constraints (Chapter 4). The concept of the Generalized F-constraints is based in the observation, that the standard F-constraint is not sufficiently strong to constrain the histogram of the normalized residuals of the structure factors to the expected Gaussian shape. Higher moments of the distribution of the normalized residuals were therefore used as the constraint in the MEM calculations. With these constraints significantly improved histograms were obtained. The efficiency of the new constraints was tested and justified in a series of calculation on a simulated noisy datasets of the oxalic acid dihydrate. A series of calculations with various resolutions, various amounts of noise and various constraints also allowed to infer some general problems of the MEM reconstructions, namely the artifacts, that occur independently of the type of constraint and independently of the amount of noise in the data. These artifacts have large amplitudes, if a flat prior electron density is used. If a procrystal prior density is used, the artifacts are strongly reduced, but they still assume amplitudes comparable with the bonding effects in the electron density and thus obscure the use of the MEM reconstructions in the accurate charge-density studies. In Chapter 4 the source of these artifacts is identified to be the tendency of the MEM to estimate incorrectly those structure factors, that are not included in the experimental dataset. In Chapter 4, it is shown in that the missing structure factors can successfully be replaced by the structure factors derived from the procrystal electron density,

that is known from the standard structure refinement. If the structure factors derived from the procrystal prior electron density (the Prior-derived F-constraints) are used as additional constraints in the MEM calculation, the result is free of sharp artifacts and the quality of the reconstruction of the electron density is comparable with the results of multipole refinements.

To test the accuracy of the MEM in superspace, the method was applied to the dataset of the misfit-layer composite structure of  $(\text{LaS})_{1.14}\text{NbS}_2$ . For this dataset a satisfactory structure model was known from the standard superspace refinement and the results of the MEM could be compared with this model. MEM calculations were performed on the experimental structure factors and on the structure factors derived from the model. In the latter case, the MEM should reproduce the model. Indeed, it has been shown, that the MEM on the model structure factors reproduces the model modulation functions with accuracy better than 10% of the pixel size of the grid, on which the electron density was sampled. The differences between the MEM on simulated and experimental data were small, thus confirming the appropriateness of the structure model based on modulation functions as a sum of two harmonics. However, differences between the MEM result and the model modulation functions have been found, especially for the modulation functions of La, that illustrate, that the MEM reconstruction is not restricted to the features already present in the model and that it is possible to reconstruct modulation functions that differ from the model.

The structure of the high-pressure phase III of Bi provided a prominent example illustrating the advantages of the MEM in superspace over the standard structure refinements (Chapter 6). Bi-III forms a complex channel composite structure at pressures between 2.8 and 7.7 GPa. The structure has been first solved in  $(3 + d)\text{D}$  space using the standard superspace refinement. The refinement turned out to be difficult, because the large number of parameters necessary to describe the modulation could not be reliably refined due to the poor quality of the data, which was an inevitable consequence of the difficulties with the diffraction experiment at high pressures. The MEM in superspace was applied to the diffraction data of Bi-III to extract more information about the modulation. The modulation functions extracted from the MEM electron density revealed a block-wave-like shape of the modulation function of the Bi atom of the host structure, that indicates shifts of the atom between two stable environments rather than smooth harmonic variation of the position indicated by the modulation function from the standard refinement. Secondly, the MEM modulation function of the Bi atoms in channels allowed to better understand the nature of the most prominent feature of the modulated structure — the occurrence of the pairs of Bi atoms along the channels. The MEM electron densities also showed that it is necessary to describe the thermal motion of the atoms by the 3<sup>rd</sup>-order anharmonic displacement parameters. This structure description is the first accurate determination

of an elemental composite structure from the single-crystal diffraction data.

The ammonium tetrafluoroberyllate  $(\text{NH}_4)_2\text{BeF}_4$  forms an incommensurately modulated structure in a narrow range of temperatures between 173 and 178 K. The intensities of the reflections of this phase have been measured using synchrotron radiation. Only satellites of order 1 were observed. The structure was solved and refined in superspace. The building units of the structure — the  $\text{BeF}_4^{2-}$  and  $\text{NH}_4^+$  complex ions — were found to be relatively rigid. The modulation comprises mainly the relative rotations and shifts of the building units. The structure has been compared to the known two-fold superstructure of  $(\text{NH}_4)_2\text{BeF}_4$ , that is stable below 175K. The low-temperature structure has been described in superspace as a commensurately modulated structure. With aid of this description the close relationship between the two structures has been found. The MEM was applied to the incommensurate structure to test the appropriateness of the refined harmonic structure model. The MEM has shown that the harmonic model is very accurate. The low-temperature structure is ferroelectric. It has been proposed that the shifts responsible for the ferroelectricity are present already in the modulated structure and that they merely order at the phase transition to produce the macroscopic spontaneous polarization. The detailed analysis of the measured dataset and of the structure revealed that this model is not correct and that the shifts responsible for the spontaneous polarization occur at the phase transition from the modulated to the ferroelectric phase.

The principal result of this thesis is that the MEM in superspace was established as a reliable tool for the structure solutions of the modulated structure. Individual chapters present various aspects of the MEM applied to reconstructions of the electron densities in general and of the superspace electron densities in particular. Together they form a framework, that allows to use the MEM in superspace to extract novel information from the diffraction data of both the periodic and aperiodic structures, that cannot be obtained from the structure refinements. The results presented here also point towards possible misinterpretations of the MEM electron densities, and offers procedures to avoid them. Misinterpretations by several authors have lead to criticism of the use of MEM, that prevented the MEM from being much more widely used in contemporary crystallography. I therefore believe that the present results represent not only an important progress in the investigation of the incommensurately modulated structures, but also a contribution to a wider acceptance of the MEM among crystallographers in general.

# Kapitel 9

## Zusammenfassung

Die Maximum Entropie Methode (MEM) ist eine statistische Methode, die zur parameterfreien Bestimmung beliebiger “Bilder” aus unvollständigen Daten angewandt werden kann. Sie kann in der Kristallographie benutzt werden um Elektronendichten im Superraum, die in mehr als drei Dimensionen definiert sind, aus den Röntgenbeugungsdaten aperiodischer Kristalle zu rekonstruieren. Die Aufgabe des Projektes, in dessen Rahmen diese Arbeit entstanden ist, war es die Methode “MEM im Superraum” zu entwickeln und sie zur Lösung realer Probleme zu verwenden. Diese Arbeit behandelt die Weiterentwicklung des Programms BAYMEM zur Anwendung der MEM im Superraum (erste Version Schneider, 2001, sowie die Entwicklung neuer Methoden in der MEM und die Anwendung der MEM zur Bestimmung modulierter Strukturen aus experimentellen Beugungsdaten.

Nach der Einführung in die Kristallographie im Superraum und in die Grundlagen der MEM werden die im Rahmen dieser Arbeit entwickelten Verbesserungen des Programms BAYMEM beschrieben. Das Programmpaket MEMSYS und wurde in das Programm integriert. Dies ermöglicht es, mit dem Cambridge Algorithmus zu arbeiten und dadurch bessere Ergebnisse zu erzielen, als es mit dem Sakata-Sato Algorithmus möglich ist. BAYMEM wurde mit Methoden erweitert, die zur Elimination oder zur Minimierung von Artefakten in den Elektronendichten dienen. Es handelt sich dabei um “Two-channel Entropy” (Zwei-Kanal Entropie; Papoular et al., 1996), “Static Weighting” (Statische Gewichtung; De Vries et al., 1994), “Generalized F-constraints” (Verallgemeinerte F-Constraints) und “Prior-derived F-constraints” (von der Referenzdichte abgeleitete F-Constraints).

Zwei neue Methoden wurden entwickelt, mit denen die Qualität der von der MEM produzierten Elektronendichten wesentlich verbessert wurde. In der Methode “Generalized F-constraints” wird die klassische Zwangsbedingung  $\sum_i (|F_{obs}(\vec{H}_i) - F_{MEM}(\vec{H}_i)|/\sigma(\vec{H}_i))^2$  durch eine Zwangsbedingung mit höherem Exponenten ersetzt. Die klassische Zwangsbedingung führt dazu, dass in der Verteilung von  $|F_{obs}(\vec{H}_i) - F_{MEM}(\vec{H}_i)|/\sigma(\vec{H}_i)$  zu grosse Werte (sog. “Outliers”) auftreten, die

zu verrauschten Elektronendichten führen. Die Anwendung der “Generalized F-constraints” löst das Problem der Outlier und somit werden die Elektronendichten glatter und genauer.

Die Methode “Prior-derived F-constraints” behebt eine andere Art von Fehler in den MEM Elektronendichten. Die MEM extrapoliert Strukturfaktoren, deren Werte nicht experimentell bestimmt worden sind. Steht keine Information über die fehlenden Strukturfaktoren zur Verfügung, dann ist diese Extrapolation die beste Schätzung, die anhand der Daten gemacht werden kann. Wenn aber die Struktur bekannt ist und die MEM nur zur Bestimmung der Bindungselektronendichte benutzt wird, ist es möglich statt der fehlenden experimentellen Strukturfaktoren die berechneten Strukturfaktoren aus dem Strukturmodell zu benutzen. Bei der richtigen Anwendung dieser Methode wird das Hochfrequenzrauschen in den Elektronendichten minimiert und Bindungselektronendichten können mit hoher Genauigkeit bestimmt werden.

Um die Genauigkeit und Auflösung der MEM im Superraum zu ermitteln, wurde die Methode auf Beugungsdaten eines  $(\text{LaS})_{1.14}\text{NbS}_2$  Kompositkristalls angewendet. Ein genaues Strukturmodell für diese Verbindung war bekannt und die Ergebnisse der MEM konnten mit dem Modell verglichen werden. Anhand der simulierten Daten hat sich gezeigt, dass die MEM im Superraum eine Genauigkeit erreichen kann, die besser als ein Zehntel der Pixelgröße ist. Die Anwendung der MEM auf die experimentellen Daten hat das Strukturmodell bestätigt.

Die Kristallstruktur der Hochdruckphase III des Bismuts wurde durch die Kombination aus Kristallstrukturverfeinerung und MEM im Superraum bestimmt. Bismut hat in der Phase III bei einem Druck zwischen 2.8 und 7.7 GPa eine Kompositstruktur mit zwei Teilsystemen. Das erste Teilsystem bildet ein dreidimensionales Gerüst mit Kanälen, in denen die Atome des zweiten Teilsystems in Form atomarer Ketten eingebaut sind. Die Struktur weist eine stark anziehende Wechselwirkung zwischen den Atomen der beiden Teilsysteme auf. Benachbarte Bismutatome haben in den Ketten keine gleichmäßigen Abstände, sondern sie bilden verbundene Paare. Die MEM hat es ermöglicht die Form der Modulationsfunktionen im Detail zu bestimmen, was zum besseren Verständnis der Struktur geführt hat.

Ammonium Tetrafluoroberylat  $(\text{NH}_4)_2\text{BeF}_4$  hat im engen Temperaturbereich zwischen 173 und 178 K eine modulierte Kristallstruktur. Diese Struktur wurde aus Synchrotronbeugungsdaten bestimmt. Die Struktur ist aus  $(\text{BeF}_4)^{2-}$ - und  $(\text{NH}_4)^+$ -Ionen aufgebaut. Durch die Modulation wird die interne Geometrie der  $(\text{BeF}_4)^{2-}$ - und der  $(\text{NH}_4)^+$ -Ionen nur wenig beeinflusst, vielmehr bewirkt sie Verschiebungen und Drehungen der Ionen. Bei Temperaturen unterhalb von 173 K besitzt Ammonium Tetrafluoroberylat eine zweifache Überstruktur. Diese Tieftemperaturstruktur ist ferroelektrisch. Die modulierte Struktur ist dieser Tieftemperaturstruktur sehr ähnlich. Es wurde vermutet (Iizumi & Gesi, 1977), dass die Verschiebungen, die für die spontane Polarisierung verant-

wortlich sind, schon in der modulierten Struktur vorhanden sind. Eine detaillierte Analyse der Struktur und der Messdaten hat jedoch gezeigt, dass dies nicht der Fall ist und dass die strukturellen Verschiebungen, die zur Ferroelektrizität der Tieftemperaturstruktur führen, erst beim Phasenübergang in die Tieftemperaturstruktur auftreten. Die MEM wurde auf diese Struktur angewendet, um eventuelle Abweichungen der Modulationfunktionen von den in der Kristallstrukturverfeinerung ermittelten Formen zu entdecken. Es hat sich gezeigt, dass die Modulation perfekt harmonisch ist und dass sie vom Modell sehr gut beschrieben wird. Durch die Anwendung der MEM auf simulierte Daten wurde nachgewiesen, dass die Vollständigkeit des Datensatzes unbedingt nötig ist um schwache Effekte in der Modulation zu bestimmen.

Diese Arbeit hat bewiesen, dass durch die Anwendung der MEM im Superraum neue Erkenntnisse über modulierte Strukturen gewonnen werden können, die man mit den üblichen Verfeinerungsmethoden nicht erzielen kann. Die Ergebnisse dieser Arbeit haben gezeigt, dass die MEM im Superraum eine zuverlässige Methode zur parameterfreien Bestimmung der Elektronendichten von modulierten Strukturen ist und dass die Analyse der von der MEM berechneten Elektronendichten zum besseren Verständniss modulierter Strukturen führt.



# Appendix A

## BayMEM - A computer program for application of the Maximum Entropy Method in reconstructions of electron densities in arbitrary dimension

### User manual

#### A.1 Introduction

The Maximum Entropy Method (MEM) is a versatile statistical method for reconstruction of images of virtually any type. One of its applications is the reconstruction of the electron density distributions from the X-ray diffraction data. As a special case, combination of the MEM and superspace approach offers new possibilities for studies of the modulation functions of modulated structures.

BAYMEM is a computer program that has been developed for applications of the MEM in charge-density reconstructions of both ordinary and modulated crystal structures.

This manual is intended to provide practical guide to the usage of BAYMEM; it will not focus on the theory of the MEM and on details of different algorithms and types of MEM available in the program. The reader can find the theoretical information in special literature: The basic foundations of the MEM are described in Jaynes (1996). A collection of articles encompassing the wide variety of applications of the MEM in science was compiled in von der Linden et al. (1998). The various applications of the MEM to the crystallographical

problems are described in a review article by Gilmore (1996). The description of the Sakata-Sato algorithm is given in Sakata & Sato (1990). The Cambridge algorithm was first published by Skilling & Bryan (1984). The commercial set of subroutines MEMSYS5, that implements the Cambridge algorithm and that BAYMEM provides interface with, has its own extensive user manual (Gull & Skilling, 1999*b*). The first version of BAYMEM has been described in a PhD. thesis by Schneider (2001). Further developments of BAYMEM are described in Chapter 2 of this thesis. An article on the theory of MEM in superspace with description of BAYMEM and examples of application is published by van Smaalen et al. (2003).

A variety of methods exist, that can enhance the performance of the MEM. Many of them are available in BAYMEM. Among them is the concept of static weighting (De Vries et al., 1994), the generalized F-constraints (Chapter 3), the two-channel entropy formalism (Papoular et al., 1996), and the prior-derived F-constraints (Chapter 4).

## A.2 Basic operation of BAYMEM

The operation of BAYMEM can be considered to be split into following steps.

- i. Reading the data: The data from the input file is read and checked for consistency. Dynamic arrays for holding the data are allocated. The format of the input file is described in Section A.5.
- ii. Initializing the MEM iteration: Before start of the iteration, three essential steps are necessary. First, the prior density is created or read from an external file. Second, the symmetry of the pixel grid is analyzed and the asymmetric unit is found. And finally, the set of unique reflections given in the input file is expanded into the whole sphere to facilitate Fast Fourier Transform performed later during the iteration.
- iii. The iteration: The heart of the program. More about the iteration process will be described in following subsections. BAYMEM can work with two different MEM algorithms. The Sakata-Sato algorithm (Sakata & Sato, 1990) has been implemented as a part of the code of BAYMEM. The MEMSYS5 set of subroutines, that implements the Cambridge algorithm (Skilling & Bryan, 1984), is commercial and must be purchased separately (Gull & Skilling, 1999*a*). BAYMEM provides interface with the MEMSYS5 package. Issues specific for the two algorithms are discussed in Section A.3.
- iv. Writing the output: After the iteration has been finished, BAYMEM writes out the electron density and other files containing information about the MEM calculation. The output is described in Section A.6.

These four steps are performed automatically by the program. The task of the user is just to prepare the input file.

## A.3 Algorithms

### A.3.1 Sakata-Sato algorithm

The Sakata-Sato algorithm is based on an approximate solution of the MEM equation (Sakata & Sato, 1990; Kumazawa et al., 1995; Section 1.2.3). The crucial point in the performance of the algorithm is selection of the value of the Lagrange multiplier  $\lambda$ . In the zeroth-order single-pixel approximation used in the Sakata-Sato algorithm the value of  $\lambda$  is not critical for the convergence of the algorithm, unless it is too large. Too large values lead to divergence of the algorithm. On the other hand, too small values of  $\lambda$  only decrease the speed of convergence. Selection of the value of  $\lambda$  is user's responsibility and does not follow from the theory.

BAYMEM offer two modes of handling  $\lambda$ . The first mode is the fixed- $\lambda$  mode. The user selects the value of  $\lambda$  at the beginning of the iteration and the value is fixed during the iteration. If divergence is encountered in this mode, BAYMEM terminates. The second mode is called the automatic  $\lambda$ -control. The starting value of  $\lambda$  is increased by an arbitrary factor  $f_i$  every cycle (currently  $f_i = 1.1$ ). If divergence is encountered,  $\lambda$  is decreased by a factor  $f_d$  (currently  $f_d = 0.75$ ) and the cycle is repeated. At the same time, the factor  $f_i$  is lowered (currently  $f_i^{new} = (f_i^{old} + 1)/2$ ), so that the increments of  $\lambda$  are not so large in following cycles.

In the majority of cases, the automatic  $\lambda$ -control gives the best possible performance of the Sakata-Sato algorithm. However, in some exceptional cases the automatic  $\lambda$ -control fails and divergence occurs, that cannot be avoided by any decreasing of  $\lambda$ . In those cases, the only solution is to turn-off the automatic  $\lambda$ -control and set  $\lambda$  to a fixed value. See description of the keyword `settings` (Section A.5.3) for information on how to select different  $\lambda$ -modes.

The Sakata-Sato algorithm works well in most cases. However, its convergence is not guaranteed. Sometimes, the speed of the convergence becomes so low, that the calculation must be stopped before the final value is reached. If the difference between the current value of the constraint and the desired stopping value is not large, the problem is usually not dramatic, because the electron density changes only very little in the last stages of the iteration. Note also, the some problems with convergence are not due to the algorithm, but due to inconsistencies in the input data. See Section A.8 for description of possible problems.

### A.3.2 MEMSYS5 package

MEMSYS5 package is a general MEM system applicable to any MEM problem, not only crystallographic. The package is commercial and must be purchased separately (Gull & Skilling, 1999a). The interface with MEMSYS5 is provided as a part of BAYMEM. The interface is written so as to avoid modifications to the code of MEMSYS5 package as much as possible. However, changes could not be avoided entirely. These changes have to be made in the source code of the MEMSYS5 package; without them BAYMEM will not work with MEMSYS5 properly. The changes are listed here. The line numbers refer to the version 1.2 of the MEMSYS5 package, released on September 6<sup>th</sup>, 1999.

- All declarations of the floating-point numbers should be changed from REAL to DOUBLE PRECISION. This can be done by replacing all occurrences of text 'REAL ' with text 'DOUBLE PRECISION ' (note the ending spaces!) in files memsys5.for, vector.for and memsys.inc.

- file memsys5.for, line 896: replace code

```
IF((METHD1.LT.1).OR.(4.LT.METHD1)) STOP ' Illegal METHOD(1) value'
by code
```

```
IF((METHD1.LT.1).OR.(5.LT.METHD1)) STOP ' Illegal METHOD(1) value'
```

- file memsys5.for, line 3409: Between lines 3409 and 3410:

```
CALL MENT4(ST,DEF, PS,PGRADS,PSUM)
END IF
```

this code must be inserted:

```
ELSEIF (METHD1.EQ.5) THEN
CALL MENT5(ST,DEF, PS,PGRADS,PSUM)
```

- file memsys5.for, subroutine MENT1: Replace the code of the subroutine MENT1 (between lines 3418 and 3440) by this code:

```

SUBROUTINE MENT1(ST,DEF,S,GS,SUM)
* One block of standard entropy
IMPLICIT CHARACTER (A-Z)
DOUBLE PRECISION ST(0:*),DEF,S,GS,SUM
DOUBLE PRECISION ZERO,A,C
PARAMETER (ZERO=0.0D0)
IF (DEF.GT.ZERO) THEN
CALL MFILL(ST,2,DEF)
CALL MMUL(ST,2,4,2)
```

```

        CALL MSUM(ST,2,A)
        CALL MDIV (ST,1,4,2)
        CALL MEXP(ST,2,2)
        CALL MSMUL(ST,2,DEF,2)
ELSE
        CALL MMUL(ST,3,4,2)
        CALL MSUM(ST,2,A)
        CALL MDIV (ST,1,4,2)
        CALL MEXP(ST,2,2)
        CALL MMUL(ST,2,3,2)
ENDIF
CALL MDOT(ST,2,4,SUM)
C=A/SUM
CALL MSMUL(ST,2,C,2)
CALL MDOT(ST,2,1,C)
S=SUM-A-C
CALL MMUL(ST,1,1,1)
CALL MDIV(ST,2,4,2)
CALL MSUM(ST,2,SUM)
CALL MDOT(ST,2,1,GS)
CALL MSQRT(ST,2,1)
CALL MMUL(ST,2,4,2)
END

```

- file memsys5.for, line 3441: Insert code of subroutine MENT5 here:

```

        SUBROUTINE MENT5(ST,DEF,S,GS,SUM)
* One block of standard entropy without normalization
        IMPLICIT CHARACTER (A-Z)
        DOUBLE PRECISION ST(0:*),DEF,S,GS,SUM
        DOUBLE PRECISION ZERO,EPS,A,C
        INTEGER I
        PARAMETER (ZERO=0.0D0,EPS=1.0D-13)
        IF (DEF.GT.ZERO) THEN
            CALL MFILL(ST,2,DEF)
            CALL MMUL(ST,2,4,2)
            CALL MSUM(ST,2,A)
            CALL MDIV (ST,1,4,2)
            CALL MEXP(ST,2,2)
            CALL MSMUL(ST,2,DEF,2)
        ELSE
            CALL MMUL(ST,3,4,2)

```

```

        CALL MSUM(ST,2,A)
        CALL MDIV (ST,1,4,2)
        CALL MEXP(ST,2,2)
        CALL MMUL(ST,2,3,2)
    ENDIF
    CALL MDOT(ST,2,4,SUM)
    CALL MDOT(ST,2,1,C)
    S=SUM-A-C
    CALL MMUL(ST,1,1,1)
    CALL MDIV(ST,2,4,2)
    CALL MSUM(ST,2,SUM)
    CALL MDOT(ST,2,1,GS)
    CALL MSQRT(ST,2,1)
    CALL MMUL(ST,2,4,2)
END

```

- file memsys5.for, lines 3661-3663: Replace code

```

5      CALL MSUB(ST,21,25,24)
      CALL MMUL(ST,24,22,24)
      CALL MDOT(ST,24,24,PLHOOD)

```

with code

```

5      CALL MSUB(ST,21,25,24)
      CALL MMUL(ST,24,22,24)
      CALL MMUL(ST,24,31,28)
      CALL MDOT(ST,28,28,PLHOOD)

```

Following changes are not necessary for proper performance of the program, but they remove some unnecessary operations on the data and thus speed up the operation of the program:

- file vector.for, lines 540-563: the original code between lines 540 and 563:

```

        IF (MORE.EQ.0) THEN
* Initialise and count disc buffers if using dynamic block sizes
        MORE=1
        NBUF=0
        :

```

```

*   held on disc
      CALL VSTACK(1,KCORE)
      IF (ACTION) CALL UFETCH(ST,KCORE,KB(J)+IOFF,LENGTH)
      ENDIF
    ENDIF

```

should be replaced by:

```

      KCORE=KB(J)
      LENGTH=KL(J)

```

- file vector.for, lines 567-589: the original code between lines 567 and 589:

```

* If using dynamic block sizes instead of fixed LBLOCK .....
      IF (MORE.EQ.1) THEN
* Calculate block size, and set up stack
      LBLOCK=KL(J)
      IF (NBUF.GT.0) THEN
          LBLOCK=MIN(LBLOCK,LWORK/NBUF)
          :
          :
*   if held on disc
          IF (ACTION) CALL USTORE(ST,KCORE,KB(J)+IOFF,LENGTH)
          CALL VSTACK(-1,KCORE)
          ENDIF
      ENDIF
* Any more elements?
      IF (IOFF+LENGTH.GE.KL(J)) MORE=0

```

should be completely removed.

Operation of MEMSYS5 is extensively described in the MEMSYS5 user manual (Gull & Skilling, 1999b). The Cambridge algorithm guarantees convergence to the proper MaxEnt solution under normal circumstances. If the computation with Cambridge algorithm does not converge, the reason is usually in the input data and the data should be checked for errors (Section A.8). However, the MEMSYS5 set of subroutines is complex and relatively rigid, and therefore difficult to adapt to non-standard problems. For this reason, some variations of the constraints are not implemented in BAYMEM with the Cambridge algorithm. This concerns the G-constraints (Section 2.5) and the generalized F-constraints (Chapter 3). These constraints work only with the Sakata-Sato algorithm.

**Important:** MEMSYS5, version 1.2, does not have a built-in option for normalization of the MEM distribution, although this option is described in the user manual. Therefore, the normalization must be achieved by adding the F(000) structure factor to the dataset with value equal to the number of electron given in the input file. For details on handling the F(000) see description of the keyword `fbegin - endf` (Section A.5.3).

## A.4 Technical details

### A.4.1 Programming language and system requirements

The program BAYMEM is written in the programming language Fortran 90. It has been compiled and tested on two computers:

- Compaq AlphaStation ES40 with 500MHz 64-bit Alpha EV6 RISC processor and with Compaq Fortran Compiler V5.5-1877-48BBF
- Silicon Graphics Fuel with 500MHz IP35 MIPS R14000 processor and with MIPSPro Fortran compiler V7.4

The program obeys Fortran 90 standards and should therefore be compilable with any F90 compiler. The program does not have any special system requirements. It does not use graphical interface and the input can be edited with any plain text editor such as `vi`, `nedit` or `emacs`. However, it should be noted that the requirements for the RAM are quite high, in order of GB for large problems.

### A.4.2 Execution

The program is executed with command

```
BayMEM input_filebase [ncycles]
```

where `input_filebase` is the name of the ASCII file containing input parameters (see Sections A.5.2, A.5.3 and A.5.4) without the extension `.BayMEM`. The extension `.BayMEM` is automatically added by the program; every input file must have this extension. If the `input_filebase` is omitted, the program will prompt for it interactively. The optional parameter `ncycles` defines the maximal number of MEM iterations. After BAYMEM performs `ncycles` iterations, it stops regardless of the degree of convergence of the job. If `ncycles` is omitted, the value `MAXCYCLES` from the module `GlobalDefinitions` in file `Variables_mod.f90` is used (currently `MAXCYCLES = 100000`).

## A.5 Specification of input

### A.5.1 Types of input

There are two types of input. The basic input is the ASCII input file: it contains all the necessary parameters of the BAYMEM run. In following sections, the expression “input file” means always the ASCII input file. The second type is a file containing the reference electron density (prior). This input is used only if the keyword `inputdensity` has another value than `flat`. Currently, BAYMEM supports electron density files in three different formats (Section A.6.1). The file with the reference electron density is referred to as a “prior density file” or “prior density” in following text.

### A.5.2 Format of the ASCII input file

The input file is a free-format file based on keywords. Each keyword represents a specific parameter of the MEM calculation and must be given a value.

Multiple spaces anywhere in the file are handled as a single space. If the sign `#` or `!` occurs anywhere in the line, the rest of the line after this sign is treated as comment and not interpreted. Blank lines anywhere in the input file are ignored. The length of the interpreted part of the line is 132 characters, any text exceeding this length is ignored.

### A.5.3 Specification of keywords

There are two basic types of keywords. The first type is followed by one or more values on the same line:

```
keyword value1 [value2 value3...]
```

The second type has the form:

```
initial_keyword  
line 1  
line 2  
...  
final_keyword
```

Each line may contain one or more values.

The name of the keyword of the first type is a single word without spaces. The name of the keyword of the second type is a pair of initial and final word (separated by a hyphen in the following text).

Each value can be a constant of type real, integer or character. The type of the parameters and their allowed values are specified. Alternative values are separated by slashes.

The keywords are either compulsory or optional. The compulsory keywords must be specified for the analysis to proceed. The optional keywords can be omitted. If an optional keyword is omitted, the default value is used. Compulsory keywords are indicated by “compulsory keyword - no default value” in the item “default”.

The item “description” describes the function of the keyword, its influence on the output and relations to other keywords.

#### A.5.3.1 name: 2channel

- value: yes/no
- default: no
- description: Activates or deactivates the two-channel entropy formalism (Papoular et al., 1996). That allows to reconstruct the maps with both positive and negative densities, for example the difference electron densities.

#### A.5.3.2 name: algorithm

- value: S-S/MEMSys [+ optional algorithm-specific settings]
- default: compulsory keyword - no default
- description: This keyword selects one of the two algorithms presently available in BAYMEM. S-S selects the Sakata-Sato algorithm, MemSys selects the Cambridge algorithm implemented in the MEMSYS5 package. Each algorithm has its own specific settings.

For `algorithm MEMSys` the settings are:

**method:** Integer. 4 for the “historical” maximum entropy ( $\chi^2 = N$ ), 1, 2 and 3 for different variants of the “Bayesian” maximum entropy (Gull & Skilling, 1999b). All choices are possible, but only method 4 has been extensively tested and the other methods did not prove to be useful in crystallographic problems.

**NRAND:** Integer. Number of random vectors used in the calculation of conjugate gradient in the MEMSYS5 package. NRAND=1 is safe for the vast majority of cases. For more details see Gull & Skilling (1999b).

**aim:** Real number. The stopping criterion  $aim = C_{final}$ , where  $C$  is the value of constraint. Usually 1.0. Lower values mean closer fit of the MEM density to the experimental structure factors.

**RATE:** Real number. Sets the user-definable factor, that influences the sizes of the steps along the conjugate-gradient vector. For more details see Gull & Skilling (1999b). Usually between 1.0 and 5.0 at the beginning of the iteration. **RATE** can be increased interactively during the iteration (Section A.7.2).

**internal accuracy:** Real number. Defines the internal accuracy in the calculation of the conjugate gradient. The recommended value is 0.05. The precise value is not crucial for the performance of the algorithm. Too small values do not improve the accuracy, but slow down the iteration.

For algorithm S-S the settings are:

**lambda:** Real number. The initial estimate of the Lagrange multiplier  $\lambda$ .  $\lambda$  is always positive. If the parameter lambda is given negative, the absolute value is taken and fixed, e.g. BAYMEM will operate in the fixed- $\lambda$  mode (Section A.3.1). If the string **AUTO** (case sensitive) occurs instead of a number, BAYMEM will estimate the starting value of  $\lambda$  automatically.

**aim:** Real number. The stopping criterion  $aim = C_{final}$ , where  $C$  is the value of constraint. Usually 1.0. Lower values mean closer fit of the MEM density to the experimental structure factors.

The settings after the specification of the algorithm can be omitted. In that case the default settings are used. The defaults are:

```
algorithm S-S ~ algorithm S-S AUTO 1.0
```

```
algorithm MEMSys ~ algorithm MEMSys 4 1 1.0 1.0 0.05
```

#### A.5.3.3 name: cell

- value:  $a b c \alpha \beta \gamma$
- default: compulsory keyword - no default
- description: Lattice parameters of the structure.

#### A.5.3.4 name: centers - endcenters

- value: Each line contains one centering vector.
- default: no centering vectors
- description: Defines the centering vectors of the (super)space group. The dimension of the centering vectors must correspond to the dimension of the structure defined by the keyword **dimension**. The components can be given both as fractions and as fractional number.

**A.5.3.5 name: centro**

- value: yes/no
- default: compulsory keyword - no default
- description: The value **yes** corresponds to a centrosymmetric structure. The value of **centro** must be consistent with the symmetry operators given in keyword **symmetry - endsymmetry!**

**A.5.3.6 name: conorder**

- value: even positive integer
- default: 2
- description: Defines the order of the generalized F-constraint (Chapter-*genf*). The generalized F-constraint of order  $n$  is defined as:

$$C_{F_n} = -1 + \frac{1}{m_n(Gauss)} \frac{1}{N_F} \sum_{i=1}^{N_F} \left( \frac{|F_{obs}(\vec{H}_i) - F_{MEM}(\vec{H}_i)|}{\sigma(\vec{H}_i)} \right)^n \quad (A.1)$$

$m_n(Gauss)$  is the value of the  $n^{th}$  central moment of the Gaussian distribution. The generalized F-constraint is implemented only in the S-S algorithm.  $n = 2$  corresponds to the standard  $\chi^2$ -constraint. If **conorder** other than 2 is combined with the MEMSys algorithm, the program writes out a warning and sets the value to 2.

**A.5.3.7 name: conweight**

- value:  $Hn$  or  $F_n$ ,  $n$  is a number between -50 and 50
- default:  $n = 0 \sim$  no weighting
- description: Static weighting according to De Vries et al. (1994). The F-constraint with the static weighting is defined as:

$$C_w = -1 + \frac{1}{N_F} \sum_{i=1}^{N_F} w(F_{obs}(\vec{H}_i)) \left( \frac{|F_{obs}(\vec{H}_i) - F_{MEM}(\vec{H}_i)|}{\sigma(\vec{H}_i)} \right)^2 \quad (A.2)$$

The weighted G-constraints can be defined analogically. Weighting factor is defined as  $w(F(\vec{H})) = 1/|\vec{H}|^n$  or  $w(F(\vec{H})) = |F(\vec{H})|^n$ , depending on the value of the keyword **conweight**.  $|\vec{H}|$  is the length of the diffraction vector and  $|F(\vec{H})|$  is the amplitude of the structure factor of every reflection. The power  $n$  can be any number, but numbers between 2 and 5 proved to be the most efficient. The weighting on  $|F(\vec{H})|$  is not applicable to G-constraints, because the separate intensities of reflections in one group are not known.

**A.5.3.8 name: correction**

- value: none/normalize/cut/flat/raise
- default: none
- description: The prior density used in BAYMEM must be positive everywhere, with exception of the two-channel entropy method. If the prior density does not fulfil this requirement, BAYMEM offers several possibilities to make the prior density positive everywhere. The meaning of the values is:

none: No correction.

normalize: The density is normalized to the number of electrons given in the input file:  $\rho_i^{corr} = \frac{N_{el}}{\sum \rho_i^{uncorr}} \rho_i^{uncorr}$ .

cut: If the minimum of the density is negative, then all pixels with  $\rho_i < |\rho_{min}|$  are assigned the value of  $|\rho_{min}|$ .

flat: Values less than zero are set to value corresponding to an equally distributed density  $\rho_{eq} = \frac{N_{el}VUC}{N_{pix}}$ .

raise: If the minimum of the density is negative, then the whole density is raised by  $1.5|\rho_{min}|$ .

The charge of the prior density must be equal to the total charge of the resulting  $\rho_{MEM}$ . Therefore, the prior densities obtained by the corrections **cut**, **flat** or **raise** are subsequently normalized to the number of electrons given in the input file.

**A.5.3.9 name: dimension**

- value: positive integer
- default: compulsory keyword - no default
- description: This keyword defines the dimension of the structure. Dimension must be larger or equal to the value of **realdimension**. Apart from this restriction, the dimension is arbitrary, however, for dimensions larger than the parameter MAXDIM in the module Globaldefinitions the parameter MAXDIM must be changed and the program recompiled. The current value of MAXDIM is 8.

**A.5.3.10 name: electrons**

- value: real number
- default: compulsory keyword - no default

- description: Gives the number of electrons in the unit cell. The resulting electron density will be normalized to this number of electrons. If the value  $F(000)$  is given in the list of structure factors (see keyword `fbegin - endf`, it must be equal to the value of `electrons`. Zero or negative value of the number of electrons is possible only with two-channel entropy (see keyword `2channel`).

#### A.5.3.11 name: `expandedlog`

- value: yes/no
- default: no
- description: If the value is yes, the log-file will contain the full list of all symmetry-expanded reflections. If the value is no, only the symmetry independent reflections are listed.

#### A.5.3.12 name: `extra - endextra`

- value: each line contains indices of one reflection with optional expected value of the structure factors of that reflection.
- default: no extra reflection
- description: The maximum entropy method is able to estimate the values of the structure factors that have not been used in the MaxEnt optimization. The estimated values of the structure factors of reflections given in the `extra - endextra` list are written to the output file `jobname.BMout` at the end of the calculation. If an expected value of structure factor is given, this value is also written in the output file and the expected and estimated values can be directly compared.

#### A.5.3.13 name: `fbegin - endf`

- value: each line contains the indices, real and imaginary part of the structure factor and its estimated standard uncertainty of one reflection from the input dataset.
- default: compulsory keyword - no default
- description: This keyword serves for definition of the input data. The format of each line is free, the order is  $\{\text{indices } A \ B \ \sigma(|F|)\}$ . A and B are the real and imaginary components of the structure factor. Number of indices must be consistent with the dimension of the structure defined in keyword `dimension`.  $F(000)$  must be present in the dataset. If  $F(000)$  is present as

the first structure factor in the input data, its value and sigma are read by BAYMEM, otherwise BAYMEM adds this structure factor automatically, and any later occurrence of F(000) will be reported as doubled reflection. The standard deviation of F(000) will be set to one third of the smallest standard uncertainty found in the input data. F(000) is not included in calculation of the starting and final R-values and values of the F-constraint, but it is included in the value of  $\chi^2$  reported by MEMSYS5.

#### A.5.3.14 name: file

- value: a valid filename without extension
- default: The first command-line argument to BAYMEM at start
- description: The user can change the base of all output files generated by BAYMEM. The default base is the base of the input file (filename without the extension .BayMEM).

#### A.5.3.15 name: gbegin - endg

- value: one or more groups of intensities (see keyword `ggroup`)
- default: no G-group
- description: The so called G-groups are groups of two or more reflections, where only sum of their intensities is known. Several such groups can be placed between the keywords `gbegin` and `gend`. Each group starts with the keyword `ggroup`.

#### A.5.3.16 name: ggroup

- value: first line: `ggroup G  $\sigma(G)$` , where  $G$  is the “group amplitude” and  $\sigma(G)$  is the standard uncertainty of  $G$ ; following lines: *ndim* integers representing the indices of reflections in the G-group.
- default: no ggroups
- description: `ggroup` defines one G-group. The “group amplitude” is defined as:

$$G = \sqrt{\sum_{j=1}^{N_g} \left( \frac{m_j}{\sum m_j} |F_j|^2 \right)} \quad (\text{A.3})$$

$N_g$  is the number of reflections in the G-group,  $m_j$  is the multiplicity of the reflection  $j$ ,  $|F_j|$  is the amplitude of the structure factor of reflection  $j$ . Each

line following the line with `ggroup` contains indices of one reflection in the G-group. The format of the whole `ggroup` is:

```
gbegin
# first ggroup ggroup g-amplitude g-sigma
h k l ...
h k l ...
  :
h k l ...
# second ggroup
ggroup g-amplitude g-sigma
  :
endg
```

#### A.5.3.17 name: `initialdensity`

- value: `flat/jana/BMascii/BMbinary`
- default: compulsory keyword - no default
- description: `initialdensity` defines the type of the prior density  $\tau$ . If `initialdensity` is set to `flat`, the prior density is assigned a uniform value of electrons/ $N_{pix}$  ( $N_{pix}$  being the total number of pixels in the unit cell; see keywords `electrons` and `voxel`). Any other `initialdensity` has to be accompanied by specification of the prior density file (see keyword `initialfile`). Formats are: `jana` = single precision .m81 format of the program package JANA2000; `BMascii` = ascii format of BAYMEM, transferable between platforms; `BMbinary` = double precision binary format of BAYMEM, usually non-transferable between different platforms.

#### A.5.3.18 name: `initialfile`

- value: a valid filename shorter or equal in length to 132 characters
- default: compulsory keyword - no default, if `initialdensity` is other than `flat`.
- description: Specifies the file containing the input electron density map. See keyword `initialdensity`.

#### A.5.3.19 name: `memcheck`

- value: positive integer

- default: no memcheck output
- description: The correctness of the MaxEnt solution can be checked by testing the set of equations:

$$\frac{\partial S}{\partial \rho_i^{MEM}} = \lambda \frac{\partial C}{\partial \rho_i^{MEM}} \quad (i = 1, \dots, N_{pix}^{au}) \quad (\text{A.4})$$

or its equivalent in reciprocal space:

$$\frac{\partial S}{\partial F_{MEM}(\vec{H}_j)} = \lambda \frac{\partial C}{\partial F_{MEM}(\vec{H}_j)} \quad (j = 1, \dots, N_F) \quad (\text{A.5})$$

where  $S$  is the entropy of the MEM density and  $C$  is the constraint. If the pairs  $\frac{\partial S}{\partial \rho_i^{MEM}}$  vs.  $\frac{\partial C}{\partial \rho_i^{MEM}}$  or  $\frac{\partial S}{\partial F_j^{MEM}}$  vs.  $\frac{\partial C}{\partial F_j^{MEM}}$  are plotted, they should be aligned on a straight line. The keyword `memcheck` can be used to produce a file `jobname.BMcheck`, that contains list of the pairs  $\frac{\partial S}{\partial \rho_i^{MEM}}, \frac{\partial C}{\partial \rho_i^{MEM}}$  and  $\frac{\partial S}{\partial F_j^{MEM}}, \frac{\partial C}{\partial F_j^{MEM}}$ . This file can be used to plot the the corresponding graphs. The list of every pixel of the asymmetric unit (Eq. A.4) could be extremely long. Therefore, only some pixels are selected. The number of selected pixels is given by the value of the keyword `memcheck`. The pairs corresponding to the equation in reciprocal space (Eq. A.5) are listed completely.

### A.5.3.20 name: outputfile

- value: a valid filename of a non-existing file
- default: `jobname.ext`, where `ext` is a format-specific extension
- description: Specifies the filename of the output electron density. If the keyword is omitted, then the name of the output file is created from the jobbase (see keyword `file`) and a format-specific extension, which is `.asc` for `outputformat BMascii`, `.raw` for `outputformat BMbinary` and `.m81` for `outputformat jana/janap1` (for description of the formats see Section A.6.1). The file must not exist. BAYMEM will never overwrite an existing density file. Instead of that, the output density is written to a file named `bmapXX.ext`, where `XX` is a serial number starting from 00. A warning is written to the logfile `jobname.BMlog`. If all hundred files (`bmap00.ext`–`bmap99.ext`) exist, the program will try to ask the user for the filename on the terminal. If the terminal, which BAYMEM has been started from, does not exist anymore, the program will stop without writing any output density file.

**A.5.3.21 name: outputformat**

- value: jana/janap1/BMascii/BMbinary
- default: compulsory keyword - no default
- description: Supported formats of the output density files are: `jana` and `janap1` = single precision .m81 format of the program package JANA2000; `BMascii` = double precision ascii format of BAYMEM, transferable between platforms; `BMbinary` = double precision binary format of BAYMEM, usually non-transferable between different platforms. The files written with format `jana` contain pixels with coordinates  $0 \dots N_i - 1$  in each direction  $i$ . Format `janap1` contains all pixels with coordinates  $0 \dots N_i$  in each direction, e.g. with the redundant border of the unit cell. For more description of the formats of the output density see Section A.6.1.

**A.5.3.22 name: priorsf**

- value: three real numbers, optional positive integer
- default: no adding of prior structure factors
- description: This keyword provides a possibility to include structure factors calculated from the prior density in the input dataset (Chapter 4). The format of the keyword is: `priorsf`  $(\sin(\theta)/\lambda)_{min}$   $(\sin(\theta)/\lambda)_{max}$  sigma [maxindex]. All structure factors with diffraction vectors between  $2(\sin(\theta)/\lambda)_{min}$  and  $2(\sin(\theta)/\lambda)_{max}$ , that are not present in the input data, are calculated from the prior density and added to the dataset as so-called “P-constraints”. These P-constraints behave exactly like the F-constraints in the MEM iteration, but they are not included in the calculation of  $\chi^2$  and therefore do not influence the stopping point of the convergence. The optional parameter `maxindex` tells the program, that only the reflections with the maximal satellite index smaller or equal to the value of `maxindex` will be added to the dataset. Default value of `maxindex` is 0. Currently, `maxindex` works correctly only for ordinary modulated structures and not for composites, because the definition of a satellite reflection is slightly different in the two cases.

**A.5.3.23 name: qvectors - endqvectors**

- value: Each line contains the components of one q-vector. There must be  $dim - rdim$  q-vectors between the start- and end-keyword.  $rdim$  is the number of real-space dimensions (keyword `realdimension`).
- default: compulsory keyword - no default; not applicable if  $dim = rdim$

- description: This keyword contains coordinates of the q-vectors.

#### A.5.3.24 name: realdimension

- value: positive integer smaller than or equal to *dim* (keyword **dimension**)
- default: 3
- description: Defines the dimension of the real space. Normally this is 3. For some special applications (two-dimensional diffraction on surfaces) other values than 3 can be chosen.

#### A.5.3.25 name: regularwidth

- value: *dim* positive real numbers
- default: regularization function not used
- description: BAYMEM has the capability of introducing a correlation between the neighboring pixels. The correlation is introduced by convolution of the “density” with a nD normalized Gaussian distribution. More about this topic can be found in Schneider (2001). The Gaussian can have different widths in different directions. The widths *w* are given as argument to **regularwidth**. The units of *w* are  $d_{min} = \frac{1}{|\vec{H}_{max}|}$ , where  $|\vec{H}_{max}|$  is the longest reciprocal vector present in the input dataset.

#### A.5.3.26 name: spacegroup

- value: text shorter or equal to 132 characters
- default: empty
- description: Symbol of the (super)space group. Currently not used in the program.

#### A.5.3.27 name: symmetry - endsymmetry

- value: each line contains definition of one symmetry operator
- default: compulsory keyword - no default
- description: This keyword contains the complete definition of the symmetry with exception of the centering vectors. Each line contains one symmetry operator. The format of the symmetry operators corresponds to the conventions used in the International Tables for Crystallography. If the symmetry operator is  $\{\mathbf{R}|\tau\}$ , then the format of each entry is:

$$\tau_1 + R_{11}x_1 + R_{12}x_2 + \dots + R_{1n}x_n \quad \tau_2 + R_{21}x_1 + R_{22}x_2 + \dots + R_{2n}x_n \quad \dots$$

Example — n-glide perpendicular to b:

$$1/2+x_1 \quad -x_2 \quad 1/2+x_3$$

The translation components can be given either as fractions or decimal numbers.

#### A.5.3.28 name: **symtable**

- value: yes/no
- default: no
- description: BAYMEM calculates so called symmetry table at the beginning of each run. This symmetry table contains all information about the symmetry of the pixel grid. This calculation is quite time-consuming. To save computer time in subsequent calculations with the same grid and symmetry, the symmetry table can be written out in a file called jobname.BMsymtb. BAYMEM will write the file jobname.BMsymtb only if setting **symtable** **yes** is present in the input file. If the file jobname.BMsymtb exists, BAYMEM reads the symmetry information from that file instead of calculating it. Generally, this option is useful only if many calculations with the same symmetry setting are planned. Note that the .BMsymtb file can be very large, up to several GB for large grids.

Once the file jobname.BMsymtb exists, BAYMEM will read it regardless of the value of **symtable**. This setting influences only the writing of the file.

#### A.5.3.29 name: **title**

- value: text shorter or equal to 132 characters
- default: compulsory keyword - no default
- description: The title of the job. It is used in the output files to identify the individual calculations. It is recommended, but not necessary, to change the title with every new calculation.

#### A.5.3.30 name: **voxel**

- value: *dim* positive integers
- default: compulsory keyword - no default

- description: Defines the division of the unit cell. Each number corresponds to the number of pixels along one axis of the (superspace) unit cell. The division must obey the symmetry of the unit cell, i.e. a center of any pixel must be mapped by the symmetry operators onto itself or onto a center some other pixel. This means that for example the numbers of pixels along the directions of the screw axes  $2_1$ ,  $3_1$ ,  $4_1$ ,  $6_2$  and  $6_1$  must be multiples of 2, 3, 4, 3 and 6, respectively. Numbers with small prime factors should be preferred, to take the full advantage of the speed of the Fast Fourier Transform. Combinations of powers of two or three are especially favorable. The largest prime factor of all divisions must be smaller than 23.

## A.5.4 Examples of typical input files

### A.5.4.1 Example 1.

This is an example of a simple input file for the calculation of a 3D electron density of a monoclinic crystal using a flat prior density. The Sakata-Sato algorithm is selected, while the alternative setting for the MEMSsys algorithm is commented out:

```

title oxalic acid
dimension 3
initialdensity flat
outputfile example1.m81
outputformat jana

algorithm S-S AUTO 1.0
#algorithm MEMSsys 4 1 1.0 1.0 0.05

cell 6.1005 3.4999 11.9554 90.0 105.781 90.0
voxel 64 32 128
spacegroup P21/n
centro yes
electrons 132

symmetry
  x1      x2      x3
  1/2-x1 1/2+x2 1/2-x3
  -x1     -x2     -x3
  1/2+x1 1/2-x2 1/2+x3
endsymmetry

fbegin
  2  0  0  25.3459292  0.0000000  0.2727374

```

```

  4  0  0  10.4668808  0.0000000  0.1478727
    .
    .
    .
  5  4 -1   4.1934419  0.0000000  0.1320773
  1  5 -1   1.9409568  0.0000000  0.1921479
  2  5 -1  -0.6319270  0.0000000  0.5103144
endf

```

#### A.5.4.2 Example 2.

The following input file can be used for determination of accurate charge density of a 4D structure. It uses prior density and prior-derived F-constraints (keyword `priorsf`). The generalized F-constraint of order 4 is used. The input and output formats are BMascii. This format allows easy transfer of the densities between different platforms.

```

title Example 2
dimension 4

initialfile prior_density.asc
initialdensity BMascii
outputfile example2.asc
outputformat BMascii

algorithm MEMSys 4 1 1. 1. 0.05
conorder 4
priorsf 0.89 1.5 0.01 1

cell 7.5281 5.8851 10.437 90. 90. 90.
voxel 128 100 162 32
spacegroup Pnma(a00)0ss
electrons 248
qvector
0.4794 0. 0.
endqvector
centro yes
centers
# the 0 0 0 0 centering vector can be omitted
# here it is given just for illustration
0.0 0.0 0.0 0.0
endcenters
symmetry
  x1      x2      x3      x4
  x1 1/2-x2  x3 1/2+x4

```

```

1/2+x1      x2 1/2-x3 1/2+x4
1/2+x1 1/2-x2 1/2-x3      x4

      -x1      -x2      -x3      -x4
      -x1 1/2+x2      -x3 1/2-x4
1/2-x1      -x2 1/2+x3 1/2-x4
1/2-x1 1/2+x2 1/2+x3      -x4
endsymmetry

```

```

fbegin
  0  0  0  0      248.0000000      0.0000000      0.1000000
  2  0  0  0      -37.4445880      0.0000000      0.2325634
  4  0  0  0       8.2858164      0.0000000      0.0570781
      .
      .
      .
  1  2  18  1       0.1344953      0.0000000      0.2110144
  2  2  18 -1      -0.1234955      0.0000000      0.2823512
  2  2  18  0       1.9918284      0.0000000      0.0583801
endf

```

## A.6 Description of the output

The most important output of the MEM calculation is the optimized electron density. Apart from this output, there are several other files containing information about the input data, data processing, symmetry, iteration and results. All files except for the density file have names of the form `jobname.BM*`. If several runs are performed with the same jobname, all the “`jobname.BM*`” files except for `.BMsymtb` are appended, not overwritten.

### A.6.1 Electron density

#### A.6.1.1 Format BMascii

In this format, the electron density of all pixels in the unit cell is written with six values per line in exponential format, preceded by a four-line header. The pixels are sorted first by increasing first coordinate, then second, then third etc.

The file has this form:

```

dimension real_dimension
pixel_division

```

lattice parameters a b c alpha beta gama volume  
 minimum and maximum of the map  
 density values, six numbers per line (multiple occurrences)  
 ⋮

For example:

```

  4   3
    128   100   162   32
  5.41530 12.33200 6.78930 90.00000 90.00000 90.00000 453.40
  1.041386E-02 4.063997E+01
  2.348115E-02 2.380756E-02 2.477587E-02 2.641150E-02 2.877340E-02 3.185024E-02
  3.561728E-02 4.012891E-02 4.537618E-02 5.122452E-02 5.765039E-02 6.476191E-02
  7.245219E-02 8.037046E-02 8.832136E-02 9.632531E-02 1.042432E-01 1.116911E-01
  ⋮

```

### A.6.1.2 Format BMbinary

This is a double precision binary format of BAYMEM. The order of numbers is the same as in the ascii format, only the minimum and maximum of the map is omitted in the binary format. Dimension, real dimension and pixel division is written as integers, all following numbers are written as double precision floating point numbers.

### A.6.1.3 Format jana, janap1

This is the format of the crystallographic software package Jana2000 (Petříček & Dušek, 2000). Its standard extension is .m81. It stores the electron density in a single-precision direct-access binary format. It is beyond the scope of this manual to fully describe this format. The density file written in the format jana contains only the pixels in one unit cell ( $0 \dots N_i - 1$  in each direction,  $N_i$  is the pixel division in the direction  $i$ ); format janap1 contains also the border of the unit cell, e. g. pixels with coordinates  $0 \dots N_i$  in each direction  $i$ .

## A.6.2 File jobname.BMout

This file contains all important information about the input data, data processing and results of the MEM run. It consist of three parts:

- Summary of the input data: This part contains the most important information collected by the program from the input file. Its content is self-explanatory. Following BMout file was produced by the input file in Example 2. (Section A.5.4.2):

```

Title: Example 2
Input: example2.BayMEM
Dimension of superspace: 4
"Real" dimensions: 3
Cellparameters (a b c alpha beta gamma Volume):          7.52810  5.88510  10.43700  \
                                                         90.00000  90.00000  90.00000  462.40
Reciprocal cellparameters (a b c alpha beta gamma Volume): 0.1328356 0.1699206 0.0958130  \
                                                         90.00000  90.00000  90.00000  2.162644E-03
Pixel (a b c...):          128  100  162  32
Electrons per unit cell:   248.0000
Type of initial density file: BMascii
Initial density filename:  prior_density.asc
Initial density correction type: none
Algorithm type is set to MEMSsys
The settings are:
  Method: 4
  NBand : 1
  Aim   : .10000D+01
  Rate  : .10000D+01
  Utol  : .50000D-01
Constrained moment order: 2

Spacegroup: Pnma(a00)0ss
Centrosymmetric structure: No Friedel-pairs are computed while expanding reflections!

q-vectors: 1
1:      0.4794000    0.0000000    0.0000000
Symmetry operations: 8

Symmetry operations: 1 through 3
  1.0  0.0  0.0  0.0  0.000  1.0  0.0  0.0  0.0  0.000  1.0  0.0  0.0  0.0  0.500
  0.0  1.0  0.0  0.0  0.000  0.0 -1.0  0.0  0.0  0.500  0.0  1.0  0.0  0.0  0.000
  0.0  0.0  1.0  0.0  0.000  0.0  0.0  1.0  0.0  0.000  0.0  0.0 -1.0  0.0  0.500
  0.0  0.0  0.0  1.0  0.000  0.0  0.0  0.0  1.0  0.500  0.0  0.0  0.0  1.0  0.500

Symmetry operations: 4 through 6
  1.0  0.0  0.0  0.0  0.500 -1.0  0.0  0.0  0.0  0.000 -1.0  0.0  0.0  0.0  0.000
  0.0 -1.0  0.0  0.0  0.500  0.0 -1.0  0.0  0.0  0.000  0.0  1.0  0.0  0.0  0.500
  0.0  0.0 -1.0  0.0  0.500  0.0  0.0 -1.0  0.0  0.000  0.0  0.0 -1.0  0.0  0.000
  0.0  0.0  0.0  1.0  0.000  0.0  0.0  0.0 -1.0  0.000  0.0  0.0  0.0 -1.0  0.500

Symmetry operations: 7 through 8
-1.0  0.0  0.0  0.0  0.500 -1.0  0.0  0.0  0.0  0.500
  0.0 -1.0  0.0  0.0  0.000  0.0  1.0  0.0  0.0  0.500
  0.0  0.0  1.0  0.0  0.500  0.0  0.0  1.0  0.0  0.500
  0.0  0.0  0.0 -1.0  0.500  0.0  0.0  0.0 -1.0  0.000

F-Constraints input/expanded: 3970 30045
P-Constraints input/expanded: 15270 118968
G-Constraints input/expanded: 0 0

```

- Information about initial and final status of the iteration: Contains starting and ending time of the iteration, initial and final R-values and related quantities. Part of the BMout file corresponding to Example 2 is show here. The lines beginning with # are comments and are not present in the file:

```
Date of iteration start: 30.01.2003 Time: 14:03.58
```

```
Initial state:
```

```
R = 0.9725      Rw = 0.7779
RF= 0.9725      RwF= 0.7779
```

```
RG= 0.0000      RwG= 0.0000
Entropy: 0.0000000E+00
```

# Sum of calculated (mem) and observed (obs) amplitudes of F- and G-constraints

```
Sum Fmem= 2.480E+02      Sum Gmem= 0.000E+00
Sum Fobs= 9.031E+03      Sum Gobs= 0.000E+00
Sum all F and G mem= 2.480E+02
F-Constraint 2.373E+03      G-Constraint 0.000E+00
```

```
Date of iteration end: 01.02.2003 Time: 09:41.56
After          38 Cycles of iteration
Elapsed CPU time:      2628 min 28 sec
```

Final state:

```
R= 0.0137      Rw = 0.0159
RF= 0.0137      RwF= 0.0159
RG= 0.0000      RwG= 0.0000
Entropy: -3.0085513E+02
Sum Fmem= 8.914E+03      Sum Gmem= 0.000E+00
Sum Fobs= 9.031E+03      Sum Gobs= 0.000E+00
Sum all F and G mem= 8.914E+03
F-Constraint: 9.964E-01      G-Constraint: 0.000E+00
```

```
F-Constraints input/expanded:      3970      30045
```

# P-constraints denote the F-constraints calculated from the prior density

```
P-Constraints input/expanded:      15270      118968
G-Constraints input/expanded:           0           0
```

- List of the reflections: The list contains information about all input reflections and (optional) extra reflection (see keyword `extra - endextra`):

```
F-Constraints:
#   h   k   l...   A/Gobs      B      A/Gmem      B      DeltaF  \
          Sigma      DeltaF/Sigma  sinth/l
1:   2   0   0   0   -37.4445880   0.0000000   -37.7395357   0.0000000   -0.2949477 \
          0.2325634      -1.2682464   0.132835
2:   4   0   0   0    8.2858164   0.0000000    8.1621250   0.0000000    0.1236914 \
          0.0570781      2.1670549   0.265671
:
:
```

All input F-constraints are listed.  $\Delta F = |F_{obs}| - |F_{calc}|$ ,  $\text{sinth}/l$  denotes  $\sin(\theta)/\lambda$ . reflections with  $\Delta F > 3 \times \text{Sigma}$  and  $\Delta F > 6 \times \text{Sigma}$  are marked with # and ! at the end of the line.

### A.6.3 File `jobname.BMlog`

This is the log-file for all messages and informations produced by BAYMEM during its run-time. The file can be separated into several parts:

- report from the reading of the input file: This part contains error messages about missing or doubled compulsory keywords, and information about missing or doubled optional keywords. The part has form:

```
Error!!! Statement either missing or doubled: cell
Error!!! Statement either missing or doubled: voxel
Info: Statement not included or doubled: expandedlog
Info: Statement not included or doubled: file
Info: Statement not included or doubled: conorder
```

```
    2 errors found in the input file!
There are    3 infos!
```

If a missing or doubled compulsory keywords are encountered, BAYMEM terminates with an error message written to the standard output. It is recommended to always check this part of the BMlog file. Even non-fatal infos can indicate a problem in the input file.

- Summary of the input data: This part is almost identical with the corresponding part of the `.BMout` file (Section A.6.2).
- List of all input reflection with components of the structure factor or square-root of the intensity of the G-constraints, amplitude of the structure factor, sigma, assignment to a g-group (zero for F-constraints; see keyword `gbegin - endg`), multiplicity of each reflection, and some other diagnostic information.
- Information about the total number of voxels and number of voxels in asymmetric unit:

```
Voxels in unitcell      :      66355200
Voxels in asymmetric unit:      8294402
```

- A list of reflections is produced, that contains all reflections that are equivalent by symmetry to other reflections in the input file. If such equivalent reflections are found, the program terminates with an error message written to the standard output and to the BMlog file.
- If the prior-derived F-constraints are used, this list will contain also the structure factors calculated from prior density. The format is identical with the format of experimental F-constraints.

- If setting `expandedlog yes` is present in the input file, then the BMlog file will contain a full list of all reflections expanded by the symmetry operators from the input file. This listing is suppressed by default. In the default case, only this summary is printed:

Listing of expanded reflections suppressed, summary follows:

Totals of expanded reflections:

```
F-Constraints:   30045
P-Constraints:  118968
G-Constraints:      0
Alltogether   :  149013
```

- Record of the progress of the iteration: The style of this part depends of the type of algorithm in use.

*Sakata - Sato algorithm*: A record identical to the record in the BMout file is written to the BMlog file at the beginning of the iteration. If the automatic determination of the starting  $\lambda$  is allowed (keyword `settings`), following information occurs in the BMlog file:

Automatic calculation of starting lambda: the value set to 0.3144E-02

Following statistics is written into the log file after each cycle:

```
Cycle:          392
Lambda: 0.1308E-01
Test: 0.2313      Charge increase factor: 1.0002
R = 7.596E-03    Rw = 6.674E-03
RF= 7.596E-03   RwF= 6.674E-03
RG= 0.000E+00   RwG= 0.000E+00
Entropy: -3.5944897E-01      Entropy shift: -4.512E-04
          L=-3.6019225E-01
Constrained moment number: 4
Sum Fmem= 4.799E+03      Sum Gmem= 0.000E+00
Sum Fobs= 4.801E+03      Sum Gobs= 0.000E+00
Sum all F and G calc= 4.799E+03
F-constrained moment 5.246E-02      G-constrained moment 0.000E+00
Combined FG Constraint :           0.998      Constraint shift: 5.136E-03
Combined FPG Constraint:           0.057      Constraint shift: 2.891E-04
Aim:                               1.000
FCon(1)= 5.231E-02      FCon(2)= 7.993E-02      GCon(1)= 0.000E+00      GCon(2)= 0.000E+00
FCon(3)= 1.688E-01      FCon(4)= 5.246E-02      GCon(3)= 0.000E+00      GCon(4)= 0.000E+00
FCon(5)= 1.635E+00      FCon(6)= 2.888E-02      GCon(5)= 0.000E+00      GCon(6)= 0.000E+00
FCon(7)= 2.806E+01      FCon(8)= 1.153E-02      GCon(7)= 0.000E+00      GCon(8)= 0.000E+00
```

The majority of the text is self-explanatory or has been explained in Section A.6.2. The meaning of the remaining statements is given here:

Lambda: The Lagrange multiplier. For more description see Section A.3.1.

Test:  $\text{Test} = 1 - \cos(\nabla S \cdot \nabla C) / (|\nabla C| \cdot |\nabla S|)$ , i.e. one minus the cosine of the angle between the gradients of the entropy and of the constraint. The angle

is zero for the ideal MaxEnt solution and consequently Test should be close to zero, too. However, there is no guarantee that the Sakata-Sato algorithm leads to an ideal MaxEnt solution. Therefore, a larger deviation of test from zero does not necessarily indicate a problem in the computation and/or input data. The higher value of Test may be caused by the inadequacy of the approximations used in the Sakata-Sato algorithm.

Charge increase factor: Ratio of total charge of the new  $\rho_{MEM}$  and  $\rho_{MEM}$  of the previous cycle before the new density is normalized. Large values of this factor indicate too large change between the two cycles. If the automatic lambda-control is enabled, the last cycle will automatically be repeated with a decreased value of lambda, if the charge increase factor exceeds 100. If the automatic lambda-control is disabled, only a warning is printed to the BMlog file.

Entropy: The total entropy of the unit cell:

$$S = - \sum_{i=1}^{N_{pix}} \rho_i \ln \frac{\rho_i}{\tau_i} \quad (\text{A.6})$$

L: The total maximized Lagrangian:

$$L = S - \lambda C \quad (\text{A.7})$$

Constrained moment number: Order of the generalized constraint (see keyword `conorder`).

Combined FG constraint: Constraint calculated only from the experimental data present in the input file. If this value becomes smaller than aim (keyword `settings`), the iteration is considered to be converged.

Combined FPG constraint: Constraint calculated from all data including the prior-derived F-constraints (keyword `priorsf`). This quantity is the measure of the convergence of the algorithm. If the constraint shift between the FPG constraints of successive cycles is negative, the calculation is considered to diverge. This line occurs only if the prior-derived F-constraints are used.

FCon(i), GCon(i): Values of the  $i^{th}$  moments of the distribution of the normalized residuals. The odd values should remain close to zero, the even values should converge to one. These values allow the user to estimate the quality of the distribution of the normalized residuals before the end of the iteration.

MEMSYS *package*: Prior to beginning of the iteration, check of consistency of the transformation routines is performed. Output of this check is a real

number. If the check is successful, the number is very small, comparable to the numerical accuracy of the calculation. For double precision calculations, the value of check should not exceed  $10^{-14}$ . The result of the check is written to the BMlog file:

Result of input data check: 0.3803E-17

**Important:** It is strongly recommended to check this number at the beginning of the calculation, especially if a completely new dataset is used. If this check fails, the calculation will not lead to correct results. For more information see Section A.8.

The information logged at each cycle is produced by the MEMSYS5 package. User should refer to MEMSYS5 manual for description of the output (Gull & Skilling, 1999b). Here only the description of the most important values will be given. The standard form of the output is:

```
Iteration      5
  Entropy === -1.4524E-01   Test === 0.0214   Chisq === 7.6539E+03
   Omega  ===  0.260387   dist === 0.2746   Alpha === 7.3870E+03
  Ntrans  ===          74   Code  === 001010
```

The most important indicators are **Test**, **Omega** and **Code**. **Test** is defined as:

$$\text{Test} = 1 - \cos(\nabla S \cdot \nabla C) / (|\nabla C| \cdot |\nabla S|)$$

i.e. one minus the cosine of the angle between the gradients of entropy and constraints. **Test** is zero for the ideal MaxEnt solution. In the MEMSYS algorithm, this value is a crucial indicator of the quality of the MaxEnt solution. The value should be low at the end of the iteration, say less than 0.1. **Omega** is an indicator of the progress of the iteration. Iteration is stopped only if **Omega** is equal to  $1 \pm$  internal accuracy (see keyword **settings**). **Code** is a string of ones and zeroes. Iteration will not stop before all digits in **Code** are zero. For the meaning of individual positions in **Code** please refer to the MEMSYS5 user manual.

Note, that one cycle of MEMSYS iteration is not comparable with one cycle of iteration of Sakata-Sato algorithm. In each iteration cycle of MEMSYS several “subcycles” are performed. The number of total direct and inverse Fourier transforms performed during one iteration cycle is given as **Ntrans** in the last line of the output of each cycle.

#### A.6.4 File `jobname.BMhst`

One of the basic assumptions underlying the principle of the F- and G-constraints is that the noise in the data is distributed randomly with a Gaussian distribution. Thus, the proper solution should produce normalized residuals ( $|F_{obs}| -$

$|F_{MEM}|/\sigma(F_{obs})$  that have a Gaussian distribution. The file jobname.BMcheck contains a representation of the histogram of normalized residuals for an easy assessment of the quality of the distribution of the normalized residuals. This is an example of the histogram:

```

Start of histogram
Title: Sample histogram
Prior type: flat
10.06.2003 Time: 09:31.08
Weighting: No
Constrained moment: 2
Rescaled by 100/ 105
|D-F|/sigma(D): # of appearances : graphical representation
-4.6  1 |X
-4.4  0 |
-4.2  0 |
-4.0  0 |
-3.8  0 |
-3.6  0 |
-3.4  0 |
-3.2  0 |\
-3.0  1 |\
-2.8  2 |X\
-2.6  1 |X \
-2.4  3 |XXX \
-2.2  2 |XX  \
-2.0  9 |XXXXXXXX \
-1.8  7 |XXXXXXX \
-1.6  20 |XXXXXXXXXXXXXXXXX \
-1.4  34 |XXXXXXXXXXXXXXXXXXXXXXXXX\
-1.2  39 |XXXXXXXXXXXXXXXXXXXXXXXXXXXX \
-1.0  49 |XXXXXXXXXXXXXXXXXXXXXXXXXXXXXXXX \
-0.8  75 |XXXXXXXXXXXXXXXXXXXXXXXXXXXXXXXXXXXX\XXXXXX
-0.6  87 |XXXXXXXXXXXXXXXXXXXXXXXXXXXXXXXXXXXXXXXXXXXX\XXXXXXXX
-0.4  96 |XXXXXXXXXXXXXXXXXXXXXXXXXXXXXXXXXXXXXXXXXXXXXXXXXXXX|XXXXXXXX
-0.2  104 |XXXXXXXXXXXXXXXXXXXXXXXXXXXXXXXXXXXXXXXXXXXXXXXXXXXXX|XXXXXXXX
0.0  105 |XXXXXXXXXXXXXXXXXXXXXXXXXXXXXXXXXXXXXXXXXXXXXXXXXXXXX|XXXXXXXX
0.2  101 |XXXXXXXXXXXXXXXXXXXXXXXXXXXXXXXXXXXXXXXXXXXXXXXXXXXXX|XXXXXXXX
0.4  98 |XXXXXXXXXXXXXXXXXXXXXXXXXXXXXXXXXXXXXXXXXXXXXXXXXXXXX|XXXXXXXX
0.6  79 |XXXXXXXXXXXXXXXXXXXXXXXXXXXXXXXXXXXXXXXXXXXXXXXXXXXXX/
0.8  69 |XXXXXXXXXXXXXXXXXXXXXXXXXXXXXXXXXXXXXXXXXXXXXXXXXXXXX/XX
1.0  45 |XXXXXXXXXXXXXXXXXXXXXXXXXXXXXXXXXXXX /
1.2  27 |XXXXXXXXXXXXXXXXXXXXXXXXXXXX /
1.4  31 |XXXXXXXXXXXXXXXXXXXXXXXXXXXX /
1.6  17 |XXXXXXXXXXXXXXXXXXXX /
1.8  24 |XXXXXXXXXXXXXXXXXX/XXXXX
2.0  8 |XXXXXXX /
2.2  8 |XXXXXX/
2.4  4 |XXX/
2.6  3 |XX/
2.8  2 |X/
3.0  1 |/
3.2  0 |/
3.4  0 |
3.6  2 |XX
3.8  0 |
4.0  0 |
4.2  0 |
4.4  0 |
4.6  1 |X
4.8  1 |X
5.0  1 |X
5.2  0 |
5.4  0 |
5.6  0 |
    
```

```

5.8  0 |
6.0  1 |X
6.2  0 |
6.4  0 |
6.6  0 |
6.8  0 |
7.0  0 |
7.2  0 |
7.4  0 |
7.6  0 |
7.8  0 |
8.0  0 |
8.2  0 |
8.4  0 |
8.6  0 |
8.8  1 |X
Statistics:
#      F          G      Combined
1  7.397E-01  0.000E+00  7.397E-01
2  1.007E+00  0.000E+00  1.007E+00
3  2.443E+00  0.000E+00  2.443E+00
4  3.552E+00  0.000E+00  3.552E+00
5  6.807E+01  0.000E+00  6.807E+01
6  3.451E+01  0.000E+00  3.451E+01
7  4.244E+03  0.000E+00  4.244E+03
8  3.434E+02  0.000E+00  3.434E+02
End of histogram

```

The header contains basic information about the MEM run. The time refers to the time of writing of the histogram and is almost equal to the time of writing the output electron density. **Weighting** and **Constrained moment** refer to the static weighting (keyword **conweight** and to the order of the generalized F-constraint (keyword **conorder**), respectively.

The main body of the histogram consists of a representation of the distribution of normalized residuals. The interval between the minimum and maximum normalized residue is divided in steps of 0.2. The number at the beginning of each line denotes the center of each interval. The next number in line gives the number of normalized residuals falling into that interval. The number of crosses (X) in each line corresponds to number of residuals in each interval, rescaled by a factor given in the header of the histogram, if the number of normalized residuals in any interval exceeds 100. Three types of slashes (\ | /) outline the ideal Gaussian distribution.

After the main body of the histogram, a list of moments of the distribution is printed, separated into contribution of F-constraints and G-constraints. The even moments are normalized so, that the expected value of the ideal Gaussian distribution is 1. Ideal Gaussian value of the odd moments is zero.

### A.6.5 File **jobname.BMcheck**

This file allows the user to graphically check the quality of the MaxEnt solution. The file is produced only if the keyword **memcheck** is present in the input file. For closer description of the underlying theory see keyword **memcheck**. The file has this format:

```

# Algorithm: MEMSys
# direct space gradient
# number    dS/drho      dC/drho    multiplicity
   686  -0.10099E+01   0.26331E-03    8
  1372  -0.10160E+01  -0.17682E-03    8
  2058  -0.10429E+01  -0.45650E-03    8
  2744  -0.10190E+01  -0.53921E-03    8
  3430  -0.10327E+01  -0.22974E-03    8
  4116  -0.10345E+01  -0.21474E-04    8
      .
      .
      .

# reciprocal space gradient:
#    j      dS/dF(j)      dC/dF(j)    multiplicity
   1    0.98691E-02   -0.26485E+01    1
   2   -0.19613E-01   -0.32598E+02    2
   3    0.93420E-02    0.21646E+02    2
   4    0.45182E-02    0.10621E+02    2
   5   -0.10662E-02   -0.14466E+01    2
   6   -0.21129E-02   -0.18777E+01    2
      .
      .
      .

```

The pixels in the direct-space gradient are sampled so, that the total number of samples corresponds to the number given by the keyword `memcheck`. The list of reflections in the reciprocal-space part is complete. If a chart of second vs. third columns is plotted, the points should form a straight line in case of an ideal MaxEnt solution.

### A.6.6 File `jobname.BMsymtb`

This is a binary file containing the information about the symmetry of the discrete unit cell. It is intended for internal use in BAYMEM. This file is written only if enabled in the input file (keyword `symtable`). If the file `jobname.BMsymtb` exists, the symmetry information is read from the file and the time-consuming calculation of the symmetry information is not performed. Having this file can be useful, if many runs with identical symmetry settings are planned. However, note that the `BMsymtb` file can be very large (several GB for more-dimensional unit cells). The file is never deleted by BAYMEM.

## A.7 Run-time interaction with the program

### A.7.1 Program-to-user communication

Almost all messages from the program are written into the BMlog file (Section A.6.3). This is because the MaxEnt runs might take very long time and the terminal BAYMEM has been run from might have been closed before the MaxEnt run has finished. Therefore, user should always check the BMlog file for possible warnings and error messages, especially in the initial stages of the runs. Few exceptions exist, when an error message is written both to the BMlog file and to the standard output. These exceptions concern problems encountered during the reading of the data, i.e. at the very beginning of the run.

### A.7.2 User-to-program communication

All information necessary to run BAYMEM is given in the input file. However, there is a limited set of commands, that can be passed to the program during its run-time. The commands must be written in the file `jobname.BMcom`. The existence and contents of this file is checked by the program and if some known command is found, it is performed and the file is deleted. No multiple commands are allowed in the BMcom file. The commands are case-sensitive. The most convenient way to pass a command to BAYMEM is to use the command echo:

```
$ echo "command" > jobname.BMcom
```

The allowed commands are:

- **DENSITY *filename***: If this command is found, the current  $\rho_{MEM}$  is written to the file specified in the command and the iteration continues.
- **STOP**: If this command is found, the iteration is stopped, like if the maximal allowed number of cycles were exceeded. The output density and all output files are written.
- **RATE *value***: This command applies only to the algorithm MEMSys. It allows the user to change the value of parameter RATE specified originally in the keyword `settings`. Higher values of RATE speed up the convergence, but too high values can cause failure of the algorithm. For more information on this problem see Section A.8. The information about the change of RATE is written in the BMlog file.

## A.8 Troubleshooting

- **Problem:** BAYMEM terminates very quickly without writing any output density.

**Solution:** Check the jobname.BMlog file for possible reports on errors in the data, like some missing or mistyped keywords or non-unique set of reflections.

- **Problem:** The “input data check” in the file jobname.BMlog returns too large value.

**Solution:** This indicates some inconsistency in the input parameters or data. Most probable reason is that the symmetry operators do not form a space group. Check also, whether the keyword `centro` is consistent with the symmetry operators. All symmetry operators of the space group must be listed, including those related by the center of symmetry. Another possibility is that the list of reflections in the input file contains reflections, that are systematically extinct. Such reflections must not be present in the input list! Such a situation can occur, if the reflections have been indexed in other symmetry (or only other setting of the space group) that the symmetry operators refer to.

- **Problem:** The Cambridge algorithm converges smoothly up to certain value of omega, but then oscillates around that value without reaching the final value  $\Omega = 1$ .

**Solution:** This usually indicates inconsistency in the number of electrons given in various places. The total number of electrons given by the keyword `electrons` must be consistent with the value of  $F(000)$  in the input reflection list and - if applicable - with the number of electrons in the prior electron density. BAYMEM does not automatically normalize the prior electron density to the expected number of electron. BAYMEM normalizes the prior electron density only on users' explicit request (keyword `correction`).

- **Problem:** The Cambridge algorithm converges very slowly, the change in Omega between cycles is very small.

**Solution:** If none of the previously described problems applies, you may have chosen too low value of RATE. Try to increase it either in the input file (keyword `settings`) or during the iteration (recommended; see Section A.7.2). In general, more symmetrical structures can have higher RATE, up to 15 or 20 in extreme cases. **Important:** Do not increase RATE too much, better increase it by small amount several times. Watch the value of Test. If Test starts to increase, do not increase Rate further.

Increasing Rate too much can (and probably will) lead to serious problems with convergence.

If the value of RATE is already high and the convergence is still slow, consider increasing the standard uncertainty of the  $F(000)$  structure factor (keyword `fbegin - endf`). But do not increase it too much, or you end up with a problem described below!

- **Problem:** The Cambridge algorithm converges, but the value of Test is high.

**Solution:** The two most probable reasons for this problem are too large value of RATE or too large value of  $\sigma(F(000))$ . Try to decrease them and repeat the calculation. Under special circumstances (with very informative prior and/or data with large standard uncertainties), the condition on the value of the constraint is reached sooner than the proper MEM path is found. This can be sometimes also solved by decreasing RATE, or by decreasing the internal accuracy (keyword `settings`).

- **Problem:** The Sakata-Sato algorithm converges very slowly, virtually stops converging.

**Solution:** The convergence of Sakata-Sato algorithm is not guaranteed. However, slow convergence can be caused by various errors in the input file. It is recommended to try calculation with the Cambridge algorithm, if possible. If the Cambridge algorithm converges, the problem is in the Sakata-Sato algorithm. If none of the two algorithms converge, the problem is in the data. In that case (or if the Cambridge algorithm is not available), try to see solutions of previous problems.

# Appendix B

## EDMA - A computer program for analysis of electron-density maps in arbitrary dimension

### User manual

#### B.1 Introduction

The Maximum Entropy Method (MEM) is nowadays well established as a powerful tool for a model-free image reconstruction. In crystallography it has found applications in the reconstruction of the electron density in the unit cell (von der Linden et al., 1998). One of its promising applications is the reconstruction of the electron density of the incommensurately modulated structures in the higher-dimensional unit cell. This can be used for a model-free determination of the shapes of the modulation functions, a result which is not achievable with the standard refinement methods.

However, the output from the MEM is a discrete  $n$ -dimensional array of values of the electron density representing a sampling of the true continuous electron density. Such a type of output does not allow a straightforward quantitative interpretation and extraction of all the relevant information, like the position of the atoms, charge partitioning between the atoms and ultimately the shape of the modulation functions. It is precisely the task of the program EDMA to provide the necessary software tools for such an analysis and extraction. The program can extract an exact position of the atomic maxima from any discrete electron density map, the charge of individual atoms, and the center of the charge, all this as a function of the superspace coordinates in case of higher-dimensional densities.

EDMA is optimized for work with the superspace densities, but since the 3D densities are but a special case of the general nD density, EDMA is fully capable of the analysis of ordinary 3D-periodic structures, too.

The theoretical and mathematical background of the various aspects of the analysis is given in Section 2.9 of this thesis.

## B.2 Technical details

### B.2.1 Programming language and system requirements

EDMA is written in the programming language Fortran 90. It has been compiled and tested on two copcomputers:

- Compaq AlphaStation ES40 with 500MHz 64-bit Alpha EV6 RISC processor and with Compaq Fortran Compiler V5.5-1877-48BBF
- Silicon Graphics Fuel with 500MHz IP35 MIPS R14000 processor and with MIPSPro Fortran compiler V7.4

The program obeys Fortran 90 standards and should be therefore compilable with any F90 compiler.

The program does not have any special system requirements. It does not use a graphical interface and the input can be edited with any plain text editor such as vi, nedit or emacs. However, it should be noted that the requirements for the system memory are quite high. The program stores the whole electron density and some smaller arrays in RAM to achieve reasonable speed of computation. Since the electron density maps can be very large (up to the order of several GB in case of high-resolution 4-D maps), the memory requirements are correspondingly high. However, these requirements are not higher than of the program BAYMEM. Thus, any computer used for computation of the electron density map with BAYMEM can be used for analysis of that map with EDMA.

### B.2.2 Execution

The program is executed with command

```
EDMA input_file
```

where `input_file` is the full name of the ASCII file containing input parameters (see Sections B.3.2, B.3.3 and B.3.4). There are no other command-line options.

### B.2.3 Standard run of the program

This is an example of a standard run of the program, if no error has been encountered in the input and during the execution:

```

Reading the density map Example.m81
t= 0.000
Extracting the electron density in real dimensions:
Integrating charge of the atoms:
t= 0.040
Extracting the electron density in real dimensions:
Integrating charge of the atoms:
67%
.
.
.

```

The last line shows always the progress of the current task in percent. The sentence "Integrating charge of the atoms" appears only if setting `centerof-charge yes` is present in the input file (Section B.3.3.6).

The output goes standardly to the standard output. Should EDMA run after closing of the terminal it was launched from, the output must be redirected to some temporary file, for example:

```
EDMA input_file > edma.tmp
```

## B.3 Specification of the input

### B.3.1 Types of input

EDMA requires two input files. The first file contains the values of the electron density. EDMA supports electron density files in the .m81 format of JANA2000 (Petříček & Dušek, 2000)<sup>1</sup>. EDMA supposes that the density was produced with the program BAYMEM. The density must be defined in points  $x_i = 0, 1/n_i, 2/n_i, \dots, (n_i - 1)/n_i$  where  $n$  is number of pixel in each direction  $i$ . This is the standard produced by BAYMEM. User is referred to the specification of BAYMEM for further details. Other formats can be added upon request.

The second file is an ASCII file containing specifications on the program parameters. In following sections, the expression "input file" means always the ASCII input file. The file with electron density is referred to as a "input density file" or "input density".

### B.3.2 Format of the ASCII input file

The input file is a free-format file based on keywords. Each keyword represents a specific parameter of the analysis and must be given a value.

---

<sup>1</sup>This crystallographic package is free and can be downloaded at <http://sun175.fzu.cz/jana/jana.html>

Multiple spaces anywhere in the file are handled as a single space. The lines containing the character '#' in the first column are treated as comments and not interpreted. Blank lines anywhere in the input file are ignored. The length of the interpreted part of the line is 132 characters, every text exceeding this length is ignored.

### B.3.3 Specification of keywords

There are two basic types of keywords. The first type is followed by one or more values on the same line:

```
keyword value1 [value2 value3...]
```

The second type has the form:

```
begin_keyword
line 1
line 2
...
end_keyword
```

Each line may contain one or more values.

The name of the keyword of the first type is a single word without spaces. The name of the keyword of the second type is a pair of initial and final word (separated by a hyphen in the following text).

- Each value can be a constant of type real, integer or character. The type of the parameters and their allowed values are specified bellow. Alternative values are separated by slashes.
- The keywords are either compulsory or optional. The compulsory keywords must be specified for the analysis to proceed. The optional keywords can be omitted. If the optional keyword is omitted, the default value is used. The compulsory keywords are indicated by "compulsory keyword - no default" in the item "default".
- description: Describes the function of the keyword, its influence on the output and relations to other keywords.

#### B.3.3.1 name: addborder

- value: positive real number
- default: 0

- description: The t-maps are non-periodic in one or more direction. However, some atomic basins span beyond the borders of the current basic-structure unit cell. The density of these parts of the atomic basins must be calculated explicitly in the aperiodic directions, if any characteristics depending on the atomic basins (see keywords `basin`, `centerofcharge`) should be computed. The keyword `addborder` controls, how large portion of the neighboring unit cell should be calculated for each t. The parameter gives the fraction of the neighboring unit cells to be added to the actual unit cell. For example, `addborder 0.4` will cause EDMA to calculate t-maps in interval -0.4 to 1.4 with respect to the actual unit cell in each aperiodic direction. It is user's responsibility to use sufficiently large value of `addborder`. If the number is too small, not all charge of the atom might be accounted for and consequently the extracted properties of the atoms at the border of the unit cell can be biased. On the other hand, the computational time increases approximately linearly with the value of `addborder` ( $t = t_{\text{addborder}=0}(1 + 2 * \text{addborder})$ ) and thus redundantly large values should be also avoided. The proper value depends on the particular crystal structure and can be determined by inspecting maps of atomic basins (see keyword `basins` and Section B.4.3).

### B.3.3.2 name: `atoms - endatoms`

- value: each line contains a name of an atom (maximum 8 characters) and three fractional basic-structure coordinates of that atom.
- default: compulsory keyword in combination with setting `maxima atoms - no default`
- description: This keyword is used only together with setting `maxima atoms` (see keyword `maxima` for more details). If used without this setting, it has no effect. Setting `maxima atoms` and omitting this keyword will lead to empty output. The analysis will proceed, but a warning will be printed on the standard output. If the keyword is present, the density is searched only for maxima close to the positions of the listed atoms (see keyword `tolerance`).

### B.3.3.3 name: `axisorder`

- value: string of *dim* non-repeating digits from 1 to *dim*, where *dim* in the dimension of the input density
- default: 123 ... *dim*

- description: The value of the keyword represents a permutation of the superspace axes to be used by the program. First three digits denote the real-space axes  $x, y, z$ , the rest determines the order of the axes in additional dimension. This setting is useful for composite structures, where the real-space and internal-space axes interchange their role for different subsystems. Consider for example a composite structure with the incommensurate direction along  $a$ . The most probable setting of the superspace axes will be  $a_1, b, c, a_2$ . Thus, the fourth axis will be the additional axis of the first subsystem and simultaneously the  $x$ -axis of the second subsystem. Consequently, to analyze the first subsystem of the composite structure, use setting `axisorder 1234`, to analyze the second subsystem, use setting `axisorder 4231`.

#### B.3.3.4 name: basins

- value: yes/no
- default: no
- description: EDMA uses Bader's formalism to assign charge to atoms (Bader, 1990; Section 2.9.2). This formalism divides the whole space into "atomic basins". The charge anywhere in the basin belongs to the atom lying in that basin. EDMA produces maps of these basins for each  $t$ , if setting `basins yes` is present in the input file. For more details about the maps of atomic basins see Section B.4.3.

#### B.3.3.5 name: cell

- value: six real numbers representing  $a b c \alpha \beta \gamma$
- default: compulsory keyword — no default
- description: Lattice parameters of the structure. If the output coordinates are fractional (see keyword `scale`) and the absolute values of atomic charges are not needed, the values of the lattice parameters do not influence the output.

#### B.3.3.6 name: centerofcharge

- value: yes/no
- default: no

- description: If **yes**, EDMA calculates the weighted average of coordinates of the pixels in the atomic basin of particular maximum, that have density values above some user defined limit (see keyword **chlimit**). These coordinates represent a center of charge of the atomic basin and thus an alternative position of the atom. This position can be more accurate than the position of maximal electron density if significant anharmonic movement is present. The atomic charges of individual atomic basins are calculated at the same time and written in the output.

#### B.3.3.7 name: **chlimit**

- value: real number between 0 and 1
- default: 0.25
- description: This keyword has effect only in combination with the setting **centerofcharge yes**. Only pixels with density  $\rho > \text{chlimit} * \rho_{max}$  ( $\rho_{max}$  is the maximum density of the atomic basin) are included in calculation of the center of charge and atomic charges.

#### B.3.3.8 name: **inputfile**

- value: valid specification of the file shorter or equal in length to 132 characters
- default: compulsory keyword - no default
- description: Specifies the file containing the input electron density map.

#### B.3.3.9 name: **maxima**

- value: **none/all/atoms**
- default: **atoms**, if atoms are defined in **atoms - endatoms**, **all** otherwise
- description: Setting **maxima all** will cause all maxima found in each t-map to be listed in the output file. Setting **maxima atoms** results in list of the maxima near the coordinates given in the keyword **atoms - endatoms**. This setting is suited for convenient extracting of the modulation functions for a list of atoms. Setting **maxima none** avoids any coordinates to be printed in the output. It can be useful if t-maps or maps of atomic basins are the only desired output. All maxima are subject to acceptance/rejection according to the keyword **plimit**.

**B.3.3.10 name: outputbase**

- value: any string of 132 or less characters valid as a part of a filename
- default: compulsory keyword - no default
- description: The value of this keyword defines the base of all output files. Each output file begins with this base and is given specific ending and/or extension. For closer description of the naming conventions see Section B.4.

**B.3.3.11 name: plimit**

- value: real number
- default: 0.0
- description: Only maxima with  $\rho_{max} > \text{plimit}$  are listed in the output. This keyword can be used to filter out spurious maxima, that are often present in the MEM maps and that are sometimes extremely increasing the number of maxima in the output.

**B.3.3.12 name: position**

- value: relative/absolute
- default: absolute
- description: Applies only to the setting `maxima atoms`. If `position` is `absolute`, the coordinates in the output are related to the origin of the unit cell. With setting `position relative` the output coordinates are relative to the basic structure coordinates specified in the keyword `atoms - endatoms`.

**B.3.3.13 name: qvectors - endqvectors**

- value: Each line contains coordinates of one q-vector. There must be  $(dim - 3)$  q-vectors between the start- and end-keyword.
- default: compulsory keyword — no default; not applicable if  $dim = 3$
- description: This keyword contains the definition of the q-vectors. The order in which they are listed must correspond to the order of axes defined in the keyword `axisorder`. For example, we can have a 5D map with a standard order of axes  $x_1 x_2 x_3 x_4 x_5$  and two q-vectors  $q_1$  and  $q_2$  corresponding to axes  $x_4$  and  $x_5$ . If the value of the keyword `axisorder` is 12345, the order of the q-vectors must be  $q_1, q_2$ . If the value of the keyword `axisorder` is 12354, the order of the q-vectors must be  $q_2, q_1$ .

**B.3.3.14 name: range**

- value: positive odd integer
- default: 7
- description: The electron density at arbitrary points is determined by spline interpolation of electron density in some neighborhood of that pixel. The keyword **range** defines the size of this neighborhood. With setting **range 7** the density of a given point is determined from the cube with side 7 pixels centered on that the point. The larger the value, the more “global” is the interpolation, but the longer computation time is needed. In practice value 7 produces almost identical results with any higher value and value 11 is perfectly safe. The value should be odd because of some symmetry of the interpolation. Even values will work too, but they are not recommended.

**B.3.3.15 name: scale**

- value: angstrom/fractional
- default: fractional
- description: Influences the scale of the atomic coordinates in output. Useful to obtain the modulation functions directly in Ångstroms.

**B.3.3.16 name: tlist - endtlist**

- value: Each line contains three real numbers between 0 and 1. There must be  $(dim - 3)$  lines between the begin- and end-keyword.
- default: compulsory keyword - no default; not applicable if  $dim = 3$
- description: Each line of this setting applies to one additional dimension in order determined by the keyword **axisorder**. Each line has format  $t_{start} t_{end} t_{step}$ .  $t_{start}$  defines starting  $t$  in that dimension,  $t_{end}$  defines ending  $t$  and  $t_{step}$  the steps between individual  $t$ 's. Real-dimensional sections are calculated starting with  $t_{start}$  in steps of  $t_{step}$  as long as the generated value does not exceed  $t_{end}$ .

**B.3.3.17 name: tmap**

- value: yes/no
- default: no

- description: Turns on/off saving of the t-sections to separate files for inspection. For the description of the output files and their naming conventions see Section B.4.2.

### B.3.3.18 name: tolerance

- value: positive real number
- default: 0.15
- description: This setting is applicable only in combination with the setting `maxima atoms`. The maximum is considered to belong to some atom (from the list of atoms defined by keyword `atoms - endatoms`) if the difference between the coordinates of the maximum and of the atom in Å is smaller than `tolerance` in all coordinates. Tolerance should be selected larger than the largest modulation. At the same time it must not be too large to avoid assigning possible neighboring maxima to the atoms.

## B.3.4 Examples of input files

### B.3.4.1 Example 1.

This is the simplest possible input file applicable only to the 3D densities. The output will be a list of fractional coordinates of all maxima present in the map. The filename of the output will be `example1.coo`.

```
inputfile example1.m81
outputbase example1
cell 1. 1. 1. 90. 90. 90.
```

### B.3.4.2 Example 2.

A run of EDMA with this input file would extract all significant maxima (above  $50 \text{ e}/\text{Å}^3$ ) from eleven t-sections. The structure is supposed to be a (3 + 1)D modulated structure. It could be used for a preliminary analysis of the map with unknown positions of the atoms. The output will contain only the fractional coordinates of the maxima. All eleven t-sections would be written to files.

```
inputfile example2.m81
outputbase example2
cell 3.128 3.128 8.245 90. 90. 120.
plimit 50.
maxima all
scale fractional
centerofcharge no
```

```
tmap yes
```

```
qvector  
0. 0. 0.2356  
endqvector
```

```
tlist  
0.0 1.0 0.1  
endtlist
```

### B.3.4.3 Example 3.

This example uses most of the options EDMA offers. It leads to determination of the modulation functions of the two listed atoms of the second subsystem of the composite structure  $(\text{LaS})_{1.14}\text{NbS}_2$ . The modulation will be listed relative to the basic-structure coordinates in Å and would contain 26 points:

```
inputfile LaSNbS_6626.m81  
outputbase LaSNbS_6626_2nd  
cell 5.7983 5.7972 22.9555 90. 90. 90.  
tolerance 0.08  
range 11  
plimit 20.  
chlimit 0.20  
axisorder 4231  
maxima atoms  
position relative  
scale angstroem  
centerofcharge yes
```

```
qvector  
1.7536 0. 0.  
endqvector
```

```
tlist  
0.0 1.0 0.04  
endtlist
```

```
atoms  
La2 0.0 0.00069 0.32733  
S2 0.0 0.50701 0.30005  
endatoms
```

## B.4 Description of the output

### B.4.1 File outputbase.coo

The principal output file has the name `outputbase.coo` (see keyword `outputbase`). It consists of two parts: the header and the data. The header contains information about the input parameters and the density map. Its contents might vary depending on the input parameters, but it is self-explaining. The header of the output file of example 3 in previous section will look like this:

```
# Analysis of the density map LaSNbS_6626.m81
# Dimension of the map : 4
# Division of the map : 64 64 256 64
# Order of the axes : 4231
# Range for spline interpolation: 11
# Cell: 3.3065 5.7972 22.9555 90.0000 90.0000 90.0000
# q-vectors:
# 1.75360 0.00000 0.00000
# limits and steps of t:
# start end step
# 0.00000 1.00000 0.04000
# The center of charge and total charge of atomic basins will be computed.
# The density in the incommensurate directions is calculated from -1.300 to 1.300
# The density limit for the pixel to be accepted in the charge calculation is 0.20*Rho(max)
# The scale of the output coordinates will be angstroem
# Positions of following atoms +- 0.080 and with density over 20.000 will be searched for maxima at each t
# Coordinates are related to the input coordinates of the atoms.
# La2 0.00000 0.00069 0.32733
# S2 0.00000 0.50701 0.30005
```

The header is terminated with a blank line.

The format of the data part depends on the value of the keyword `maxima`. If the setting `maxima atoms` is present in the input file, the data part is divided into blocks corresponding to individual atoms. Each line in the block corresponds to coordinates of the atom at one `t`-setting (see Example 1 below). Blocks are separated by two blank lines. The setting `maxima all` will divide the data part into blocks corresponding to different `t` settings. Each line in one block corresponds to one maximum found in that `t`-section (see Example 2 below). The blocks are separated by two blank lines.

Each non-blank line of the data part is either a comment (name of the atom or the `t` setting) or represents one maximum. The format in which the maxima are written is:

$$[t_1, t_2\dots] x_{max} y_{max} z_{max} [x_{coc} y_{coc} z_{coc} \text{charge}] \rho_{max}$$

Subscript *max* denotes coordinates of the maximum density, subscript *coc* denotes coordinates of the center of charge. The values of `t` appear only with the setting `maxima atoms` in the input file, the coordinates of the center of charge and the total charge is present only with the setting `centerofcharge yes` in the input file.

*Example 1:* This example corresponds to the input file of Example 3. in Section B.3.4:

```
# La2
0.000      0.000000  0.090418  -0.009751  0.000000  0.087569  -0.014710  39.2694  1545.26
0.040     -0.016656  0.088507  -0.010179  -0.018866  0.085161  -0.014261  39.1792  1480.91
0.080     -0.033310  0.083125  -0.010803  -0.035440  0.077808  -0.011317  38.2003  1329.34
.
.
.
0.920      0.033310  0.083125  -0.010803  0.035440  0.077808  -0.011317  38.2003  1329.34
0.960      0.016656  0.088507  -0.010179  0.018866  0.085161  -0.014261  39.1792  1480.91
1.000      0.000000  0.090418  -0.009751  0.000000  0.087569  -0.014710  39.2694  1545.26

# S2
0.000      0.000000  0.030583  0.015285  0.000000  0.024386  0.017255  8.6366  238.66
0.040      0.006026  0.031678  0.014303  0.007160  0.028037  0.012887  8.6486  238.53
0.080      0.011000  0.034211  0.011461  0.009563  0.035063  0.005891  8.6872  238.75
.
.
.
0.920     -0.011000  0.034211  0.011461  -0.009563  0.035063  0.005891  8.6872  238.75
0.960     -0.006026  0.031678  0.014303  -0.007160  0.028037  0.012887  8.6486  238.53
1.000      0.000000  0.030583  0.015285  0.000000  0.024386  0.017255  8.6366  238.66
```

*Example 2:* This example illustrates the output of the run with settings `maxima all` and `centerofcharge no`:

```
# t= 0.000
0.286588  0.423447  -0.000043  1646.19
0.859758  0.423054  0.000144  1686.35
0.000002  0.922324  -0.000232  1676.74
.
.
.
0.859758  0.423054  1.000144  1686.35
0.000002  0.922324  0.999768  1676.74
0.565829  0.922539  1.000209  1670.88

# t= 0.040
0.263647  0.423486  -0.000014  1664.99
0.836763  0.423222  0.000115  1648.99
-0.020935  0.922352  -0.000231  1648.26
.
.
.
0.836763  0.423222  1.000115  1648.99
-0.020935  0.922352  0.999769  1648.26
0.545323  0.922432  1.000222  1680.50

# t= 0.080
0.238186  0.423490  0.000012  1651.24
0.812799  0.423351  0.000080  1679.12
0.523123  0.922357  0.000231  1643.32
.
.
.
```

The readers using the plotting program `GNUPLOT` will have already recognized that the output is designed to be easily viewed with this program. The sign #

indicates comment lines, which are not interpreted by GNUPLOT, and double blank lines separate individual fields.

### B.4.2 t-maps

Sometimes it is desirable to have the opportunity to view the real-dimensional sections of the superspace density. EDMA calculates these sections and upon request (setting `tmap yes`) saves them as so called t-maps in the `.m81` format. The saved files can be then viewed with program CONTOUR of the software package JANA2000. The names of the t-maps follow the pattern

`outputbase_t1_t2...tn.m81`

`t1` etc. stands for the value of `t` in the corresponding dimension given to two decimal places. For 4D maps only one `t` is present, of course. `outputbase` represents the value of the keyword `outputbase` in the input file. The t-maps contain one basic unit cell extended according to the value of the keyword `addborder` in each non-periodic direction. Consequently, setting `addborder` to (say) 3 will produce a t-map, which covers 7 basic unit cells in each non-periodic direction. No t-maps can be produced from ordinary 3D maps.

Note on the naming of the t-maps and maps of atomic basins (Section B.4.3): The `t` coordinates are written in the file name with 2 decimal digits. If the real coordinates have more than two significant decimal digits, they are rounded in the filename (but not in the actual calculation). This can cause problems, if the step in `t` is smaller than 0.01 (see keyword `tlist - endtlist`). Two consecutive maps will then have the same name and the program will deny to write the second map with an error message

**Error! Cannot open density file *mapname***

The problem can be overcome by first writing all `t` maps with step larger or equal to 0.01 and then, in the second run, writing another set of t-maps with a modified `outputbase`.

### B.4.3 Atomic basins

According to Bader's formalism (Section 2.9.2), each point in the space can be assigned to one atom. This results in a division of the space into so called atomic basins. These basins are used to calculate the total charge of the atom and the center of charge. The atomic basins can be saved in the format `.m81` (see Section B.3.1). Each pixel in the map of atomic basins is assigned a number of maximum it belongs to. If such a map is viewed in the plotting program CONTOUR of the crystallographic package JANA2000, it appears in 2D sections as a mosaic of black fields (constant "density" = atomic basin of one atom) separated by lines on the border of the atomic basins, where an abrupt change of the number takes place. Due to the interpolation scheme used in CONTOUR, some borders

(those with large difference between the numbers of maxima) are separated by several close-lying lines rather than by a single line. The names of the maps of basins follow the pattern

`outputbase_basins_t1-t2...tn.m81`

`t1` etc. stands for the value of `t` in corresponding dimension. `outputbase` represents the value of the keyword `outputbase` in the input file. In the 3D case the map of basins has the name `outputbase_basins.m81`.

For a note on the naming of the output files see Section B.4.2.



# Bibliography

- Bader, R. F. W. (1990), *Atoms in Molecules: A Quantum Theory*, Clarendon Press, Oxford Science Publications, Oxford.
- Bagautdinov, B., Luedecke, J., Schneider, M. & Van Smaalen, S. (1998), ‘Disorder in the crystal structure of Cs<sub>2</sub>HgCl<sub>4</sub> studied by the maximum entropy method’, *Acta Crystallogr. B* **54**, 626–634.
- Becker, P. J. & Coppens, P. (1974), ‘Extinction within the limit of validity of the Darwin transfer equations. I. General formalism for primary and secondary extinction and their applications to spherical crystals’, *Acta Crystallogr. A* **30**, 129–152.
- Benabicha, F., Pichon-Pesme, V., Jelsch, C., Lecomte, C. & Khmou, A. (2000), ‘Experimental charge density and electrostatic potential of glycyl-L-threonine dihydrate’, *Acta Crystallogr. B* **56**, 155–165.
- Carvalho, C., Hashizume, H., Stevenson, A. & Robinson, I. (1996), ‘Electron-density maps for the Si(111) 7 × 7 surface calculated with the maximum-entropy technique using X-ray and electron-diffraction data’, *Physica B* **221**, 469–486.
- Collins, D. M. (1982), ‘Electron density images from imperfect data by iterative entropy maximization’, *Nature* **298**, 49–51.
- Coppens, P. (1997), *X-Ray Charge Densities and Chemical Bonding*, Oxford University Press, New York.
- Cucka, P. & Barrett, C. S. (1962), ‘The crystal structure of Bi and of solid solutions of Pb, Sn, Sb and Te in Bi’, *Acta Crystallogr.* **15**, 865–872.
- De Vries, R. Y., Briels, W. J. & Feil, D. (1994), ‘Novel treatment of the experimental data in the application of the maximum-entropy method to the determination of the electron-density distribution from X-ray experiments’, *Acta Crystallogr. A* **50**, 383–391.

- De Vries, R. Y., Briels, W. J. & Feil, D. (1996), 'Critical analysis of non-nuclear electron-density maxima and the maximum entropy method', *Phys. Rev. Lett.* **77**, 1719–1722.
- de Wolff, P. M., Janssen, T. & Janner, A. (1981), 'The superspace groups for incommensurate crystal structures with a one-dimensional modulation', *Acta Crystallogr. A* **37**, 625–636.
- Dinnebier, R. E., Schneider, M., Van Smaalen, S., Olbrich, F. & Behrens, U. (1999), 'Disorder determined by high-resolution powder diffraction: structure of pentamethylcyclopentadienyllithium', *Acta Crystallogr. B* **55**, 35–44.
- Dušek, M., Chapuis, G., Meyer, M. & Petříček, V. (2003), 'Sodium carbonate revisited', *Acta Crystallogr. B* **59**, 337–352.
- Garg, A. & Srivastava, R. C. (1979), 'Ammonium Tetrafluoroberyllate(II)', *Acta Crystallogr. B* **35**, 1429–1432.
- Giacovazzo, C., Monaco, H., L., Viterbo, D., Scordari, F., Gilli, G., Zanotti, G. & Cati, M. (1995), *Fundamentals of Crystallography*, Oxford University Press, Oxford, UK.
- Gilmore, C. J. (1996), 'Maximum entropy and Bayesian statistics in crystallography: a review of practical applications', *Acta Crystallogr. A* **52**, 561–589.
- Gull, S. F. & Daniel, G. J. (1978), 'Image reconstruction from incomplete and noisy data', *Nature* **272**, 686–690.
- Gull, S. F. & Skilling, J. (1984), 'Maximum entropy image reconstruction', *IEE Proc.* **131F**, 646–659.
- Gull, S. F. & Skilling, J. (1999a), *MEMSYS5 v1.2 program package, September 6, 1999*, Maximum Entropy Data Consultants Ltd., Suffolk, U.K.
- Gull, S. F. & Skilling, J. (1999b), *Quantified Maximum Entropy, MEMSYS5 Users' Manual*, Maximum Entropy Data Consultants Ltd., Suffolk, U.K.
- Haussermann, U., Soderberg, K. & Norrestam, R. (2002), 'Comparative study of the high-pressure behavior of As, Sb, and Bi', *unpublished*.
- Hirshfeld, F. (1977), 'Bonded-Atom Fragments for Describing Molecular Charge Densities', *Theoret. Chim. Acta* **44**, 129–138.
- Hogervorst, A. C. R. (1986), *Comparative study of the modulated structures in Rb<sub>2</sub>ZnBr<sub>4</sub> and in related compounds*, PhD. thesis, Delft, The Netherlands.

- Iizumi, M. Axe, J. D., Shirane, G. & Shimaoka, K. (1977), 'Structural phase formation in  $\text{K}_2\text{SeO}_4$ ', *Phys. Rev. B* **15**, 4392–4411.
- Iizumi, M. & Gesi, K. (1977), 'Incommensurate phase in  $(\text{ND}_4)_2\text{BeF}_4$ ', *Solid State Commun.* **22**, 37–39.
- Iversen, B. B., Jensen, J. L. & Danielsen, J. (1997), 'Errors in Maximum-Entropy Charge-Density Distributions Obtained from Diffraction Data', *Acta Crystallogr. A* **53**, 376–387.
- Janssen, T., Janner, A., Looijenga-Vos, A. & De Wolff, P. M. (1992), Incommensurate and commensurate modulated structures, *in* A. J. C. Wilson, ed., 'International Tables for Crystallography Vol. C', Kluwer Academic Publishers, Dordrecht, p. 797.
- Jauch, W. (1994), 'The maximum-entropy method in charge-density studies. II. General aspects of reliability', *Acta Crystallogr. A* **50**, 650–652.
- Jauch, W. & Palmer, A. (1993), 'The maximum-entropy method in charge-density studies: aspects of reliability', *Acta Crystallogr. A* **49**, 590–591.
- Jaynes, E. T. (1996), *Probability theory: The Logic of Science.*, <http://www.bayes.wustl.edu/etj/postscript>, Fragmentary Edition.
- Jobst, A. & van Smaalen, S. (2002), 'Intersubsystem chemical bonds in the misfit layer compounds  $(\text{LaS})_{1.13}\text{TaS}_2$  and  $(\text{LaS})_{1.14}\text{NbS}_2$ ', *Acta Crystallogr. B* **58**, 179–190.
- Kuhs, W. F. (1992), 'Generalized atomic displacements in crystallographic structure analysis', *Acta Crystallogr. A* **48**, 80–98.
- Kumazawa, S., Takata, M. & Sakata, M. (1995), 'On the Single-Pixel Approximation in Maximum Entropy Analysis', *Acta Crystallogr. A* **51**, 47–53.
- Makita, Y. & Yuiko, Y. (1974), 'Super-Lattice Structure of Ferroelectric  $(\text{NH}_4)_2\text{BeF}_4$  in the Nonferroelectric Phase below 182K', *J. Phys. Soc. Japan* **37**, 1470–1470.
- McMahon, M. I., Degtyareva, O. & Nelmes, R. J. (2000), 'Ba-IV-Type incommensurate crystal structure in group-V metals', *Phys. Rev. Lett.* **85**, 4896–4899.
- McMahon, M. I., Degtyareva, O., Nelmes, R. J., van Smaalen, S. & Palatinus, L. (2003), 'Incommensurate modulations of Bi-III', *Phys. Rev. Lett.* **submitted**.
- McMahon, M. I., Rekhi, S. & Nelmes, R. J. (2001), 'Pressure dependent incommensuration in Rb-IV', *Phys. Rev. Lett.* **87**, 055501.

- Neaton, J. B. & Ashcroft, N. W. (1999), 'Pairing in dense lithium', *Nature* **400**, 141–144.
- Nelmes, R. J., Allan, D. R., McMahon, M. I. & Belmonte, S. A. (1999), 'Self-hosting incommensurate structure of Barium IV', *Phys. Rev. Lett.* **83**, 4081–4084.
- Onodera, A. & Shiozaki, Y. (1979), 'X-Ray Study of Crystal Structures and Phase transition in Ferroelectric Ammonium Fluoberyllate  $(\text{NH}_4)_2\text{BeF}_4$ ', *J. Phys. Soc. Japan* **46**, 157–166.
- O'Reilly, D. E., Peterson, E. M. & Tsang, T. (1967), 'Nuclear Magnetic Resonance and Nonexponential Spin-Lattice Relaxation in Ferroelectric Ammonium Fluoroberyllate', *Phys. Rev.* **160**, 333–336.
- Palatinus, L. & van Smaalen, S. (2002), 'The Generalized F-constraint in the Maximum Entropy Method — a study on simulated data', *Acta Crystallogr. A* **58**, 559–567.
- Papoular, R. J., Collin, G., Colson, D. & Viallet, V. (2002), Direct imaging of fractional oxygen  $O_\delta$  in Hg-based High- $T_c$  superconductors, in B. Fry, ed., 'Proceedings of the 21<sup>st</sup> Workshop on Bayesian Inference and Maximum Entropy Methods in Science and Engineering', American Institute of Physics, Melville, NY.
- Papoular, R. J. & Gillon, B. (1990), 'Maximum entropy reconstruction of spin density maps in crystals from polarized neutron diffraction data', *Europhys. Lett.* **13**, 429–434.
- Papoular, R. J., Vekhter, Y. & Coppens, P. (1996), 'The Two-Channel Maximum-Entropy Method Applied to the Charge Density of a Molecular Crystal:  $\alpha$ -Glycine', *Acta Crystallogr. A* **52**, 397–407.
- Pepinsky, R. & Jona, F. (1957), 'New Ferroelectric Crystal Containing No Oxygen', *Phys. Rev.* **105**, 344–347.
- Petříček, V. & Dušek, M. (2000), *The crystallographic computing system JANA2000*, Institute of Physics, Praha, Czech Republic.
- Petříček, V., Gao, Y., Lee, P. & Coppens, P. (1990), 'X-ray analysis of the incommensurate modulation in the 2:2:1:2 Bi-Sr-Ca-Cu-O superconductor including the oxygen atoms', *Phys. Rev. B* **42**, 387–392.
- Pichon-Pesme, V., Lachekar, H., Souhassou, M. & Lecomte, C. (2000), 'Electron density and electrostatic properties of two peptide molecules: tyrosyl-glycyl-glycine monohydrate and glycyl-aspartic acid dihydrate', *Acta Crystallogr. B* **56**, 728–737.

- Pillet, S., Souhassou, M., Lecomte, C., Schwarz, K., Blaha, P., Rérat, M., Lichanot, A. & Roversi, P. (2000), 'Recovering experimental and theoretical electron densities in corundum using the multipolar model: IUCr Multipole Refinement Project', *Acta Crystallogr. A* **57**, 290–303.
- Press, W. H., Teukolsky, S. A., Vetterling, W. T. & Flannery, B. P. (1996), *Numerical Recipes in Fortran 77, Second Edition*, Cambridge University Press.
- Roversi, P., Irwin, J. J. & Bricogne, G. (1998), 'Accurate charge-density studies as an extension of Bayesian crystal structure determination', *Acta Crystallogr. A* **54**, 971–996.
- Sakata, M. & Sato, M. (1990), 'Accurate structure analysis by the maximum-entropy method', *Acta Crystallogr. A* **46**, 263–270.
- Sakata, M. & Takata, M. (1996), 'The Principle of the Maximum Entropy Method', *High Press. Res.* **14**, 327–333.
- Schneider, M. (2001), *Ph.D. thesis*, University of Bayreuth, Bayreuth, Germany.
- Schneider, M. & van Smaalen, S. (2000), 'Discrete Fourier transform in arbitrary dimensions by generalized Beevers-Lipson algorithm', *Acta Crystallogr. A* **56**, 327–333.
- Schwarz, U., Takemura, K., Hanfland, M. & Syassen, K. (1998), 'Crystal structure of Cesium-V', *Phys. Rev. Lett.* **81**, 2711–2714.
- Shannon, C. E. (1948), 'A mathematical theory of communication', *Bell Sys. Tech. J.* **27**, 379–423, 623–656.
- Sheldrick, G. M. (1997), *Computer program SADABS*, University of Gottingen.
- Shmueli, U., ed. (1996), *International Tables for Crystallography, vol. B*, Kluwer Academic Publishers, Dordrecht.
- Shore, J. E. & Johnson, R. W. (1980), 'Axiomatic derivation of the principle of maximum entropy and the principle of minimum cross-entropy', *IEEE Trans. Inform. Theory* **IT-27**, 26–37.
- Sivia, D. S. (1997), *Data Analysis — A Bayesian Tutorial*, Clarendon Press, Oxford, UK.
- Skilling, J. & Bryan, R. K. (1984), 'Maximum entropy image reconstruction: general algorithm', *Mon. Not. R. Astr. Soc.* **211**, 111–124.
- Srivastava, R. C., Klooster, W. T. & Koetzle, T. F. (1999), 'Neutron structures of ammonium tetrafluoroberyllate', *Acta Crystallogr. B* **55**, 17–23.

- Steurer, W. (1991), The N-dim Maximum-Entropy Method, *in* J. M. Perez-Mato, F. J. Zuniga & G. Madariaga, eds, 'Methods of Structural Analysis of Modulated Structures and Quasicrystals', World Scientific, Singapore, pp. 344–349.
- Strukov, B. A., Skomorokhova, T. L., Koptsik, V. A., Boiko, A. A. & Izrailenko, A. N. (1973), 'Thermal properties of ammonium fluoroberyllate crystals over a wide temperature range', *Sov. Phys. Cryst.* **18**, 86–88.
- Su, Z. & Coppens, P. (1997), 'Relativistic X-ray Elastic Scattering Factors for Neutral Atoms  $Z = 1-54$  from Multiconfiguration Dirac-Fock Wavefunctions in the  $0-12 \text{ \AA}^{-1} \sin(\theta)/\lambda$  Range, and Six-Gaussian Analytical Expressions in the  $0-6 \text{ \AA}^{-1}$  Range', *Acta Crystallogr. A* **53**, 749–762.
- van Smaalen, S. (1991*a*), 'Superspace group approach to the modulated structure of the inorganic misfit layer compound  $(\text{LaS})_{1.14}\text{NbS}_2$ ', *J. Phys. Condens. Matter* **3**, 1247–1263.
- van Smaalen, S. (1991*b*), 'Symmetry of composite crystals', *Phys. Rev. B* **43**, 11330–11341.
- van Smaalen, S. (1995), 'Incommensurate crystal structures', *Crystallogr. Rev.* **4**, 79–202.
- van Smaalen, S., Palatinus, L. & Schneider, M. (2003), 'Maximum Entropy Method in superspace', *Acta Crystallogr. A* **59**, 459–469.
- Villars, P. & Calvert, L. D. (1996), *Pearson's handbook of crystallographic data for intermetallic phases — Second Edition*, The Materials Information Society, Materials Park, Ohio, U.S.A.
- von der Linden, W., Dose, V., Fisher, R. & Preuss, R., eds (1998), *Maximum Entropy and Bayesian Methods*, Kluwer Academic Publishers, Dordrecht.
- Šlouf, M. (2001), *Ph.D. thesis*, Charles University, Prague, Czech Republic.
- Wang, C.-R., Tsutomu, K., Tomiyama, T., Yoshida, T., Kobayashi, Y., Nishibori, E., Takata, M., Sakata, M. & Shinohara, H. (2001), 'A Scandium Carbide Endohedral Metallofullerene:  $(\text{Sc}_2\text{C}_2)\text{C}_{84}$ ', *Angew. Chem. Int. Ed.* **40/2**, 397–399.
- Wieggers, G. A. (1996), 'Misfit layer compounds: structures and physical properties', *Prog. Solid State Chem.* **24**, 1–139.
- Wilson, A. J. C. & Prince, E., eds (1999), *International Tables for Crystallography, vol. C*, Kluwer Academic Publishers, Dordrecht.

- Yamamoto, A. (1982), 'Structure factor of modulated crystal structures', *Acta Crystallogr. A* **38**, 87–92.
- Yamamoto, K., Takahashi, Y., Ohshima, K., Okamura, F. & Yukino, K. (1996), 'MEM analysis of Electron-Density Distributions for Silicon and Diamond using Short-Wavelength X-rays (W  $K\alpha_1$ )', *Acta Crystallogr. A* **52**, 606–613.



# List of Figures

1.1	Schematic representation of a two-dimensional modulated crystal	3
1.2	Schematic representation of a two-dimensional composite crystal	4
1.3	Diffraction pattern of a modulated crystal	5
1.4	Diffraction pattern of a modulated crystal as a projection of the more-dimensional weighted lattice	7
1.5	Construction of the atomic domain in superspace	10
1.6	Schematic representation of a diffraction pattern of a composite crystal	11
1.7	Schematic representation of a superspace description of a composite structure	12
2.1	Section through $\rho_{MEM}$ of $\alpha'$ - $\text{NaV}_2\text{O}_5$ obtained with the classical and with the "true Bayesian" stopping criterion	27
2.2	Graphical representation of Eq. 2.24, and Eq. 2.25	28
2.3	Comparison of the electron densities obtained with the Sakata-Sato and Cambridge algorithms	29
2.4	Interpolation process in two dimensions	38
2.5	The assignment of a point to a local maximum in a continuous electron density and in a discrete electron density	42
3.1	The sections of the true electron density showing the oxalic acid molecule	50
3.2	Distribution of $ F_{obs} - F_{prior} /\sigma(F_{obs})$ as function of the resolution for different noise levels	52
3.3	Sections through the difference electron density map $\rho_{diff}$ showing one COOH group	55
3.4	The histograms of $\Delta F(\vec{H})/\sigma(\vec{H})$ for different constraints	56
3.5	The even central moments $m_2$ to $m_{16}$ of the histograms of all MEM-runs on the n2 datasets	57
3.6	$\rho_{MEM}$ and $\rho_{diff}$ obtained with the n2r1.00 dataset and with the uniform prior	60
3.7	MEM deformation electron density, $\rho_{MEM} - \rho_{pro}$	61

4.1	The true 1D density sampled on the grid with 128 pixels . . . . .	68
4.2	The difference densities from the calculations f12p0, f12p32 and f12p48 . . . . .	70
4.3	The structure factors $F_{MEM}$ , $F_{true}$ and $F_{prior}$ corresponding to $\rho_{MEM}$ from calculations f12p0, f12p32 and f12p48 . . . . .	71
4.4	The difference densities from the calculations f20p0, f20p32 and f20p48 . . . . .	72
4.5	The structure factors $F_{MEM}$ , $F_{true}$ and $F_{pro}$ corresponding to $\rho_{MEM}$ from calculations f20p0, f20p32 and f20p48 . . . . .	73
4.6	The difference densities from the calculations f28p0, f28p32 and f28p48 . . . . .	74
4.7	The structure factors $F_{MEM}$ , $F_{true}$ and $F_{pro}$ corresponding to $\rho_{MEM}$ from calculations f28p0, f28p32 and f28p48 . . . . .	75
4.8	Sections of $\rho_{MEM} - \rho_{true}$ of oxalic acid dihydrate in the plane of the oxalic acid molecule . . . . .	78
5.1	The average structure of $(\text{LaS})_{1.14}\text{NbS}_2$ . . . . .	80
5.2	Sections of the electron density $\rho_{obs}^{MEM}$ at the position of La . . . . .	81
5.3	Overview of the modulation functions of the independent atoms of $\text{LaS}_{1.14}\text{NbS}_2$ . . . . .	83
5.4	Modulation of the temperature factor and the occupancy of La compared to the values of $\rho_{calc}^{MEM}$ and $\rho_{obs}^{MEM}$ at the positions of the La atoms . . . . .	88
6.1	The basic structure of Bi-III projected along the tetragonal c-axis . . . . .	90
6.2	Perspective view of the supercell of Bi-III . . . . .	99
6.3	The modulation functions for displacements along $x$ of Bi1 and along $z$ of Bi2 . . . . .	101
6.4	2D sections of the electron density $\rho^{MEM}(\vec{x}_s)$ . . . . .	102
6.5	Distances between Bi1 and the neighboring atoms as a function of the fourth superspace coordinate . . . . .	104
6.6	Distances between Bi2 and the neighboring atoms as a function of the fourth superspace coordinate . . . . .	104
7.1	$x_2 - x_4$ sections of the difference Fourier map at the position of the F(2) atom . . . . .	114
7.2	A $x_2 - x_4$ section of the MEM electron density at the position of atom F(2) . . . . .	119
7.3	Modulation functions $u_i^y$ of the non-hydrogen atoms . . . . .	120
7.4	Modulation along $z$ of atom N(1) in the hypothetical incommensurate structure with second-order harmonic modulation . . . . .	121
7.5	View of the basic structure of AFB along the b-axis with axes of rotation of individual ions . . . . .	122

7.6	Perspective view of the basic structure along the b-axis with the layers with correlated modulations of the ions . . . . .	126
7.7	H...F distances shorter than 2.6 Å as a function of t . . . . .	127
7.8	Experimental and simulated profiles through the positions of the reflections -5 0 13 0, -6 0 13 2 and -1 5 0 0, -2 5 0 2 . . . . .	130



# List of Tables

2.1	Areas of the array ST used in BAYMEM . . . . .	21
3.1	Basic characteristics of the structure of the oxalic acid dihydrate .	49
3.2	Parameters of the simulated datasets of the oxalic acid dihydrate	51
3.3	The coincidence factors $C = \sum_{i=1}^{N_p}  \rho_{MEM}^i - \rho_{true}^i  / \sum_{i=1}^{N_p} \rho_{true}^i$ for Max-Ent calculations using the uniform prior and $\rho_{fou}$ . . . . .	54
3.4	The coincidence factors $C = \sum_{i=1}^{N_p}  \rho_{MEM}^i - \rho_{true}^i  / \sum_{i=1}^{N_p} \rho_{true}^i$ for Max-Ent calculations using the procrystal prior and $\rho_{pro} + \rho_{df}$ . . . . .	58
3.5	Extremals of the artifacts at different resolutions for noise level n0 and F <sub>2</sub> -constraint . . . . .	60
4.1	Parameters of the Gaussians $G = A \exp\left(\frac{-(x-c)^2}{2\sigma^2}\right)$ used to construct the prior and true 1D densities . . . . .	68
4.2	Entropy of $\rho_{MEM}$ from different calculations . . . . .	76
5.1	Computational details and results for the MEM calculations on LaS <sub>1.14</sub> NbS <sub>2</sub> . . . . .	82
5.2	The difference between the modulation functions extracted from $\rho_{calc}^{MEM}$ and those contained in the model . . . . .	85
5.3	The difference between the modulation functions extracted from $\rho_{calc}^{MEM}$ and those contained in the model . . . . .	85
6.1	Experimental data of Bi-III . . . . .	93
6.2	R-values for the refinements of the basic structure and three different models for the modulation . . . . .	95
6.3	Values of parameters after the refinements of Models 1, 2 and 3 .	96
6.4	Atomic parameters for the approximate superstructure model . .	98
6.5	Parameterization of the electron density and resulting R-values of the MEM calculations . . . . .	100
7.1	Experimental data of AFB . . . . .	112

7.2	Basic structure coordinates of the incommensurate structure corresponding to the final refined model. . . . .	115
7.3	Modulation functions of the displacive modulation . . . . .	115
7.4	Basic structure coordinates of the superspace description of the low temperature structure . . . . .	117
7.5	Modulation functions of the superspace description of the low temperature structure . . . . .	118
7.6	Parameters of the MEM calculations . . . . .	119
7.7	Summary of the geometric parameters of the crystallographically independent complex ions in the incommensurate structure . . . .	123
7.8	Selected interatomic distances and angles in the refined structure of the incommensurate phase . . . . .	124
7.9	Characteristics of the rotations of the complex ions . . . . .	124

## Acknowledgements

At first place I would like to express my sincere thanks to my supervisor Prof. Dr. Sander van Smaalen. He has encouraged me to work on a very exciting topic and he has supported me during my work by uncountable hints and very fruitful discussions. I want to thank Peter Daniels for his support and cooperation during the X-ray diffraction experiments at DESY, Hamburg and Dipl. Chem. (FH) Karl-Ludwig Stork for almost immediate fulfilling of my wishes concerning synthesis of crystals. I am thankful to Dipl. Ing. (FH) Franz Fischer for his help with technical and administrative problems, especially with the maintaining of the computers. Dr. Markus Wunschel helped me a lot with the translation of the German summary of the thesis. Generally, the friendly atmosphere in the team of the Laboratory of Crystallography was an important factor for creation of this work. I would also like to thank to RNDr. Václav Petříček, CSc. and RNDr. Michal Dušek, CSc. for prompt answering of my questions and introducing new features “on request” in the computer program JANA2000. My thanks and acknowledgement go to my partner Ludmila Nývltová for reading the manuscript and especially for her comprehension and support during the long time of our separation.

This work was supported by Project SM55/1-4 of DFG.



# Erklärung

Dieses Dokument wurde vom Autor selbständig und nur mit den angegebenen Quellen und Hilfsmitteln erstellt. Der Autor hat bisher keine Promotionsversuche unternommen.

Bayreuth, den 03.09.2003